Cucurbit[*n*]uril-Dye Conjugate for Biorelevant Analytes Recognition and Distinction in Aqueous Media and Biofluids

Zur Erlangung des akademischen Grades eines

DOKTORS DER NATURWISSENSCHAFTEN

(Dr. rer. nat.)

von der KIT-Fakultät für Chemie und Biowissenschaften

des Karlsruher Instituts für Technologie (KIT)

genehmigte

DISSERTATION

von

M.Sc. Changming Hu

1. Referent: Prof. Dr. Pavel Levkin
2. Referent: Prof. Dr. Stefan Bräse

Tag der mündlichen Prüfung: 20. July 2022

Erklärung zur Dissertation

Hiermit erkläre ich, dass ich meine Dissertation selbstständig und ohne Benutzung anderer als der angegebenen Hilfsmittel angefertigt habe. Diese Dissertation wurde noch keiner Prüfungsbehörde oder einer anderen wissenschaftlichen Einrichtung zur Begutachtung vorgelegt.

I hereby declare that I have completed my dissertation independently, without using any other resources other than indicated. This dissertation has not yet been submitted to any examination authority or for grading at other academic institutions.

Changming Hu

Table of contents

1. Abstract

As a nature-inspired and nature-derived scientific field, supramolecular chemistry has contributed dramatically to achievements in various scientific fields ranging from catalysis to drug delivery and accelerated the advancement of the entire subject of chemistry. In this context, supramolecular chemists use non-covalent intermolecular interactions, which can be dynamic, to design molecular aggregates with unique physicochemical properties. Such non-covalent interactions are, for example, the hydrophobic interaction, π-π interaction, hydrogen bonding, electrostatic interaction, and the solvent effect. As synthetic molecular recognition systems and macrocyclic host-guest chemistry have advanced, more and more artificial synthetic host molecules with a recognition motif for specific guest(s) have been discovered and extensively investigated. Following the example of the naturally occurring host molecule cyclodextrin, the new generation of artificial synthetic host molecules is represented by cryptands, cucurbit[n]urils, calix[n]arenes, pillar[n]arenes, to name a few. More than a hundred years after their first synthesis, cucurbit[n]urils play a prominent role among macrocyclic hosts due to their outstanding binding affinities for guest molecules, resulting in the formation of host-guest complexes to be exploited in a variety of fields ranging from catalysis, materials chemistry and drug delivery applications.

Cucurbit[n]uril-based chemosensing systems have also been widely utilized in medical diagnostics to meet the requirement of biorelevant analytes recognition and detection by taking advantage of high binding affinities with drugs or metabolites. In combination with the indicators that equip the chemosensor with photophysical responsiveness, the reliable indicator displacement assay (IDA)-based chemosensing system has been researched by many supramolecular scientists for monitoring biophysical and enzymatic processes. However, besides their solubility limitations, the development of cucurbit[n]uril-based chemosensor that predictably binds to guests in biological buffers or fluids remains a challenge because ubiquitous salts play a negative role in the host-guest system, resulting in the dissociation of the non-covalent complex.

In this thesis, the novel cucurbit[7]uril IDA-based unimolecular chemosensors were synthesized, and the sensing strategies for biorelevant analytes recognition with salt-resistance in biological media were designed. In the first section of this work, a high-affinity indicator, berberine, linked CB7 unimolecular conjugate through a short ethylene glycol linker (CB7-BC) was developed and fully characterized. The chemosensors displayed exceptional resistance to dilution and salt effect other than traditional non-covalent reporter CBn pairs – an important aspect when it comes to the application of chemosensors in a real-world scenario. This chemosensor can selectively and quantitatively respond to Parkinson's drug amantadine (at the micromolar range) in a physiologically buffered media and genuine biofluids (*e.g.*, urine and saliva) even in the presence of potential competitors. The second section introduced an innovative salt-induced adaptive strategy to detect biorelevant analytes using a nitrobenzoxadiazole-cucurbit[7]uril chemosensor (CB7-NBD), allowing discrimination of multiple analytes in real biofluids such as urine, saliva, and human blood serum in the micromolar range. The readout fluorescent signal is individual and unique for each analyte due to the varied salt-adaptive behaviors of chemosensor and

Abstract

analyte complexes following the addition of different salts. This information can be translated into an intuitive pairwise difference using a data-driven approach. In addition, ion mobility measurements combined with density functional theory (DFT) calculation were used to investigate the binding mechanism and assess the potential conformation of complexes. Notably, this salt-adaptive system was exploited for sensing applications in real biofluids such as urine, saliva, and blood serum.

In summary, novel cucurbit[*n*]uril-based conjugated chemosensors were given as a practical solution to overcome the inevitable disintegration and dysfunction of traditional non-covalent host-guest chemosensors in the buffered medium with high salinity. These unimolecular conjugated chemosensors can realize the detection and recognition of biologically relevant analytes, and it opens up a constructive suggestion for the design of future functional macrocyclic chemosensors.

Kurzzusammenfassung / Abstract in German

Die supramolekulare Chemie hat als ein von der Natur inspiriertes und abgeleitetes wissenschaftliches Gebiet entscheidend zu den Errungenschaften in verschiedenen wissenschaftlichen Bereichen - von der Katalyse bis zur Verabreichung von Medikamenten - beigetragen und den Fortschritt der Chemie allgemein beschleunigt. In diesem Zusammenhang nutzen supramolekulare Chemiker nicht-kovalente intermolekulare Wechselwirkungen, welche dynamisch sein können, um molekulare Aggregate mit einzigartigen physikalisch-chemischen Eigenschaften zu entwickeln. Solche nicht-kovalenten Wechselwirkungen sind beispielsweise die hydrophobe Wechselwirkung, die π-π-Wechselwirkung, die Wasserstoffbrückenbindung, die elektrostatische Wechselwirkung und der Lösungsmitteleffekt. Mit den Fortschritten der synthetischen molekularen Erkennungssysteme und der makrozyklischen Wirts-Gast-Chemie wurden mehr und mehr künstliche synthetische Wirtsmoleküle mit einem Erkennungsmotiv für bestimmte Gäste entdeckt und eingehend untersucht. Neben dem natürlich vorkommenden Wirtsmolekül Cyclodextrin, gibt es eine neue Generation an künstlichen Wirtsmolekülen wie beispielsweise Kryptanden, Cucurbit[*n*]urile, Calix[*n*]arene oder Pillar[*n*]arene. Mehr als hundert Jahre nach ihrer ersten Synthese spielen Cucurbit[*n*]urile unter den makrozyklischen Wirtsmolekülen aufgrund ihrer hervorragenden Bindungsaffinitäten für Gastmoleküle und den daraus resultierenden Wirt-Gast-Komplexen eine herausragende Rolle, denn sie können in einer Vielzahl von Bereichen wie Katalyse, Materialchemie und Arzneimittelverabreichung genutzt werden.

Auch in der medizinischen Diagnostik werden auf Cucurbit[n]uril basierende Chemosensorsysteme häufig eingesetzt, um die Anforderungen an die Erkennung und den Nachweis biorelevanter Analyten zu erfüllen, wobei die oben erwähnten hohen Bindungsaffinitäten mit Arzneimitteln oder Metaboliten genutzt werden. In Kombination mit Indikatoren, welche den Chemosensor mit einer photophysikalischen Ansprechbarkeit ausstatten, wurde von vielen supramolekularen Wissenschaftlern der bewährte Indikatorverdrängungsassay (IDA) auf der Basis von Cucurbit[*n*]uril zur Überwachung biophysikalischer und enzymatischer Prozesse erforscht. Allerdings bleibt nicht nur aufgrund ihrer Löslichkeitsbeschränkung die Entwicklung eines Chemosensors auf Cucurbit[*n*]uril-Basis, welcher vorhersagbar Gäste in biologischen Puffern oder Flüssigkeiten bindet, eine Herausforderung, sondern auch durch die in Puffern und Biomedien allgegenwärtigen Salze , da diese zur Dissoziation des nicht-kovalenten Chemosensorkomplexes führt

Im Rahmen dieser Arbeit wurden das Design und die Synthese neuartiger, unimolekularer Chemosensoren auf Cucurbit[7]uril-IDA-Basis sowie eine Sensing-Strategie für die Erkennung biorelevanter Analyten mit Salzresistenz im biologischen Medium entwickelt. Im ersten Teil dieser Arbeit wurde ein hochaffiner Indikator, Berberin, welcher über einen kurzen Ethylenglykol-Linker mit dem unimolekularen Konjugat CB7 verbunden ist (CB7-BC), hergestellt und vollständig charakterisiert. Dieser Chemosensor zeigte im Vergleich zu herkömmlichen nicht-kovalenten Reporter-CB*n*-Paaren eine außergewöhnliche Resistenz gegenüber Verdünnung sowie Salzeffekten - ein wichtiger Aspekt, wenn es um die Anwendung von Chemosensoren in einem realen Szenario geht. Der Chemosensor reagiert

selektiv und quantitativ auf das Parkinson-Medikament Amantadin (im mikromolaren Bereich), in physiologisch gepufferten Medien und echten Bioflüssigkeiten (z. B. Urin und Speichel), sogar im Beisein von Kompetitoren.

Im zweiten Abschnitt wurde eine innovative, salzinduzierte, adaptive Strategie zum Nachweis biorelevanter Analyten unter Verwendung eines Nitrobenzoxadiazol-Cucurbit[7]uril-Chemosensors (CB7-NBD) eingeführt, welcher die Unterscheidung von mehreren Analyten in echten Bioflüssigkeiten wie Urin, Speichel und menschlichem Blutserum im mikromolaren Bereich ermöglicht. Das ausgelesene Fluoreszenzsignal ist für jeden Analyten individuell und einzigartig, da sich die Komplexe von Chemosensor und Analyt nach Zugabe verschiedener Salze unterschiedlich verhalten. Diese Information kann mit Hilfe eines datengesteuerten Ansatzes in eine intuitive paarweise Differenz übersetzt werden. Darüber hinaus wurden Ionenmobilitätsmessungen in Kombination mit Dichtefunktionaltheorie (DFT)-Berechnungen verwendet, um den Bindungsmechanismus zu untersuchen und die mögliche Konformation der Komplexe zu bewerten. Insbesondere wurde dieses salzadaptive System für Sensoranwendungen in realen Bioflüssigkeiten wie Urin, Speichel und Blutserum genutzt.

Zusammenfassend wurden im Rahmen dieser Arbeit neuartige konjugierte Chemosensoren auf Cucurbit[*n*]uril-Basis entwickelt, welche als praktische Lösung zur Überwindung des unvermeidlichen Zerfalls und der Funktionsstörung herkömmlicher nicht kovalenter Wirt-Gast-Chemosensoren in gepuffertem Medium mit hohem Salzgehalt dienen. Diese unimolekularen konjugierte Chemosensoren können sowohl den Nachweis als auch die Erkennung biologisch relevanter Analyten realisieren und ermöglichen einen neuen Weg für die Entwicklung künftiger funktioneller makrozyklischer Chemosensoren.

2. General Introduction

2.1. Supramolecular host-guest chemistry

In contrast to the more traditional covalent chemistry, supramolecular chemistry is generally defined as 'chemistry beyond the molecule' and based on non-covalent intermolecular forces.[1-4] The importance of supramolecular chemistry was accentuated by the 1987 Nobel Prize for Chemistry, recognizing the development and investigations of crown ether, host-guest, and molecular recognition chemistries through the outstanding contributions of Charles J. Pedersen, Jean-Marie Lehn, and Donald J. Cram.[5-7] Actually, the exploration of supramolecular chemistry has been underway for a century. Johannes Diderik van der Waals first postulated the existence of intermolecular forces in 1873. Emil Fischer hypothesized the fundamental principles of molecular recognition and host-guest chemistry, which took the form of a 'lock and key' model imitated from enzyme and substrate interaction in 1894.[8] Latimer and Roderbush described the hydrogen bond in 1920. The supramolecular chemistry originated from our environmental living biological processes, such as the substrate binding to the receptor, assembling nucleic acid and protein complex, forming cellular membranes, signal induction by neurotransmitters, and various biological processes.[9] Nowadays, supramolecular interactions are rationalized as tools for developing structures with specific functions. In 2016, Jean-Pierre Sauvage, Sir J. Fraser Stoddart, and Bernard L. Feringa shared the Nobel Prize in Chemistry for the design and synthesis of molecular machines,[10-12] and their work ranged from the reliable synthesis of catenanes and rotaxanes to molecule knots, rotary motors, shuttles, elevators, and even a nanocar. Meanwhile, more supramolecular chemists, *e.g.,* Bert Meijer (E. W. Meijer), Takuzo Aida, Samuel I. Stupp, *etc.,* explored supramolecular applications and expand the integration with other chemical fields.

After nearly half a century, supramolecular chemistry has moved from the conceptual stage into various practical application fields.[13-17] The key feature of supramolecular chemistry is the dynamic character of construction and exchange of components spontaneously.[18] This property endows the supramolecular entities to adjust to external stimuli, such as temperature, ion strength, pH, redox, and light.[19-23]

Among a series of non-covalent interactions (hydrogen bonding, electrostatic interaction, Van der Waals force, π-π stacking, metal-ligand coordination, hydrophobic interaction, *etc.*),[24] host-guest chemistry, as a branch of supramolecular chemistry, describes that the complexes are composed of two or more molecules that are held together in a unique structural relationship by forces other than covalent bonds.[25, 26] Host-guest systems are currently researched for various applications such as drug delivery,[27-29] detection and sensing[30, 31], environmental monitoring,[32-35] and the preparation of functional materials[36-38]. Typically, the hosts are equipped with a cavity corresponding to specific guest molecules with suitable structural properties. Macrocyclic components have been extensively studied and investigated in recent years, including cyclodextrin, cucurbit[*n*]uril, pillar[*n*]arene, calix[*n*]arene, *etc.* (Figure 2.1). They all exhibit the dynamically reversible complexation capabilities for a wide range of guest components.
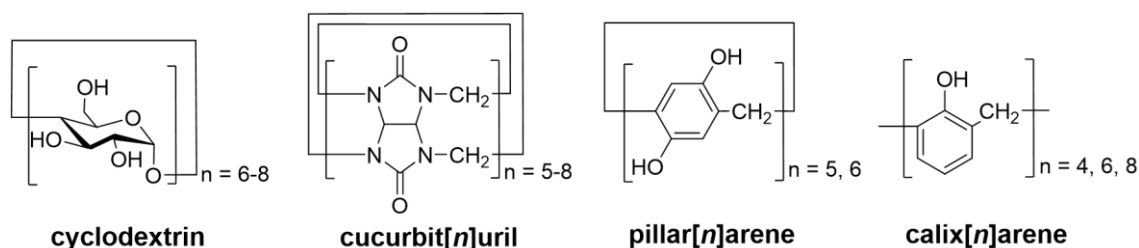
Figure 2.1 Chemical structures of typical macrocyclic hosts.

2.2. Cucurbit[*n*]uril in host-guest system

2.2.1.Historical development of cucurbit[*n*]uril

Among the numerous natural and artificial synthetic macrocyclic host molecules, Cucurbit[n]urils are widely employed in various research areas. In 1904, Eberhard Meyer firstly synthesized by chance CB6 by the condensation reaction between glycoluril and formaldehyde,[39] then the results were published by Behrend and co-workers in the following year.[40] However, it was only in 1981 that the cyclic structure of CB6 was experimentally confirmed by Freeman and coworkers when X-ray crystal data revealed the presence of six glycoluril units linked by pairs of methylene bridges[41] (Figure 2.2 (a)). Due to a general resemblance of this product to a gourd or pumpkin (family Cucurbitaceae), they proposed the trivial name *cucurbituril* for it. After another 20 years of development, new cucurbituril homologues containing five, seven, eight, and ten glycoluril units, were synthesized and characterized by the groups of Kim and Day.[42, 43] Since their discovery, the range of applications of cucurbituril has been expanded, as the larger cavity of larger CB*n* allows them to associate with a variety of guest molecules of different sizes and polarity (Figure 2.2 (b)). Also, higher CB*n* homologues were discovered gradually in the following time, such as inverted CB*n*,[44] *nor-seco*-CB*n*,[45] twisted CB14,[46] and others, CB5-CB8 have been studied and explored in a wide range of scientific research and fundamental applications.

	CB[5] (n=0)	CB[6] (n=1)	CB[7] (n=2)	CB[8] (n=3)
Portal diameter (Å)	2.4	3.9	5.4	6.9
Cavity diameter (Å)	4.4	5.8	7.3	8.8
Cavity volume (Å^3)	82	164	279	479
Outer diameter (Å)	13.1	14.4	16.0	17.5
Height (Å)	9.1	9.1	9.1	9.1
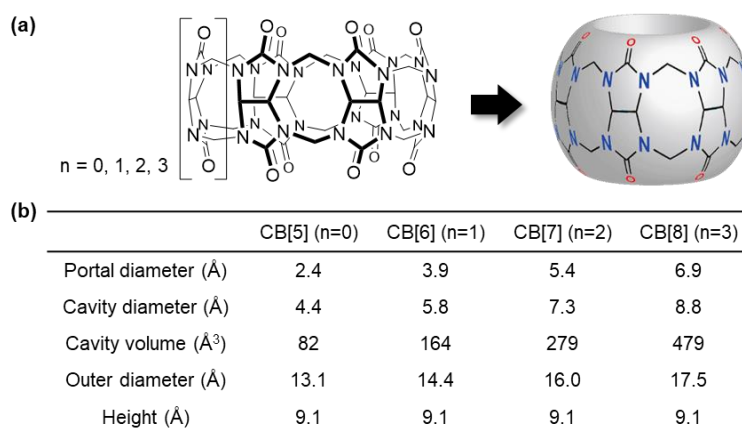
Figure 2.2 (a) Chemical structure and schematic illustration of cucurbit[*n*]uril. (b) Structural parameters of CB5 to CB8.

2.2.2.Synthesis and properties of cucurbit[*n*]uril

The synthesis of cucurbituril still follows the early acid-catalyzed condensation reaction of glycoluril and formaldehyde (Figure 2.3). According to Kim and Day's research,[42, 43] the yield ratio of each homologue can be controllable by adjusting the reaction conditions. The temperature of reaction and the acid concentration significantly impact the formation of CB*n*. The final distribution of each CB*n* homologue in the mixture is decided by the cyclization of precursor oligomers. For instance, almost no CB7 and CB8 are formed when the condensation reaction is done at high dilution because the high-dilution experimental conditions kinetically limited the rate that oligomers achieved a length beyond 5 or 6 units before they condensed. In another case, no CB*n* formed in concentrated HCl after 1 month at room temperature, but CB6 was almost quantitatively produced after 2 months in concentration H_2SO_4 due to the dehydrating ability of concentrated H_2SO_4.[43]
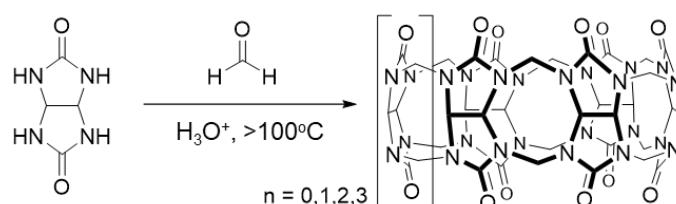
Figure 2.3 CB*n* synthesis by acid-catalyzed condensation reaction

CB*n*, particularly CB6, is characterized by excellent thermal stability and chemical inertness. The beginning of CB*n* decomposition is around 250°C, and the foremost step of decomposition can even reach 425°C.[47] Moreover, CB*n* is fully adapted in the whole pH range or in the presence of strong redox reagents. The non-toxic and photochemical inert properties of CB*n* make it an interesting candidate for biological and spectroscopic sensing applications.[48-50] The evaluation of the biocompatibility of CB*n* has been carried out by many researchers in mice and in blood cells, which exhibited excellent profiles and no apparent damage to the cell directly.[51, 52] These features can pave the road for the application of biomaterial fabricated by CB*n* in drug delivery and have been proved *via* numerous published related works.

The solubility of CB*n* is commonly low in the water compared to the similarly-sized cyclodextrin homologues in size relatively, except for CB5 and CB7 (20~30 mM). However, all of CB*n* homologues are well soluble in acidic water as well as the in aqueous alkali metal ion solution.[53]

In contrast to the well-known macrocyclic host of cyclodextrin, the structural features of CB*n* are characterized by the symmetric and barrel-shaped structure with highly electron-density carbonyl portals and a hydrophobic cavity. Notably, the portal diameter of CB*n* is almost approximately 2 Å narrower than the cavity diameter, which results in significant steric barriers to guest association and dissociation.[54] Thus, the size-selectivity of CB*n* to guests exceeds those for cyclodextrin. Except for the analytes with a negative charge, almost organic molecules with the fit size to the CB*n* cavity are bound with an appreciable affinity. Due to the ion-dipole interaction with carbonyl portals, positively charged guests show a relatively higher affinity than their neutral counterparts.[55-58] Taking advantage of the relatively

rigid structure, CBn can provide a great size- and charge-selectivity for many biologically and medicinally relevant analytes in aqueous media.

As shown in the electrostatic potential map (Figure 2.4 (a)), a more negative electrostatic potential (blue-colored) is observed at the portals of CB7 than β-cyclodextrin (β-CD)[53], and this feature is also prevalent in other CB homologues. (Figure 2.4 (b)).[59] In contrast to the high electronegative CBn portals, the inner cavity of CBn is significantly hydrophobic without any functional groups or electron pairs. This combined feature endows CBn the high affinity and selectivity for specific classes of guest molecules, *e.g.,* protonated hydrophobic amino acids, alkylated ammonium, and imidazolium. Furthermore, the electrostatic effects and hydrophobic interactions play an essential role in the binding properties of CBn homologues.
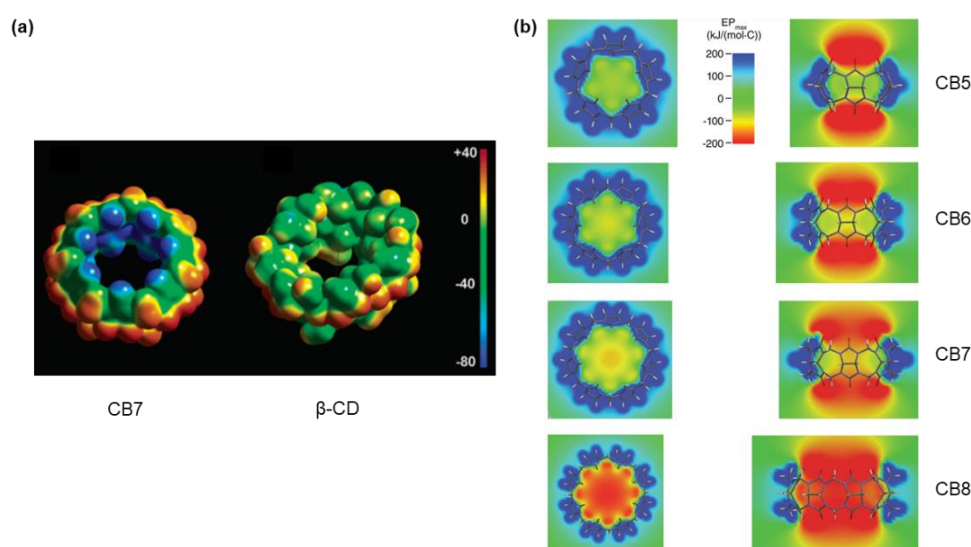
Figure 2.4 Electrostatic potential surfaces of CB7 and β-CD. Reprinted by permission from ref.53. Copyright © 2003, American Chemical Society. (b) Calculated electrostatic potential for CB5, CB6, CB7, CB8. Reprinted by permission from ref.59. Copyright © 2012, American Chemical Society.

Additionally, the size selectivity is also an essential factor for determining the binding affinity of guests to CBn. The packing coefficient (PC) is frequently used to estimate the fit goodness of inclusion complexes.[60] As shown in equation 2.1, the PC of a compound is defined as the ratio between the sum (V_w) of the van der Waals volumes (v_w) of the n molecules in given volume (V) and the volume (V). A PC value of around $55 \pm 8\%$ is considered the best binding affinity between host and guest species according to the Mcozzi-Rebek rule.[61] The higher or lower PC values would accompany a lower affinity. Nau and coworkers reported that the PC value analysis for known guests with hydrophobic binding motifs revealed average values of 47% for CB5, 58% for CB6, 52% for CB7, and 53% for CB8, which are well in agreement with 'the 55% solution' rules.[60]

$$PC = \frac{\sum_{i=1}^{n} v_w^i}{V} = \frac{V_W}{V} \tag{2.1}$$

In addition to size selectivity (*e.g.,* PC value), hydrophobic effects and ion-dipole interactions are the main effects responsible for the strong binding affinities observed in CBn, and the release of 'high-energy'

water as the primary driving force is also one of the most potent interpretations (Figure 2.5). In general, due to the water competing strongly for hydrogen bonds and solvating charged species, the complexation binding affinity of other non-covalent systems is typically weakened in the presence of water compared to the organic environment. However, in the case of complexation with neutral guests by CBn, the release of the confined water in the cavity is a critical determinant in the binding process.[62-64] The substantial enthalpic gain caused by these confined water molecule releases, namely 'high-energy water release', plays a primary driving force upon guests binding and the expelled water then engages in more robust H-bonding networks in aqueous bulk. The smaller cavity volume will limit the number of high-energy water molecules (*e.g.,* CB5 and CB6), but the larger volume of the cavity will allow the H-bonding among the cavity water (*e.g.,* CB8). This principle explained that these rigid macrocycles display a solid affinity to uncharged guests, and CB7 shows a higher binding affinity in comparison with smaller homologues CB5/CB6 and larger CB8.

= high-energy H$_2$O   = bulk H$_2$O
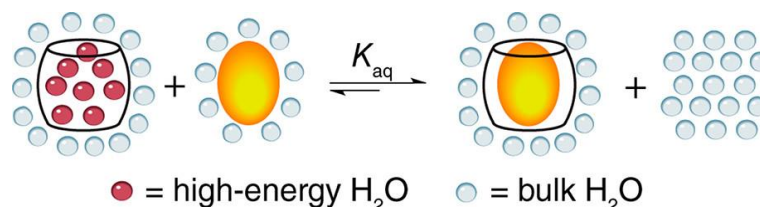
Figure 2.5 Schematic illustration of the release of high-energy water molecules upon guest-binding. Reprinted by permission from ref.63. Copyright © 2012, American Chemical Society

2.2.3. Specific Binding properties for each cucurbit[*n*]uril homologues

CB5, as the current smallest among the CBn homologues, is limited to encapsulating guests by a size-dependent parameter and binds guests, which fit in its relatively small cavity volume (82 Å). Nevertheless, the electronegative carbonyl portals of CB5 can form complexes with cationic species, a feature observed for other CBn homologues.[65] This finding also explains why the solubility of CBn is increased in acidic aqueous media or in the presence of cationic species. CB5 and its derivatives have been reported to form the portal complexes with alkali, alkaline earth, ammonium cations, and multi-charged cation.[66, 67] Apart from this, CB5 has been demonstrated to encapsulate with gas molecules such as N$_2$, O$_2$, Ar, N$_2$O, CO, CO$_2$, noble gases, CH$_4$, ethane, as well as solvent molecules such as methanol and acetonitrile.[68-71] Interestingly, the selective encapsulation of nitrate and chloride ions by CB5 was observed by crystallography.[72-74] Due to the lack of suitable signal transduction ways, CB5 and analogues are still not useable as gas sensors.

As the highest-yielding component from the acid-catalyzed condensation reaction, CB6 is well-known to form high-affinity complexes with aliphatic amines and small aromatic hydrocarbons.[60, 75] Especially for protonated alkylammonium, alkyldiammonium, and their derivatives,[57, 76, 77] CB6 exhibits ultra-high affinities due to the complementary size selectivity and strong interactions between positively charged amines and electronegative carbonyl portals. Meanwhile, taking advantage of the binding properties of CB6 with imidazolium-based guests, the poor solubility of CB6 in water has been dramatically improved[78-80] and consequently used for CB6 functionalization or separation.[81, 82] Notably, CB6 also can

be a recognition receptor for lanthanide ions,[83, 84] noble gases molecule (*e.g.,* ^{129}Xe) for NMR/MRI studies,[85-87] and alkali ions at the portals for exploring the coordinative binding behaviors with other guests.[88, 89]

CB7 plays a predominant role among the cucurbit[*n*]uril family, owing to its relatively large cavity volume of 279 Å^3 and its much better water solubility (20 - 30 mM) than that of CB6 and CB8 ($<$ 0.1 mM). Compared to the limited cavity volume of CB6, a more comprehensive range of guests can be encapsulated into CB7 with high binding affinities from 10^7 M^{-1} to 10^{17} M^{-1}.[90] The latter value is even equal to that of the natural biotin-avidin system.[91-93] Due to the maximal high-energy water release driving force for CB7 than other homologues, CB7 exhibits the largest binding affinities and enthalpies,[63] exemplified by the complexation of ferrocene and adamantylamine derivatives. Owing mainly to the excellent water solubility and high binding affinity observed for CB7, its use in supramolecular and materials science has become popular.

In addition to encapsulating all guests that fit into the CB7 cavity, CB8, equipped with 1.7 times larger volume than CB7, is unique because of its ability to form 2:1 or 1:1:1 ternary complexation with two identical or different guests.[94-96] Most CB8-based sensing application for aromatic recognition is designed and established according to this specific binding property.[97, 98] Besides, CB8 can also form complexes with other macrocyclic guests for catalysis application or with two functional moieties guests to yield supramolecular polymeric materials.[99-102] However, it is noteworthy that the solubility of CB8 is much poor than other CB*n*, which restricts the applications of CB8 when high concentrations are required.

2.3. Application of covalently functionalized cucurbit[*n*]uril

The primary challenge for CB*n* is the water solubility, which is a key point for the implementation of utilizing CB*n*-based material and exhibiting the binding functions in aqueous media. In 1992, the first relevant substituted CB*n* work was reported by Stoddart and coworkers, in which decamethylcucurbit[5]uril (Me$_{10}$CB5) was synthesized from dimethylglycoluril with formaldehyde under acidic conditions.[103] Later, Kim and coworkers isolated the fully substituted cyclohexanecucurbit[*n*]urils (CyH$_5$CB5 and CyH$_6$CB6) and reported their good water solubility (up to 200 mM).[104] In both cases mentioned above, although CB*n* was substituted with the non-polar alkyl group, the increasing solubility presumably comes from the perturbation of stable packing in the solid-state.[103] Since then, a variously of symmetrical or unsymmetrical alkyl-substituted CB*n* were reported (Figure 2.6),[105] such as diphenylcucurbit[6]uril (Ph$_2$CB6),[106] partially cyclopentane-substituted cucurbit[6]uril (CyP$_n$CB6, n = 2, 3, 4),[107] dimethyl-substituted cucurbit[7]uril (Me$_2$CB7), fully cyclopentane-substituted cucurbit[*n*]uril (CyP$_n$CB*n*, n = 5, 6, 7),[108] tetramethyl-substituted cucurbit[8]uril (Me$_4$CB8) and dicyclohexanecucurbit[8]uril (Cy$_2$CB8),[109] hemimethyl-substituted cucurbit[7]uril ((HMe)$_7$CB7),[110] fully cyclobutene or cyclobutane-substituted cucurbit[*n*]uril (CyB$_n$CB*n*, n = 5, 6, 7, 8),[111] and dodecamethyl-substituted cucurbit[6]uril (Me$_{12}$CB6).[112] In principle, these alkyl-substituted CB*n* derivatives generally are better soluble than their corresponding parent CB*n* and expand the horizons of CB*n* synthesis

approaches. However, the second gap between CBn to their practical applications is still existing due to the difficulty of functionalization.
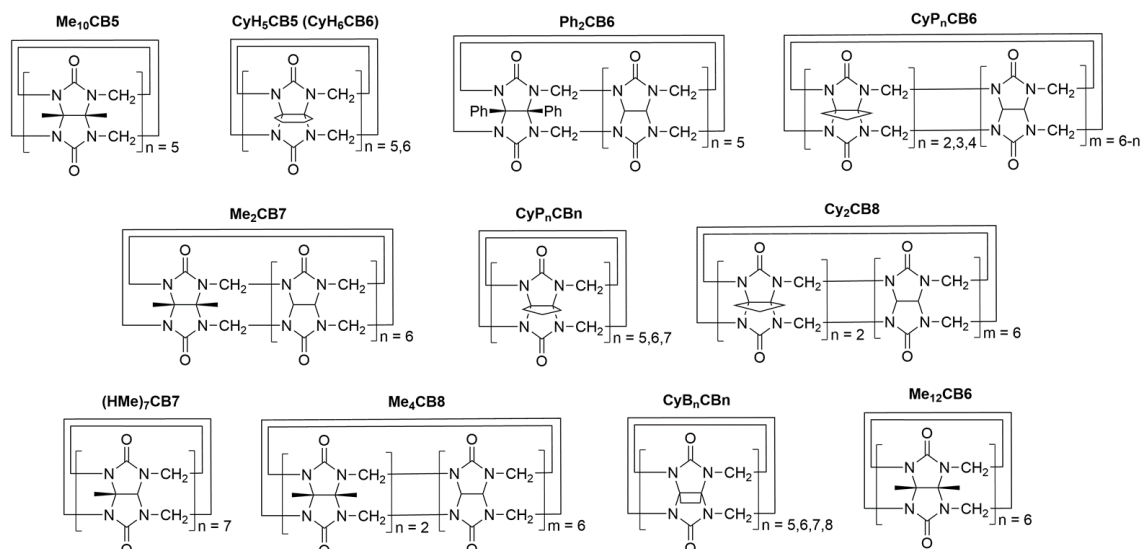
Figure 2.6 Chemical structures of substituted CBn.

2.3.1. Approaches for the synthesis of functionalized cucurbit[n]uril

The instalment of reactive groups on CBn is the first step for further functionalization.[113] In 2003, Kim and coworkers firstly reported a facile direct functionalization of CBn by reactions with $K_2S_2O_8$ in water. The obtained perhydroxylCBn (CBn-(OH)$_{2n}$) can be modified to provide tailored CBn derivatives with further functional groups.[114] A photochemical method using H_2O_2 as the oxidant and UV light irradiation to synthesize the hydroxyl-substituted CBn was later reported by Ouari and co-workers.[115] The authors obtained a high yield and purity of monohydroxylated CBn (n = 5-8), and also first isolated the CB8 derivatives and revealed the mechanism for the difficulty of functionalization of CB8 derivatives through the DFT method. The isolation of monohydroxylated CB7 in this thesis referred to this work, and the detailed experimental procedure will be presented in the following sections.

In contrast to 'post-modification' with oxidizing, inspired by the above approaches for alkyl-substituted CBn synthesis, Isaacs and coworkers presented a building-block approach for monofunctionalized CBn fabrication. Firstly, they reported the templated synthesis of methylene bridged glycoluril hexamer and this hexamer was reacted with substituted phthalaldehydes in the presence of p-xylylenediammonium ion to yield a CB6 with a mono-naphthalene fluorophore (Figure 2.7)[116]. The fluorophore equipped CB6 binding with metal ion as a 'turn-on' probe was used for specific analytes detection (*e.g.,* nitrosamines[117] and amino acids[118]) *via* the responses of fluorescent intensity. Moreover, a similar approach was utilized to synthesize the monofunctionalized CB6 with a 'clickable' alkyne for further versatile functionalization (Figure 2.7).[119] This strategy also created a new entrance for the synthesis of a series of monofunctionalized CB7 derivatives or substituted CB8 derivatives by reacting the pre-functionalized glycoluril with the glycoluril hexamer (Figure 2.7).[109, 120]
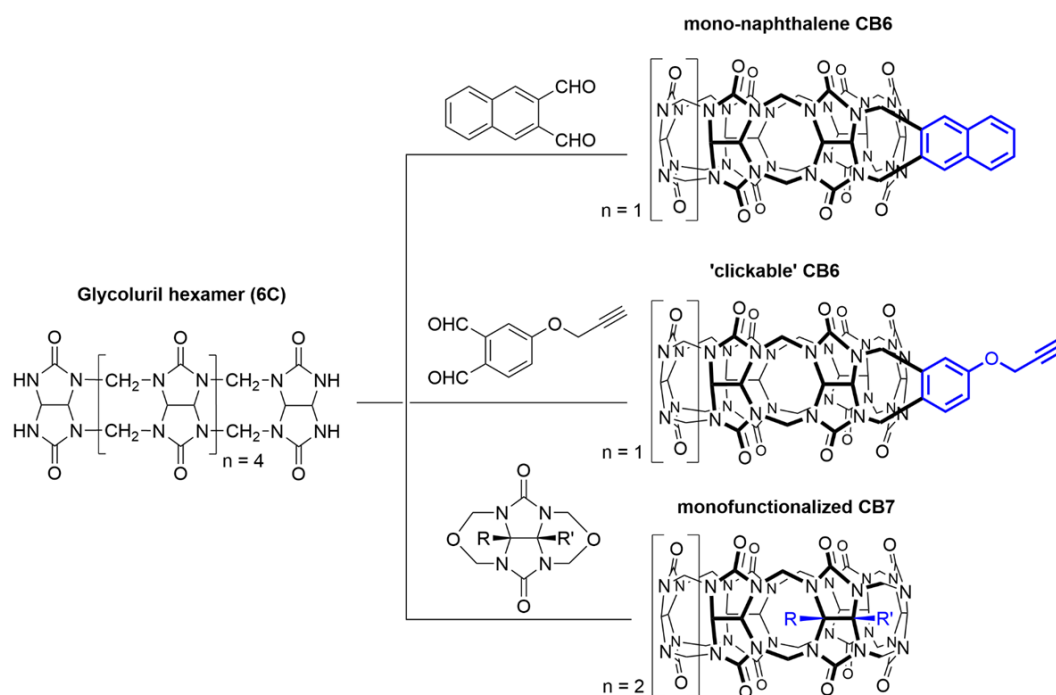
Figure 2.7 Building-block approach for the synthesis of monofunctionalized CB*n* by reaction with glycoluril hexamer.

2.3.2. Biorelevant imaging and bioprocess monitoring

Compared to a non-covalent IDA chemosensor, the covalent connection of the indicator ensured that the host could be observed directly for cellular imaging and avoid the random diffusion of the displaced indicator by analytes in cells. Monofunctionalized CB*n* enables the preparation of their respective dye conjugates, representing an exciting class of unimolecular host-guest systems that can be explored for bioimaging applications in solution or living cells and organisms. In 2016, Urbach and coworkers designed and synthesized a CB7-tetramethylrhodamine conjugate (Q7R), which displayed a concentration-dependent fluorescent response upon binding to different biorelevant guests.[121] The preparation of Q7R was accomplished through a 1,3-dipolar cycloaddition reaction between azide and alkyne.

As the potential live-cell probes, the endocytosis and excretion pathways of two dye-conjugated CB7, CB7-cyanine 3 conjugate (CB7-Cy3) and CB7-rhodamine X conjugate (CB7-ROX), was studied *via* a series of experiments with different cellular process inhibitors and the results revealed the moiety of CB7 has a substantial influence on both cellular processes.[122]

The fluorescence resonance energy transfer (FRET) signal was also utilized for specific cellular process imaging and monitoring. In 2017, Park and coworkers reported an ultra-stable binding pair to visualize different organelles and fusion processes in live cells.[123] As shown in Figure 2.8 (a), CB7-Cy3 and adamantylamine-cyanine 5 conjugate (Ada-Cy5) as the supramolecular FRET donor and acceptor, respectively, translocated into mitochondria and lysosomes. A time-dependent increasing FRET signal indicated the occurrence of fusion *via* the binding of CB7-Cy3 with Ada-Cy5. These supramolecular FRET pairs have also been utilized for monitoring the flickering dynamics of the fusion pore using

neuronal SNARE (soluble *N*-ethylmaleimide-sensitive factor attachment protein receptor)-reconstituted vesicles.[124] Recently, a visualization of organelle-specific autophagy events was reported, which is also monitored by the FRET pair consisting of CB7-Cy3 and borondipyrromethene-adamantylammonium conjugate (BDP-Ada)(Figure 2.8 (b)).[125] Furthermore, they demonstrate this supramolecular FRET pair as a latching system for bio-orthogonal anchoring of small molecules in a live animal model (*C. elegans*) and also showed a potential application on *in vivo* cancer imaging by Ada-Cy5 and pre-targeted CB7-antibody conjugate (CB7-Erbitux) in a live mouse model (Figure 2.8 (c)).[126] This supramolecular latching system was also utilized for protein imaging of cell surface *via* a pre-labelled ultra-stable binding pair, like adamantly- and ferrocenyl-ammonium, on the cell membrane. Mainly, the internalized proteins into cells can be visualized and spatially controllable by temperature.[127]
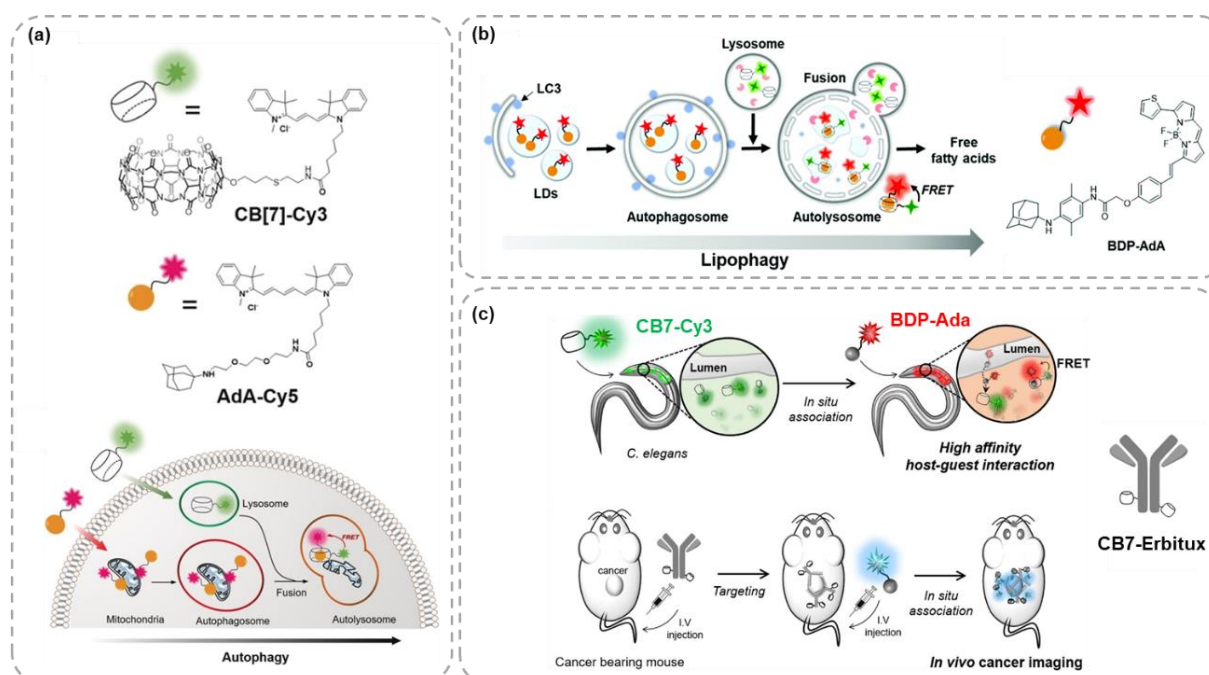
Figure 2.8 (a) Organelles imaging and fusion process monitoring of FRET signal *via* the binding of CB7-Cy3 and Ada-Cy5. Reprinted by permission from ref.123. Copyright © 2018, Wiley-VCH Verlag GmbH & Co. KGaA, Weinheim. (b) Visualization of lipophagy of FRET signal *via* the binding of CB7-Cy3 and BDP-Ada. Reprinted by permission from ref.125. Copyright © 2021, Royal Chemical Society. (c) Latching system for imaging *in vivo* in a live animal model *via* the binding of CB7-derivatives and Ada-dye. Reprinted by permission from ref.126. Copyright © 2019, American Chemical Society.

Likewise, taking advantage of the ultra-high affinity between CB7 and adamantylamine, Agasti and coworkers introduced a biorthogonal assembly strategy based on the supramolecular interaction between CB7 with the primary targeting agent and ADA conjugated fluorophore, which enabled simultaneous biorthogonal labelling and multiplexed imaging in cells as well as tissue sections with high imaging resolution for visualizing structure rather than traditional biotin-avidin based labelling platform.[128] Later, they demonstrated that fluorescently labelled hexamethylenediamine (HMD) forming the dynamic complexation with CB7 could provide the fluorescent blinking with prescribed brightness and frequency

to enable a super-resolution imaging with 10-folded better resolution than the diffraction-limited imaging.[129]

Different from the traditional fluorescent dyes that are subjected to aggregation-caused quenching (ACQ), Wang and coworkers synthesized and reported an aggregation-induced emission (AIE) fluorophores tethered CB7 (CB7-AIE) conjugate for subcellular bioimaging and versatile theranostic applications.[130] In a weakly acidic aqueous environment, this conjugate can spontaneously self-assemble into a compact nanoaggregation, which leads to the enhancement of fluorescent emission and generation of singlet oxygen. Besides, the CB7-AIE nanoaggregates can be enriched explicitly on lysosomes and display enhanced photodynamic cytotoxicity against cancer cells *in vitro*. Based on supramolecular host-guest interaction between CB7 and drugs, this conjugate also exhibits the potential application in supramolecular chemotherapy.

2.3.3. Nanostructure and drug delivery system

The noncovalent approach for the preparation of CB*n*-based functionalized nanostructure or drug delivery system has been extensively researched and received increasing attention. Compared with the conventional covalent modification, the noncovalent approach is more flexible and provides a versatile method to endow the vesicles with new properties and functions.

In 2005, a fully substituted amphiphilic CB6 was synthesized through a reaction of CB6-(allyloxy)$_{12}$ with mPEG$_3$-SH and reported that this CB6 derivative could form assembly vesicles in aqueous media.[131] Through the high binding affinity between CB6 and polyamine (logK_a > 6), the different tags-polyamine conjugates (*e.g.,* mannose-spermidine, FITC-spermidine, and galactose-spermidine) were easily modified onto the surface and provide the vesicles with a specific function (Figure 2.9). Fully allyloxylated CB6 offered a versatile platform for a variety of functionalization with different building units and further allowed the applications in stimuli-responsive drug delivery systems and targeted bioimaging.[132-137]
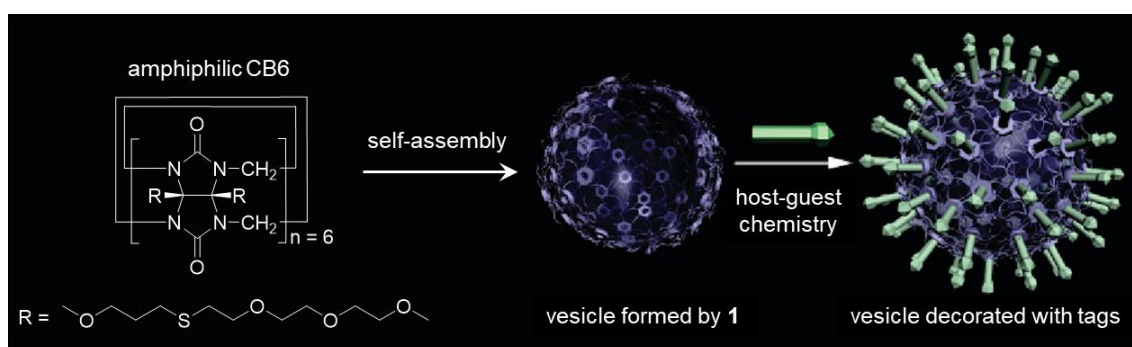
Figure 2.9 Vesicle formed by an amphiphilic CB6 derivative and post-decoration with functional tags *via* host-guest interactions. Reprinted by permission from ref.131. Copyright © 2005, American Chemical Society.

In 2018, the research group discovered that mono-allyloxylated CB7 (CB7-OAl) acts as an unconventional amphiphile that could also directly self-assemble into a vesicle (a diameter of 200 nm with a membrane thickness of 3 nm) in water and exhibit a light-responsive morphology change by reaction with thiol molecule *via* thiol-ene conjugation.[138] Similarly, mono-hexanoate conjugated CB7

(CB7-OC$_5$COO$^-$), which is exceptionally high water-soluble (600 mg/mL) in contrast to parent CB7, exhibits a specific property of well-defined pH responses on intermolecular assembly. Based on this ability, the capsulated guest molecules, such as drugs, can be controllably released upon changing pH value.[139] A monofunctionalized CB7 with a hydrophobic alkane tail (n = 7, 9), synthesized and reported by Isaacs and coworkers, showed a self-inclusion behaviour. After being mixed with tetracationic and zwitterionic *p*-xylylene derivatives guests, the complexes acted as supramolecular amphiphile resulting in the formation of vesicle-type assemblies and is capable of loading the fluorescent dye as a drug model. Upon addition of surfactant (*e.g.,* Triton X-100), the disassembly of structure can be achieved and show a potential stimuli responsiveness with other competitive guests.[140]

As one of the most practical application directions, targeted delivery of chemotherapy drugs complexed in CB*n* to cancer cells, was extensively and deeply researched. In 2013, a biotin monofunctionalized CB7 (CB7-biotin) which maintained the ability to encapsulate guests, was synthesized and exhibited a specific targeting property to cell lines that overexpress biotin receptors. The complex of CB7-biotin with clinical antitumor drug (*e.g.,* oxaliplatin) displayed approximately an order of magnitude higher bioactivity in the MTS bioactivity assay with the above cell line *in vivo* than oxaliplatin alone.[141] Apart from oxaliplatin, doxorubicin (DOX) as a drug model was delivered by a metal-organic polyhedron with covalently functionalized CB7, which enabled the stimuli-responsive release of the encapsulated drug upon the addition of competitive binders. Meanwhile, this vesicle can also release the drug by (1) a dual pH-chemical stimulus through adamantane carboxylate in different protonation states or by (2) a dual pH-photochemical stimulus through stilbene derivative in different photoisomerization states.[142] Similar to the aforementioned 'Plug and Play' CB6-based vesicle, Wang and coworkers proposed a 'Lego-likewise' functionalization strategy on nanoparticles surface *via* the CB7 binding to its corresponding guests labelled with functional units, such as folate, polyethylene glycol, and FITC. This CB7-decorated PLA/PLGA nanoparticle can also load the drug inside the vesicle or into the CB7 cavity and provide a multi-functionalized opportunity for combination drug therapy (Figure 2.10).[143]
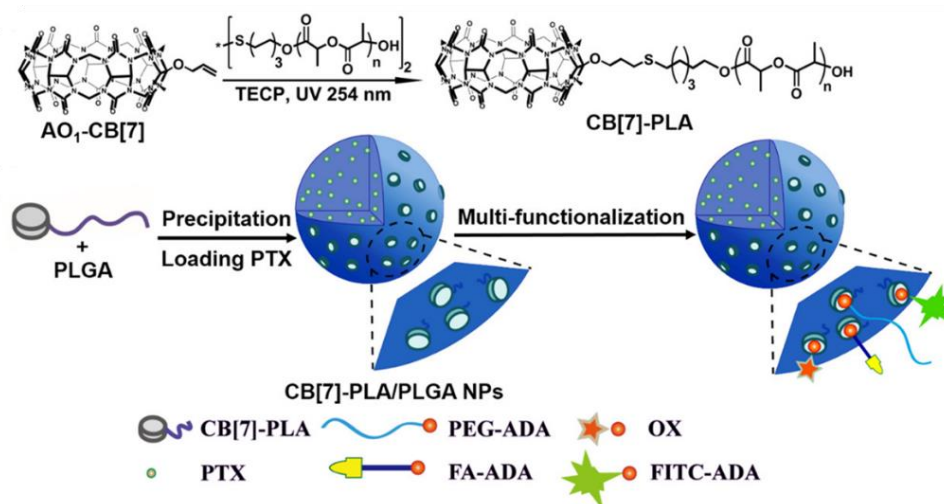
Figure 2.10 Synthesis route of CB7-decorated PLA and schematic illustration of CB7-decorated PLA/PLGA nanoparticle with a non-covalent tailorable surface for post-modification of functional units. Reprinted by permission from ref.143. Copyright © 2018, American Chemical Society.

A similar idea was applied for synergistic photodynamic therapy and hypoxia-activated chemotherapy. Hydrophobic chlorin e6 (Ce6) as photosensitizer conjugated with CB7 through the PEG linker (CB7-PEG-Ce6) can spontaneously form supramolecular micelles. Banoxantrone (AQ4N) as a hypoxia-responsive prodrug and folate-amantadine (Ada-FA) as a tumor-targeting molecule were loaded onto the vesicle surface *via* strong host-guest interaction. After the internalization by cancer cells, the AQ4N can be released in response to the competitive spermine, which is overproduced in tumor cells, and the enhanced hypoxic environment by PDT can activate AQ4N to chemotherapeutic AQ4.[144]

2.3.4. Surface functionalization

One of the application directions of CB*n* functionalization is to graft the CB*n* onto the material surface or interfaces through covalent modification so that the surface can be non-covalently further bound to other components *via* the unoccupied cavity of CB*n*.[145, 146] The earliest report referring to covalently grafting CB*n* onto the surface also came from Kim's group in 2003, when they first proposed the hydroxylation of CB*n* with $K_2S_2O_8$ as an oxidant. Allyloxylated CB6 was anchored on a patterned thiol-terminated glass substrate by irradiating UV light. After immersion of the modified glass into fluorophore-labelled spermine aqueous solution, the appearance of the corresponding fluorescent pattern indicated that CB6 was successfully modified on the surface.[114] Based on this concept, the same group developed the protein immobilized surface as a biosensor *via* the anchored CB7 and ferrocene (Fc) labelled proteins, which demonstrated good performance for glucose sensing.[147] Additionally, a supramolecular Velcro based on the high affinity of CB7 and Fc offered a reversible adhesion strategy without any external curing agents in a water environment, and the redox-active of Fc moiety is potential for the application of electroactive responsive adhesive material.[148] In biorelevant analytes sensing and detection, the groups of Hirtz and Biedermann demonstrated a patterned immobilization CB*n*/indicator chemosensors into microarray for multiplexed and sensitive analytes detection based on IDA, which is in combination with the technique of microchannel cantilever spotting (*μ*CS). The automated *μ*CS process

controls the dot size within a narrow distribution (<10 μm for average dot radius*)*. A series of alkyne-functionalized CB*n* (CB6, CB7, and CB8) was linked on the thiol-functionalized silica surface to obtain the specific microarrays (Figure 2.11). After encapsulating corresponding indicators, the multiplexed microarrays with multi-CB*n*/indicator pairs demonstrated the differentially responding to different analytes, *e.g.,* spermine, cadaverine, and amantadine.[149] The CB*n*/indicator microarrays possess a sensitivity in nanomolar range.
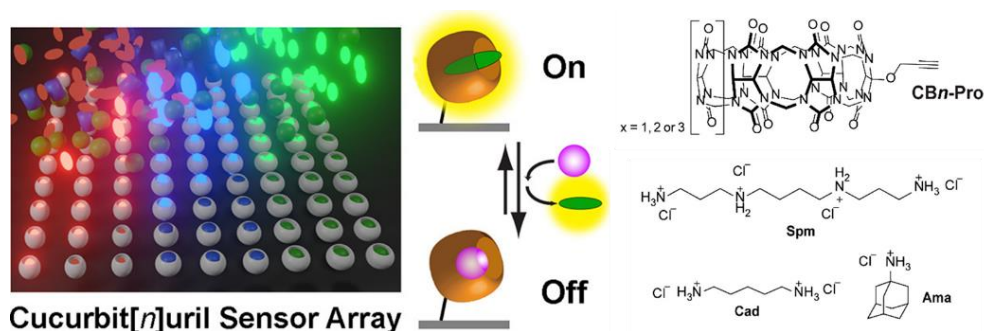
Figure 2.11 Schematic illustration of CB*n*-immobilized sensor array for analyte detection based on IDA and the chemical structures of proparaylated CB*n* and analytes. Reprinted by permission from ref.149. Copyright © 2021, American Chemical Society.

Apart from the covalent immobilization of CB*n* on the surface, many strategies vary from electrostatic adsorption generating a self-assembled monolayer (SAM) of parent CB*n* on gold surface[150-154] or guest-mediated immobilization *via* noncovalent host-guest chemistry.[155, 156]

The immobilization of functionalized CB*n* onto the surface has also been adapted to expand microbeads or nanoparticles' applications. Taking the advantages of ultra-high affinity between CB7 and Fc derivatives, Kim and coworkers established CB7 conjugated Sepharose microbeads by treating NHS beads with hydroxylated CB7. These functionalized CB7 beads enabled to selectively capture of the membrane proteins labelled with Fc moiety from heterogeneous protein mixtures, and then the captured proteins could be recovered and collected by treatment with a stronger binding Fc derivative.[157] With different labelling high-affinity guests, *e.g.,* adamantane, they implemented and enriched specific intracellular protein from cell lysate using the CB7 beads *via* the host-guest interaction.[158] CB*n* (mainly CB7 and CB8) have also been shown to bind selectively and predictably to the N-terminal aromatic residue phenylalanine (Phe), tyrosine (Tyr), and tryptophan (Trp).[97, 159-162] In 2011, Urbach and coworkers investigated that CB7 binds to the N-terminal Phe residue of the insulin B-chain with a 1000-fold preference over other aromatic sites (Figure 2.12 (a)).[163] This result offered that the identity of the terminal residue is sufficient to prescribe the selective recognition of proteins. Similar to the approach of CB7 immobilization on sepharose resin through NHS esterification, the azidobutyl CB7 was coupled to the alkyne modified resin *via* Cu[1]-mediated click reaction (Figure 2.12 (b)). After incubation with the proteins mixture and washed with diethylamine (DEA) or N, N'-diethyl-1,6-diaminohexane (DEDAH) solution, the results from SDA-PAGE demonstrated that the insulin and human growth hormone (hGH) which equipped with an N-terminal Phe residue are bound to the CB7-resin and can be displaced by competitive

high-affinity guests (Figure 2.12 (c)).[164] This is the first example of native proteins recognition by synthetic host molecule in the complex biological mixture.
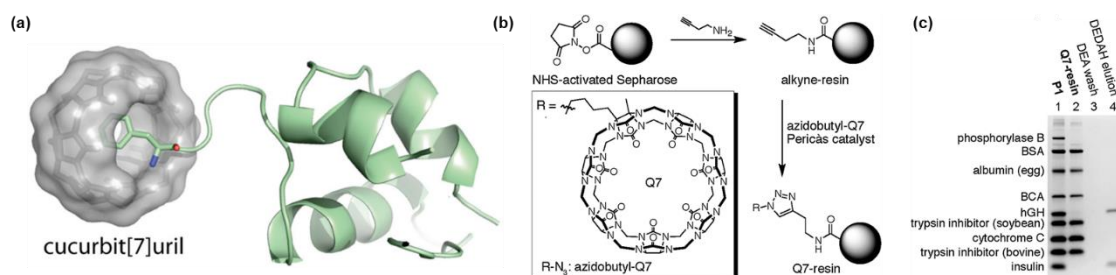
Figure 2.12 (a) Crystal structure of CB7 and insulin complex. The terminal Phe on B-chain is bound inside CB7 cavity. Reprinted by permission from ref.163. Copyright © 2011, American Chemical Society (b) Preparation of CB7 decorated resin *via* click reaction. (c) Presentative SDS-PAGE gel of protein mixture before and after treatment with CB7-resin and resulting resin after treatment with DEA and DEDAH elution. Reprinted by permission from ref.164. Copyright © 2016, Royal Chemical Society.

2.3.5. Other applications of functionalized CB*n*

Owing to the high binding affinity between CB7 and N-Phe of insulin, a platform approach to biopharmaceutical modification of insulin was developed. A series of poly (ethylene glycol) (PEG) conjugated CB7 (CB7-PEG) were shown to significantly increase the stability of protein drugs and limit aggregation for biopharmaceutical formulations. This strategy can endow the protein drugs with the benefits of PEGylating without necessitating covalent modification or even other functional molecules.[165]

In 2018, Nau and coworkers reported that a DNA quantitative sensing system consisting of a host-guest FRET pair, CB7 labelled with carboxyfluorescein (CB7-CF) as an acceptor and the nucleic stain 4',6-diamidino-2-phenylindole (DAPI) as a donor, was established *via* the supramolecular interaction.[166] This DAPI/CB7-CF system shows a great larger linear-response range than commercial DNA stain.

CB7 grafted hyaluronic acid (HA) (CB7-HA) involved a supramolecular strategy to induce the mitochondrial aggregation, and fusion was developed for potential treatment to address mitochondrial fission/fusion imbalance related disease.[167] Dually tagged PEG with triphenylphosphonium (TPP) and adamantane (Ada) (TPP-PEG-Ada) was introduced into the cell and targeted the surface of mitochondria. Then, the addition of CB7-HA induced the supramolecular aggregation of mitochondria *via* the high affinity between CB7 and Ada located on the mitochondria. This strategy successfully protected the cells and zebrafish neurons under chemical stress *in vitro* and *vivo*. CB*n* grafted hyaluronic acid was also utilized to prepare supramolecular hydrogel as artificial extracellular matrices (ECMs), which demonstrated the spatio-temporal control of engineered mesenchymal stem cells (eMSCs) for transgene expression.[168]

In summary, functionalized CB*n* has broad application prospects in various aspects, and it sets up a convenient 'non-covalent' bridge between the substrates and functional components. More importantly, numerous successful reported cases have greatly expanded the vision and strategies of functional material development and enriched the synthetic methods for CB*n* functionalization.

2.4. Cucurbit[*n*]uril-based supramolecular chemosensors

In contrast to the conventional biological detection strategy based on an expensive antigen-antibody or aptamer system, CB*n* is a macrocyclic artificial receptor with a kilogram level of production. As the primary candidate among the numerous macrocyclic hosts, CB*n* can be utilized for a wide range of components sensing or biosensing owing to its high affinity, fast binding kinetics and biocompatibility.[56, 169-171]

2.4.1.Strategies for cucurbit[*n*]uril-based sensing assay

Because the pristine CB*n* does not absorb or emit light in the visible range of the electromagnetic spectrum, CB*n* hosts are restricted to sensing inherently photophysical transparent analytes. In order to generate the readable signals, using of indicator displacement assays (IDA),[172-177] associative binding assays (ABA),[59, 94, 178, 179] and guests displacement assays (GDA)[180, 181] were introduced to widen the scope of analytes detection by CB*n*-based chemosensors.

For chromophoric and emissive guest molecules, the complexation with CB*n* can usually result in significant photophysical signal changes (Figure 2.13 (a)).[182] Basically, the differences in the polarity of the local environment between bulk water and the CB*n* cavity will cause a significant change in emission intensity or hypochromic/hyperchromic shift in the absorbance spectrum of the indicator molecules. The different signals readout on guests caused by changes in the microenvironment are also applicable to other characterization technologies, such as NMR/MRI, CD and MS.

In many circumstances, however, guests are spectroscopically silent, and their corresponding complexation is also without typical absorbance or emission signal responses. In order to meet the requirement of binding detection under this case, an additive indicator dye with spectroscopically active was introduced, and an indicator displacement assay (IDA) was established accordingly. In the presence of guests, the indicator is displaced from the hosts resulting in distinctly different photophysical properties for its bound and unbound form. (Figure 2.13 (b))

For guests with poor solubility in aqueous media, the traditional IDA is limited by the difficulty of avoiding the introduction of other non-polar solvents and cosolvents but ensuring sufficient concentrations of guests as well. Guest displacement assay (GDA) proposes the addition of indicator dye into a re-equilibrated host-guest complexation solution. As the complementary approach to IDA, GDA method is superior for insoluble and weakly binding guests. (Figure 2.13 (c))

Compared with the above assays, associative binding assays (ABA) is a unique guest detection mode based on CB8. The formation of a 1:1:1 heteroternary complex for CB8 with other two aromatic compounds facilitate the charge transfer (CT) from electron-rich molecules to electron-poor molecules that do not occur in the same concentration range in the absence of CB8. In combination with a chromophoric dye with CB8 in many ABA cases, the large space in the CB8 cavity allowed for the simultaneous binding of a second guest with a high affinity and a sensitive absorbance/ emission response. ABA is more sensitive to analytes sensing than IDA in the energetic aspect. (Figure 2.13 (d))
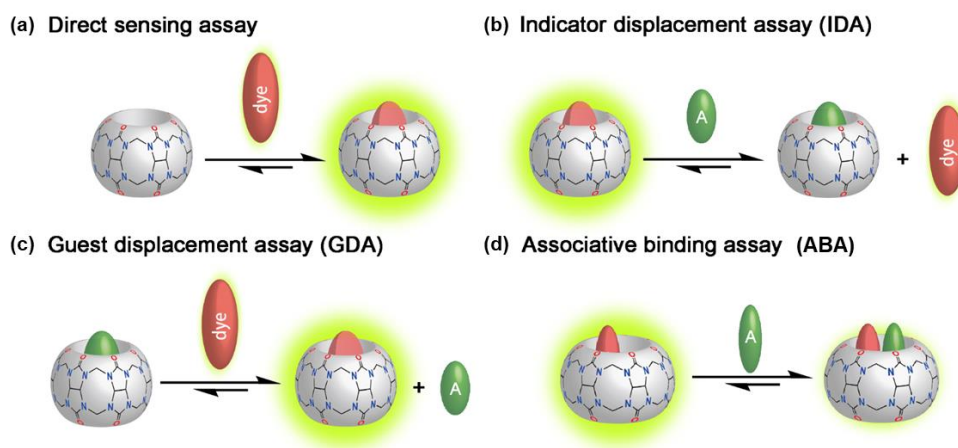
Figure 2.13 (a) Schematic illustration of a direct sensing assay. (b) Schematic illustration of an indicator displacement assay (IDA). (c) Schematic illustration of a guest displacement assay (GDA). (d) Schematic illustration of an associative binding assay (ABA).

2.4.2. Metal ions sensing

As introduced in the previous chapters, the entire family of CBn and its derivatives bind (metal) cations *via* the ion-dipole interaction.[35, 65, 183] This property is generally the cause of buffered medium dependence of CBn-guests binding constants. Mostly, the binding affinity between CBn and cations increases with the larger cation radius and increasing valence of ions. Taking advantage of this feature, CBn-based system can be utilized for sensing Al^{3+},[184] Hg^{2+},[184-187] Fe^{3+},[188-191] Ag^{+},[189, 192] Ba^{2+},[188] Pb^{2+},[193] Cd^{2+},[194, 195] and other metal cations[116, 196-200] by employing the electrochemical and photophysical techniques.

2.4.3. Amino acids, peptides and proteins sensing

The detection and recognition of biologically relevant small molecules (*e.g.,* amino acids, peptides, and metabolites) is essential to evaluate physical conditions and diagnose diseases. Due to the unique binding properties of CBn (size-selective, charge-selective and hydrophobic) and feasible sensing strategies (IDA, GDA, or ABA), CBn has come out as a special macrocyclic receptor for biorelevant molecule sensing. Among the 20 common amino acids for protein building, hydrophobic and electroneutral amino acids are all potential binding guests for CBn but have differences in binding affinity, respectively. The amino acids primarily used for the research of CBn binding include the ones equipped with an aromatic group, phenylalanine (Phe), tyrosine (Tyr), and tryptophan (Trp).[159, 201-206] The binding constant of typical amino acids is listed in Table 2 with their corresponding CBn receptor and experimental information.[98, 159, 162, 178, 207-209] Summarizing from the reported information, these three aromatic amino acids always bind to CB7 in the form of a 1:1 model and CB8 in the form of a 1:2 with an auxiliary guest (indicator or two identical homogeneous guests) but cannot form a stable complex with CB6. Notably, Isaacs and coworkers synthesized and reported a 'CB6-analogues', which show a higher affinity to the above amino acids than CB8.[210] Except for the classic cyclic CBn members, acyclic cucurbit[n]uril is a famous member of the CBn family which is rid of the size restrictions for guests binding and minimized the difficulty of functionalization in comparison with other typical CBn.[117, 211-214]

Including the recognition of amino acids,[215, 216] acyclic cucurbit[n]uril displays the general binding behavior to cations as well,[117] but bind much larger entities, such as single-walled nanotubes (SWNTs).[217] Additionally, the binding interactions of the asymmetrical inverted CBn (iQ[7]) with essential amino acids were also explored by Xiao and coworkers,[218] which deeply investigated the unique binding performance and expanded the horizon of molecular recognition by CBn.

Table 2.1 Binding constant of common amino acids to CBn

	receptor	K_a (M^{-1})	strategy	indicator	medium
Phenylalanine (Phe)	CB6	1.4×10^3	Direct	-	50 % (v/v) aqueous formic acid
	CB8	5.3×10^3	ABA	Methyl viologen	10 mM sodium phosphate, pH 7.0
	CB7	8.2×10^5	Direct	-	water
	CB7	1.5×10^5	IDA	TMSP	water
	CB7	1.8×10^6	Direct	-	water
Tryptophan (Trp)	CB8	4.3×10^4	ABA	Methyl viologen	10 mM sodium phosphate, pH 7.0
	CB8	4.2×10^5	ABA	DPT	-
	CB8	3.4×10^4	ABA	MBBI	10 mM sodium phosphate, pH 7.0
	CB7	3.7×10^5	Direct	-	water
	CB7	1.9×10^3	Direct	-	10 mM NH$_4$OAc buffer at pH 6.0
	CB7	1.6×10^3	IDA	Dapoxyl	10 mM NH$_4$OAc buffer at pH 6.0
Glycine (Gly)	CB6	4.7×10^3	Direct	-	50 % (v/v) aqueous formic acid
Histidine (His)	CB7	80	Direct	-	water
	CB7	400	IDA	Dapoxyl	10 mM NH$_4$OAc buffer at pH 6.0
Glutamic acid (Glu)	CB7	100	Direct	-	water
Methionine (Met)	CB7	270	Direct	-	water
Arginine (Arg)	CB7	330	Direct	-	10 mM NH$_4$OAc buffer at pH 6.0
	CB7	310	IDA	Dapoxyl	10 mM NH$_4$OAc buffer at pH 6.0
Alanine (Ala)	CB6	1.0×10^3	Direct	-	50 % (v/v) aqueous formic acid
	CB7	36	Direct	-	water
Lysine (Lys)	CB7	800	Direct	-	10 mM NH$_4$OAc buffer at pH 6.0
	CB7	870	IDA	Dapoxyl	10 mM NH$_4$OAc buffer at pH 6.0
Valine (Val)	CB6	1.4×10^3	Direct	-	50 % (v/v) aqueous formic acid
	CB7	440	Direct	-	water
Tyrosine (Tyr)	CB8	2.2×10^3	ABA	Methyl viologen	10 mM sodium phosphate, pH 7.0
	CB7	2.3×10^5	Direct	-	water
	CB7	2.2×10^4	Direct	-	10 mM NH$_4$OAc buffer at pH 6.0
	CB7	2.4×10^4	IDA	Dapoxyl	10 mM NH$_4$OAc buffer at pH 6.0

TSMP - 3-(trimethylsilyl)propionic-2,2,3,3-d_4 acid; DPT - 2,7-dimethyldiazaphenanthrenium; MBBI - tetramethylbenzobis(imidazolium)

Compared to amino acids, peptides, such as oligoamide or polyamide, consist of the amino acid chain. Taking into account the binding characters to CBn with amino acids, the features of peptides create both challenges and opportunities for molecular recognition. Early reports about peptides binding by CBn were focused on oligopeptides (dipeptides or tripeptides). Remarkably, the type of amino acid at the N-terminal position is always decisive for the binding behaviors of the entire peptide because of its exposed free amino group with less spatial constrictions and no -COOH groups nearby. Like the above, CB6 shows a

small affinity to peptides that usually does not exceed the range up to 10^4 M^{-1}.[219-221] In recent years, more and more attention has been paid to the mild affinity between CB6 or CB6 analogues with lysine.[161, 222] Especially for an alkyl substituted CB6, hemimethyl-substituted cucurbit[6]uril ((HMe)$_6$CB6) reported by Zhu and coworkers, showed the binding affinity to lysine up to 4.5×10^6 M^{-1} determined by fluorescent IDA.[222] However, the widely applied one is the inclusion complex of CB7 to N-terminal phenylalanine (Phe) peptide systems. Taking the advantages of 1) hydrophobic interaction between terminal Phe residues and CB7 cavity, 2) ion-dipole interaction, and 3) H-bond interaction between terminal ammonium group and carbonyl portal, CB7 can form strong complexes with N-terminal Phe residue of peptide and protein up to the K_a of ~10^7 M^{-1} in water.[223] This feature was utilized for protein analysis,[224] site-selective modification,[225] sequence-specific inhibition of protease,[226] and modulation of protein fibrillation or aggregation.[227-230] The most known case of protein recognition by CB7 with human insulin exhibits a 100- even 1000-fold affinity than the manual peptides or proteins in the absence of N-Phe.[163] Additionally, methylated lysine (methyllysine) also showed a high affinity to CB7 and was studied for specific protein purification and recognition applications.[231-233] In analogy with the high affinity between CB7 and N-terminal Phe, CB8 equipped with one equivalent methyl viologen (MV) also displays a particular affinity to the peptide with N-terminal tryptophan (Trp) (Figure 2.14 (a)). The system demonstrated sequence-specific peptide recognition by CBn receptors, $e.g.$, K_a of 1.3×10^5 M^{-1} for TrpGlyGly (WGG) tripeptide but K_a only 2.1×10^4 M^{-1} for GWG and 3.1×10^3 M^{-1} for GGW sequence, respectively.[159] Furthermore, CB8 with MBBI system for peptides selectively recognition was reported as having a similar advantageous binding property and better stability and intense fluorescence.[209] Apart from the detection by the change of emission signal, Biedermann and coworkers utilized the circular dichroism (CD) and fluorescence-detected circular dichroism (FDCD) with supramolecular host-guest system for the detection and chiral sensing of chiral amino acids and proteins, as well as for reaction monitoring.[215, 234] Likewise, CB8 binding with two identical amino acids at the stoichiometry at 1:2 is also appropriate for peptides. Urbach and coworkers discovered that CB8 can bind to two PheGlyGly (FGG) with the K_a value of 1.5×10^{11} M^{-2}, and this selectivity even is larger than WGG owing to an enthalpic advantage (Figure 2.13 (b)).[160] According to this concept, Brunsveld and coworkers reported a series of works about N-terminal FGG peptide motif modified protein dimerization induced by interaction with CB8 (Figure 2.13 (c)).[235, 236]
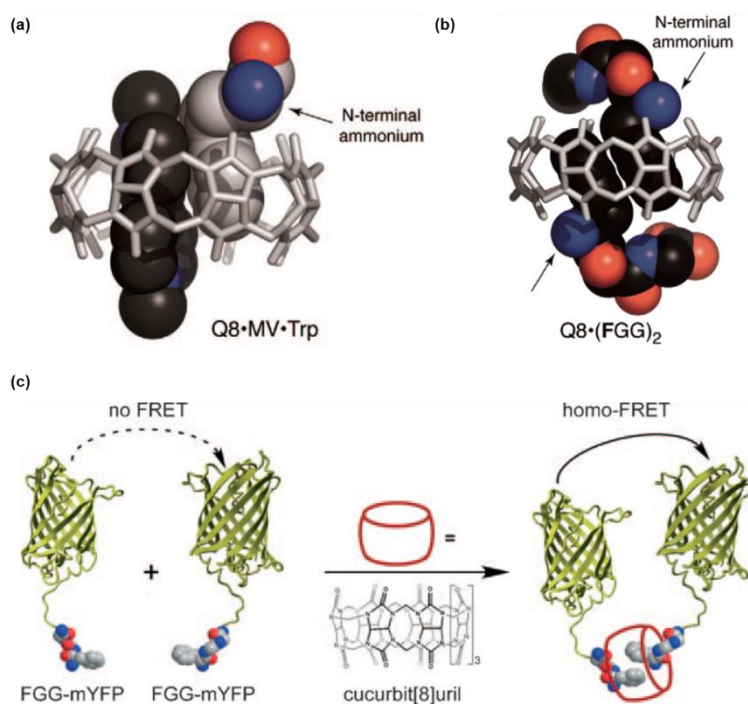
Figure 2.14 (a) Energy minimized computer model of CB8 bound to MV and Trp showing both aromatic groups stacked face-to-face inside the cavity. (b) Crystal structures of CB8 are bound to two equivalents of FGG. Reprinted by permission from ref.159. Copyright © 2011 WILEY-VCH Verlag GmbH & Co. KGaA, Weinheim. (c) Schematic representation of two YFP proteins equipped with N-terminal FGG motif induced by interactions with CB8. Reprinted by permission from ref.235. Copyright © 2010 WILEY-VCH Verlag GmbH & Co. KGaA, Weinheim.

2.4.4. Metabolites and drugs sensing

Except for recognizing amino acids and peptides, CB*n* host-guest chemistry found its analytical applications in detecting biorelevant metabolites and drugs.[237] Acetylcholine (ACh$^+$), an important neurotransmitter involved in numerous nervous system activities, showed a selectively binding affinity to CB6. In 2012, ion-selective electrodes (ISEs) for ACh$^+$ detection by using their fully allyloxylated CB6 (CB6-(allyloxy)$_{12}$) as an ionophore were prepared. These ISEs exhibited an extraordinary selectivity to ACh$^+$ over its metabolite choline (Ch$^+$) in the presence of other interfering quaternary ammoniums.[238] Afterwards, this strategy was transformed onto the field-effect transistor platform and amplified the detection capacity of ACh$^+$ down to the limit of 1×10^{-12} M.[239] In addition to the recognition of ACh$^+$ by CB*n* systems, CB*n* exhibits the high affinities to polyamines in aqueous media as well. The formation of their pseudoreotaxane structure was widely studied and applied to the construction of supramolecular complexes in early reports.[57, 240-244] However, the biogenic polyamines also play an essential role in some physiological processes as primary metabolites, such as cell growth, proliferation, and differentiation. Determination of polyamines in biofluids has a practical clinical significance. Kim and coworkers demonstrated an array of CB*n* and dye complexes as sensor elements for pattern recognition of several polyamines (*e.g.,* putrescine, cadaverine, spermidine, spermine, *etc.*). In combination with PCA data analysis, this approach displayed the potential to detect biomarkers of diseases.[245] Other CB*n*-based

probes for polyamines detection systems associated with the aggregation-induced emission (AIE) effect were also reported as a sensitive and selective tool in biorelevant fluids.[246, 247] CB*n* combined with mass spectrometry techniques also offered a highly sensitive detection of polyamines.[248, 249] However, it is no doubt that the reports of polyamine detection based on fluorescent IDA were still dominant.[250-253]

In the aspect of the drugs capsulation and recognition, hundreds of candidates have been investigated on their binding behaviors and sensing performance with CB*n* systems, for instance, methamphetamine,[254-256] opiates and their metabolites,[257] alkaloids,[258] fluoroquinolone,[259] illegal stimulants,[260] addictive over-the-counter drugs,[261] *etc*.

2.4.5. Supramolecular tandem enzyme assays

Enzymatic reaction monitoring is a sensing application by the host-guest systems in combination with the IDA strategy. In 2007, Nau and coworkers first introduced a label-free continuous enzyme assay to monitor decarboxylase's enzymatic process with several amine acids (Figure 2.15). According to the transformation of substrate charge (for instance, from lysine to cadaverine), macrocyclic receptors would be predisposed to binding to guests with the complementary size and charge (cadaverine). Thus, the signal changes indirectly reflect the information on enzymatic kinetic.[262] Since then, different chemosensor pairs, substrates, enzymes, and required co-factors were further studied and reported.[177, 179, 263-266]
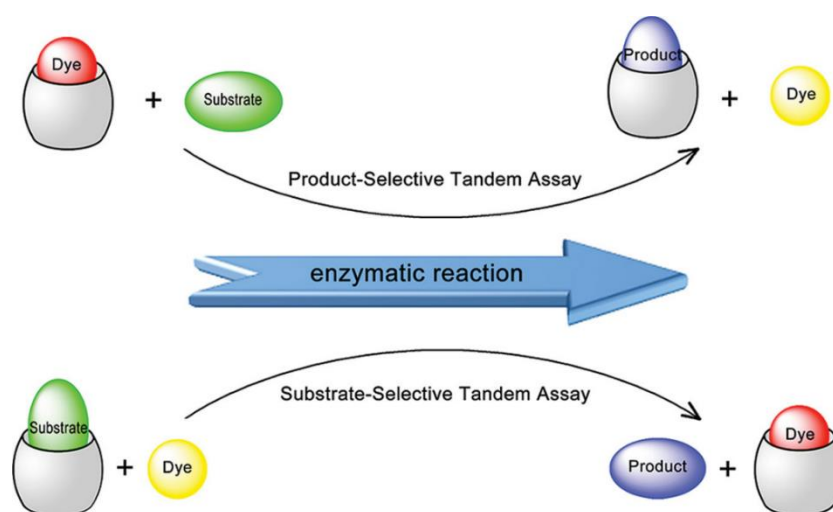
Figure 2.15 Product- *versus* substrate-selective tandem assays for monitoring enzymatic activity. Reprinted by permission from ref.247. Copyright © 2009, American Chemical Society.

2.4.6. Supramolecular tandem membrane assays

The efficient monitoring of membrane translocation or permeability for drugs and biomolecules was allowed *via* the fluorescent-based supramolecular tandem membrane assays. This method is feasible to continuously follow the changes in concentration of analytes, for instance, the accumulation of analytes inside the compartmentalized structures.[266] In 2013, Nau and coworkers firstly introduced this concept for the screening of diverse classes of analytes, channel proteins, and modulators.[267] As shown in Figure 2.16, the analytes transported through the lipid bilayer will bind to a macrocycle and result in a displacement of dye in line with IDA. Thus, monitoring of analytes or related bioprocesses can be tracked by fluorescent in real-time. Afterwards, this strategy was utilized for monitoring the membrane transport

of cell-penetrating peptides (CPPs) inside large unilamellar vesicles (LUVs) and giant unilamellar vesicles (GUVs).[268]
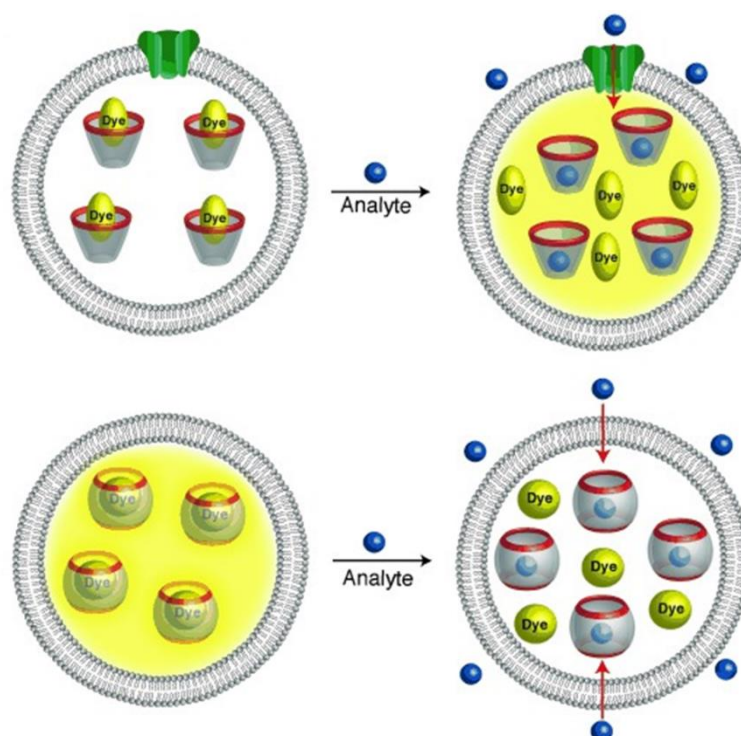
Figure 2.16 Schematic illustration of host-guest complex inside liposome before and after translocation of the analytes through a channel protein or the membrane directly. Reprinted by permission from ref.250. Copyright © 2014 WILEY-VCH Verlag GmbH & Co. KGaA, Weinheim.

Likewise, they established a real-time parallel artificial membrane permeability assay, namely RT-PAMPA, in combination with the fluorescent IDA to monitor and evaluate drug permeability across the biomembrane systems in a high-throughput screening format.[269] Additionally, to improve the limited scope to strongly binding and slowly translocating analytes based on IDA, Biedermann and Nau introduced another model for spatiotemporally resolved monitoring of biomembrane permeability referred to as fluorescent artificial receptor-based membrane assay (FARMA), which exploited ABA instead of IDA strategy. With FAMRA, the permeation of hundred compounds through membranes has been monitored in real-time with high sensitivity.[270]

3. Aim of this thesis

Cucurbit[*n*]uril (CB*n*)-based host-guest supramolecular chemistry provides a versatile platform for the chemosensors design owing to its superior chemical properties and numerous successful cases of CB*n* functionalization as aforementioned. However, CB*n* binding to a wide range of guests with the structural matched conditions (*e.g.,* packing coefficient, ionization state, *etc.*) seems to be a constraint for the selectivity of CB*n* as a versatile chemosensor. In general, the non-negligible affinity of metal cations to the carbonyl-fringed CB*n* portals, which induces the dissociation between CB*n* and guest molecules (such as in biorelevant media, normal saline, and biofluids), makes the recognition of analytes by chemosensors only in pure water or low salt concentration buffer environment (Figure 3.1). The dilution is prone to induce the dissociation of non-covalent weak reporter pairs as well. For some indicators with high affinity to CB*n*, the competition with cation is alleviated, but the binding of analytes is restricted at the same time. After that, CB*n*-based chemosensors have been limited due to a lack of analyte selectivity for a long time. Unlike the 'lock and key' type chemosensor, there is not always a significantly different detection response on certain analytes by CB*n*-based chemosensor. However, the increasing development of differential sensing provides a promising solution to this open challenge.
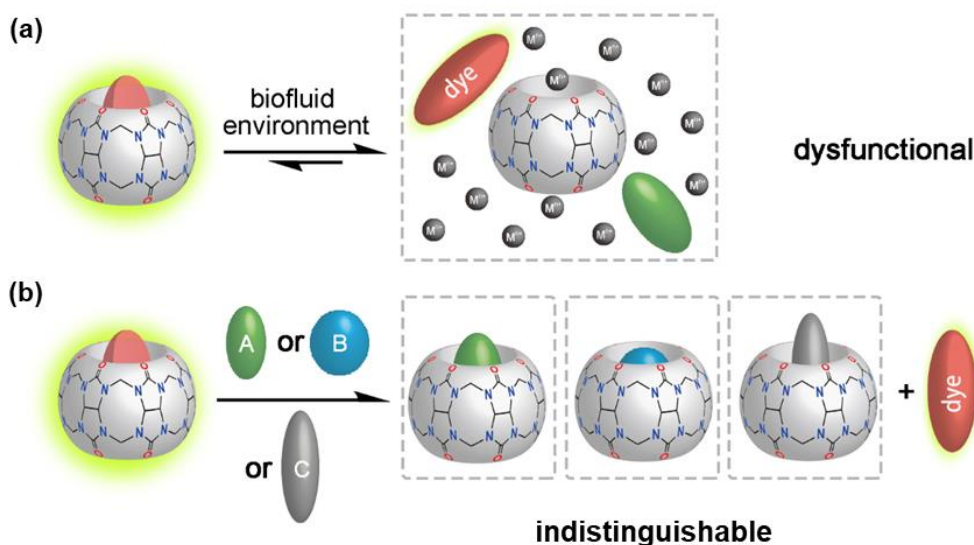
Figure 3.1 Schematic illustration of (a) the inevitable cation-competition induced dissociation of the non-covalent reporter dyes with macrocyclic receptors in high salinity medium or real biofluids. (b) The inefficiency of analytes selectivity by non-covalent chemosensor in the presence of varied analytes with uncertain concentration.

Inspired by Urbach's work about mono-tetramethylrhodamine labelled CB7 for cell imaging[121] and Isaacs's work about naphthalene modified CB6 derivatives for drugs detection in human urine,[261] my alternative design strategy aims to overcome dilution issues and reduce the effects of salts on the chemosensor performance in biofluids by integrating the indicator and receptor into a single, non-dissociable unimolecular chemosensor. Converting intermolecular supramolecular interactions into

intramolecular supramolecular interactions is likely to change the original properties and applicability of the CB*n*-based chemosensor. Due to CB7's exceptionally high binding affinity for many hydrophobic or cationic bioactive molecules and the better water solubility compared to other CB*n* homologues, unimolecular host-dye conjugates based on cucurbit[7]uril macrocycles can be promising chemosensors for analyte detection in the biologically relevant environments in the presence of competitive cations.

= interferents (salts, competitors)
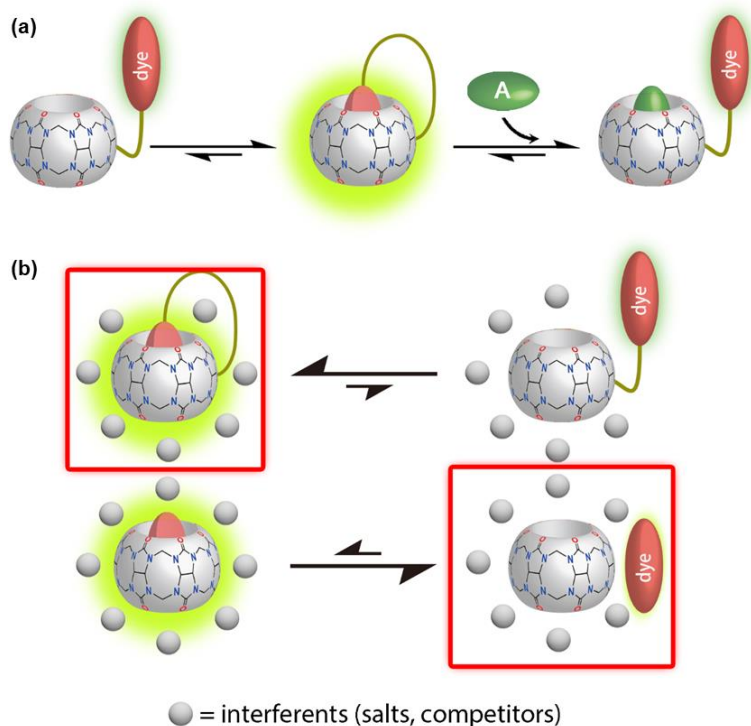
Figure 3.2 (a) Schematic representation of analyte-induced conformational changes of CB7-dye conjugates that can be detected by emission spectroscopy; (b) Schematic representation of the equilibrium between free- and bound-formation of CB7-dye with/without linker in the presence of a high concentration of interferents.

    Taking this idea as the starting point, the synthetic method to connect the CB7 with a matched indicator is the first issue for constructing a unimolecular chemosensor. Learning from the numerous established CB*n*-functionalization related literature and detailed synthesis information, the subsequent modification of the functional moiety onto CB7 through the click reaction should be the most convenient and reliable route. It is not only because of referring to the similar successful cases but also in line with my experimental conditions and existing experiences on CB*n* synthesis. Considering further sensing applications that require enough conformational freedom for the inclusion of indicators into conjugated CB*n* in aqueous media, the modifiable hydrophilic ethylene glycol with a certain length, *e.g.,* tetraethylene glycol or more units, is a promising candidate as the suitable linker. The fluorescent emission-based assay is commonly regarded as the most sensitive and intuitive analytical method for selecting indicators, so I decided to utilize the fluorescent dye as an indicator with the noticeable intensity

change between bound and unbound CB7 in aqueous media. A deeper description of the underlying ideas for selecting the dye will be introduced in the following sections.

In order to verify the definite conformation of unimolecular conjugated chemosensors, NMR, mass spectrometry (MS), and ion mobility experiments were used to help characterize the geometry of conjugates or complexes with binding guests. Meanwhile, density functional theory (DFT) calculation was utilized for understanding and predicting the possible conformations from an energetically perspective.

In the main section of measurements with analytes, absorption and emission spectrometry were used as the primary techniques to reflect the interactions between analytes and chemosensors in aqueous media through the changes in spectra or intensity. A fluorescent plate reader format was used for the cases with multiple samples and repetitions.

The ultimate purpose of my thesis was to achieve the analytes sensing by the conjugated chemosensor in biofluids, that is in real human urine, saliva and serum.

4. Monofunctionalized cucurbit[7]uril-berberine conjugate for drug detection in biofluids

This chapter is derived from the context of the following publication: **Hu, C.**; *Grimm, L.; Prabodh, A.; Baksi, A.; Siennicka, A.; Levkin, P. A.; Kappes, M. M.; Biedermann, F. Chem. Sci. 2020, 11, 11142-11153. The synthesis, analysis, and data organization were carried out by me under the supervision of Dr. Frank Biedermann. The co-authors contributed by draft revision: Laura Grimm, Prof. Dr. Manfred Kappes, and Prof. Dr. Pavel Levkin. Other detailed contributions will be stated in the corresponding sections. Sections in this chapter have been reproduced from the published work[271] with permission from the Royal Society of Chemistry.*

Non-covalent cucurbit[*n*]uril (CB*n*) based chemosensors have been widely used in proof-of-concept sensing applications. However, as aforementioned, the disintegration of CB*n* and indicators in the saline medium is hard to avoid. In this chapter, it is described that covalent cucurbit[7]uril-indicator dye (berberine, BC) conjugates with different length linkers are stable in high salinity media and allow for selective sensing of Parkinson's drug amantadine in biofluids (*e.g.,* human urine and saliva), where the traditional non-covalent CB7⊃dye complex is dysfunctional. A detailed analysis of the covalent host–dye conjugates in the gas-phase and deionized *versus* saline aqueous media revealed structural, thermodynamic, and kinetic effects relevant to the design of CB*n*-based supramolecular chemosensors. This research also presents a new high-affinity indicator dye for CB7, revealing one of the most significant shortcomings of indicator displacement assays (IDA) with high K_a values, namely an impractically slow equilibration time. Different from non-covalent CB*n*⊃dye reporter pairs, the conjugate chemosensors can also work *via* an S_N2-type guest–dye exchange mechanism, shortening test durations and allowing for novel avenues for tailoring analyte-selectivity.

4.1. Introduction

In recent decades, emission-based detection and analysis employing supramolecular assemblies, such as host-guest systems, have been a popular study topic. Supramolecular complexes were extensively investigated regarding their use in drug detection[14, 25, 272] and enzymatic reaction monitoring.[177, 273] Although CB*n*-based chemosensors possess advantageous high binding affinities and fast binding kinetics for many biorelevant small molecules in deionized water,[75, 91, 274] the non-covalent interaction between CB*n* and guest is strongly modulated by salt due to competitive[65] (or cooperative)[275] cation binding to the carbonyl-fringed CB*n* portals. Furthermore, non-covalent CB*n*⊃dye reporter pairs, like any other bimolecular non-covalent complex, are inherently prone to dissociate when diluted. As a result, many reported CB*n*-based chemosensors are operational for sensing applications in deionized water or "minimal buffers" but are often not suitable for saline media or biofluids, especially if their salt concentration varies from sample to sample (matrix effects).[276, 277] Biedermann and coworkers recently demonstrated that using a high-affinity dye for CB8 enabled the detection of the drug memantine by IDA in blood serum.[278] However, this approach can have serious fundamental limitations, *e.g.*, for CB7-based assays, which are described further below.

As a result, combining the indicator and receptor into a single, non-dissociable unimolecular chemosensor appears to be a promising alternative design method for overcoming dilution problems and reducing the impact of salts on the chemosensor performance in biofluids. For example, emissive naphthalene units were modified on cavity walls in *de novo* cucurbit[*n*]uril-derivatives,[215] functional in human urine to detect addictive over-the-counter drugs.[261]

Because of CB7's exceptionally high binding affinity for many hydrophobic or cationic bioactive molecules such as steroids and polyamines,[91, 279] can reach up to astonishing ~10^{15} M^{-1} for adamantane derivatives,[280] unimolecular host-dye conjugates based on CB7 macrocycles can be promising chemosensors. In this chapter, unimolecular CB7-based chemosensors with flexible and hydrophilic linkers that allow self-encapsulating of the indicator dye in the host cavity (Figure 3.2) were presented.

4.2. Results

4.2.1. Design and synthesis of CB7-dye conjugates

Synthetic advances have enabled mono-functionalized CB7[115, 120, 138, 281-283] to be derivatized with chemically reactive groups covalently attached to dye molecule. For instance, CB7 was covalently tethered to tetramethylrhodamine, for example, and the resulting conjugate displayed CB7-like binding properties for typical CB7-guests.[121] However, such CB7-dye conjugates were connected by short linkers, which cannot enable the self-encapsulation of the dye into the CB7 cavity.

Several fluorescent reporter dyes are known for CB7,[284] out of which many are pK_a shift-dyes, *e.g.,* acridine dyes[285] and quinone-imine dyes.[286] These dyes are commonly protonated and will result in the enhancement of emission intensity upon inclusion in the CB7 cavity that is well-known to stabilize positively charged species. In buffered aqueous conditions with a set pH, such pK_a shift dyes perform well. When biological fluids with changing pH, *e.g.,* urine, are employed, however, undesired matrix-dependent signal changes are observed. In this section, berberine was chosen as an indicator dye because it shows a considerable intensity enhancement on inclusion in CB7,[287] a high binding constant of 10^7 M^{-1} in deionized water,[288] and because it can be chemically functionalized by a demethylation-alkylation method (Figure 4.1 (a)).[289] Ethylene glycol-based linkers were chosen as relatively hydrophilic and flexible connectors between CB7 and berberine moieties.[290] Chemical modelling suggested that a linker length of at least four ethylene glycol units is necessary to enter and exit the berberine dye from the CB7 cavity. In order to evaluate the effect of the linker-length, hexaethylene glycol (HEG) and tetraethylene glycol (TEG) were utilized as linkers.

The host-dye conjugates cucurbit[7]uril-HEG-berberine (chemosensor **1**) and cucurbit[7]uril-TEG-berberine (chemosensor **2**) were prepared through a convergent synthetic route shown in Figure 4.1. For the purpose of minimising the number of synthetic steps with CB7-species, the HEG or TEG linkers were connected to berberine, resulting in azide-ended berberine-hexaethylene glycol-azide (BC-HEG-N₃) or berberine-tetraethylene glycol-azide (BC-TEG-N₃) conjugates (Figure 4.1 (a)). A Huisgen 1,3-dipolar

cycloaddition was used to couple the conjugated to alkyne-functionalized CB7 (Figure 4.1 (c)), which was chosen for its known high reactivity and lack of side products. Particularly, BC-HEG-N$_3$ and BC-TEG-N$_3$ were prepared through a three-step procedure from commercial berberine hydrochloride (see the experimental section for details) in an overall yield of 54 % on a 50 mg scale, and mono-propargyloxylated CB7 (CB7-(Opr)$_1$) was synthesized through a two-step hydroxylation-alkylation procedure with an overall yield of 5 % on a 20 mg scale. The modest yield is in line with the literature but fortunately not problematic because CB7 can be readily prepared at a gram scale. Flash column chromatography on silica was used to purify the BC-HEG-N$_3$ and BC-TEG-N$_3$ dye-linker conjugates, and mono-propargyloxylated CB7 was obtained *via* the reaction between propargyl bromide and mono-hydroxylated CB7, which was purified using CHP20P resin columns. The coupling of BC-HEG-N$_3$ or BC-TEG-N$_3$ with CB7-(Opr)$_1$ was then carried out in the presence of CuSO$_4$ and L-ascorbate in DMSO/H$_2$O (v/v = 55/45). To eliminate unreacted starting material and catalyst, CB7-HEG-BC and CB7-TEG-BC were purified using a preparative HPLC column and a solvent of acetonitrile and 0.1 % trifluoroacetic acid (TFA) aqueous (v/v = 1/3) mixture.
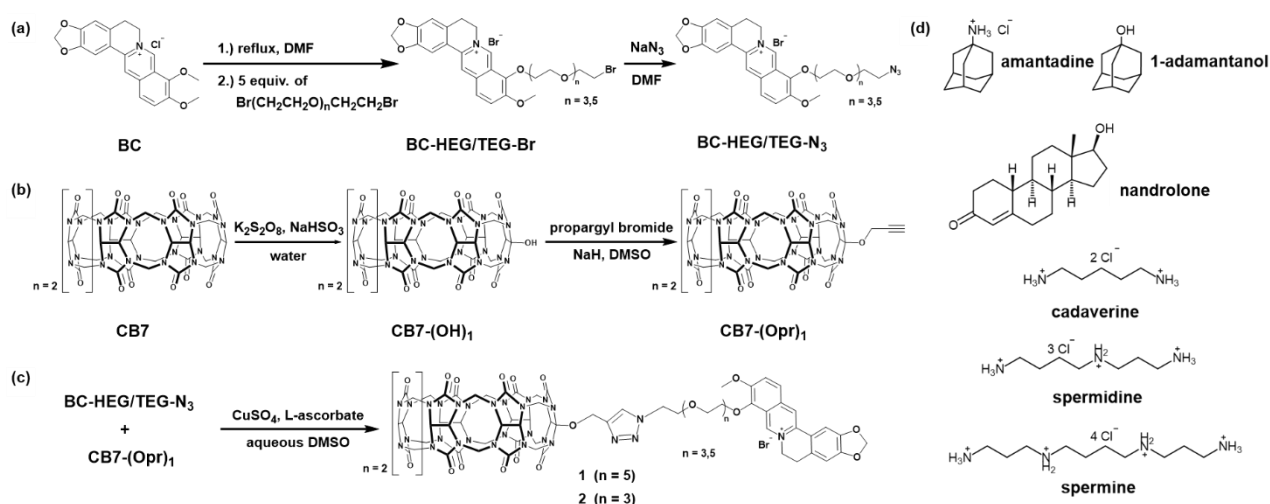

Figure 4.1 Synthesis routes of (a) berberine-HEG/TEG-azide, (b) mono-propargyl cucurbit[7]uril, (c) chemosensor **1** and **2**. (d) Chemical structure of all guests whose binding affinities were investigated in this work.

4.2.2. Characterization and conformation of CB7-dye conjugates

The part of mass spectrometry and ion mobilogram experiments in this section was done in cooperation with Dr. Ananya Baski and Prof. Manfred M. Kappes.

The supramolecular behavior of the CB7-linker-BC conjugates was characterized by mass spectrometry experiments, ^{1}H NMR, absorbance, and emission spectroscopy to determine if the CB7-linker-BC conjugates adopt the expected self-bound, "folded" conformation (Figure 3.2), or if the linkers impose constraints. Furthermore, ion mobility spectrometry was performed to get an insight into the inherent conformation of complex **1** in the absence of solvents. For chemosensor **1**, the peak appeared at m/z 925.3130 as dicationic species, which can be assigned as $(\mathbf{1} + Na)^{2+}$ (Figure 4.2 (a)). In the ion mobilogram, this species had a drift time of 5.62 ms, resulting in a cross-section of 410 Å^2 (Figure 4.2 (c)).
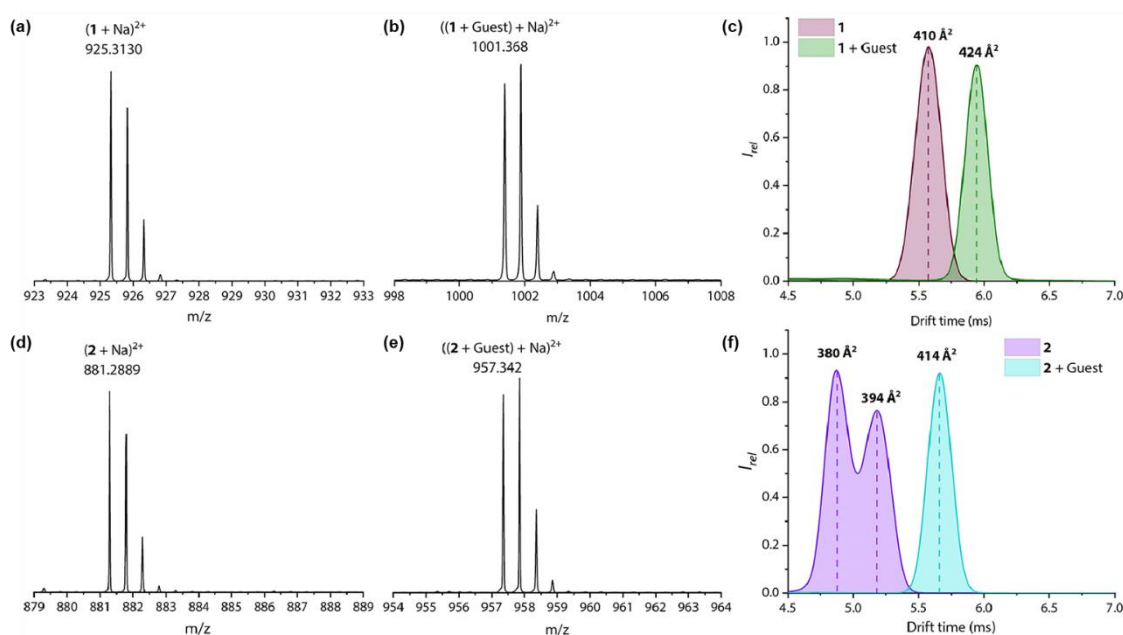

Figure 4.2 ESI-MS of (a) chemosensor **1** and (b) chemosensor **2** in a mixture of water and acetonitrile (v/v =2/1) in the positive model. ESI-MS of (b) chemosensor **1** and (d) chemosensor **2** in the presence of 1-adamantanol as the guest in a mixture of water and acetonitrile (v/v =2/1) in the positive model. Ion mobilogram of (c) chemosensor **1** and (f) chemosensor **2** in the presence of 1-adamantanol showing a significant increase in collision cross-section (CCS) for the inclusion complex, confirming the successful inclusion of the guest.

Only one defined conformation, *i.e.,* the bound or unbound state, occurs in the gas phase, but not a mixture, as evidenced by the uniform, symmetric curve shape. Upon addition of the guest, 1-adamantanol, the characteristic complex was found at m/z 1001.368 and was assigned as $((\mathbf{1} + 1\text{-adamantanol}) + Na)^{2+}$ (Figure 4.2 (b)). This species now has a substantially longer drift time at 5.94 ms and a corresponding collision cross-section of 424 Å^2 in the ion mobilogram. The relatively large increase in the collision cross-section upon guest binding can be understood by the displacement of the bound BC moiety, which results in the unfolding of the conformation. For comparison, if chemosensor **1** had occurred in an

unfolded conformation in the gas phase, guest inclusion into the cavity of CB7 would not have affected the BC moiety, and the drift time would have remained the same.[291] The ion mobilogram for chemosensor **2** with the shorter TEG-linker exhibits two peaks in drift time (4.87 and 5.17 ms, respectively) that likely both adopt folded conformations but differ in the penetration depth of the BC into the CB7 cavity (Figure 4.2 (f)). The unfolding of chemosensor **2** occurs with the addition of 1-adamantanol (Figure 4.2 (d) and (e)), as demonstrated by the appearance of a single peak at a substantially longer drift time (5.66 ms) (Figure 4.2 (f)).

Table 4.1 Assigned mass peaks with formula, experimental mass, drift time and CCS.

Ion	Formula	m/z	Drift time (ms)	CCS (Å²)
$(1 + Na)^{2+}$	$C_{76}H_{83}O_{24}N_{32}Na$	925.299	5.62	412
$((1 + Guest) + Na)^{2+}$	$C_{86}H_{99}O_{25}N_{32}Na$	1001.368	5.94	424
$(2 + Na)^{2+}$	$C_{72}H_{75}O_{22}N_{32}Na$	881.289	4.87/5.17	397
$((2 + Guest) + Na)^{2+}$	$C_{82}H_{92}O_{23}N_{32}Na$	957.324	5.66	414

Experiments in D_2O were conducted to see if unimolecular, self-folding of the CB7-dye conjugates happened in solution as well. The aromatic peaks from the BC moiety (indicated with red numbers) to the CB7 host and the HEG linker are attributed to three sets of peak areas in the ^{1}H NMR spectrum of **1** in D_2O (Figure 4.3). The singlet at 8.10 ppm (indicated with a green square) confirms the formation of a triazole moiety by the click reaction. Furthermore, when compared to the ^{1}H NMR spectrum of the corresponding BC-HEG-N₃, it becomes clear that the aromatic protons of **1** exhibited both substantial upfield and downfield shifts. In analogy to literature reports,[287] this can be interpreted by the inclusion of the 1,3-benzodioxole of BC into the CB7 cavity (shielding region of CB*n*),[79, 287] while the isoquinoline moiety resides in the deshielding carbonyl-fringed portal region of CB7.
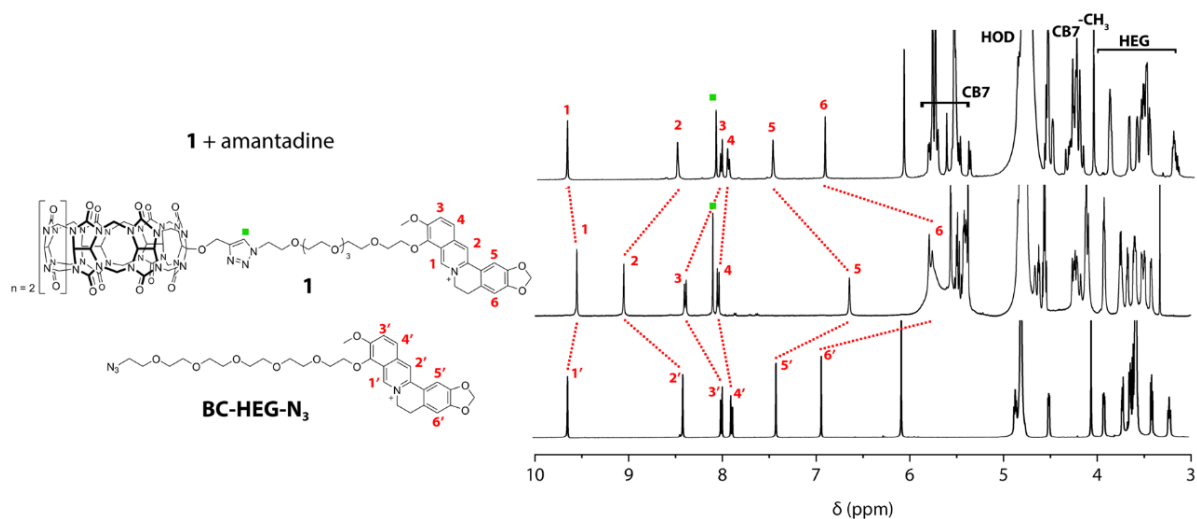
Figure 4.3 Overlay of ^{1}H NMR (500 MHz, D$_2$O) spectra of BC-HEG-N$_3$ (bottom), chemosensor **1** (middle) and chemosensor **1** with the same equivalent of amantadine (top).

Investigation of chemosensor **2** leads to similar conclusions (Figure 4.5). Notably, the ^{1}H NMR spectra of chemosensor **2** show broader peaks in the folded conformation than those of **1**, indicating that the distribution of conformers of **2** is present in the solution. This finding agrees with the conformer distribution seen in the ion mobilogram of folded **2**. After adding amantadine to the solution of chemosensor **1** or **2**, the aromatic protons of the berberine moiety were shifted to indicate displacement of the BC moiety from the host cavity (Figure 4.3 and 4.4). Note the characteristic differences in the chemical shifts of the linker ethylene glycol proton signals between the folded and unfolded structure, particularly the sharpening of the ^{1}H NMR peaks of chemosensor **2** upon unfolding.
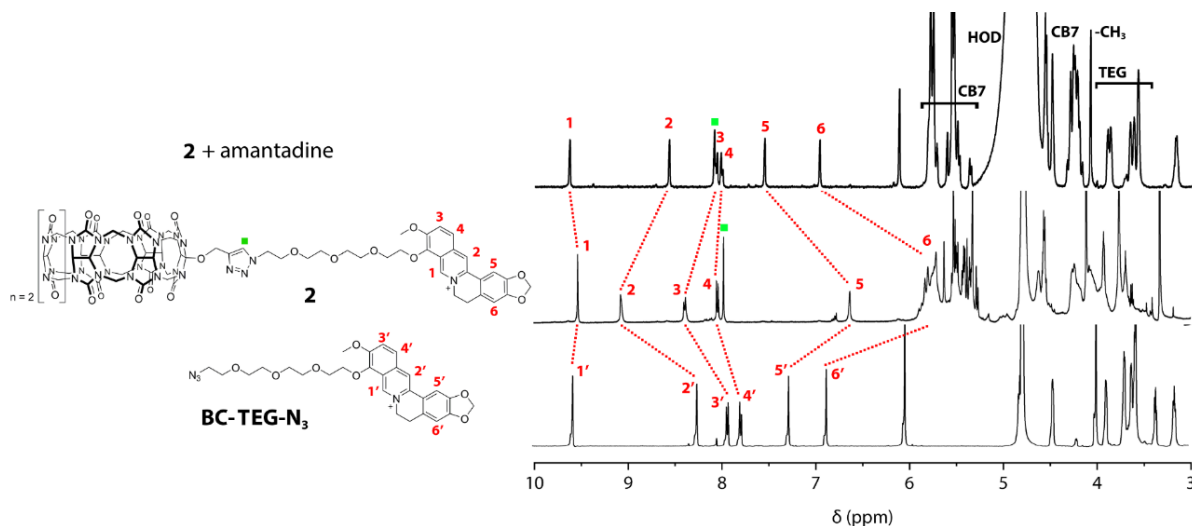
Figure 4.4 Overlay of ^{1}H NMR spectra (500 MHz, D$_2$O) of BC-TEG-N$_3$ (bottom), chemosensor **2** (middle) and chemosensor **2** upon the addition of the same equivalent of amantadine (top).

Additionally, absorbance and emission spectroscopy were utilized because they allow for probing the supramolecular behavior of the chemosensors at many orders of magnitude lower concentrations than NMR. The UV-Vis spectra of chemosensor **1** in water show an indicative 5 nm bathochromic shift at 350 nm compared to BC-HEG-N$_3$ (Figure 4.5 (a)), which in analogy to literature reports[287] shows that the

BC chromophore is included in the CB7 cavity at the micromolar concentration range as well. The emission spectra of chemosensor **1** show a maximum at 540 nm by excitation at 350 nm (Figure 4.5 (b)).
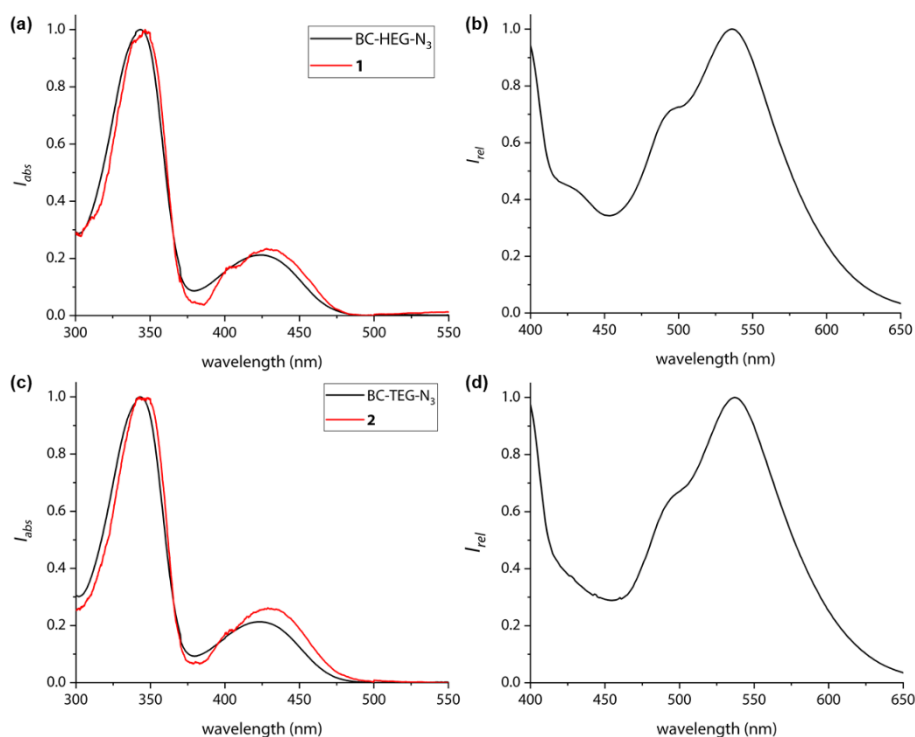
Figure 4.5 (a) UV-Vis absorption spectra of BC-HEG-N$_3$ and chemosensor **1**, each 5 µM in water. (b) Fluorescence emission spectrum (λ_{ex} = 350 nm) of 1 µM chemosensor **1** in water. (c) UV-Vis absorption spectra of BC-TEG-N$_3$ and chemosensor **2**, each 5 µM in water. (d) Fluorescence emission spectrum (λ_{ex} = 350 nm) of 1 µM chemosensor **2** in water.

Because the BC fluorophore emits a higher emission intensity inside the hydrophobic CB7 cavity than in water, the addition of amantadine leads to a strong decrease in emission intensity, indicating that the BC moiety is displaced from the cavity of chemosensor **1** (Figure 4.6).[287]

Figure 4.6 Fluorescence emission spectra (λ_{ex} = 350 nm) of 1 µM chemosensor **1** before and after addition of 1.5 eq. amantadine in water.

Similarly, the covalently bound CB7-dye conjugate is suitable as an indicator if the BC chromophore is still encapsulate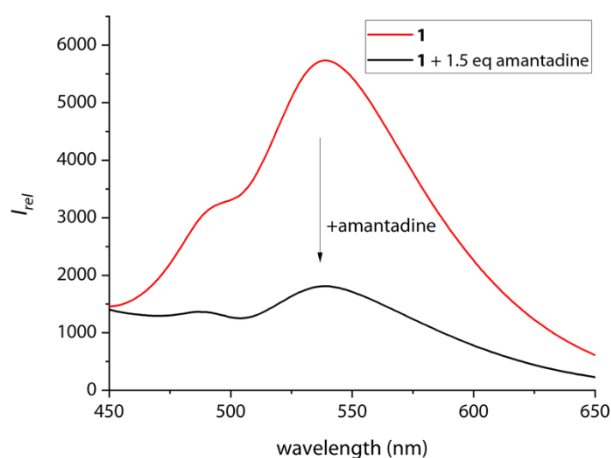d by the host upon dilution. Indeed, it was shown that a highly linear curve of the emission intensity *versus* the chemosensor **1** or **2** even after several times of dilution down to 30 nM (Figure 4.7, solid line). Conversely, the intensity-concentration plot for the non-covalent bimolecular CB7⊃BC complex had a convex curved shape (see dotted line in Figure 4.7) because complex dissociation occurred at a low concentration. (In both experiments, excess NaCl was used to weaken the unimolecular chemosensors' binding strength). Thus, photophysical experiments also indicate that chemosensor **1** and **2** adopts a unimolecular, folded structure, as is graphically depicted in Figure 3.2.
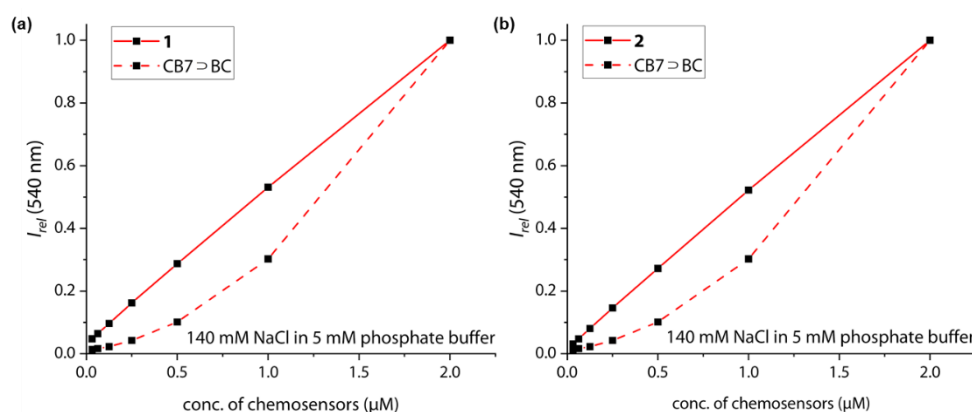

Figure 4.7 Plot of normalized emission intensity at 540 nm in 5 mM phosphate buffer containing 140 mM NaCl *versus* concentration of CB7⊃BC complex (dashed line) and (a) chemosensor **1** or (b) chemosensor **2** (solid line), λ_{ex} = 350 nm.

4.2.3. Stability of CB7⊃dye complexes *versus* CB7-BC conjugates in saline media

The stability of CB7-BC conjugates was examined as a foundation for subsequent analyte detection experiments in saline media. Typically, the stability of many CB*n*⊃dye complexes falls dramatically in the presence of salts, which reduces their utility for IDA sensing applications.[54, 65, 279, 287, 292-294] Indeed, as shown in Figure 4.8 (black line), the presence of approximate 100 mM sodium chloride leads to complete decomposition of the bimolecular CB7⊃BC assembly, which is consistent with the prediction of competitive binding of sodium cations to CB*n* portals (K_a = 2.57 × 10^3 M^{-1} for CB7 with Na$^+$).[65] Clearly, the bimolecular CB7⊃BC complex will dissociate in biorelevant media such as biofluids with typically high salt concentrations, *e.g.,* 20-40 mM Na$^+$ in urine and 135-145 mM Na$^+$ in plasma for healthy humans.[295] In contrast, the residual fluorescence intensity for CB7-BC conjugate remains at around 70 % even at 800 mM NaCl (Figure 4.8, red line). Note that the moderately reduced emission intensity of **1** and **2** in saline media likely results from the formation of CB7-BC⊃Na$^+$, in which the BC moiety remains encapsulated inside the CB7 cavity while the metal cation co-binding to the opposite CB7-portal.[275] (ESI-MS experiments gave additional evidence that the binary complex of CB7-BC conjugate with Na$^+$ is prominently present also in the gas phase, and which was the species used for the ion-mobility studies.)
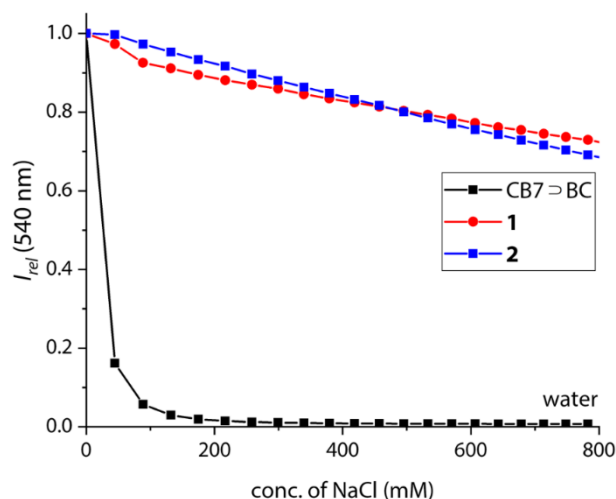
Figure 4.8 Plot of emission intensity at 540 nm of 1 µM CB7⊃BC complex (black), 1 µM chemosensor **1** (red) and 1 µM chemosensor **2** (blue) in water versus concentration of NaCl, λ_{ex} = 350 nm

4.2.4. Binding affinities of biorelevant analytes with the chemosensor 1 and 2

The host-guest binding characteristics of chemosensors **1** and **2** were studied in water *versus* saline media. Several adamantyl derivatives (amantadine, 1-adamantanol),[280] polyamines (cadaverine, spermine, spermidine)[245] and steroids (nandrolone)[279] were chosen as representative guests because of their known high binding affinities for CB7

When competitively binding guests, the BC moiety was displaced from the cavity of both chemosensors **1** and **2** respond with emission quenching; the difference in emission intensity is slightly larger for **2** than for **1**, demonstrating that the linker length has a minor but considerable effect on structures adopted in solution. Interestingly, the binding curve of amantadine with **1** (Figure 4.9 (b)) or **2** (Figure 4.9 (d)) remains very steep even in 10X PBS, and binding may be even stronger than in deionized water (Figure 4.9 (a) and (c)).

Figure 4.9 Fitting plots of normalized emission intensity at 540 nm of 1 μM chemosensor **1** in water (a) and 10X PBS (b), 1 μM chemosensor **2** in water (c) and 10X PBS (d) upon addition of amantadine (λ_{ex} = 350 nm) at 25°C. Intervals between titration steps: 500 seconds in water, 200 seconds in 10X PBS.

Likewise, for the non-charged steroid nandrolone, a very similar binding affinity with chemosensor **2** was found in 10X PBS and water (Table 4.2, Figure 4.10).
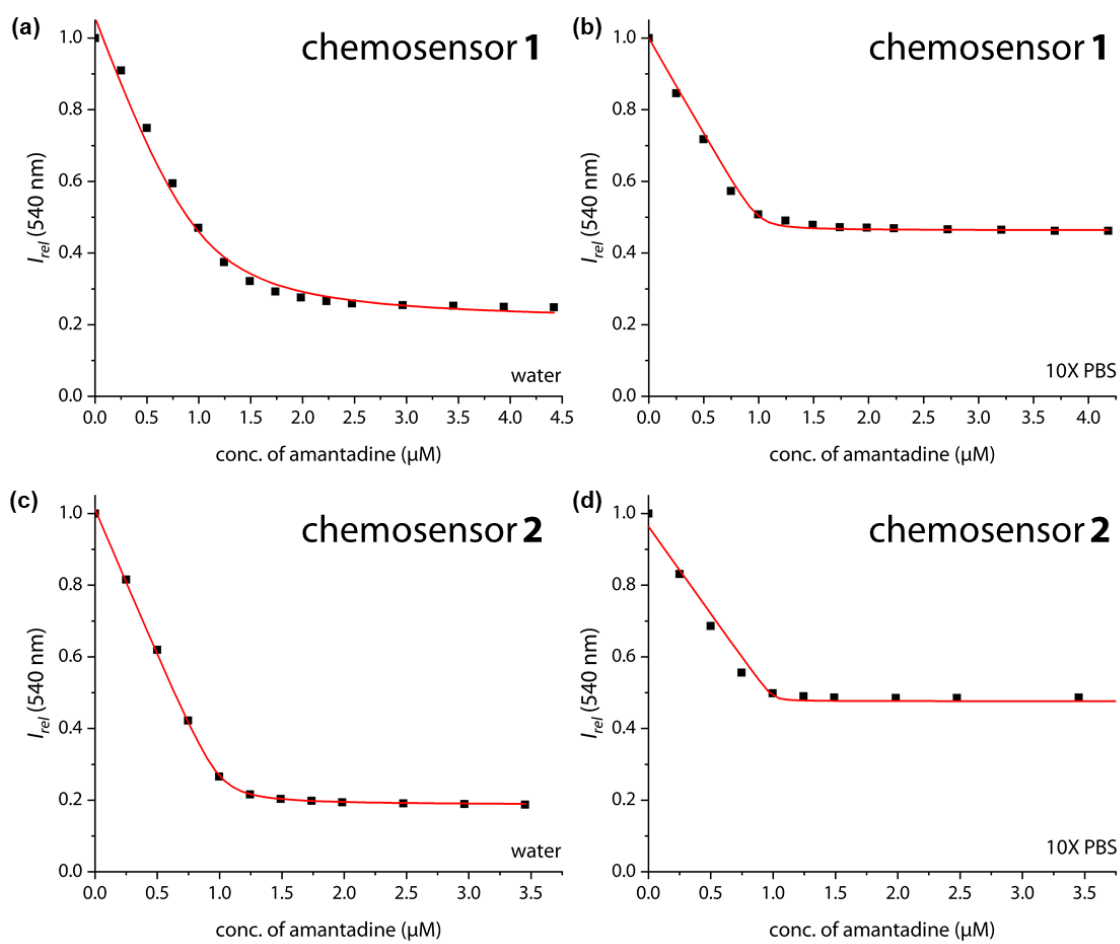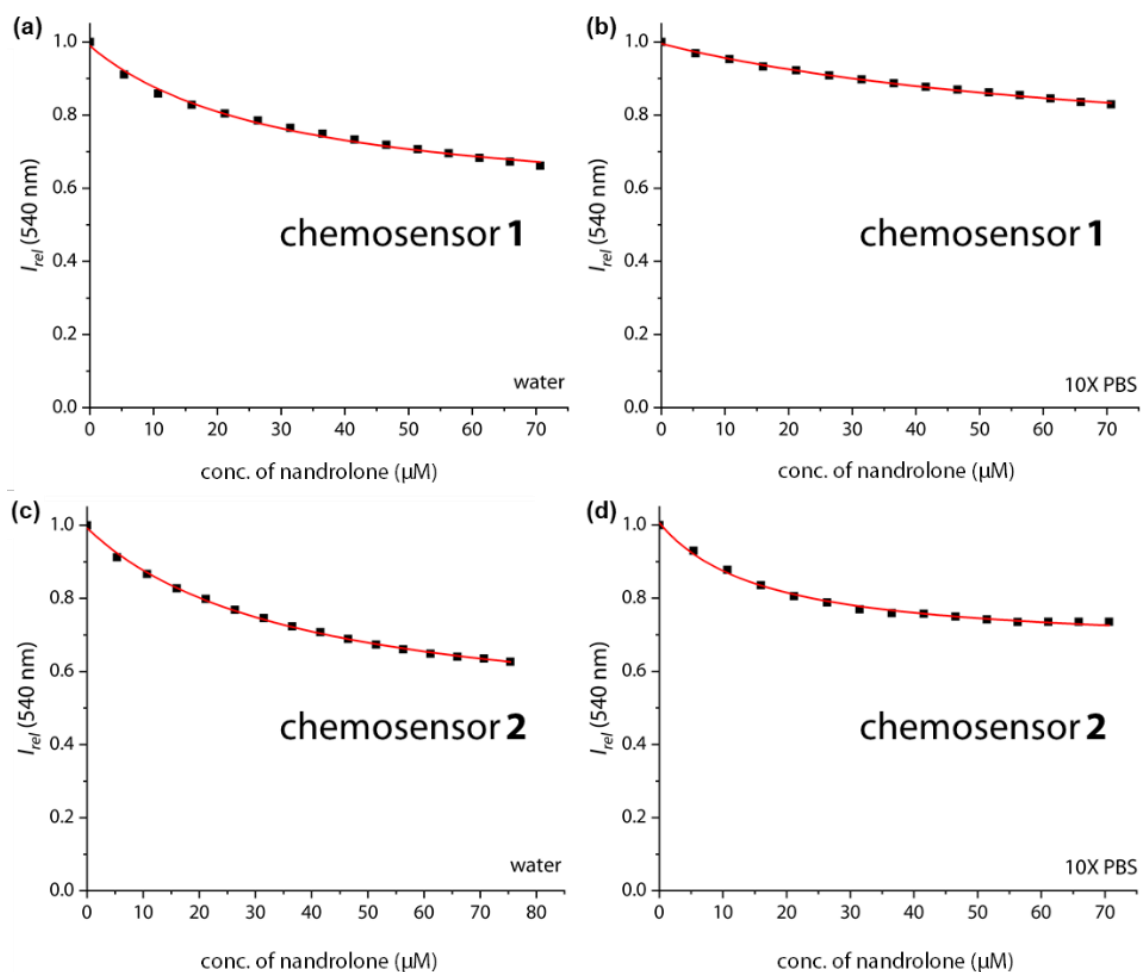
Figure 4.10 Fitting plots of normalized emission intensity at 540 nm of 1 μM chemosensor **1** in water (a) and 10X PBS (b), 1 μM chemosensor **2** in water (c) and 10X PBS (d) at 25°C, upon addition of nandrolone, λ_{ex} = 350 nm. Intervals between titration steps: 1000 seconds in water, 200 seconds in 10X PBS.

However, in deionized or minimal buffers, CB7 is a known high-affinity binder of polyamines such as spermidine (Table 4.2). Indeed, chemosensor **1** is also responsive to polyamines in deionized water (see details in the supplementary data) and is shown that binding affinity in a range of 10^3 to 10^5 M^{-1} in the order spermidine > cadaverine ≥ spermine (Table 4.2). However, unlike amantadine or non-charged guest, in the saline 10X PBS the polycationic guests, cadaverine, spermine, and spermidine do not bind at all to CB7-BC chemosensors.

Table 4.2 Summary of the binding constants determined by fluorescence titration experiments with chemosensors **1** and **2** at 25ºC. The estimated error of $\log K_a$ is 0.2.

guest	medium	$\log K_a$		
		chemosensor **1**	chemosensor **2**	CB7
amantadine	water	7.4	7.9	12.6[c]
	1X PBS	> 8 [a]	> 8 [a]	-
	10X PBS	> 8 [a]	> 8 [a]	-
	surine	> 8 [a]	> 8 [a]	-
cadaverine	water	3.7	4.0	8.4[d]
	1X PBS	3.5	3.7	-
	10X PBS	<1 [b]	<1 [b]	-
spermine	water	3.6	3.9	7.4[e]
	1X PBS	3.4	3.6	-
	10X PBS	<1 [b]	<1 [b]	-
spermidine	water	4.6	4.5	-
	10X PBS	<1 [b]	<1 [b]	-
1-adamantanol	10X PBS	> 8 [a]	7.5	-
nandrolone	water	4.5	4.5	7.1[d]
	1X PBS	4.3	4.4	6.6[f]
	10X PBS	4.1	4.8	-

[a] Lower estimate on the binding affinity. [b] The binding affinity is too small to be fitted by fluorescence titration. [c] Determined by NMR.[207] [d] Determined with berberine as indicator.[180, 279] [e] Determined with cyanostilbene as indicator.[296] [f] Determined by isothermal titration calorimetry (ITC).[279] 1X PBS is consisting of 137 mM NaCl, 2.7 mM KCl, 10 mM Na_2HPO_4 and 1.8 mM KH_2PO_4.

Furthermore, the binding titrations revealed that TEG-linker-based **2** forms a more strained folded conformation than HEG-linker-based **1**, as evidenced by the fact that chemosensor **2** had somewhat greater binding affinities than chemosensor **1** for studied guests.

4.2.5. Binding kinetics of biorelevant analytes with the chemosensors 1 and 2

The binding kinetics of chemosensors revealed some interesting characteristics: While amantadine, 1-adamantanol and the polycationic amines are all relatively strongly bound to chemosensors in water, the equilibration times follow the order polyamines (n^+) > amantadine (1^+) >> 1-adamantanol/nandrolone, ranging from seconds (polyamines, amantadine) to thousands of seconds for non-charged guests, indicating a charge-accelerating effect on the binding kinetics, see details in the supplementary data. Positively charged guests can form exclusion complexes with CB7 prior to a flip-flop mechanism into the cavity, speeding up the binding kinetics.[297] In fact, the binding kinetics of 1-adamantanol were so slow in desalinated water that no binding isotherms for determining K_a value determination could be obtained in reasonable measurement times (Figure 4.11 (a)). In PBS, the binding kinetics of amantadine

binding is much faster than in water (Figure 4.11), providing a practically convenient way to shorten assay times by adding salts. Notably, amantadine and 1-adamantanol may still be readily differentiated according to their kinetic features, allowing for selective sensing of amantadine in the presence of other non-charged high-affinity competitors (Figure 4.11 (b) and (c)).
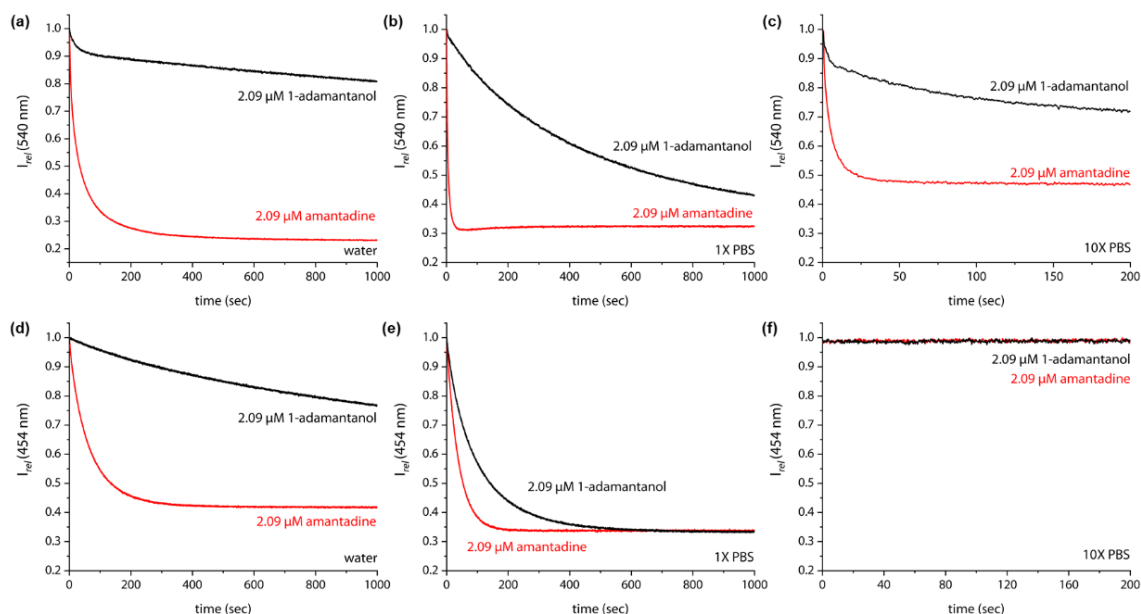

Figure 4.11 Fluorescence-based kinetic traces at 540 nm of 1.2 μM chemosensor **2** upon addition of 2.09 μM amantadine (red) or 1-adamantanol (black) in (a) water, (b) 1X PBS and (c) 10X PBS (λ_{ex}= 350 nm) at 25°C; Kinetic traces based on fluorescence at 454 nm of 1.8 μM MDAP, 1.2 μM CB7 upon addition of 2.09 μM amantadine (red) or 1-adamantanol in (d) water, (e) 1X PBS and (f) 10X PBS at 25°C, λ_{ex}= 339 nm.

4.2.6. Features and limitations of non-covalent CB7⊃dye reporter pairs.

The titration experiments with MDAP in this section were done in cooperation with Amrutha Prabodh.

As an alternative to using a covalently CB7-dye linked unimolecular chemosensor, the bimolecular CB7⊃dye can be employed for selective sensing of amantadine in saline media and biofluids (see next section) when using suitable high-affinity dyes. According to the known binding affinities for CB7 with cations, it is feasible to estimate the apparent binding constant of bimolecular CB7⊃guest (or CB7⊃dye) complexes in the presence of salts *via*[65, 298]

$$K_{\text{CB7⊃guest, saline media}} = \frac{K_{\text{CB7⊃guest, water}}}{1 + K_{\text{CB7•M}^+}[M^+]_0} \quad \text{for } [M^+]_0 >> [\text{CB7}]_0 \quad (4.1)$$

For instance, in the presence of 220 mM Na$^+$, the affinity of CB7 for amantadine still is expected as ~10^{12} M^{-1}, with $K_{\text{CB7•Na}^+} = 2.6 \times 10^3$ M^{-1} for the competitive interaction of Na$^+$ with CB7.[65] Following the analysis for the design of a CB8⊃dye IDA assay in biofluids reported by Biedermann's group, one would conclude that indicator dyes within an affinity range of $K_{\text{CB7⊃dye, saline media}} = 10^7$-$10^{11}$ M^{-1} is ideally suitable for selectively detecting amantadine in the presence of salts and other weaker binding interferents, *e.g.,* biogenic amines. However, this assumption turned out to be impractical:

2,7-dimethyldiazapyrenium diiodide
(MDAP)

trans-4-[4-(Dimethylamino)styryl]-1-adamantylpyridinium bromide
(DASAP)

Figure 4.12 Chemical structures of MDAP and DASAP

1) The lack of pH-unresponsive, high-affinity indicator dyes for CB7 is the first "trivial" hindrance to developing IDA-based amantadine sensing assays in biofluids. MDAP is one indicator dye for CB7 with the highest K_a value, $2.7 \cdot \times 10^9$ M^{-1} in deionized water (see Figure 4.12 for structure).[275, 299] With increasing salt content, its affinity to CB7 strongly drops, reaching 1.8×10^6 M^{-1} in 1X PBS (Figure 4.13 (a)). In 10X PBS, its K_a value became so weak ($K_a = 4.2 \times 10^3$ M^{-1}) that the CB7⊃MDAP reporter pair could not be used in the micromolar concentration range (Figure 4.13 (c)). As a result, the bimolecular CB7⊃MDAP complex can be used to detect amantadine in saline media if the salt concentration does not exceed that of 1X PBS. However, matrix effects will be encountered if the salinity differs significantly between the biofluid samples.

Figure 4.13 Normalized fitting plot of emission intensity at 454 nm of 2.5 μM MDAP in 1X PBS (a) and 10X PBS (c) upon addition of CB7 ($\lambda_{ex} = 339$ nm) at 25°C. Interval time between titration steps: 100 seconds; Normalized fitting plot of kinetic traces based on fluorescence of 1.8 μM MDAP with 1.1 μM CB7 in 1X PBS (b) and 2.7 μM MDAP with 54.1 μM CB7 in 10X PBS (d) ($\lambda_{ex} = 339$ nm) at 25°C. The excess CB7 addition in the case of 10X PBS was used to ensure a significant intensity change.

The CB7⊃MDAP reporter pair exhibits the ability of covalent chemosensors to kinetically distinguish the positively charged amantadine from the non-charged analogue 1-adamantanol (Figure 4.11 (d)) in deionized water. However, the distinguishability of amantadine and 1-adamantanol by CB7⊃MDAP is worsened by increasing salinity to 1X PBS (Figure 4.11 (e)). In 10X PBS, the detection of amantadine through CB7⊃MDAP was not possible anymore due to the disintegration of the non-covalent host-dye complex (Figure 4.11 (f)). Furthermore, the amantadine equilibration with the CB7⊃MDAP complex takes substantially longer than with the unimolecular chemosensors, resulting in longer assay times.

2). To overcome the affinity limitations of the CB7⊃MDAP host-dye complex that leads to its susceptibility to salts, a novel, pH-unresponsive, high-affinity indicator dye for CB7 was developed. Given the strong binding affinities of adamantane for CB7,[56, 75, 274] and the favorable photophysical properties of stilbene-type dyes,[65, 284] DASAP (Figure 4.12) was regarded as a promising indicator dye, which could be synthesized in 2 steps in 17.0% yield (see the experimental part). DASAP showed ideal properties as an indicator dye for CB7, with a 10-fold increase in its emission intensity upon binding, a substantial Stokes shift (125 nm), a more red-shifted absorption and emission spectra than MDAP, and a high binding affinity with CB7 both in deionized water and in 10X PBS (Figure 4.14). Even in 10X PBS, its binding affinity for CB7 was estimated to exceed 10^7 M^{-1}. At first sight, it appears that the desired non-pH-dependent, high-affinity dye for CB7 was discovered. However, its use proved to be completely impractical in an IDA format;
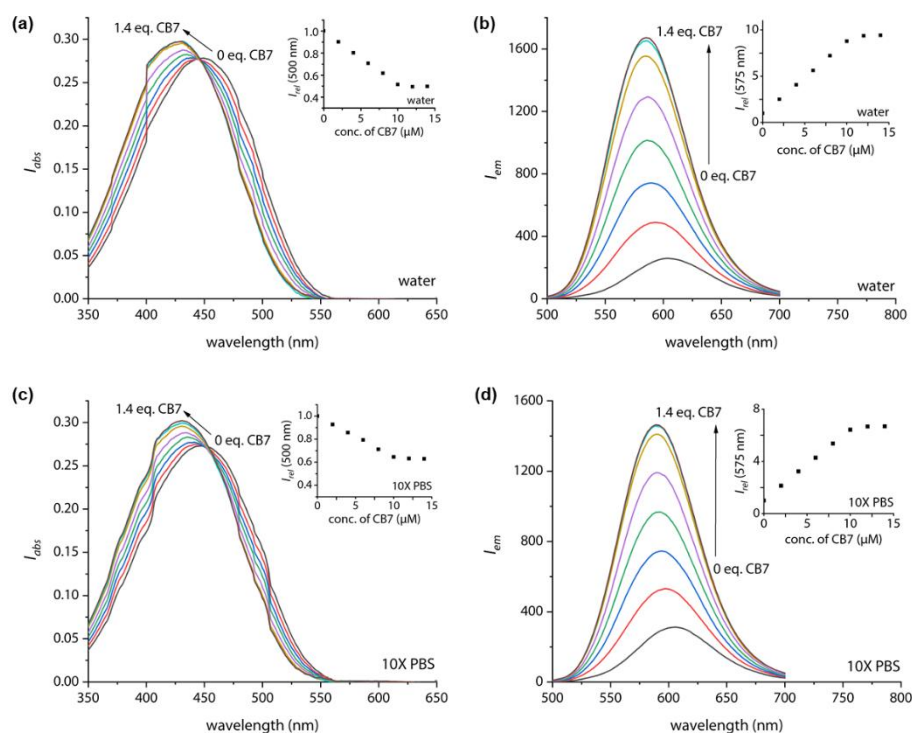

Figure 4.14 UV-Vis absorption spectra of 10 μM DASAP in water (a) and 10X PBS (c) upon addition of CB7 at 25°C. Inset: plot of normalized absorption intensity at 500 nm. Emission spectra of 10 μM DASAP upon addition of CB7 in water (b) and 10X PBS (d) at 25°C, λ_{ex} = 450 nm. Inset: plot of normalized emission intensity at 575 nm. The Interval time between each titration step is 50 seconds.

No appreciable change in the emission intensity of the CB7⊃DASAP complex dissolved in water or 10X PBS was observed within 500 seconds of assay time even upon the addition of 100X excess of amantadine, demonstrating that the CB7⊃DASAP complex is kinetically inert on the practically relevant time scale (Figure 4.15 (a) and (b)). Likewise, attempts to set up a guest-displacement-assay[180] by addition of DASAP to the pre-equilibrated CB7⊃amantadine complex failed, again due to slow unbinding kinetics for high-affinity guests from CB7 (Figure 4.15 (c) and (d)).
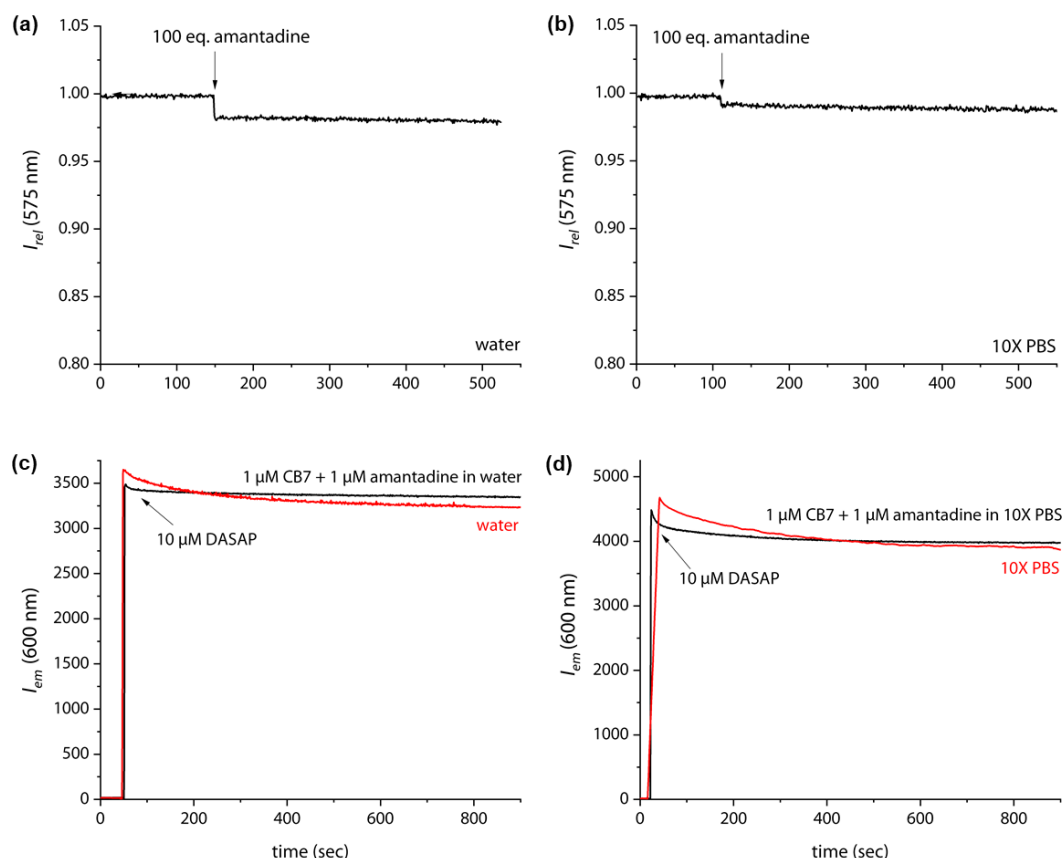

Figure 4.15 Normalized kinetic traces based on fluorescence monitored at 575 nm of 5 µM CB7⊃DASAP and 500 µM amantadine (100 equivalents) in water (a) and 10X PBS (b) (λ_{ex} = 450 nm) at 25°C. (c) Kinetic traces based on fluorescence at 600 nm of 10 µM DASAP into water (red) and 1 µM CB7⊃amantadine (0.1 eq.) in water (black) (λ_{ex} = 530 nm); (d) Kinetic traces based on fluorescence at 600 nm of 10 µM DASAP into 10X PBS (red) and 1 µM CB7⊃amantadine (0.1 eq.) in 10X PBS (black) (λ_{ex} = 530 nm).

4.2.7. Quantitative determination of amantadine in biofluids

Encouraged by the ability of chemosensors to detect amantadine even in ultra-high concentrated saline media (Figure 4.9, about 1.37 M NaCl) in comparison with the ineffectiveness of CB7⊃BC complexes in such environments, the binding studies were carried out in synthetic urine ("surine") as a well-defined media and then to real human urine and saliva.

Amantadine is usually recommended in 100-200 mg daily doses to Parkinson's patients and is typically excreted by 15-50% unchanged in the urine.[300, 301] Thus, amantadine concentration of ≥ 40 µM will be found for up to 24 h in urine. Following established routines for spectroscopic urine diagnostics,[276,]

[277, 302] urine samples were diluted with water in a 1:4 ratio to reduce the absorbance of real urine and avoid inner filter effects. Because the analyte concentration in urine samples is usually unknown, a new method was devised for using chemosensor **1** or **2** for quantifying amantadine in real urine samples. In brief, chemosensors **1** and **2** were utilized as titrants to determine the amantadine concentration in several real urine samples (Figure 4.16 (a)). In the negative control samples (urine from a healthy donor who is not receiving any drug treatment), the proportional increase of the chemosensor concentration results in a linear curve when chemosensor **1** is added to the assay medium (Figure 4.16 (b)). As a result, the unfolding of the chemosensor does not occur in the negative control media, showing that the components present in this urine sample do not affect chemosensor **1**. Indeed, polyamines such as cadaverine and spermidine present in human urine at a low micromolar concentration did not unfold the chemosensor, which is in accordance with their low binding affinity for the chemosensors in the saline medium.

In order to simulate urine from patients taking amantadine, urine samples from three healthy donors were each spiked with 10 μM amantadine and subsequently diluted by water to reach a final concentration of 2 μM amantadine at the biological relevant concentration. As shown in Figure 4.16 (c-e), the fluorescence intensity showed a significant two-stage distribution as a function of chemosensor concentration. The amantadine concentration crosses the two straight lines described by two sets of data points: (1) those acquired with titrant concentrations under 1.0 equivalent and (2) those obtained with titrant concentrations greater than 1.0 equivalent. After plotting the two stages together, the intersection was found at around 2 μM amantadine corresponded to the spiking amantadine concentration of 2 μM in 4:1 diluted urine medium (and hence 10 μM amantadine in urine). Experiments were implemented in three different urine samples to probe the influence of sample-to-sample matrix variations and gave in each instance the expected result (Figure 4.16 (c-e)). The data for chemosensor **2** is similar, as shown in Figure 4.17.
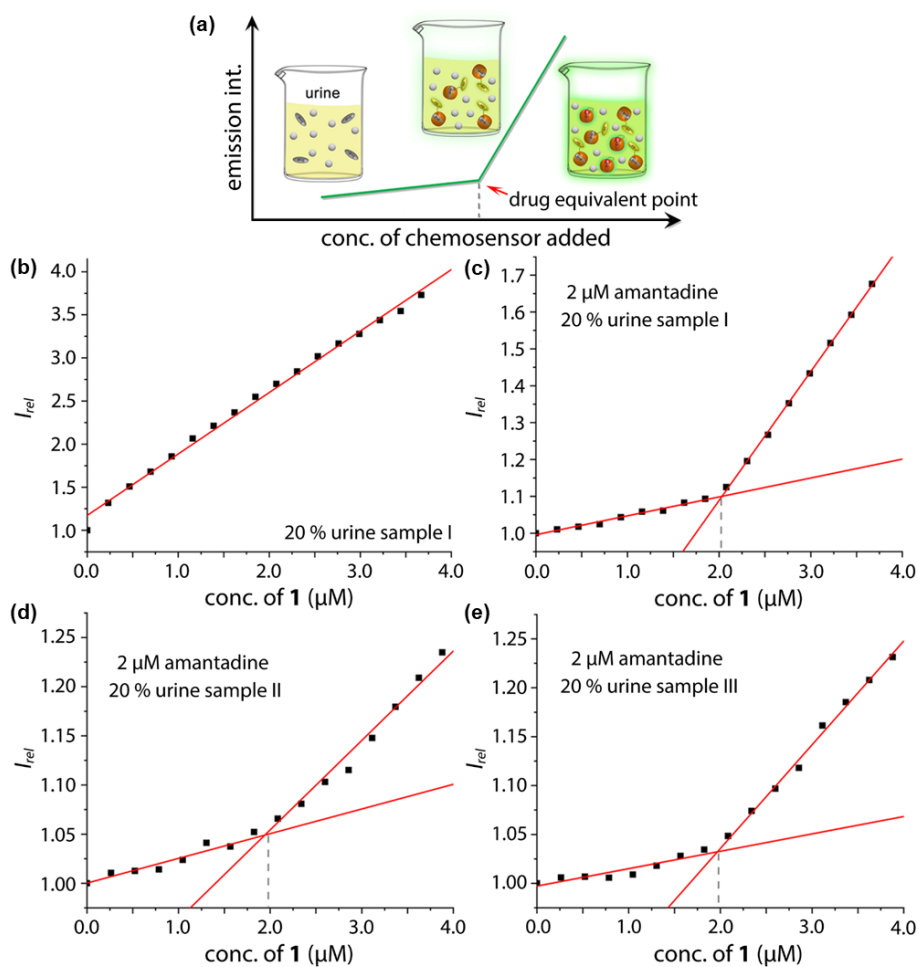
Figure 4.16 (a) Schematic representation of the analyte detection with CB7-dye conjugate chemosensors in real urine media; (b) The normalized fitting plot of emission intensity at 540 nm *versus* concentration of chemosensor **1** in 20% urine sample I; The normalized fitting plot of emission intensity at 540 nm *versus* concentration of chemosensor **1** in 20% urine (c) sample I, (d) sample II and (e) sample III spiked with 2 μM amantadine at 25°C.
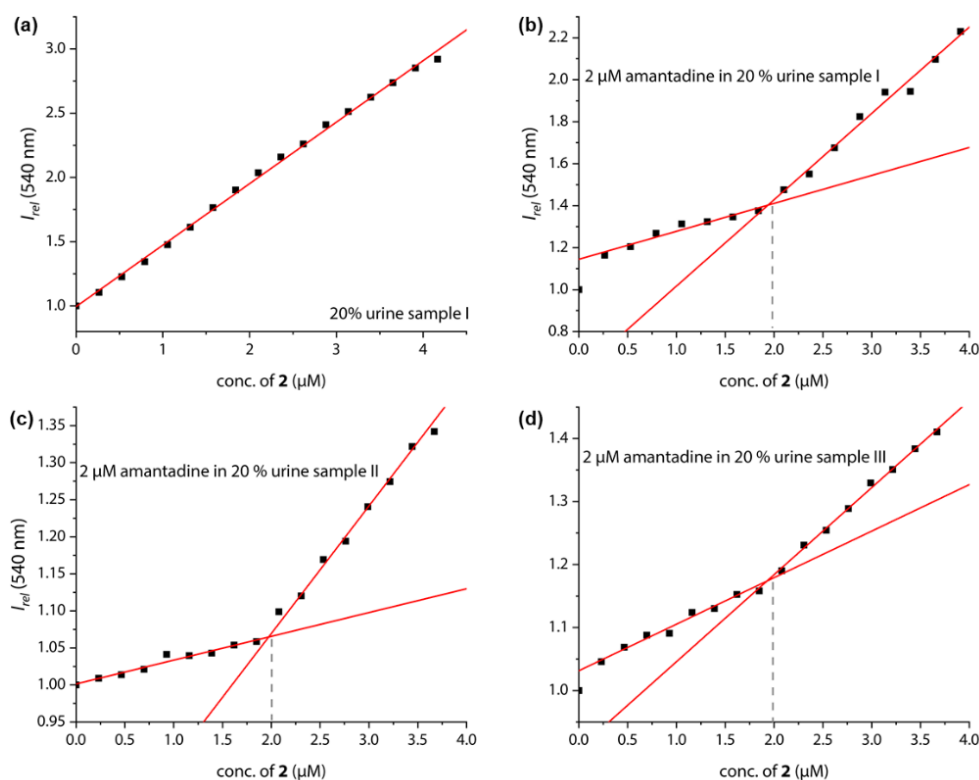
Figure 4.17 (a) Fitting plot of the normalized emission intensity at 540 nm *versus* concentration of chemosensor **2** in 20% urine sample I; Fitting plot of the normalized emission intensity at 540 nm *versus* concentration of chemosensor **2** in 20% urine (b) sample I, (c) sample II and (d) sample III with a final concentration of 2 μM amantadine at 25°C.

It should be emphasized that amantadine detection in surine was also possible using CB7⊃MDAP reporter pair, and the presence of biogenic amines simulated in the experiment only caused little interference (Figures 4.18 (b) and (d)). The amantadine binding to CB7⊃MDAP, on the other hand, is slower than for the unimolecular chemosensors, and its susceptibility to interference by salts or other CB7-binding compounds is higher. Thus, it remains to be observed whether the CB7⊃MDAP-based assay is reliable under practical conditions, such as in real urine with varying concentrations of salts and organic components (*e.g.,* other drugs).
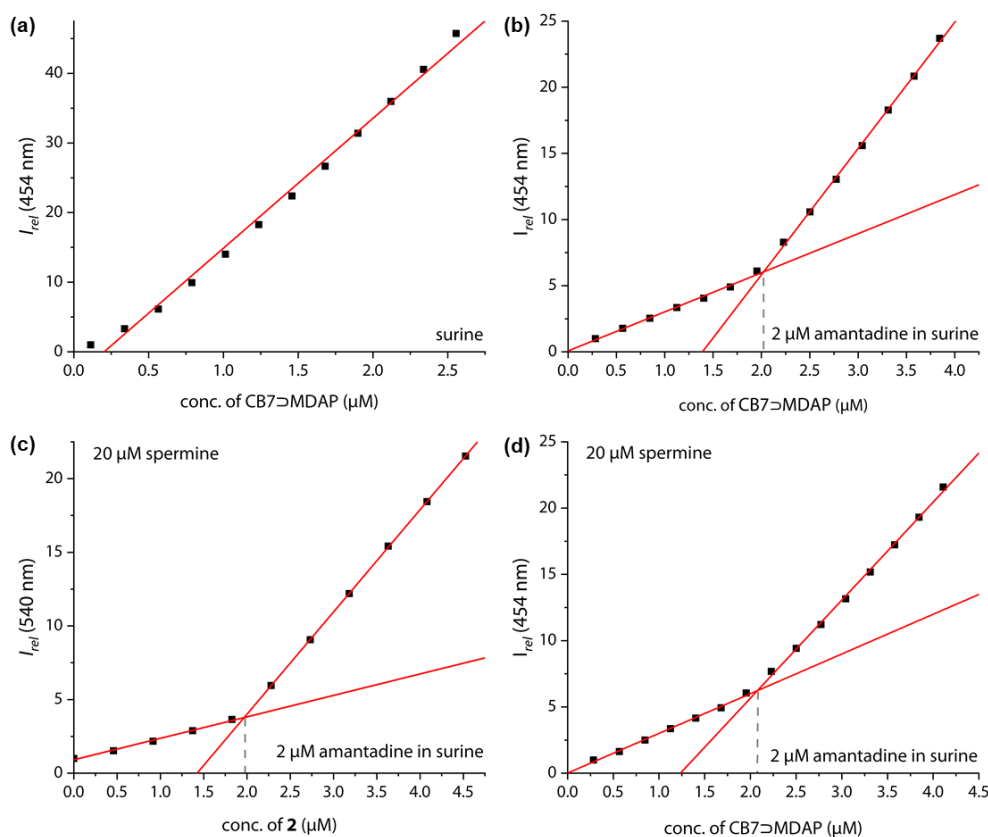
Figure 4.18 Fitting plot of the normalized emission intensity at 454 nm *versus* CB7⊃MDAP (a) in surine and (b) surine spiked with 2 μM amantadine at 25°C, respectively (λ_{ex} = 339 nm). Interval time between titration steps: 200 seconds. The fitting plot of the normalized emission intensity *versus* concentration of (c) **2** at 540 nm, λ_{ex} = 350 nm and (d) CB7⊃MDAP at 454 nm in surine spiked with 2 μM amantadine and 20 μM spermine at 25°C (λ_{ex} = 339 nm). Interval time between titration steps: 50 seconds for **2** and 200 seconds for CB7⊃MDAP.

After oral administration, amantadine is found in different body fluids, such as nasal, saliva and cerebrospinal fluid (CSF).[303, 304] For instance, the levels of amantadine in saliva equal approximately those in the serum in the range of 0.3 μg/mL to 0.8 μg/mL (around 2 μM to 5 μM).[305] However, saliva contains much higher concentrations of biogenic amines (up to 400 μM cadaverine)[306] than urine while being less saline, causing unwanted interferences for indicator displacement assays with non-covalent CB7⊃dye reporter pairs. Fortunately, chemosensors **1** and **2** were discovered to work in human saliva as well: For qualitative testing, saliva samples from healthy donors were spiked with 5 μM chemosensor **1** and the emission was measured using a microplate reader prior and after spiking with 5 μM amantadine (Figure 4.19 (a) and (c)), resulting in the expected emission intensity decrease caused by unfolding of the chemosensor after complexing with amantadine. This assay can be performed directly in non-diluted saliva. The determination of the amantadine concentration in non-diluted saliva was set and 2 μM of drug spiking was used as a presentative showcase, similar to the assay type introduced for quantification of amantadine in urine.
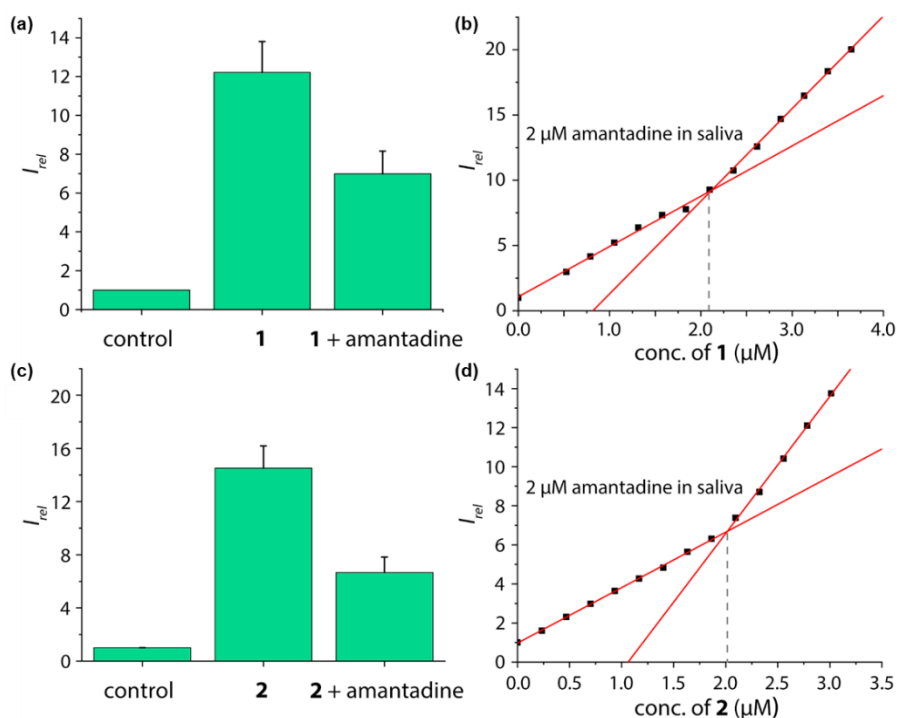
Figure 4.19 Normalized emission intensity at 540 nm of 5 μM chemosensor **1** (a) and chemosensor **2** (c) in human saliva prior to and after the addition of 5 μM amantadine. Error bars represent the standard deviation of the mean (n = 3). b) Fitting plot of the normalized emission intensity at 540 nm obtained by the stepwise addition of chemosensor **1** (b) and chemosensor **2** (d) to saliva that was spiked with 2 μM amantadine.

The predicted amantadine concentration was returned from the assay in three different saliva samples by using chemosensors **1** and **2** (Figure 4.19 (b) and (d)). The performance of the reporter pair CB7⊃MDAP in detecting amantadine in artificial saliva was comparable to that of the chemosensors. However, the simulated presence of cadaverine that can reach high micromolar concentrations in the saliva for some patients[306] showed a stronger impact on CB7⊃MDAP than on **2** (Figure 4.20).
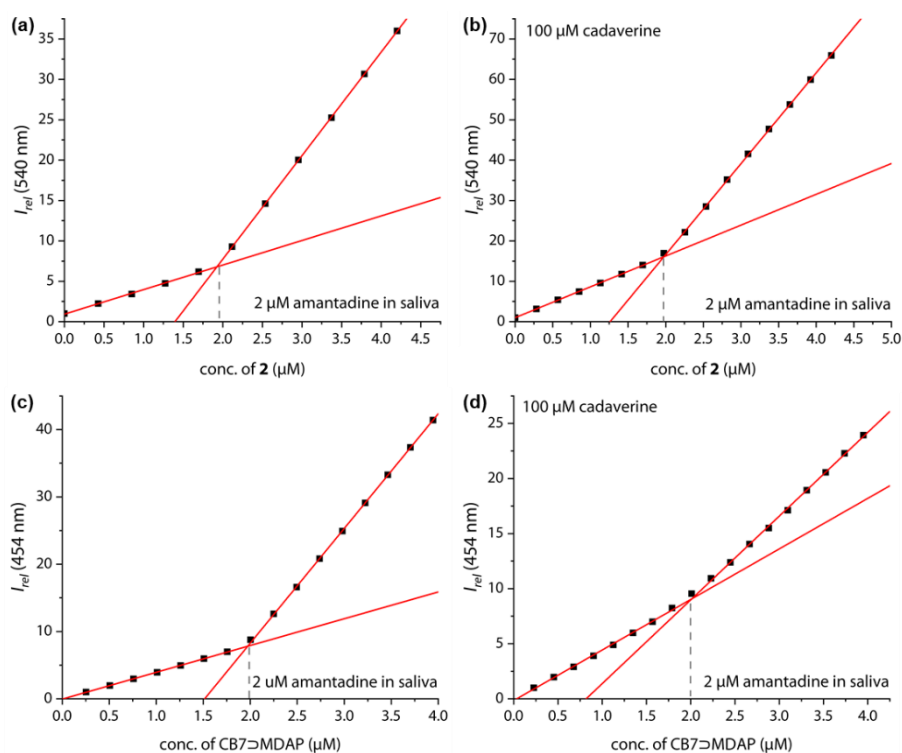
Figure 4.20 Fitting plot of the normalized emission intensity at 540 nm *versus* concentration of chemosensor **2** in artificial saliva spiked with 2 μM amantadine (a) and additional 100 μM cadaverine (b) at 25°C (λ_{ex} = 350 nm); Fitting plot of the normalized emission intensity at 454 nm *versus* concentration of CB7⊃MDAP, λ_{ex} = 339 nm in artificial saliva spiked with 2 μM amantadine (c) and additional 100 μM cadaverine (d) at 25°C. Interval time between titration steps: 50 seconds for chemosensor **2** and 200 seconds for CB7⊃MDAP.

The design of unimolecular chemosensor is compared to the frequently adopted use of non-covalent biomolecular reporter pairs in the following:

The increase of the dye's affinity for the host through covalent tethering, resulting in a higher degree of complexation in the face of disruptive competitors, enables the employment of intrinsically weakly binding indicator dyes with acceptable photophysical properties. Due to the disintegration of the non-covalent reporter pair complex, non-charged or monocationic CB7-indicator dyes like berberine (BC) cannot be used in biofluids, *e.g.,* K_a = 2.4 × 10^7 M^{-1} for CB7⊃BC in water but less 1.9 × 10^5 M^{-1} in the presence of 50 mM NaCl.[287] The choice of indicators was limited to the few known high-affinity dyes for CB7, mostly dicationic aromatic species such as MDAP[275, 299] and 2,7-dimethyldiazaphenanthrenium (MDPT)[178], due to their electron-poor and symmetric structures, which have rather unimpressive photophysical properties. For example, this section demonstrated that the CB7⊃MDAP reporter pair is functional for indicator displacement assays in a typical biorelevant saline buffer such as 1X PBS while maintaining a high K_a value of 1.8 × 10^6 M^{-1}. Higher salinity, on the other hand, was not tolerated by this reporter pair. From a photophysical standpoint, MDAP is an applicable fluorophore ($\lambda_{em, max}$ = 454 nm), which absorb and emit in the visible region of the electromagnetic spectrum. The host-dye conjugation

strategy widens the range of functional chemosensors that can be prepared in (saline) aqueous media by lifting the previous constraints on searching for high-affinity dyes with suitable photophysical properties.

Inspired by the reported adamantly-BODIPY conjugate developed as a pK_a shift indicator dye for CB7,[307] a novel pH-independent push-pull type high-affinity indicator dye (DASAP) for CB7 that functions both in water and in strongly saline buffers were developed. At first, this design appeared to overcome the affinity and the photophysical limits encountered by MDAP, but practice uncovered a fundamental restriction of indicator displacement assay-based sensing for CB7⊃dye reporter pairs. Most indicator dyes attain a critical length such that upon inclusion of complex formation with CB7, both portals of the hosts are occupied by the dye, as seen in Figure 4.21. This structural feature is also adopted by the high-affinity CB7⊃dye complexes with dicationic dyes and has important implications on the equilibration times for sensing assay times. Basically, the guest-exchange process for host-guest complexes can occur through an S_N1-type or S_N2-type-mechanism. Considering the situation of non-covalent CB7⊃dye complexes, the S_N1 mechanism appears to be the major pathway,[181] proceeding through the exit of the dye from the host as the first and rate-limiting step (Figure 4.21 (a)).

Conversely, an S_N2-type dye-guest exchange mechanism would require the formation of a guest•CB7•dye transient complex, which is hampered by the protruding indicator dye from the CB7 portal. (BC may be one exception as the dye does not enter the whole cavity, allowing simultaneous binding with cationic species, *e.g.,* metal ions.[275] However, the CB7⊃BC complex is salt labile and cannot be used in biofluids, see above).
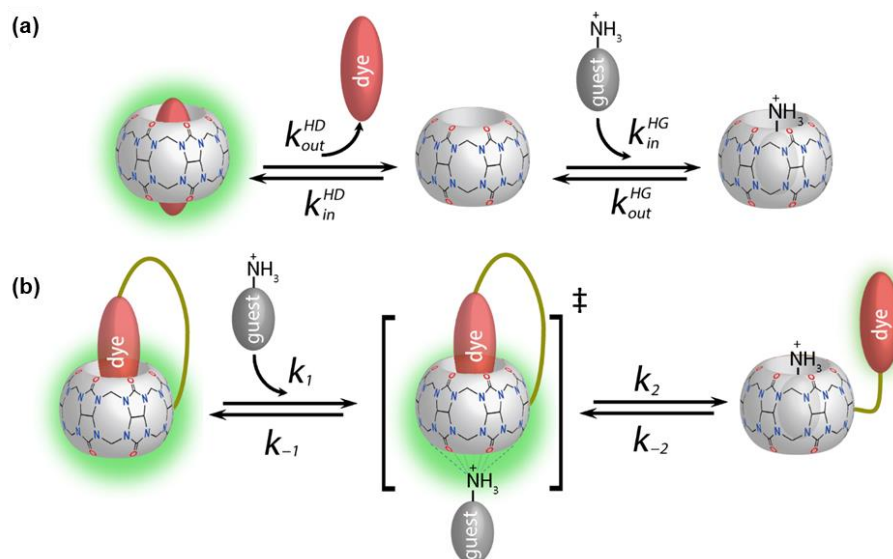

Figure 4.21 (a) Schematic representation of an S_N1-type-mechanism for the guest-exchange process on analyte-induced conformational changes of non-covalent CB7⊃dye reporter pair complexes and (b) an S_N2-type-mechanism for the guest-exchange process on analyte-induced conformational changes of CB7-dye conjugates.

With most CB7⊃dye reporter pair complexes restricted to an S_N1-type dye-guest exchange mechanism, it becomes clear that the higher affinity of the dye to the host, the lower rate constant for the exit of the dyes from the host because $k_{out} = k_{in} \cdot K_a^{-1}$ and k_{in} are relatively similar among different guests for the same

CBn homologue.[181, 275, 308, 309] These counteracting effects result in a severe limitation for applying CBn-based IDA with non-covalent reporter pairs for sensing applications in biofluids. On the one hand, the affinity between the host and the dye needs to be high enough to avoid the disintegration of the CBn⊃dye reporter pair in the presence of other competitively binding salts or interferents. On the other hand, ultra-high-affinity dyes cause overall slow exchange kinetics, which results in prolonged assay times. Note that a similar rationale holds for guest-displacement assays (GDA),[180] which likewise show impractically slow equilibration times for detecting high-affinity guests such as amantadine.

Fortunately, the thermodynamic and kinetic parameters of the CB7⊃MDAP complex are counterbalanced ($K_a = 2.7 \times 10^9$ M^{-1}, $k_{in} = 2.4 \times 10^7$ M^{-1} s^{-1}, $k_{out} = 9.0 \times 10^{-3}$ s^{-1} in water)[181], so it can be practically used for sensing applications in saline media and biofluids. The high-affinity CB7⊃DASAP complex was impracticable as a reporter pair for amantadine detection despite its excellent salt stability and favorable photophysical properties. Similarly, the previously reported CB8⊃MPCP pair ($K_a = 3.9 \times 10^{12}$ M^{-1}, $k_{in} = 2.0 \times 10^7$ M^{-1} s^{-1}, $k_{out} = 5.1 \times 10^{-6}$ s^{-1} in water) [181, 278] was also limited and resulting in assay times of several minutes even the accelerating effect of salts present in biofluids. It is worth mentioning that CB8 has a lower inherent affinity to biorelevant metal cations such as Na$^+$, K$^+$ and Ca^{2+} than CB7.[65] Therefore, CB8⊃dye reporter pairs are less influenced by salts and allowed the use of the dye with a lower affinity than for the analogous CB7⊃dye pairs in saline media. On the contrary, CB6-based chemosensing assays will not be operational in biofluids because the ingression rates are relatively low for CB6 complexes due to the constricted portal region[54, 181] (thus limiting the acceptable affinity for the CB6⊃dye pairs). On the other hand, CB6 has a sizeable affinity for Na$^+$, K$^+$ and Ca^{2+}.[65] The design of a covalent chemosensor overcomes these issues and will be particularly attractive for CB6-based chemosensors.

For chemosensors **1** and **2**, the conjugated indicator (berberine) does not occupy both CB7 portals but remains one portal accessible, as confirmed by ^{1}H NMR experiments and molecular modeling. The situation is graphically depicted in Figure 4.21 (b) that berberine as the indicator dye does not fully penetrate the CB7 cavity and from the restricted linker lengths. The accessible CB7-portal region can form transient complexes with positively charged guests *via* cation-carbonyl interactions. In this case, the S$_N$2 dye-guest exchange mechanism can be adopted by positively charged guests such as amantadine, explaining why much faster equilibration of chemosensors **1** and **2** than CB7⊃MDAP with cationic target analyte and the kinetic differences observed between amantadine and 1-adamantanol binding. The covalent chemosensor design strategy opens new opportunities for increasing the distinguishability of different analytes *via* their characteristic binding kinetics.

The research also revealed new supramolecular effects that the significantly attenuated binding affinity of the chemosensors for polyamines can be observed in saline buffer, in contrast to the modest attenuated binding affinity for neutral and mono-charged guests as salinity increases in the medium. Thus, an increase in the salinity of the medium can improve practical assay performance, such as reducing the equilibration times. However, a similar strategy cannot be applied to the CB7⊃MDAP (or CB7⊃BC)

reporter pair-based assays because the bimolecular host-dye complex dissociates in high salinity media. In addition, the characteristic effects on the thermodynamics and kinetics of analyte binding to CBn through the addition of salts to the assay medium will be useful for pattern recognition-based differential sensing of organic analytes.

4.3. Conclusion

In this chapter, two novel CB7-based unimolecular chemosensors were designed and synthesized. Their conformation as a back-folded unimolecular structure was confirmed in the gas phase and solution and reported on their interaction with biologically relevant molecules. Both conjugates displayed exceptional resistance to dilution and salt effects and remained functional chemosensors even in ~10^6 times excess NaCl. In biologically relevant buffered saline and real urine, the chemosensors displayed a great selectivity for Parkinson's drug amantadine in potential interferents such as polyamines (low-affinity binding in saline media) or hydrophobic, non-charged guests such as the steroid nortestosterone (slow binding). To the best of my knowledge, this is the first CBn-based unimolecular chemosensor that can be utilized to detect a blockbuster drug, *i.e.,* amantadine, in the medically relevant concentration range in human urine and saliva.[310] While the non-covalent CB7⊃MDAP reporter pair may also be a viable option for amantadine detection in biofluids, the investigation nevertheless uncovered important and general shortcomings of using high-affinity host-guest. It appears promising that the covalent chemosensor design strategy can overcome many of these limitations and increase the selectivity for analyte-detection by offering access to an S_N2-type guest exchange mechanism.

The "chemosensor-standard-addition-method" used here for amantadine quantification is particularly advantageous since it circumvents the otherwise often observed matrix-to-matrix effects between different biofluid specimens, such as differences in color, emission backgrounds or salinity of urine samples. The simplicity and speed of the supramolecular analytical approach proposed may find future use in established diagnostic laboratories or point-of-care applications.

4.4. Experimental part

4.4.1. Material and method

4.4.1.1. Material

All purchased chemicals and solvents were used as received from suppliers without any further purification. 2,7-dimethyldiazapyrenium diiodide (MDAP) [311] and 1,1'-(octane-1,8-diyl)bis(3-methyl-1H-imidazol-3-ium) bromide (C$_8$mimBr$_2$)[312] was synthesized according to established literature methods. The buffer solutions of 1X (137 mM NaCl, 2.7 mM KCl, 10 mM Na$_2$HPO$_4$ and 1.8 mM KH$_2$PO$_4$) and 10X (1.37 M NaCl, 27 mM KCl, 100 mM Na$_2$HPO$_4$ and 18 mM KH$_2$PO$_4$) phosphate-buffered saline (PBS) at pH 7.45 were prepared from GibcoTM PBS tablets by dissolving a tablet in 500 mL or 50 mL of distilled water, respectively. The artificial saliva was ordered from Pickering Laboratories and used as received. Surine was ordered from Cerilliant and used as received. MDAP, CB7, chemosensor **1** and chemosensor **2** stock solutions were prepared in Milli-Q water and then diluted in 1X or 10X PBS. The concentration of berberine hydrochloride (BC), MDAP, and nortestosterone stock solutions were

accurately determined according to their molar absorption coefficients (BC: 22300 $M^{-1}cm^{-1}$ at 344 nm, MDAP: 7800 $M^{-1}cm^{-1}$ at 393 nm, and nortestosterone: 15320 $M^{-1}cm^{-1}$ at 248 nm) by UV-Vis absorption titration measurements in Milli-Q water. The concentration of CB7 and amantadine hydrochloride stock solution were determined by fluorescence titration against a known concentration of MDAP dye and CB7⊃MDAP receptor complex, respectively, by exciting the sample at 339 nm and collecting the emission intensity at 454 nm in Milli-Q water. The concentration of the 1-adamantanol stock solution was determined by ITC measurements. The stock solution concentrations of chemosensors **1** and **2** were determined by fluorescence titration with a known concentration of amantadine hydrochloride by exciting the sample at 350 nm and detecting the emission intensity at 540 nm in Milli-Q water. The stock solution of polyamine (cadaverine, spermine and spermidine) were prepared to the aqueous solution with a certain concentration directly by weighing. In general, chemosensor solutions should be stirred for 30 minutes in the desired medium to ensure full equilibration along with a stable baseline for spectroscopical measurements.

4.4.1.2.   Nuclear Magnetic Resonance (NMR) Spectroscopy.

^{1}H and ^{13}C NMR spectra were recorded either in deuterium oxide, Chloroform-d_3 or DMSO-d_6 on a Bruker Avance 500 spectrometer at 25ºC. The ^{1}H and ^{13}C NMR chemical shifts (δ) are given in ppm and refer to residual protons on the corresponding deuterated solvent.

4.4.1.3.   High-Performance Liquid Chromatography (HPLC).

Analytical HPLC experiments were performed on an LC-2000Plus HPLC system equipped with a UV-2075 UV-Vis detector and a Kromasil 100 C18 5 µM LC column (250 × 4.6 mm, Agela) at a flow rate of 0.8 mL/min. Preparatory HPLC was performed on the same system but equipped with a Kromasil 100 C18 5 µM LC precolumn (50 × 20 mm, Agela) and a Kromasil 100 C18 5 µM LC preparative column (250 × 50 mm, Agela) for purification of CB7-HEG-BC (**1**) and CB7-TEG-BC (**2**) at a flow rate of 12 mL/min. All crude samples were dissolved in a mixture of water and ACN (v/v = 3/1) to get a final concentration of 1.5 mg/mL with one drop of TFA to improve the solubility.

4.4.1.4.   Electrospray Ionization Ion Mobility-Mass Spectrometry (ESI-IM-MS).

This part of the work was done in cooperation with Dr. Ananya Baksi.

All samples (only for chemosensors **1** and **2**) were dissolved in Milli-Q water to reach a final concentration of 500 µM. The stock solutions were diluted 20 times with Milli-Q water and then diluted with ACN (v/v = 1/2). 20 µL formic acid was added to acidify 2 mL diluted samples, which were directly infused into a Waters' Synapt G2S HDMS mass spectrometer with an ESI source coupled with an ion mobility cell. All data were collected in positive ion mode in the mass range of 200-2000 m/z. Optimized parameters are as follows: flow rate: 5 µL/min, capillary voltage: 1 kV, cone voltage: 20 V, source offset: 30 V, source temperature: 80ºC, desolvation temperature: 200ºC, cone gas flow: 0 L/min, desolvation gas flow: 400 L/min, nebulizer: 2.5 bar. Guest inclusion was confirmed by IMS, where additional optimized parameters used are as follows: He flow: 180 mL/min, IMS gas flow: 90 mL/min, trap: 2 mL/min, IMS wave velocity: 850 m/S, wave height: 40 V. Collision cross-sections were calibrated using polyalanine

(2^+ ions). The mass resolution was 35000, and the IMS resolution was 25-30. About 300 spectra acquired over 5 min were averaged for each measurement.

4.4.1.5. Electrospray Ionization Mass Spectrometry (ESI-MS).

The mass spectrum was performed on a microOTOF-Q (208-320 Vac, 50/60 Hz, 1800VA), Bruker. A small amount of samples were dissolved into 1 mL MeOH and then treated in an ultrasound bath for 30 seconds. All the data were collected in the positive mode in the mass range m/z 100-2000. Optimized parameters are as follows: dry temperature: 100ºC, dry gas: 3.0 L/min, ion energy: 5.0 eV, collision energy: 10.0 eV, collision RF: 800 Vpp, transfer time: 120 μs, prepuls storage: 10 μs.

4.4.1.6. Absorbance Spectra.

Absorbance spectra were measured in Milli-Q water on a Jasco V-730 double-beam UV-Vis spectrophotometer at 25ºC. PMMA cuvettes with a light path of 10 mm and dimensions of 10×10 mm from Brand with a spectroscopic cut-off at 220 nm were utilized for UV-Vis absorption experiments. The samples were equilibrated using a water thermostatic cell holder STR-812, while the cuvettes were equipped with a stirrer allowing rapid mixing.

4.4.1.7. Fluorescence Spectra.

Steady-state emission spectra and time-resolved emission profiles were recorded on a Jasco FP-8300 fluorescence spectrometer equipped with a 450 W Xenon arc lamp, double-grating excitation and emission monochromators. Standard correction curves corrected the emission spectra for source intensity (lamp and grating) and the emission spectral response (detector and grating). All titration and kinetic experiments were carried out at 25ºC using a water thermostatic cell holder STR-812, while the cuvettes were equipped with a stirrer allowing rapid mixing. PMMA cuvettes with a light path of 10 mm and dimensions of 10×10 mm from Brand with a spectroscopic cut-off at 300 nm were utilized for fluorescence-based titration experiments.

4.4.1.8. Amantadine determination by a chemosensor in urine and saliva

In order to simulate urine from Parkinson's patients receiving amantadine treatment, urine samples from three healthy donors were each spiked with 10 μM amantadine and subsequently diluted with water to reach a final concentration of 2 μM amantadine following the biorelevant concentration. The urine was used for measurements without any processing steps. It was used within 3 days after excretion and stored in the fridge. Morning and daily urine samples were used to probe different urine compositions. However, the higher concentration of ingredients in the morning urine did not affect the sensors. The fitting curves were obtained through a linear fit function using the software Origin.

In order to simulate saliva from Parkinson's patients receiving amantadine treatment, saliva samples from three healthy donors were each spiked with 2 μM amantadine following the biological relevant concentration. The saliva was used after centrifuging at 8000 rpm for 10 minutes to get rid of the insoluble component. It was used within 3 days after excretion and stored in the fridge. The fitting curves were obtained through a linear fit function using the software Origin.

4.4.2.Synthesis and characterization

4.4.2.1.   Synthesis of glycoluril
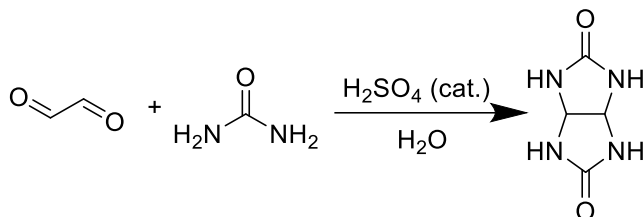
According to the procedures in the literature,[313] glyoxal (50 g, 861 mmol, 1.0 eq, 125 ml of a 40wt. % solution in H_2O), urea (129.4 g, 2.154 mol, 2.5 eq), and 250 mL of H_2O were added into a 1 L round-bottom flask equipped with a stirrer. The reaction mixture was heated to 90°C and was stirred for 5 min. Concentrated H_2SO_4 (10 mL) was added dropwise over 5 min, and a white solid formed 10 min after adding the acid. The reaction mixture was stirred for an additional 12 h. The reaction mixture was cooled to room temperature, and 50% NaOH aqueous solution was added until the pH of the reaction was adjusted to 14. The stirring was stopped, and the reaction mixture was cooled to 0°C. The suspension was isolated by vacuum filtration on a Büchner funnel, and the solid was washed with cold water (2 x 1000 mL). The solid was left to dry on the Büchner funnel under suction for 3 h, was transferred to a 700 mL beaker, and was dried for 16 h at 80°C to yield 45.0 g (304 mmol, 92% yield) of glycoluril as an off-white powder.

^{1}H NMR (500 MHz, DMSO-d_6) δ 7.17 (s, 4H), 5.24 (s, 2H).
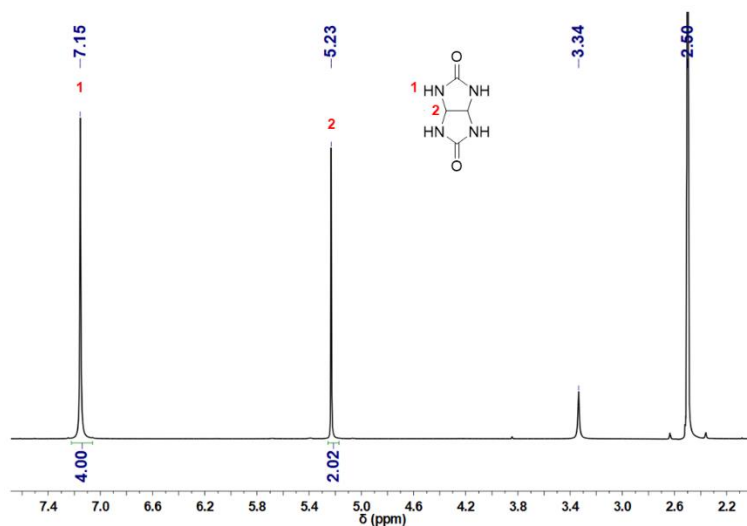
Figure 4.22 ^{1}H-NMR of glycoluril in DMSO-d_6

4.4.2.2.   Synthesis and purification of CB7
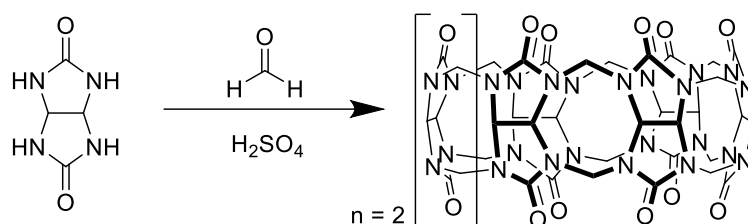
According to the procedures in the literature,[314] formaldehyde (14 mL of a 37% aqueous solution, 182 mM) was mixed with sulfuric acid (60 mL of a 9 M aqueous solution), and the magnetically stirred mixture was cooled down to 5°C. Glycoluril (11.4 g, 80 mM) was added, which dissolved slowly to produce a thick transparent gel. After 30 min, the gel became too viscous to allow further stirring, and at this point, the temperature was elevated to 100°C, resulting in the gel dissolved again. The reaction mixture was heated for 72 h and then poured into 200 mL of distilled water. Upon adding 800 mL of acetone, all CBn oligo- and polymers were precipitated from the solution. The solid mixture was filtered and subsequently washed with 1.5 L of cold acetone/water (v/v = 8:2) to remove the acid and produce a mixture of CBn as a white powder. 400 mL of distilled water was added, and all water-soluble CBn was dissolved except for CB6 and CB8. When the filtrate was treated with 300 mL of acetone, a new precipitate mainly containing CB7 appeared. This precipitate was dissolved into 100 mL of distilled water again, and 20 mL of acetone was added, which caused the precipitation of CB7 with other unidentified homologues. The further addition of acetone (100 mL) into filtrate led to the precipitation of the major fraction of CB7. The product was washed with acetone and methanol and subsequently dried under vacuum at 80°C for 24 h.

^{1}H NMR (500 MHz, D$_2$O) δ 5.78 (d, J = 15.4 Hz, 14H), 5.54 (s, 14H), 4.24 (d, J = 15.4 Hz, 14H).
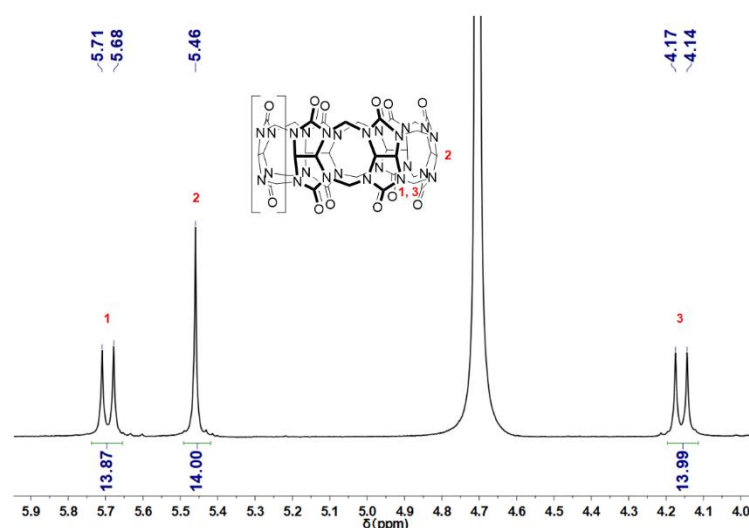

Figure 4.23 ^{1}H NMR of CB7 in D$_2$O

An additional consistent step for CB7 isolation was carried out with imidazolium salt sometimes because a small amount of other CBn residual exists in the product by following the above procedure. In contrast to conventional isolation of CBn homologues based on the solubility differences in water or acid,

the imidazolium salt is capable of complexing with one CBn resulting in significant solubility changes and readily tunable by the exchange of counter ion, *e.g.,* C4mimBr for CB5 and CB7 isolation; NpmimBr for CB6 and CB8. The CB7 isolation from crude products involving the imidazolium salt was briefly discussed. According to the procedure in the literature,[81] the crude CB7 product (5 g, ≤ 4 mmol) was dissolved into water (220 mL). After the ultrasound and fully stirring for a half-hour, the insoluble solid was removed by filtration. C4mimBr (4.5 mmol, 1 g) was added into filtrate to form the complex with CB7. Then, NH4PF6 salt (4.5 mmol, 734 mg) was added to exchange the Br ion and resulting in the precipitation of the CB7⊃C4mimPF6 complex, which was collected by centrifugation. The solid product of the complex was dissolved again into water (200 mL) in the presence of C4mimBr (5 mmol, 1.1 g) and heated to 80°C until most of the solid dissolved. After the counter ion was exchanged from PF6- to Br-, the solution of CB7⊃C4mimBr complex was concentrated at 50 mL and precipitated upon the addition of methanol (150 mL). A solid-state metathesis (SSM) was employed to remove the C4mimBr from the CB7 cavity. Briefly, the CB7⊃C4mimBr complex was suspended into 50 mL DCM, and then NH4PF6 salt (5 mmol, 815 mg) was added and refluxed for several days. ^{1}H NMR was employed to monitor the decomposition of CB7⊃C4mimBr complex. The final product was obtained by centrifugation and washed with methanol.

4.4.2.3. Synthesis and separation of mono-hydroxylated CB7 (CB7-(OH)1)
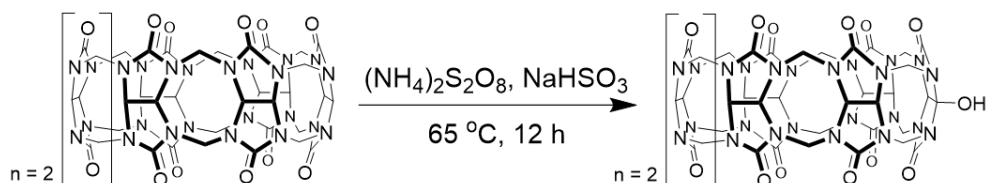
The mono-hydroxylation of CB7 was based on Kaifer's procedure.[283] Briefly, CB7 (500 mg, 0.43 mmol), (NH4)2S2O8 (147.2 mg, 0.645 mmol) and NaHSO3 (67.1 mg, 0.645 mmol) were placed into a 100 mL round-bottomed flask. Afterwards, 60 mL of purified water was added and kept at 65°C for 12 h. After finishing the reaction, the flask was connected to a rotary evaporator in a 70°C water bath to concentrate the reaction mixture further. When the volume of the reaction mixture was reduced to about 15 mL, the evaporation was stopped, and the resulting solution in the flask was cooled to about 30°C and ready for chromatography.

The concentrated solution was loaded onto the CHP20P resin column. The column was then eluted with purified water (15 mL per fraction). The fractions were monitored by ESI-MS, for which species was mixed with an excess of C8mimBr2. The CB7 peak is at m/z 719^{2+} (CB7⊃C8mim), CB7-OH is at m/z 727^{2+} (CB7-OH⊃C8mim) and CB7-(OH)2 is at m/z 735^{2+} (CB7-(OH)2⊃C8mim). The fractions in which CB7-OH was the dominant portion were collected. After evaporation, the product was obtained as a white powder (89.7 mg, 0.076 mmol, 17.7%).

^{1}H NMR (500 MHz, D2O) δ 5.77 (d, *J* = 15.4 Hz, 2H), 5.67 (d, *J* = 15.5 Hz, 10H), 5.45 (m, 14H), 5.21 (s, 1H), 4.42 (d, *J* = 15.6 Hz, 2H), 4.16 (m, 12H). ESI-MS: [M⊃C8mim]$^{2+}$ Calcd. for: 727.2844; found: 727.2900.
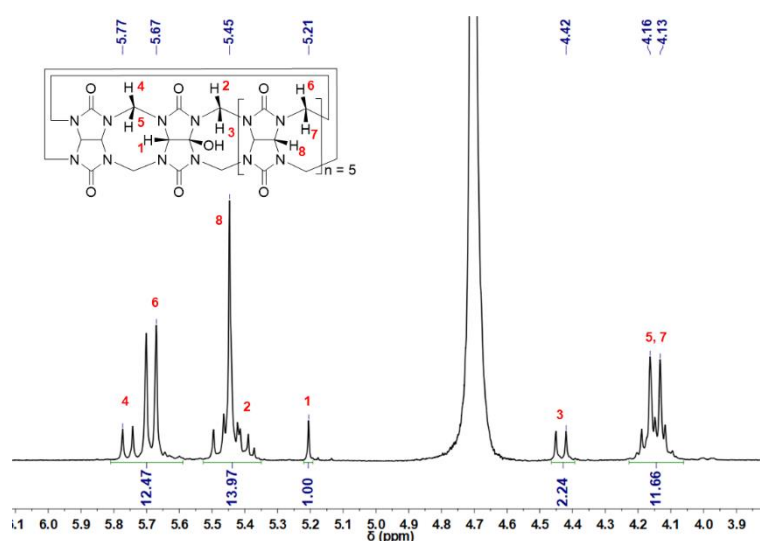
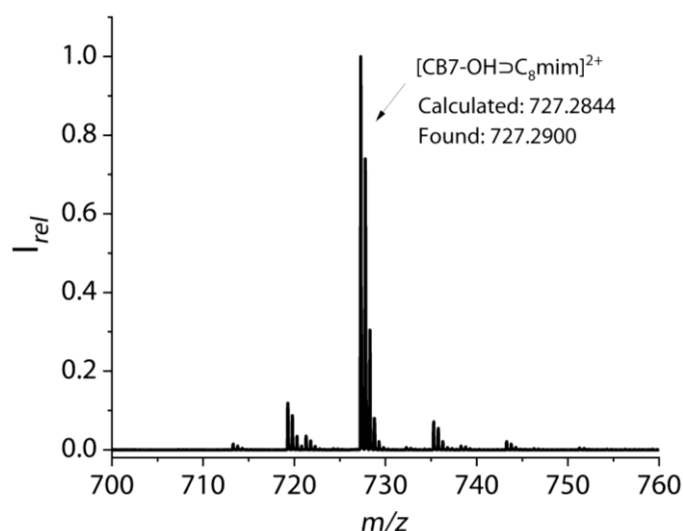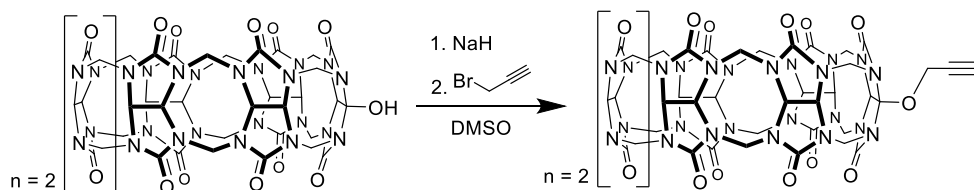**Figure 4.24** ^{1}H NMR spectrum (500 MHz) of CB7-(OH)$_1$ in D$_2$O.

Figure 4.25 ESI-MS of CB7-(OH)$_1$ with C$_8$mimBr$_2$ in the mixture of water and methanol (v/v = 1:1).

4.4.2.4. Synthesis of mono-propargylated CB7 (CB7-(OPr)$_1$)

According to the procedures in the literature,[166] CB7-OH (50 mg, 42.4 µmol, 1 eq) was dissolved in 5 mL anhydrous DMSO. NaH (24.9 mg, 1.04 mmol, 24.5 eq) was added under N$_2$ at 0°C, and the mixture was stirred at room temperature for 2 h. Subsequently, the mixture was cooled to 0°C, propargyl bromide (1.04 mmol, 24.5 eq, 144 µL) was added under N$_2$, and the reaction mixture was stirred at room temperature for 24 h. 30 mL mixture of diethyl ether and MeOH (v/v = 1:1) was added, and the resulting precipitate was three times triturated with 25 mL MeOH and dried in the oven at 80°C. The product was obtained as a brown powder (36.2 mg, 0.030 mmol, 70%).
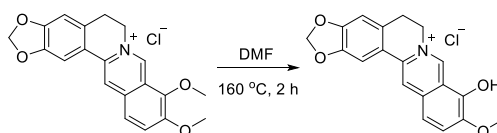
61
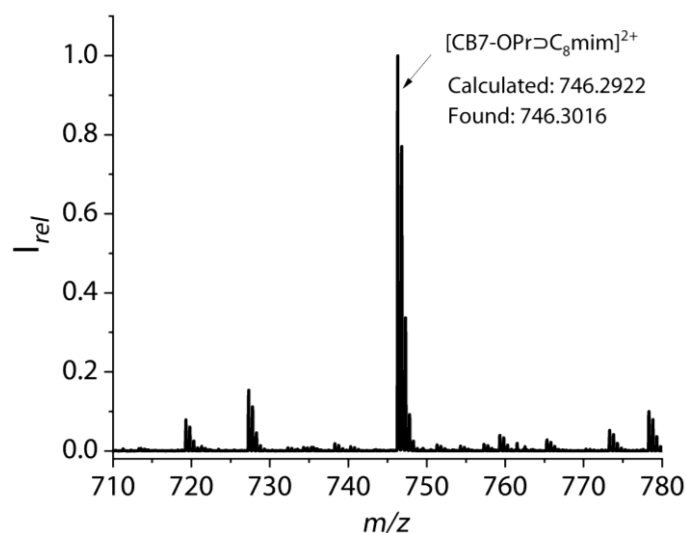
Figure 4.26 ESI-MS of CB7-(OPr)$_1$ with C$_8$mimBr$_2$ in the mixture of water and methanol (v/v = 1:1).

4.4.2.5. Synthesis of berberrubine (BC-OH)

According to literature procedures,[289] berberine hydrochloride (740 mg, 2.0 mmol) was dissolved in 4 mL DMF. After heating and stirring at 160°C for 2 h, the solvent was removed under reduced pressure to yield a dark red solid. The crude product was purified by column chromatography (silica, CH$_2$Cl$_2$/methanol (v/v = 10/1)) to give berberrubine as red solid (497 mg, 1.6 mmol, 70 %).

^{1}H NMR (500 MHz, DMSO-d_6) δ 9.07 (s, 1H), 7.98 (s, 1H), 7.61 (s, 1H), 7.21 (d, J = 7.8 Hz, 1H), 6.96 (s, 1H), 6.35 (d, J = 7.8 Hz, 1H), 6.09 (s, 2H), 4.48 (t, J = 6.1 Hz, 2H), 3.72 (s, 3H), 3.04 (t, J = 6.1 Hz, 2H) ppm. ^{13}C NMR (126 MHz, DMSO-d_6) δ 167.5, 150.1, 148.8, 147.7, 146.2, 133.7, 132.5, 129.7, 122.3, 121.7, 120.4, 117.6, 108.7, 105.2, 102.0, 101.3, 56.1, 52.8, 28.0 ppm. ESI-MS: Calcd. for [M-Cl]$^+$: 322.1074; found: 322.1341.
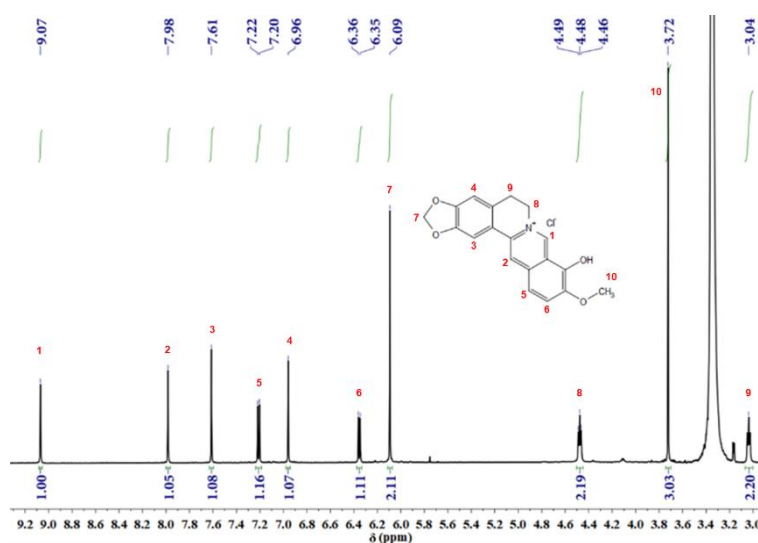

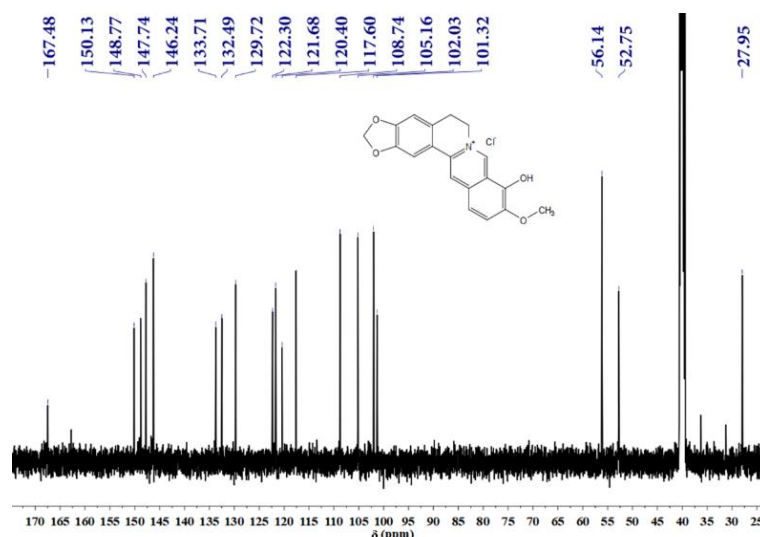**Figure 4.27** ^{1}H NMR spectrum (500 MHz) of BC-OH in DMSO-d_6.

Figure 4.28 ^{13}C NMR spectrum (126 MHz) of BC-OH in DMSO-d_6.
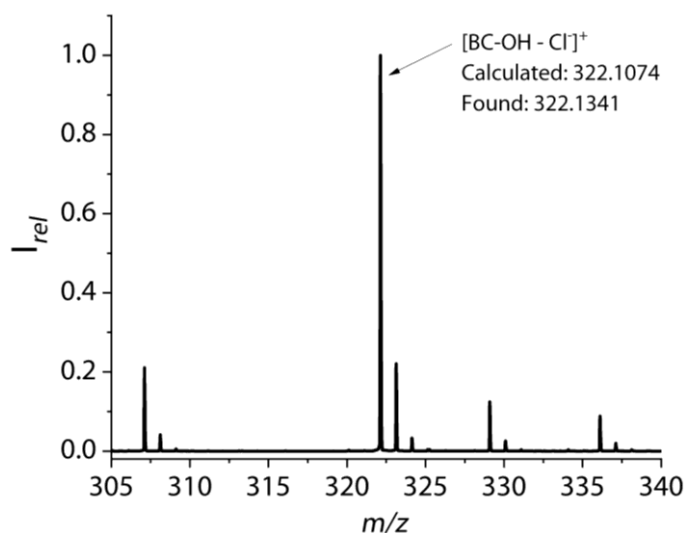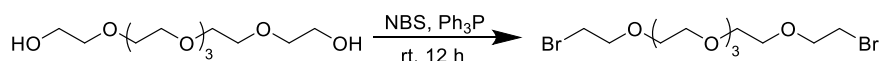

Figure 4.29 ESI-MS of BC-OH in the mixture of water and methanol (v/v = 1:1).

Additional information on details is available *via* the Chemotion repository:

https://dx.doi.org/10.14272/reaction/SA-FUHFF-UHFFFADPSC-GYFSYEVKFO-UHFFFADPSC-NUHFF-NUHFF-NUHFF-ZZZ

4.4.2.6. Synthesis of Dibromo-hexaethylene glycol (Br-HEG-Br)

According to literature procedures,[6] 100 mL CH$_2$Cl$_2$ were cooled down to −78°C using a cooling mixture of dry ice and acetone. NBS (8.72 g, 49.0 mmol) and triphenylphosphine (12.84 g, 49.0 mmol) were added into a round bottom flask under stirring. After 10 min, hexaethylene glycol (4.23 g, 15.0 mmol) was added to the solution, and the reaction mixture was stirred overnight. CH$_2$Cl$_2$ was removed under reduced pressure, and the crude product was purified on a silica column, eluted with hexane/ethyl acetate (v/v = 2/1). The product was obtained as a colorless oil (3.98 g, 9.8 mmol, 65 %).

63

^{1}H NMR (500 MHz, CDCl$_3$) δ 3.81 (t, *J* = 3.2 Hz, 4H), 3.66 (m, 16H), 3.47 (t, *J* = 3.2 Hz, 4H) ppm. ^{13}C NMR (126 MHz, CDCl$_3$) δ 71.36, 70.83, 70.75, 70.69, 30.47 ppm.
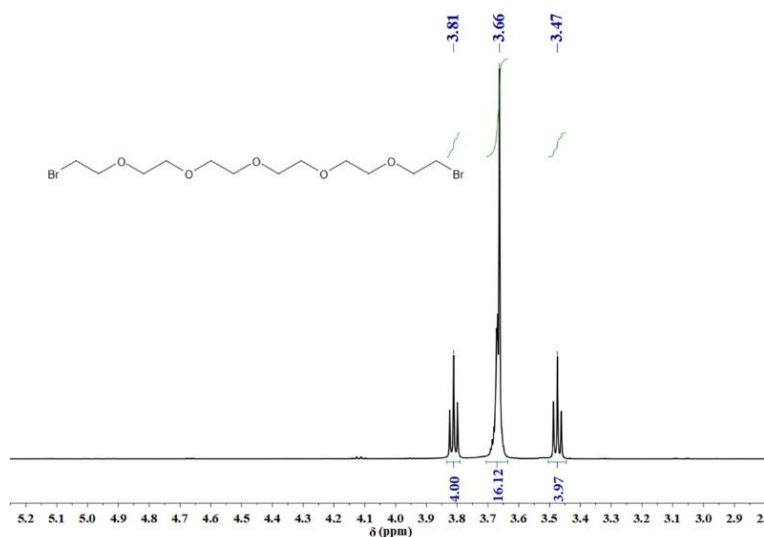

Figure 4.30 ^{1}H NMR spectrum (500 MHz) of Br-HEG-Br in CDCl$_3$.
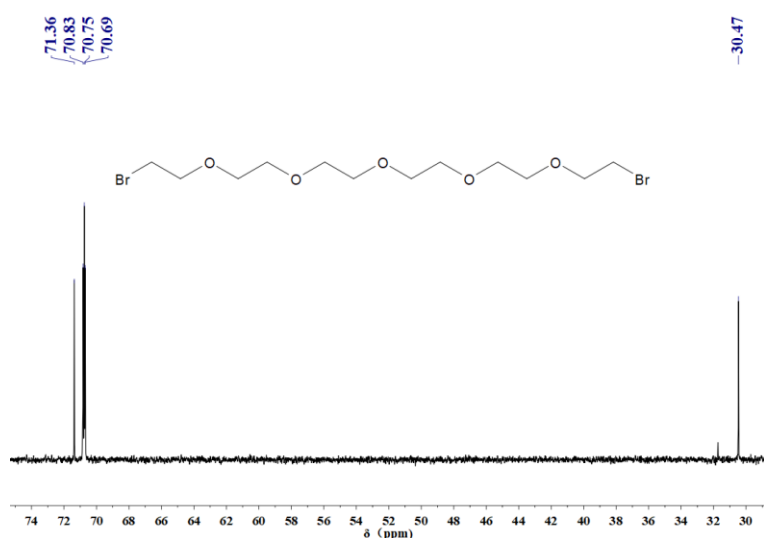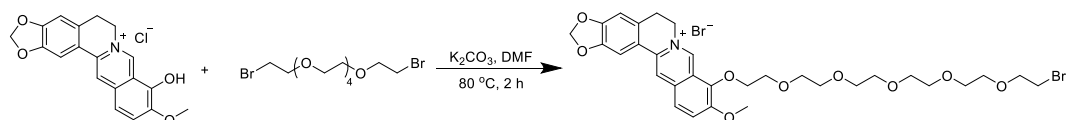

Figure 4.31 ^{13}C NMR spectrum (126 MHz) of Br-HEG-Br in CDCl$_3$.

Additional information on details is available *via* the Chemotion repository:

https://dx.doi.org/10.14272/reaction/SA-FUHFF-UHFFFADPSC-LACSKPODWQ-UHFFFADPSC-NUHFF-NUHFF-NUHFF-ZZZ

4.4.2.7. Synthesis of berberine-hexaethylene glycol-bromide (BC-HEG-Br)

A solution of BC-OH (50.0 mg, 140 µmol), K$_2$CO$_3$ (58.0 mg, 420 µmol) and Br-HEG-Br (285 mg, 700 µmol, 180 µL) in 2 mL DMF was heated to 80°C under N$_2$ for 2 h. Excess of Br-HEG-Br was used to obtain preferentially the mono-substituted product. Afterwards, the mixture was cooled to room

temperature and poured in 40 mL Et$_2$O. The crude product precipitated immediately. The crude product was dissolved in DCM and subjected to an isocratic silica column, eluted with DCM/methanol (v/v = 10/1), and therefore purified to give a yellow powder of BC-HEG-Br (73.8 mg, 110 μmol, 81 %). ^{1}H NMR (500 MHz, DMSO-d_6) δ 9.77 (s, 1H), 8.95 (s, 1H), 8.20 (d, J = 9.1 Hz, 1H), 8.01 (d, J = 9.1 Hz, 1H), 7.81 (s, 1H), 7.10 (s, 1H), 6.18 (s, 2H), 4.93 (t, J = 6.2 Hz, 2H), 4.42 (t, J = 4.6 Hz, 2H), 4.07 (s, 3H), 3.80 (t, J = 4.6 Hz, 2H), 3.68 (t, J = 5.8 Hz, 2H), 3.60 - 3.43 (m, 18H), 3.21 (t, J = 6.3 Hz, 2H) ppm. ^{13}C NMR (126 MHz, DMSO-d_6) δ 150.6, 149.9, 147.7, 145.5, 142.5, 137.5, 132.9, 130.7, 126.6, 123.6, 122.0, 120.5, 120.2, 108.5, 105.4, 102.1, 73.1, 70.3, 69.8, 69.7, 69.7, 69.5, 69.5 69.5, 69.4, 69.3, 57.0, 55.5, 39.5, 32.2, 26.4 ppm. ESI-MS: Calcd. for [M]$^+$: 648.1083; found: 648.1792.
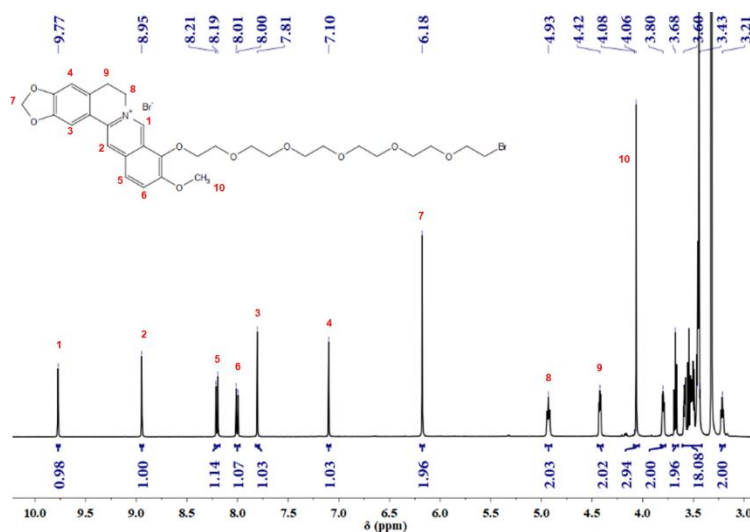

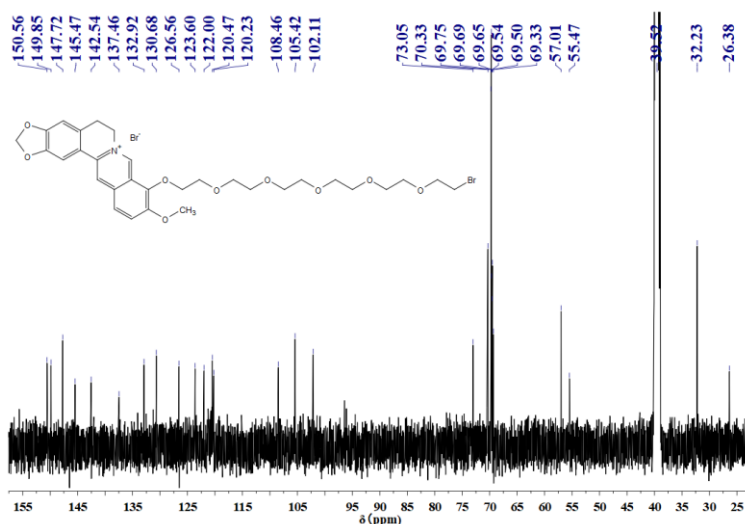**Figure 4.32** ^{1}H NMR spectrum (500 MHz) of BC-HEG-Br in DMSO-d_6.

Figure 4.33 ^{13}C NMR spectrum (126 MHz) of BC-HEG-Br in DMSO-d_6.
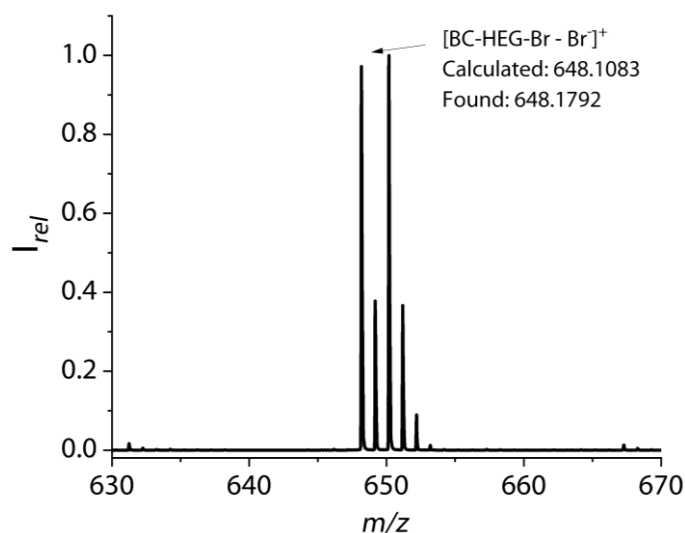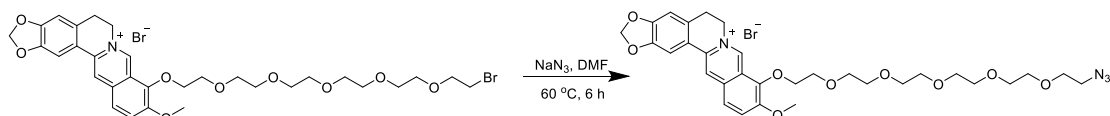
Figure 4.34 ESI-MS of BC-HEG-Br in the mixture of water and methanol (v/v = 1:1).

Additional information on details is available *via* the Chemotion repository:

https://dx.doi.org/10.14272/reaction/SA-FUHFF-UHFFFADPSC-ZGCIPCWPNL-UHFFFADPSC-NUHFF-MUHFF-NUHFF-ZZZ

4.4.2.8. Synthesis of berberine-hexaethylene glycol-azide (BC-HEG-N₃)

To a solution of BC-HEG-Br (73.8 mg, 100 µmol) in 1 mL DMF, NaN$_3$ (32.9 mg, 500 µmol) was added at room temperature. After stirring at 60°C for 6 h, the mixture was cooled to room temperature. 50 mL CH$_2$Cl$_2$ were added and 3 x 50 mL NaCl saturated solution was added in extraction cycles. The combined organic extracts were dried over anhydrous Na$_2$SO$_4$. The crude solution was concentrated and purified by an isocratic silica column eluted with CH$_2$Cl$_2$/methanol (v/v = 10/1) to give BC-TEG-N$_3$ as yellow powder (66.6 mg, 95.0 µmol, 95 %). ^{1}H NMR (500 MHz, D$_2$O) δ 9.60 (s, 1H), 8.29 (s, 1H), 7.94 (d, *J* = 8.7 Hz, 1H), 7.82 (s, *J* = 8.9 Hz, 1H), 7.30 (s, 1H), 6.90 (s, 1H), 6.06 (s, 2H), 4.84 (t, *J* = 6.0 Hz, 2H), 4.49 (t, *J* = 3.1 Hz, 2H), 4.02 (s, 3H), 3.92 (t, *J* = 3.1 Hz, 2H), 3.72 (t, *J* = 3.5 Hz, 2H), 3.65 – 3.58 (m, 16H), 3.41 (t, *J* = 4.3 Hz, 2H), 3.20 (t, *J* = 6.0 Hz, 2H) ppm. ^{13}C NMR (126 MHz, D$_2$O) δ 151.8, 150.6, 150.1, 147.7, 144.3, 141.9, 137.6, 133.2, 130.2, 126.3, 123.9, 121.9, 119.9, 108.4, 104.9, 102.3, 72.9, 69.8, 69.6, 69.5, 69.5, 69.5, 69.5, 69.4, 69.4, 69.3, 69.2, 56.6, 56.0, 50.1, 26.7 ppm. ESI-MS: Calcd. for [M]$^+$: 611.2712; found: 611.2696.

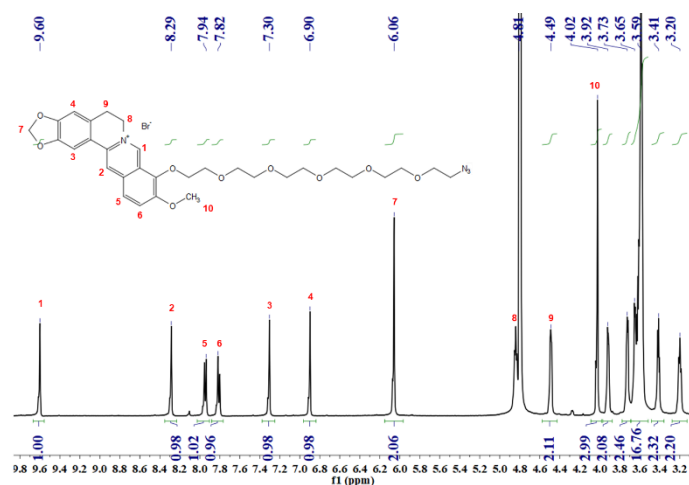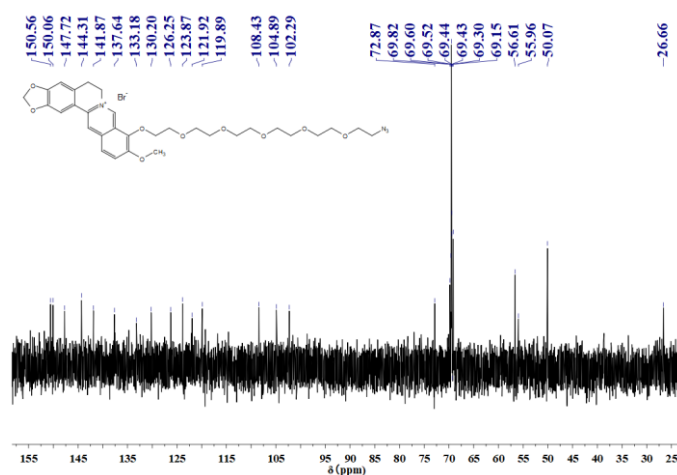**Figure 4.35** ^{1}H NMR spectrum (500 MHz) of BC-HEG-N$_3$ in D$_2$O.

Figure 4.36 ^{13}C NMR spectrum (126 MHz) of BC-HEG- N$_3$ in D$_2$O.
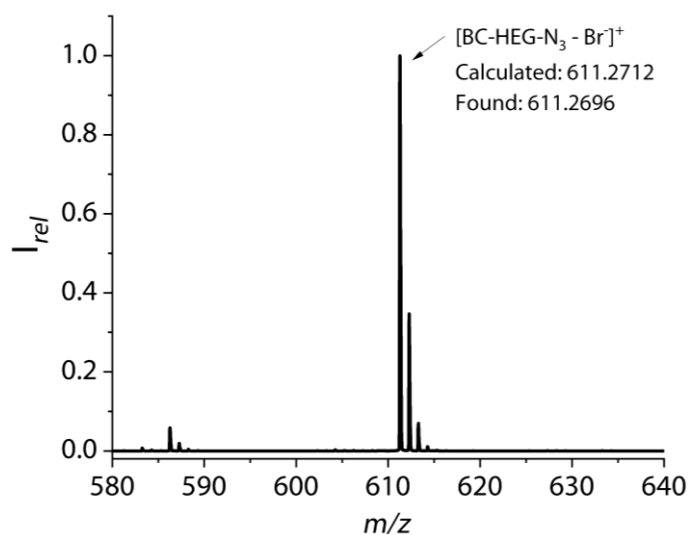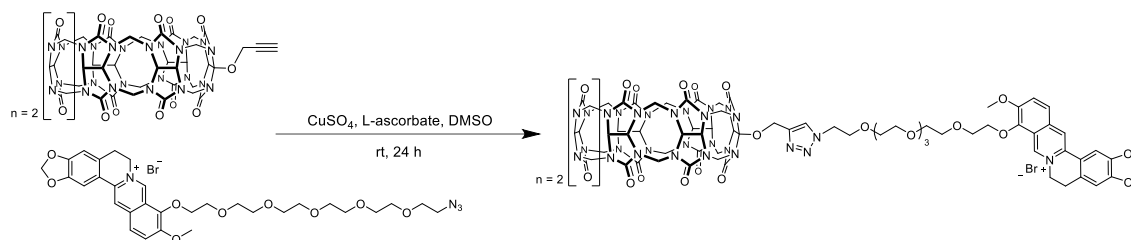

Figure 4.37 ESI-MS of BC-HEG-Br in the mixture of water and methanol (v/v = 1:1).

Additional information on details is available *via* the Chemotion repository:

https://dx.doi.org/10.14272/reaction/SA-FUHFF-UHFFFADPSC-FIXMWOGOKF-UHFFFADPSC-NUHFF-MUHFF-NUHFF-ZZZ

4.4.2.9.   Synthesis of cucurbit[7]uril-HEG-berberine conjugate (1)

CB7-(Opr)$_1$ (8.7 mg, 7.2 µmol) and BC-HEG-N$_3$ (9.0 mg, 13.0 µmol) were dispersed in 0.7 mL DMSO. Then, sodium *L*-ascorbate (10.0 mg, 50.0 µmol) was added into 2.8 mL 55% DMSO aqueous solution containing CuSO$_4$ (4.5 mg, 28.0 µmol). These two solutions were mixed and stirred at room temperature for 24 h. Afterwards, 50 mL diethyl ether was added, and the resulting precipitate was washed three times with 25 mL methanol. Drying under a high vacuum afforded a dark solid. The product was purified by HPLC (C18, v (acetonitrile) / v (0.1% TFA aqueous) = 1/3) and obtained as yellow solid (3.6 mg, 1.9 µmol, 27 %). ESI-MS: [M + Na]$^{2+}$ Calcd. for: 925.3076; found: 925.3130. Due to the complex structure, a precise characterization by ^{1}H and ^{13}C NMR was not possible. However, as described in the previous section, the formation and purity of the compound were characterized by several methods.
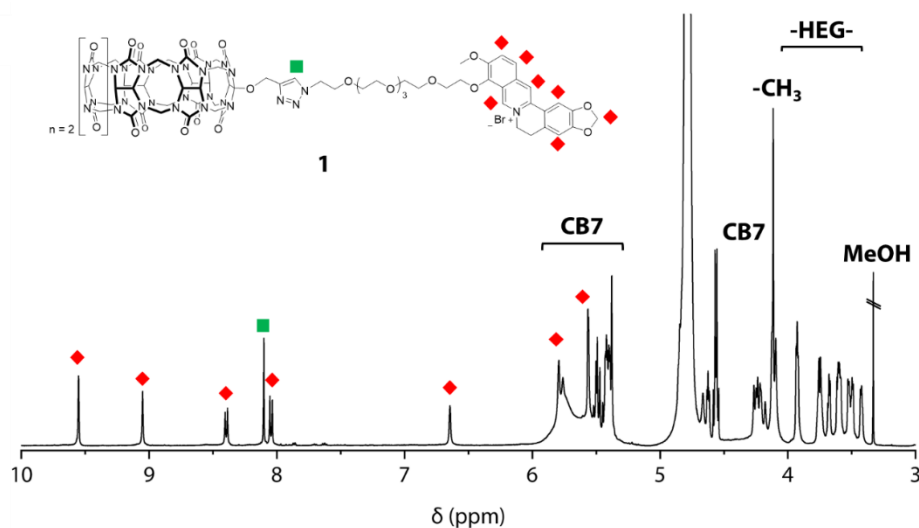

Figure 4.38 ^{1}H NMR spectrum (500 MHz) of chemosensor **1** in D$_2$O.
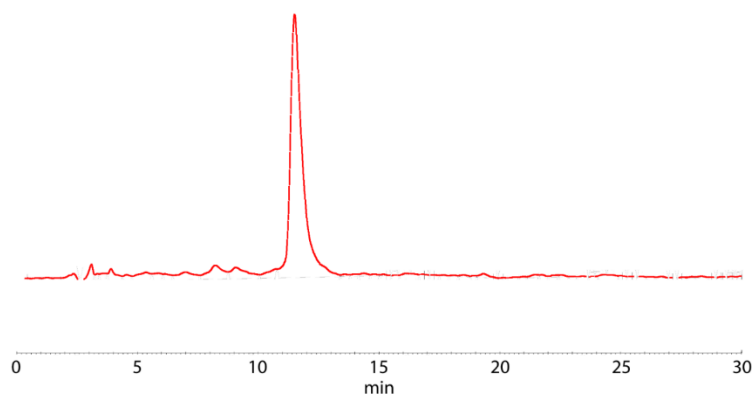
Figure 4.39 Analytical HPLC trace at 350 nm of chemosensor **1** using a 25 % acetonitrile/75 % 0.1 % TFA aqueous as eluents.

Additional information on details is available *via* the Chemotion repository:

https://dx.doi.org/10.14272/reaction/SA-FUHFF-UHFFFADPSC-PLPZWDLHCM-UHFFFADPSC-NUHFF-MUHFF-NUHFF-ZZZ

4.4.2.10. Synthesis of Dibromo-tetraethylene glycol (Br-TEG-Br)
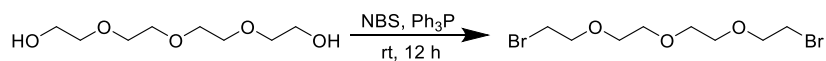
According to literature procedures, 100 mL CH$_2$Cl$_2$ was cooled down to −78°C using a cooling mixture of dry ice and acetone. NBS (4.36 g, 24.5 mmol) and triphenylphosphine (6.42 g, 24.5 mmol) were added to the reaction mixture under stirring. After 10 min, tetraethylene glycol (2.13 g, 11.0 mmol) was added, and the solution was stirred overnight. The solvent was removed under reduced pressure, and the crude product was purified by an isocratic silica chromatography with hexane/ethyl acetate (v/v = 4/1) as eluents. The product was obtained as a colorless oil (3.15 g, 9.9 mmol, 90 %). ^{1}H NMR (500 MHz, CDCl$_3$) δ 3.82 (t, J = 3.2 Hz, 4H), 3.68 (s, 8H), 3.48 (t, J = 3.2 Hz, 4H) ppm. ^{13}C NMR (126 MHz, CDCl$_3$) δ 71.2, 70.7, 70.6, 30.4 ppm.
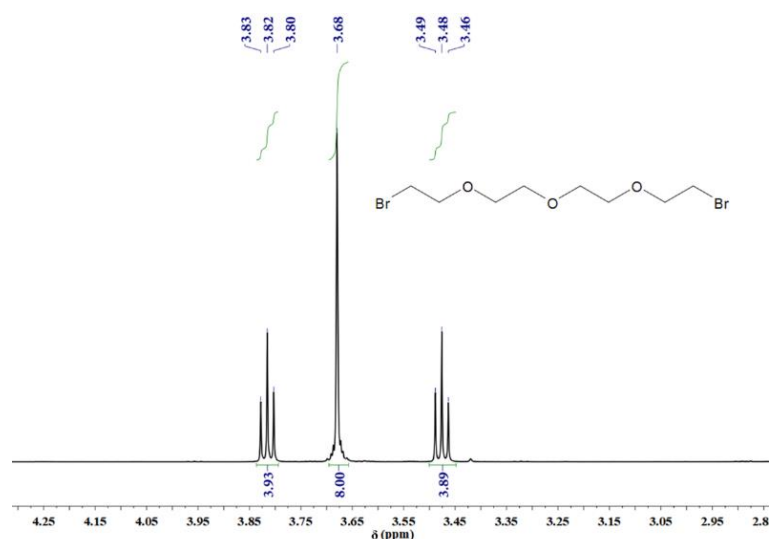
Figure 4.40 ^{1}H NMR spectrum (500 MHz) of Br-TEG-Br in CDCl$_3$.
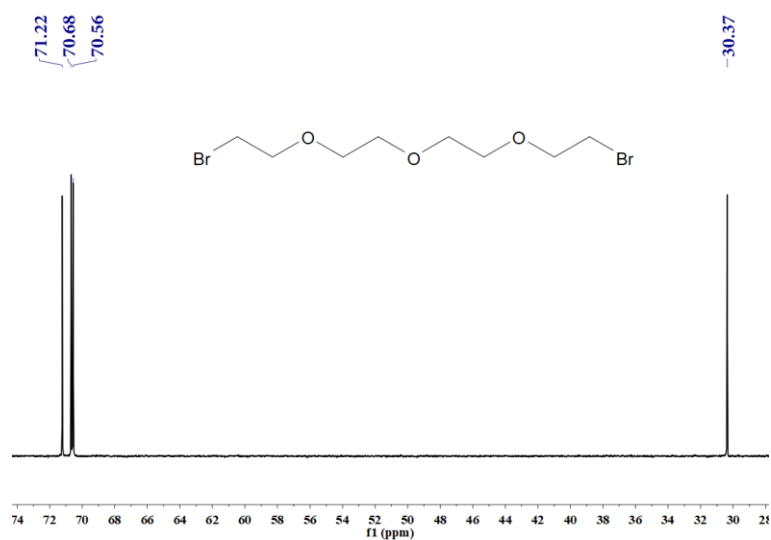
Figure 4.41 ^{13}C NMR spectrum (126 MHz) of Br-TEG-Br in CDCl$_3$.

Additional information on details is available *via* the Chemotion repository:

https://dx.doi.org/10.14272/reaction/SA-FUHFF-UHFFFADPSC-IJFMWHWXEB-UHFFFADPSC-NUHFF-NUHFF-NUHFF-ZZZ

4.4.2.11. Synthesis of berberine-tetraethylene glycol-bromide (BC-TEG-Br)
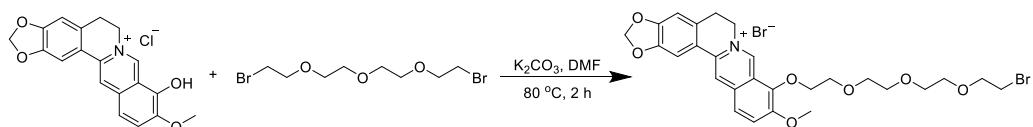
A solution of BC-OH (122 mg, 300 µmol), K$_2$CO$_3$ (141 mg, 1.0 mmol) and Br-TEG-Br (546 mg, 1.7 mmol, 1.1 mL) in 2 mL anhydrous DMF was heated to 80°C under nitrogen atmosphere for 2 h. Excess of Br-TEG-Br was used to obtain preferentially the mono-substituted product. Afterwards, the mixture was cooled to room temperature and poured in 40 mL Et$_2$O. The crude product precipitated immediately. The crude product was dissolved in DCM and purified by an isocratic silica column

chromatography with CH_2Cl_2/methanol (v/v = 10/1) as eluents. After removal of the solvents, BC-TEG-Br was obtained as a yellow powder (69 mg, 100 µmol, 35 %). ^{1}H NMR (500 MHz, DMSO-d_6) δ 9.78 (s, 1H), 8.95 (s, 1H), 8.20 (d, J = 9.2 Hz, 1H), 8.01 (d, J = 9.1 Hz, 1H), 7.81 (s, 1H), 7.10 (s, 1H), 6.18 (s, 2H), 4.93 (t, J = 6.2 Hz, 2H), 4.42 (t, J = 4.4 Hz, 2H), 4.06 (s, 3H), 3.81 (t, J = 4.4 Hz, 2H), 3.65 (t, J = 5.8 Hz, 2H), 3.60 – 3.46 (m, 10H), 3.22 (t, J = 3.1 Hz, 2H) ppm. ^{13}C NMR (126 MHz, DMSO-d_6) δ 151.0, 150.3, 148.2, 145.9, 143.0, 137.9, 133.4, 131.1, 127.0, 124.1, 122.9, 120.9, 120.7, 108.9, 105.9, 102.6, 73.5, 70.8, 70.2, 70.1, 70.0, 69.9, 69.8, 57.5, 55.9, 32.7, 26.9 ppm. ESI-MS: Calcd. for [M][+]: 560.1218; found: 560.1365.
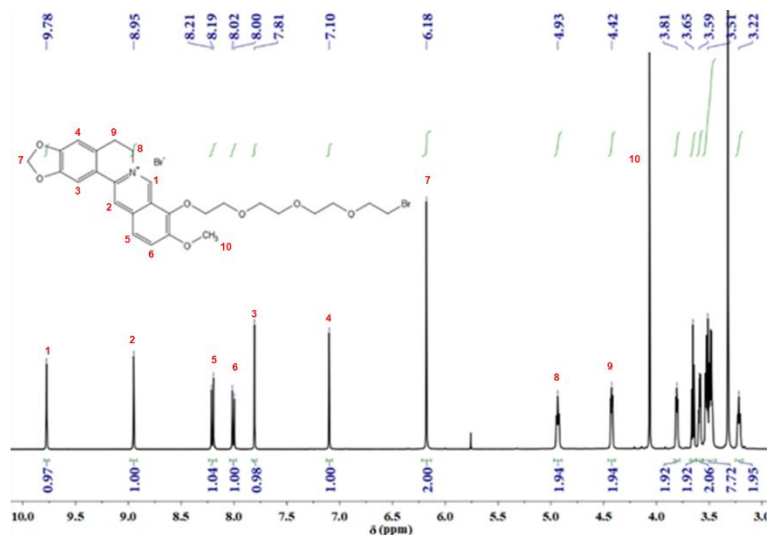
Figure 4.42 ^{1}H NMR spectrum (500 MHz) of BC-TEG-Br in DMSO-d_6.
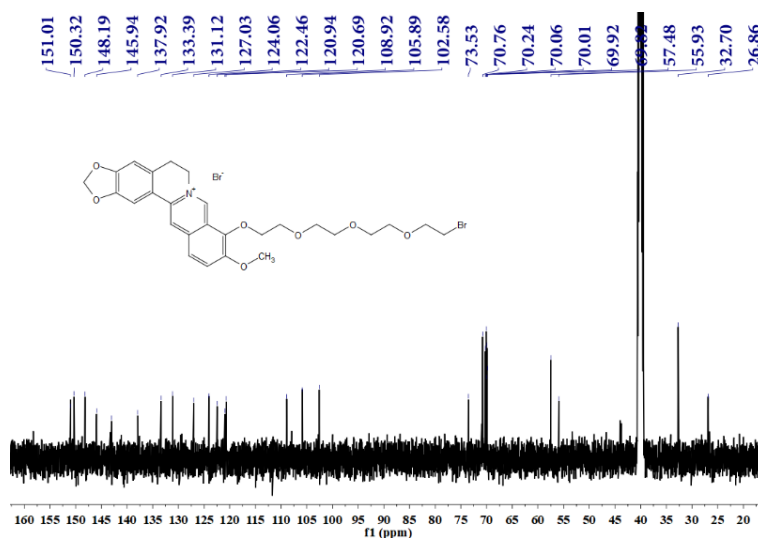
Figure 4.43 ^{13}C NMR spectrum (126 MHz) of BC-TEG-Br in DMSO-d_6.

Figure 4.44 ESI-MS of BC-TEG-Br in the mixture of water and methanol (v/v = 1:1).

Additional information on details is available *via* the Chemotion repository:

https://dx.doi.org/10.14272/reaction/SA-FUHFF-UHFFFADPSC-BTUNLJUIAC-UHFFFADPSC-NUHFF-MUHFF-NUHFF-ZZZ

4.4.2.12.   Synthesis of berberine-tetraethylene glycol-azide (BC-TEG-N$_3$)

To a solution of BC-TEG-Br (55 mg, 8.6 μmol) in 1 mL DMF, NaN$_3$ (56 mg, 900 μmol) was added at room temperature. After stirring at 60°C for 6 h the mixture was cooled down to room temperature. 50 mL CH$_2$Cl$_2$ were added and washed by 3 x 50 mL NaCl saturated solution. The combined organic extracts were dried by anhydrous Na$_2$SO$_4$. The crude solution was concentrated to 2 mL and purified by an isocratic silica column with CH$_2$Cl$_2$/MeOH (v/v = 10/1) as eluents to obtain BC-TEG-N$_3$ after solvent removal as yellow powder (50 mg, 8.3 μmol, 96 %). ^{1}H NMR (500 MHz, DMSO-d_6) δ 9.78 (s, 1H), 8.95 (s, 1H), 8.20 (d, J = 9.2 Hz, 1H), 8.01 (d, J = 9.1 Hz, 1H), 7.81 (s, 1H), 7.10 (s, 1H), 6.18 (s, 2H), 4.93 (t, J = 6.2 Hz, 2H), 4.42 (t, J = 4.4 Hz, 2H), 4.06 (s, 3H), 3.81 (t, J = 4.4 Hz, 2H), 3.60 – 3.48 (m, 12H), 3.22 (t, J = 3.1 Hz, 2H) ppm. ^{13}C NMR (126 MHz, DMSO-d_6) δ 150.6, 149.9, 147.7, 145.5, 142.6, 137.5, 133.0, 130.7, 126.6, 123.6, 122.0, 120.3, 120.3, 108.5, 105.5, 102.1, 73.1, 69.8, 69.6, 69.6, 69.5, 69.4, 69.2, 57.0, 55.5, 50.0, 26.4 ppm. ESI-MS: Calcd. for [M]$^+$: 523.2187; found: 523.2245.

72
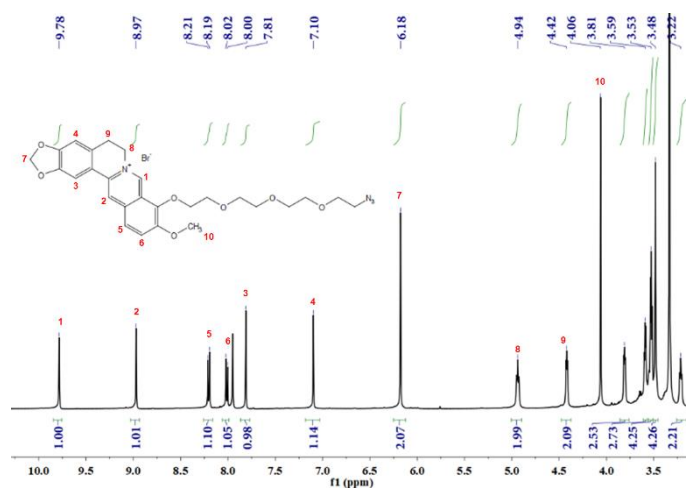
**Figure 4.45** ^{1}H NMR spectrum (500 MHz) of BC-TEG-N$_3$ in DMSO-d_6.
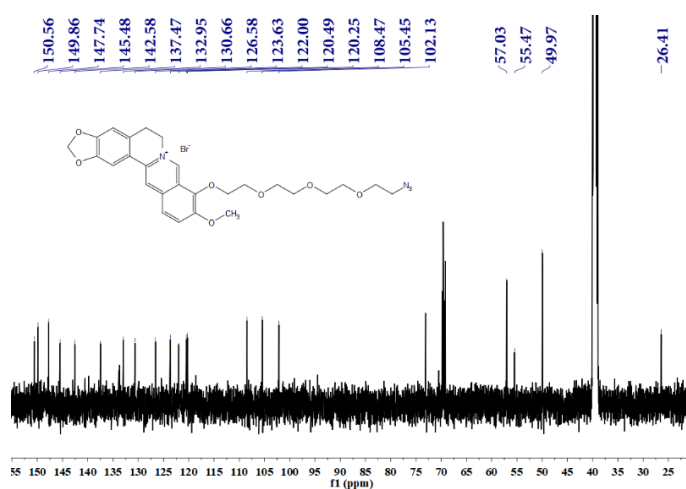
Figure 4.46 ^{13}C NMR spectrum (126 MHz) of BC-TEG-N$_3$ in DMSO-d_6.
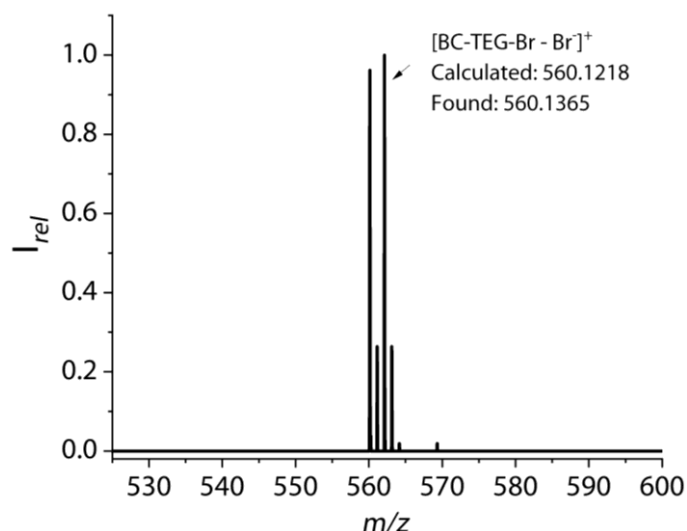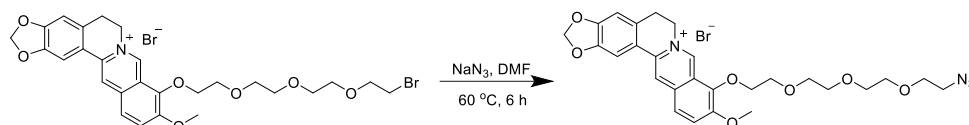

Figure 4.47 ESI-MS of BC-TEG-N$_3$ in the mixture of water and methanol (v/v = 1:1).

Additional information on details is available *via* the Chemotion repository:

https://dx.doi.org/10.14272/reaction/SA-FUHFF-UHFFFADPSC-RJLCCSUQZU-UHFFFADPSC-NUHFF-MUHFF-NUHFF-ZZZ

4.4.2.13. Synthesis of cucurbit[7]uril-TEG-berberine conjugate (2)

CB7-(Opr)$_1$ (8.7 mg, 7.2 µmol) and BC-TEG-N$_3$ (7.9 mg, 13.0 µmol) were dissolved in 700 µL DMSO. In a second flask, sodium *L*-ascorbate (10.0 mg, 50.0 µmol) was added to 2.8 mL 55% DMSO aqueous solution containing CuSO$_4$ (4.5 mg, 28.0 µmol). The two solutions were mixed and stirred at room temperature for 24 h. Afterwards, 50 mL diethyl ether was added, and the resulting precipitate was washed three times with 25 mL MeOH. Drying under a high vacuum afforded a dark solid. The product was purified by HPLC (C18, v (acetonitrile) / v (0.1% TFA aq.) = 1/3) and obtained as yellow solid (1.2 mg, 690 nmol, 10 %). ESI-MS: [M+Na]$^{2+}$ Calcd. for: 881.2814; found: 881.2889. Due to a precise characterization of the complex structure by ^{1}H and ^{13}C NMR was not possible.
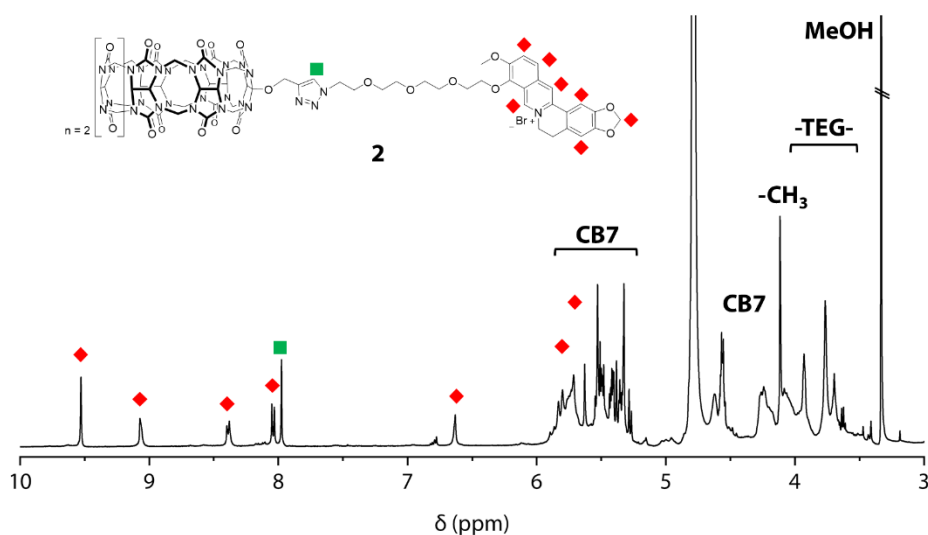
Figure 4.48 ^{1}H NMR spectrum (500 MHz) of chemosensor **2** in D$_2$O.
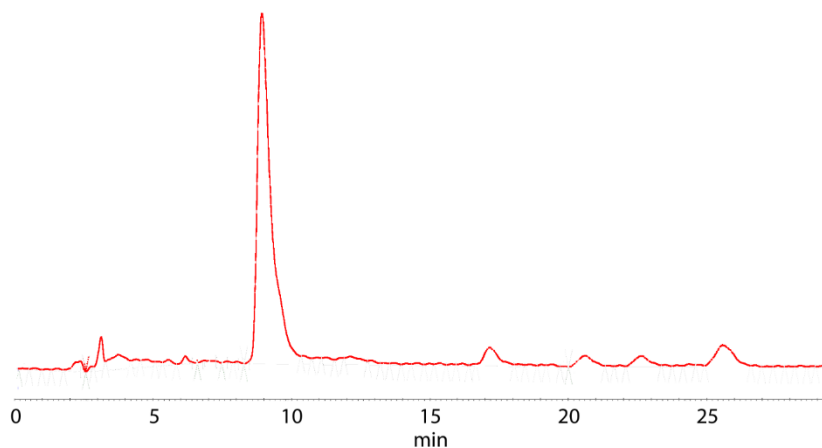
Figure 4.49 Analytical HPLC trace at 350 nm of chemosensor **2** using a mixture of 25 % acetonitrile/75 % 0.1 % TFA aqueous for elution.

Additional information on details is available *via* the Chemotion repository:

https://dx.doi.org/10.14272/reaction/SA-FUHFF-UHFFFADPSC-SCCUVBVHKK-UHFFFADPSC-NUHFF-MUHFF-NUHFF-ZZZ

4.4.2.14.   Synthesis of *N*-adamantyl-4-methylpyridine (Ad-MePy)

The synthesis of DASAP and of the starting materials were carried out by Alicja Siennicka.
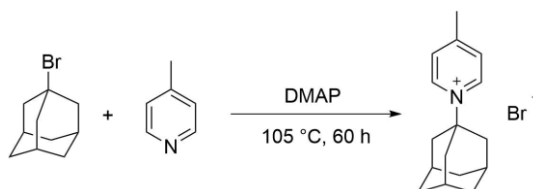
According to the literature procedures,[315] 1-bromoadamantane (2.15 g, 10.0 mmol), 4-(dimethylamino) pyridine (60.0 mg, 500 μM) and picoline (4.67 g, 50.2 mmol, 4.82 mL) were mixed under nitrogen atmosphere. After adding 180 μL distilled water (180 mg, 10.0 mmol), the mixture was refluxed for 60 h. Afterwards, the mixture was cooled down to room temperature and slowly poured into chloroform. A white precipitate was formed immediately and washed several times with chloroform. The product was dried and obtained as a white solid. (2.30 g, 7.49 mmol, 75 %). ^{1}H NMR (500 MHz, D$_2$O) δ 8.89 (d, J = 6.9 Hz, 2H), 7.86 (d, J = 6.6 Hz, 2H), 2.63 (s, 3H), 2.36 (s, 3H), 2.29 (d, J = 2.6 Hz, 6H), 1.81 (dd, J = 28.3, 12.5 Hz, 6H) ppm. ^{13}C NMR (126 MHz, D$_2$O) δ 159.2, 139.8, 128.2, 68.6, 41.7, 34.6, 29.8, 20.9 ppm. ESI-MS: Calcd. for [M]$^+$: 228.1447; found: 228.1739.
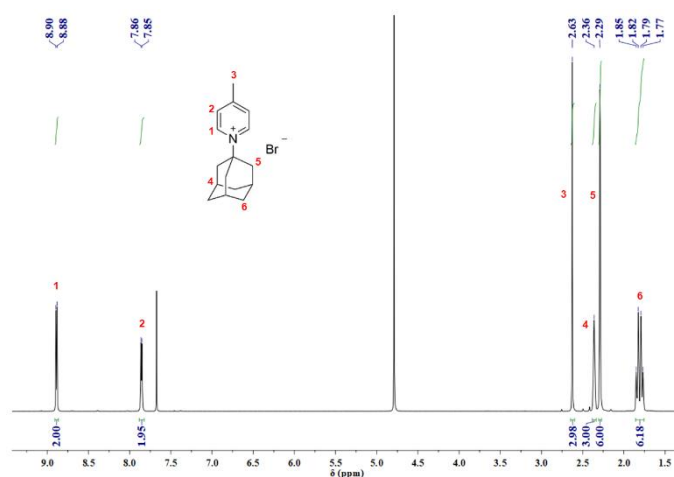
Figure 4.50 ^{1}H NMR spectrum (500 MHz) of Ad-MePy in D_2O.
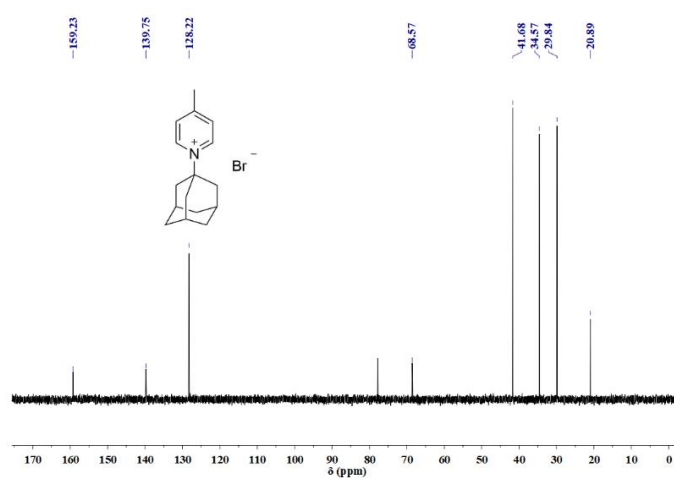
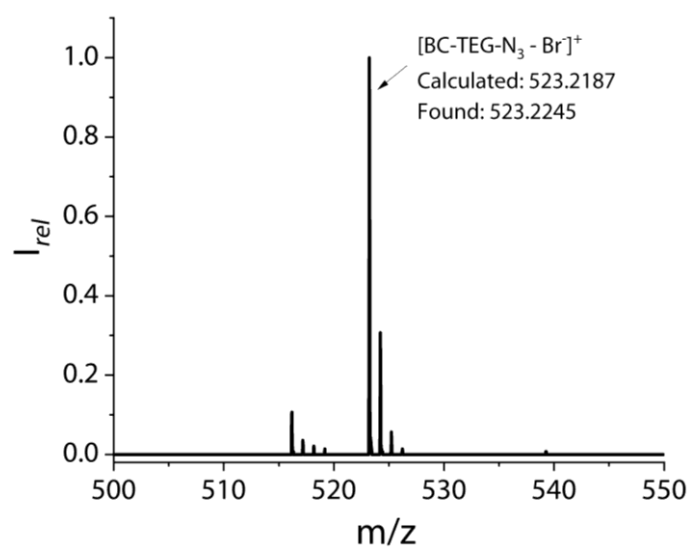**Figure 4.51** ^{13}C NMR spectrum (126 MHz) of Ad-MePy in D_2O.

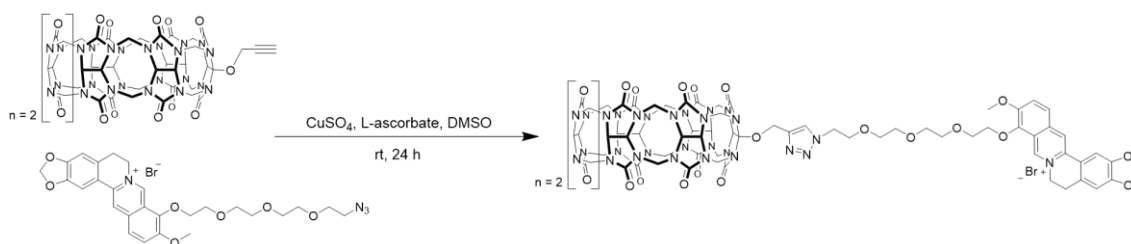**Figure 4.52** ESI-MS of Ad-MePy in the mixture of water and methanol (v/v = 1:1).

Additional information on details is available *via* the Chemotion repository:

https://dx.doi.org/10.14272/reaction/SA-FUHFF-UHFFFADPSC-JROBPRZYLG-UHFFFADPSC-NUHFF-MUHFF-NUHFF-ZZZ

4.4.2.15. Synthesis of 4-[4-(Dimethylamino)styryl]-1-adamantylpyridinium (DASAP)
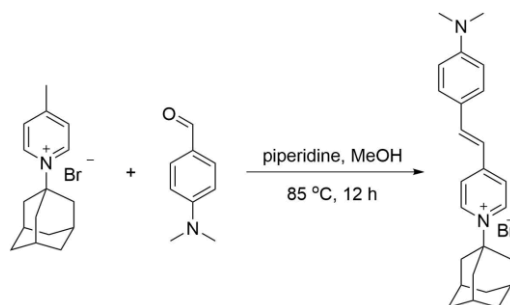
Ad-MePy (250 mg, 814 μM) was dissolved in MeOH (3 mL). To this solution, 4-dimethylamino benzaldehyde (121 mg, 814 μM) and 2-3 drops of piperidine were added, and the reaction mixture was heated to 85°C and kept stirring overnight under a nitrogen atmosphere. Afterwards, the mixture was cooled down to room temperature, and 10 mL of ethyl acetate was added. After storage at 5°C overnight, the precipitate was collected and washed three times with ethyl acetate, one time with hexane and one time with diethyl ether. The residue was then recrystallized from a mixture of dichloromethane and ethyl acetate (v/v =1/2) to give a red-purple solid (108 mg, 247 μmol, 30 %). In analogy to the commercial dye 4-[4-(Dimethylamino)styryl]-1-methylpyridinium iodide that is commonly abbreviated as DASP, the abbreviation **DASAP** for the herein introduced dye 4-[4-(Dimethylamino)styryl]-1-adamantylpyridinium bromide is suggested. ^{1}H NMR (500 MHz, MeOH-d_3) δ 8.85 (s, 2H), 7.98 (d, J = 6.3 Hz, 2H), 7.85 (d, J = 15.8 Hz, 1H), 7.62 (d, J = 8.1 Hz, 2H), 7.10 (d, J = 15.9 Hz, 1H), 6.79 (d, J = 7.4 Hz, 2H), 3.07 (s, 6H), 2.42 – 2.22 (m, 9H), 1.87 (s, 6H) ppm. ^{13}C NMR (126 MHz, MeOH-d_3) δ 155.9, 154.0, 144.4, 141.0, 131.6, 124.2, 123.6, 117.6, 113.1, 68.7, 43.0, 40.2, 36.2, 31.6 ppm. ESI-MS: Calcd. for [M]$^+$: 359.2482; found: 359.2506.
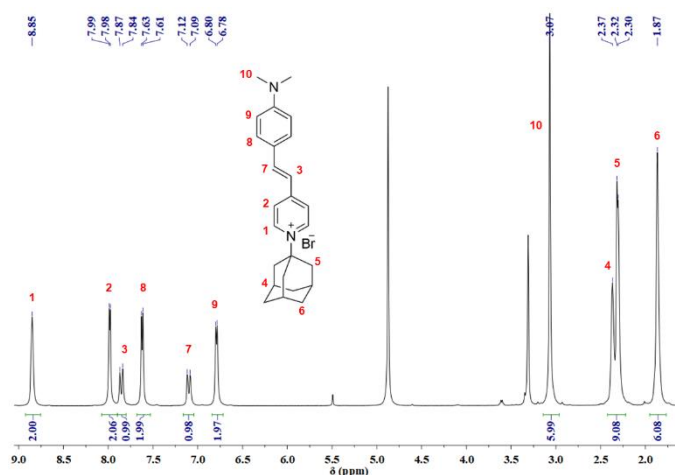
Figure 4.53 ^{1}H NMR spectrum (500 MHz) of DASAP in MeOH-d_3.
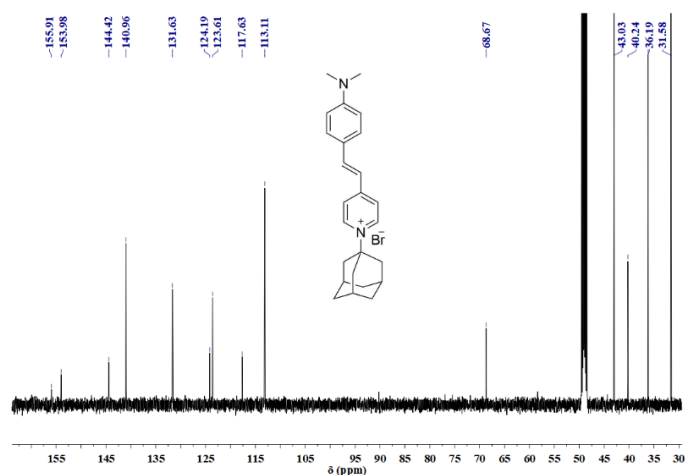
Figure 4.54 ^{13}C NMR spectrum (126 MHz) of DASAP in MeOH-d_3.
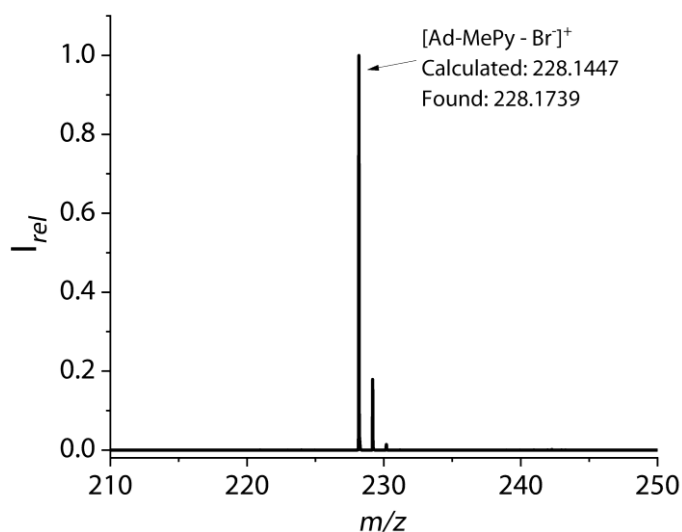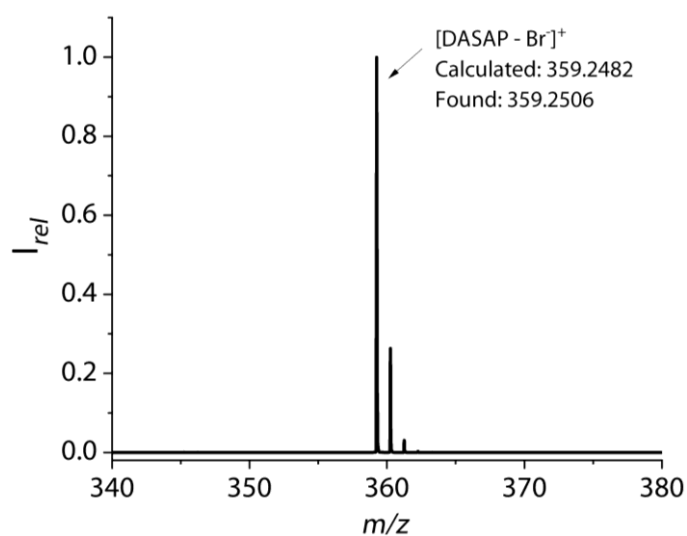

Figure 4.55 ESI-MS of BC-TEG-N$_3$ in the mixture of water and methanol (v/v = 1:1).

Additional information on details is available *via* the Chemotion repository:

https://dx.doi.org/10.14272/reaction/SA-FUHFF-UHFFFADPSC-ULNWEZYJTN-UHFFFADPSC-NUHFF-MUHFF-NUHFF-ZZZ

4.5. Supplementary data

4.5.1. Emission-based titration of cucurbit[7]uril to berberine and its derivatives
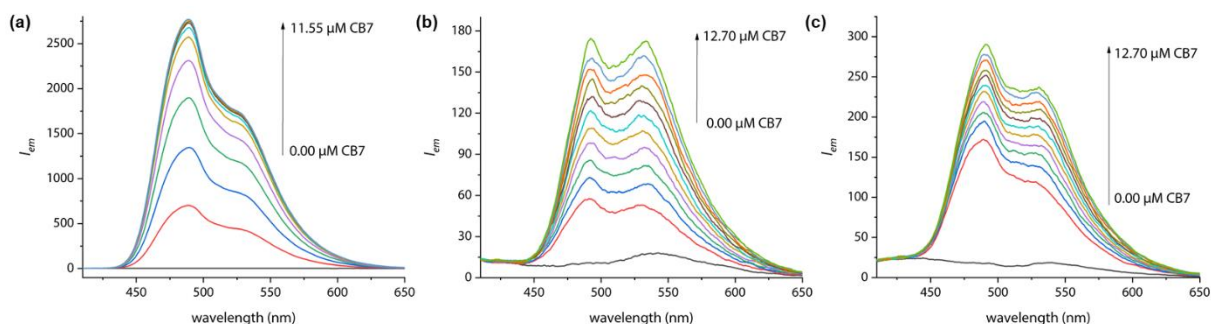
Figure 4.56 Emission spectra of (a) 5 μM berberine, (b) 5 μM BC-HEG-N$_3$, and (c) 5 μM BC-TEG-N$_3$ upon addition of CB7 in water, λ$_{ex}$= 350 nm. Interval time between each titration step: 50 seconds.

4.5.2. Fluorescence titration of guests to chemosensors

4.5.2.1. Amantadine
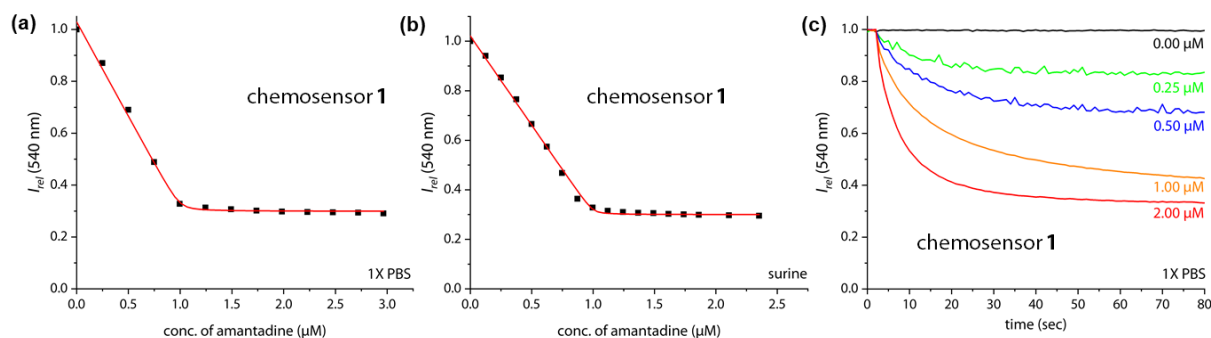
Figure 4.57 Fitting plots of normalized emission intensity at 540 nm of 1 μM **1** in (a) 1X PBS and (b) surine at 25°C, upon addition of amantadine. Intervals between titration steps: 200 seconds. Normalized fluorescence-based kinetic traces at varied concentrations of amantadine and 1 μM **1** in 1X PBS at 25°C. Concentration of amantadine for each curve: 0, 0.25, 0.50, 1 and 2 μM, λ$_{ex}$ = 350 nm.
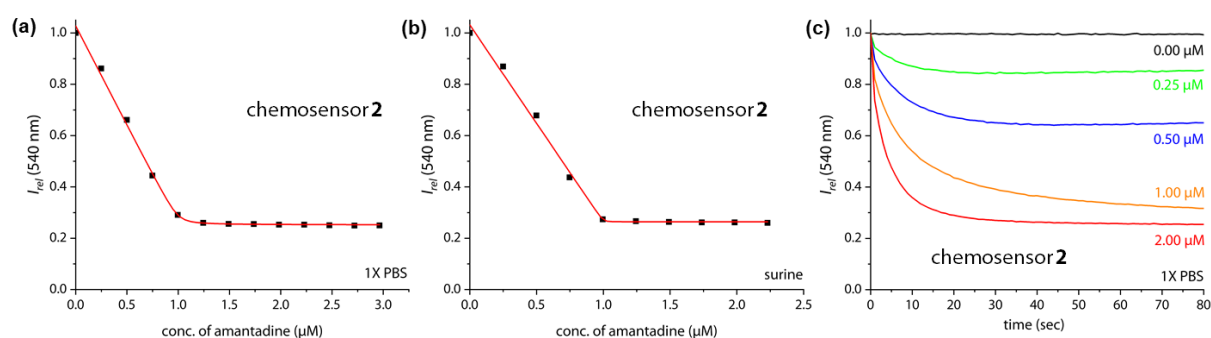
Figure 4.58 Fitting plots of normalized emission intensity at 540 nm of 1 μM **2** in (a) 1X PBS and (b) surine at 25°C, upon addition of amantadine. Intervals between titration steps: 200 seconds. Normalized fluorescence-based kinetic traces at varied concentrations of amantadine and 1 μM **2** in 1X PBS at 25°C. Concentration of amantadine for each curve: 0, 0.25, 0.50, 1 and 2 μM, λ$_{ex}$ = 350 nm.

4.5.2.2. Cadaverine
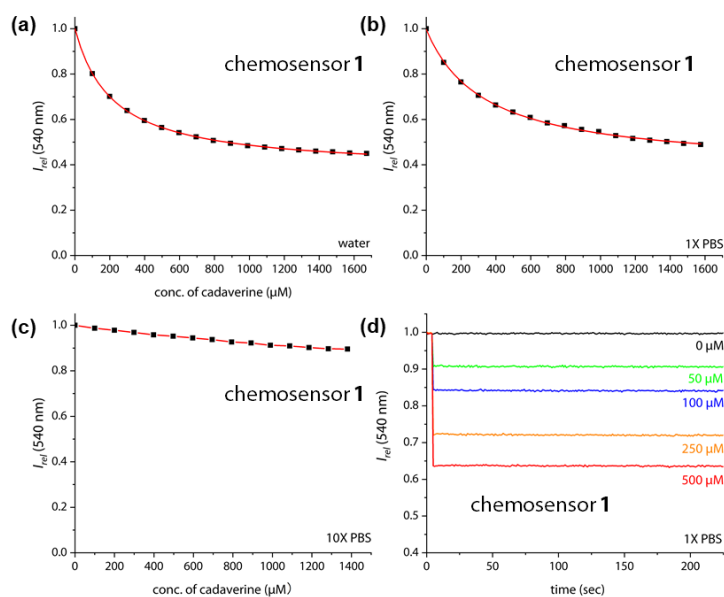
Figure 4.59 Fitting plot of normalized emission intensity at 540 nm of 1 μM **1** in water (a), 1X PBS (b) and plot of normalized emission intensity at 540 nm of 1 μM **1** in 10X PBS (c) at 25°C, upon addition of cadaverine. Interval time between titration steps: 200 seconds in water, 20 seconds in 1X PBS and 10X PBS. (d) Normalized fluorescence-based kinetic traces at varied concentrations of cadaverine and 1 μM **1** in 1X PBS at 25°C. The concentration of cadaverine for each curve: 0, 50, 100, 250 and 500 μM, λ_{ex} = 350 nm.
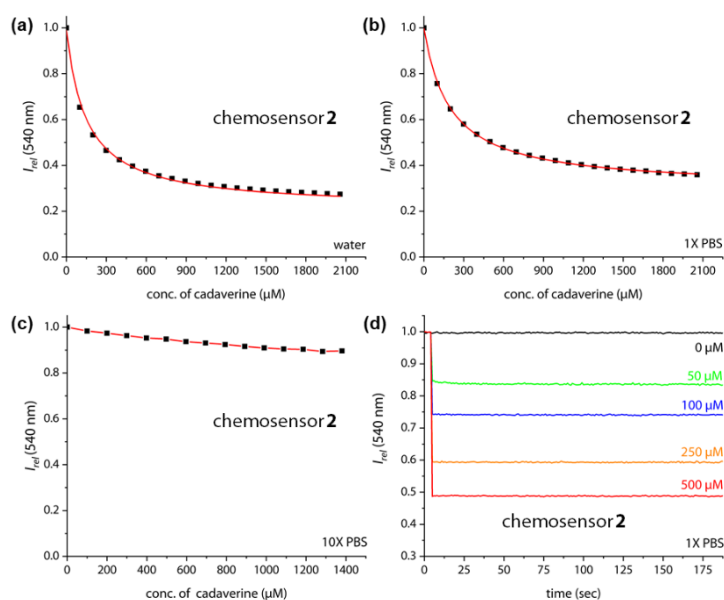
Figure 4.60 Fitting plot of normalized emission intensity at 540 nm of 1 μM **2** in water (a), 1X PBS (b) and plot of normalized emission intensity at 540 nm of 1 μM **2** in 10X PBS (c) at 25°C, upon addition of cadaverine. Interval time between titration steps: 200 seconds in water, 20 seconds in 1X PBS and 10X PBS. (d) Normalized fluorescence-based kinetic traces at varied concentrations of cadaverine and 1 μM **2** in 1X PBS at 25°C. The concentration of cadaverine for each curve: 0, 50, 100, 250 and 500 μM, λ_{ex} = 350 nm.

80

4.5.2.3. Spermine
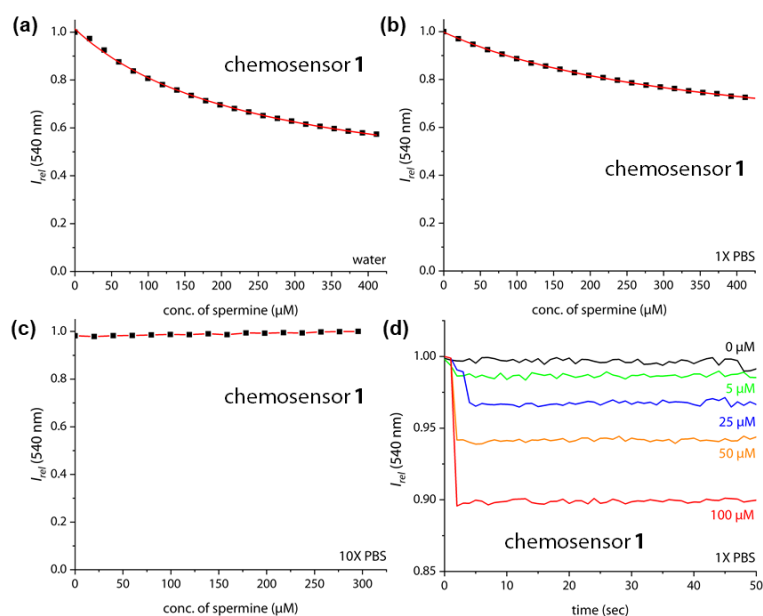
Figure 4.61 Fitting plot of normalized emission intensity at 540 nm of 1 μM **1** in water (a), 1X PBS (b) and plot of normalized emission intensity at 540 nm of 1 μM **1** in 10X PBS (c) at 25°C, upon addition of spermine. Interval time between titration steps: 200 seconds in water, 20 seconds in 1X PBS and 10X PBS. (d) Normalized fluorescence-based kinetic traces at varied concentrations of spermine and 1 μM **1** in 1X PBS at 25°C. The spermine concentration for each curve: 0, 5, 25, 50, and 100 μM, λ_{ex} = 350 nm.
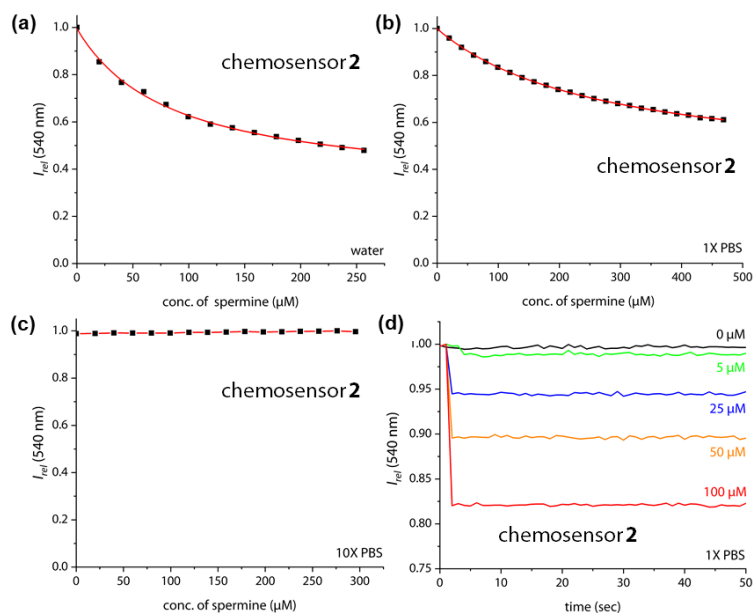
Figure 4.62 Fitting plot of normalized emission intensity at 540 nm of 1 μM **2** in water (a) ,1X PBS (b) and plot of normalized emission intensity at 540 nm of 1 μM **2** in 10X PBS (c) at 25°C, upon addition of spermine. Interval time between titration steps: 200 seconds in water, 20 seconds in 1X PBS and 10X PBS. (d) Normalized fluorescence-based kinetic traces at varied concentrations of spermine and 1 μM **2** in 1X PBS at 25°C. Concentration of spermine for each curve: 0, 5, 25, 50 and 75 μM, λ_{ex}= 350 nm.

4.5.2.4. Spermidine
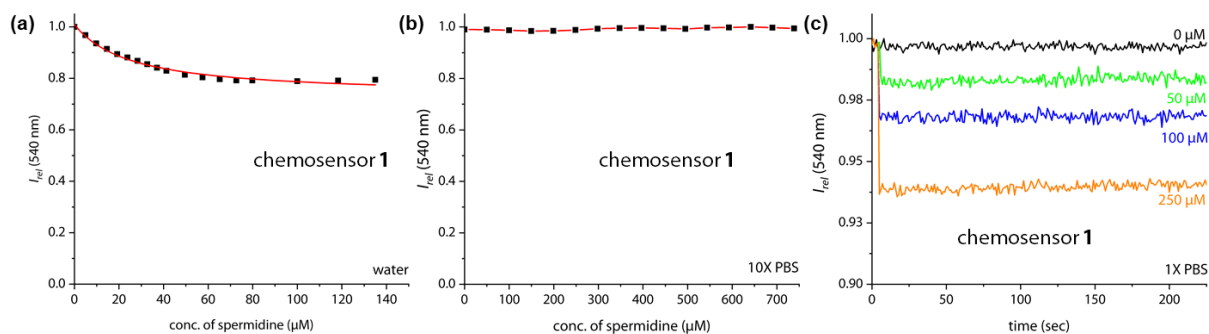
Figure 4.63 Fitting plot of normalized emission intensity at 540 nm of 1 μM **1** in water (a) and plot of normalized emission intensity at 540 nm of 1 μM **1** in 10X PBS (b) at 25ºC, upon addition of spermidine. Interval time between titration steps: 200 seconds in water and 20 seconds in 10X PBS; (c) Normalized fluorescence-based kinetic traces at varied concentrations of spermidine and 1 μM **1** in 1X PBS at 25ºC. The spermidine concentration for each curve: 0, 50, 100, and 250 μM, λ_{ex}= 350 nm.
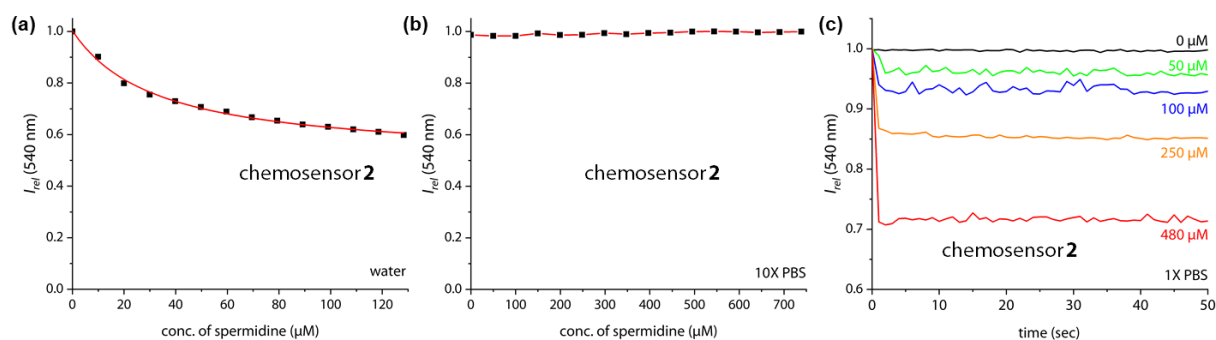
Figure 4.64 Fitting plot of normalized emission intensity at 540 nm of 1 μM **2** in water (a) and plot of normalized emission intensity at 540 nm of 1 μM **2** in 10X PBS (b) at 25ºC, upon addition of spermidine. Interval time between titration steps: 200 seconds in water and 20 seconds in 10X PBS. (c) Normalized fluorescence-based kinetic traces at varied concentrations of spermidine and 1 μM **2** in 1X PBS at 25ºC. Concentration of spermidine for each curve: 0, 50, 100, 250 and 480 μM, λ_{ex}= 350 nm.

4.5.2.5. 1-Adamantanol
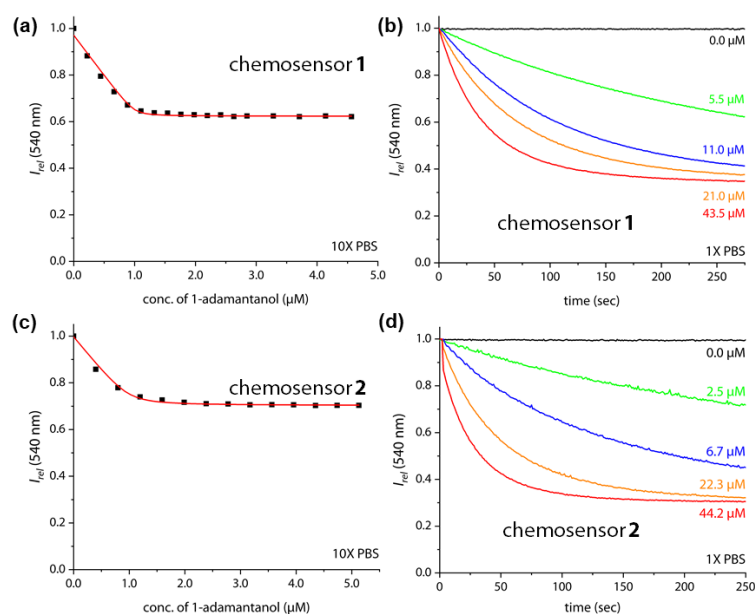
Figure 4.65 Fitting plot of normalized emission intensity at 540 nm of 1 μM (a) **1** and (b) **2** in 10X PBS at 25ºC, upon addition of 1-adamantanol. Interval time between titration steps: 3000 seconds in 10X PBS. (c) Normalized fluorescence-based kinetic traces at varied concentrations of 1-adamantanol and 1 μM **1** in 1X PBS at 25ºC. Concentration of 1-adamantanol for each curve: 0.0, 5.5, 11.0, 21.0 and 43.5 μM. (d) Normalized fluorescence-based kinetic traces at varied concentrations of 1-adamantanol to 1 μM **2** in 1X PBS at 25ºC. Concentration of 1-adamantanol for each curve: 0.0, 2.5, 6.7, 22.3 and 44.2 μM, $\lambda_{ex} = 350$ nm.

4.5.2.6. Nandrolone
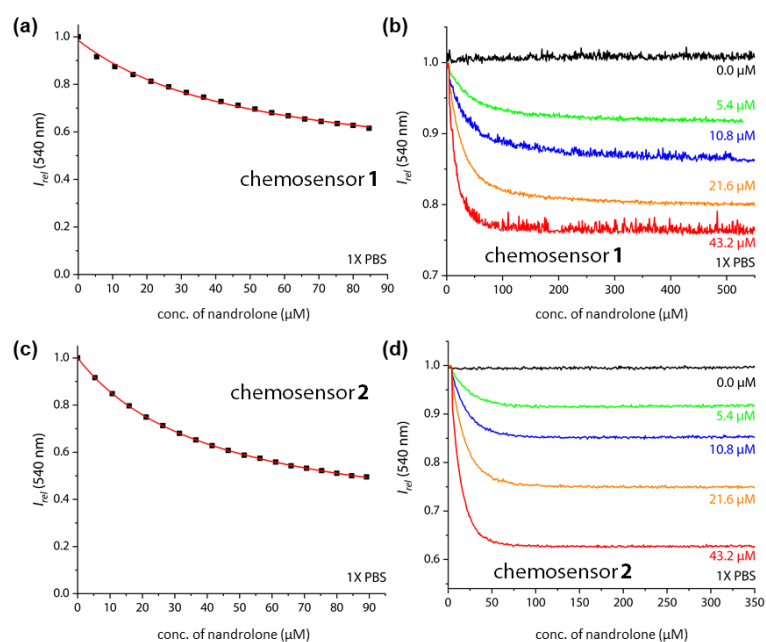
Figure 4.66 Fitting plot of normalized emission intensity at 540 nm of 1 μM (a) **1** and (b) **2** in 1X PBS at 25ºC, upon addition of nortestosterone. Interval time between titration steps: 500 seconds in 1X PBS.

Normalized fluorescence-based kinetic traces at varied concentrations of nortestosterone and 1 μM (c) **1** and (d) **2** in 1X PBS at 25°C. Concentration of nortestosterone for each curve: 0.0, 5.4, 10.8, 21.6 and 43.2 μM, λ_{ex}= 350 nm.

4.5.3. Overlay of kinetic traces on the addition of amantadine to 1 and 2
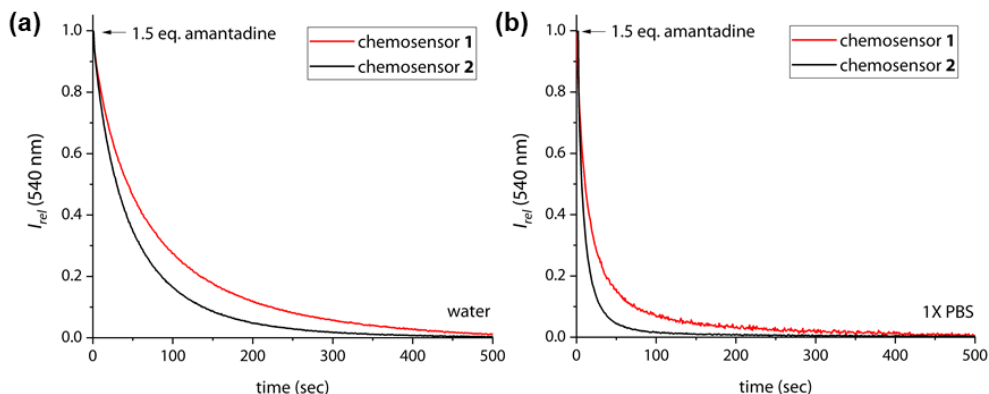
Figure 4.67 Overlay of normalized fluorescence-based kinetic traces for the addition of 1.5 μM amantadine to 1 μM **1** (red line) and 1 μM **2** (black line) in water (a) and 1X PBS (b) at 25°C, λ_{ex} = 350 nm. (Normalization method [0,1] in Origin software package was used).

4.5.4. Detection limit of chemosensor 2 for amantadine
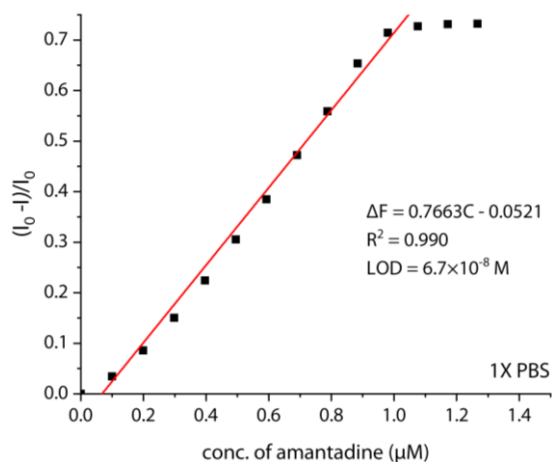
Figure 4.68 Fitting plot of emission intensity monitored at 540 nm of 1 μM **2** in 1X PBS at 25°C, upon addition of amantadine, λ_{ex} = 350 nm. The emission intensity of **2** without any amantadine was measured for five individual samples in 1X PBS, and based on these measurements, the standard deviation (σ) was determined. The limit of detection (LOD) was then calculated with the equation 3σ/S. S is the slope between intensity *versus* amantadine concentration (ΔF is the ratio of fluorescence intensity change, and C is the concentration of amantadine in μM).

4.5.5.100 nM amantadine detection by chemosensor 2 in surine
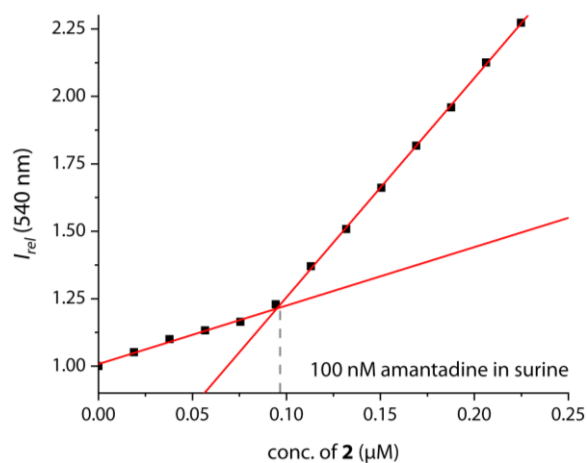
Figure 4.69 Fitting plot of the normalized emission intensity at 540 nm *versus* concentration of **2** in surine spiked with 100 nM amantadine at 25°C, $\lambda_{ex} = 350$ nm. Interval time between titration steps: 200 seconds.

5. Distinguishing biorelevant analytes by salt-responsive CB7-based chemosensor in biofluids

*This chapter is derived from the work that has been submitted to the Journal of the America Chemical Society (after final revision): **Hu, C.**; Jochmann, T.; Chakraborty, P.; Neumaier, M.; Levkin, P. A.; Kappes, M. M.; Biedermann, F. The synthesis, analysis, and data organization were carried out by me under the supervision of Dr. Frank Biedermann. The PCA and pairwise pattern analysis was carried out in cooperation with Thomas Jochmann. The part of mass spectrometry, ion mobilogram experiments and DFT calculation were collaborated with Papri Chabraborty, Dr. Marco Neumaier and Prof. Dr. Manfred M. Kappes. The manuscript was written and revised through the contributions of all authors above.*

The dissociation caused by the salt competitive binding to supramolecular receptors is one of the major constraints for most host-guest chemosensors in biofluids or similar environments. Many relevant metabolites share a similar affinity with artificial binders, so it is difficult to distinguish them using established emission-based chemosensing methods such as indicator displacement assay (IDA). In this chapter, a novel cucurbit[7]uril-dye conjugate was applied, namely CB7-NBD, which can respond to salt-induced adaptation on analytes distinction *via* the facile approach with different salt types and concentrations. The new parameters provide additional information about the system at a low synthetic effort. In addition, an intuitive data-driven way of translating human-visible differences in curves into pairwise differences is presented. Combining ion mobility experiments with density functional theory (DFT) calculations yielded new insight into the binding mechanism and revealed an unprecedented ternary complex geometry for CB7. This chapter presents the non-selectively binding but salt-adaptive cucurbit[*n*]uril system for sensing applications in biofluids such as urine, saliva, and blood serum.

5.1. Introduction

Artificial receptors that utilize non-covalent recognition motifs are crucial elements in the design of fast-response, facile, low-cost, and parallelizable sensing technology, *e.g.,* for monitoring biochemical processes and molecular diagnostics.[272, 316-319] Over the years, supramolecular research has focused on a complex with a static structure, taking advantage of preorganization and template effects to prepare them.[320-323] Recently, there has been a growing interest in studying and exploiting labile interactions between molecular components in supramolecular systems. So far, mainly dynamic covalent bonding motifs were built into molecular frameworks to adapt the constitution to internal or external factors by reorganizing and exchanging building blocks.[324-328] Similarly, synthetic receptors were developed with these concepts.[329, 330] However, most receptor designs have been based on "static" macrocyclic systems with no obvious way to incorporate dynamic covalent bonds into the framework.[41, 331-335]

Most synthetic receptors that display high binding affinities for small bioactive molecules, *e.g.,* metabolites, neurotransmitters, and drugs, have been constructed from macrocyclic hosts with a deep binding cavity, taking advantage of multivalent binding,[336, 337] preorganization[320] and of the non-classical hydrophobic effect,[338, 339] *i.e.,* high-energy water release,[63] gain of differential cavitation energies[69] or the chaotropic effect.[340] Representative examples are cryptands,[19, 341] calix[*n*]arenes,[342-344] cavitands,[345-347]

naphthotubes,[348-350] and cucurbit[*n*]urils.[117, 215] Unfortunately, these macrocyclic systems are structurally symmetric and consequently rather unselective receptors. Besides, they do not mimic the asymmetric and selective binding pocket of proteins.

As the introduction mentioned above, though the propensity of CB*n* to strongly bind a wide range of biorelevant analytes [241 351 279] has spurred the development of assays for bioprocess monitoring, the applications of CB*n*-based chemosensor in biofluids remain scarce yet [56, 352] because of the relatively low selectivity and the subject to competitive binding by salts occurring in biofluids.

To confront these issues, in the previous chapter, an indicator-CB7 conjugated strategy for designing a responsive supramolecular system was provided to detect ultra-high binding affinity drug amantadine in biofluid. Nevertheless, this unimolecular chemosensor cannot sense analytes with less binding affinity. According to the established systems, it always required the preparation of a series or library of differentially selective chemosensors combined with multivariant data analysis.[343, 353, 354]

This line of thought should have led us to prepare a library of CB*n*-based chemosensors to achieve the differential array sensing of less binding analytes. However, established CB*n* analogues with particular structures (*e.g.,* chiral CB*n*, acyclic CB*n*, and nor-seco-CB*n*) have not brought the desired achievements.

Given the above situation, a potential strategy that could convert the 'enemy factors' into 'assistant tools' for the differential sensing of analytes was figured out. Instead of the library of chemosensors, the type and concentration of salt were set as the variable parameters to modulate the binding propensity between CB*n* and analytes. According to the distinctive and distinguishable responsiveness of each host-guest combination to the different salt types and concentrations, a tailored signal output can be obtained with individual features, namely the salt-adaptive CB*n* chemosensor.

5.2. Results

5.2.1. Design and preparation of CB7-based chemosensor

To satisfy the chemosensor with tunable features responded by metal-cation addition, the idea of following the chapter 4 that covalently tethered reporter dye onto CB*n*, which endows the chemosensor with the resistance of dilution and competitive salt binding, was adopted here firstly. However, the inevitable enhancement of binding strength *via* covalently tethered the strong binding dye resulted in the limited detection of ultra-high analytes rather than other weakly ones by chemosensors, such as CB7-BC conjugates. On the other hand, positively charged berberine moiety will electrostatically repel the metal ions and prevent their binding to CB*n* portals. This feature would only ensure the resistance of cation and stability in a high salinity medium but no salt-responsiveness. Thereby, both relatively weakly binding affinity and non-charge of the dye were prerequisites for designing a salt-responsive unimolecular CB*n*-based chemosensor, which could be regulated by salt while considering the displacement by the guest with weak affinity.

After screening the dye with a suitable size for the encapsulation by CB7 and the feature of environment-responsive non-charged fluorescent, a highly solvent-polarity responsive fluorescent dye, namely nitrobenzoxadiazole (NBD),[355] was identified as a promising potential dye for establishing the

chemosensor. Firstly, the binding performance of NBD to CB7 was investigated *via* photophysical characterization. In principle, the significant emission changes for this polarity-sensitive dye should be observed after encapsulated into the hydrophobic cavity of CB7 if the binary complex is formed. As expected, any hardly detectable spectral change of NBD upon addition of CB7 can be detected for the emission spectra in aqueous media by excitation at 475 nm (max absorption for NBD). Notably, the NBD was conjugated with a short flexible tetraethylene-glycol-azide (NBD-TEG) as a control compound for CB7-NBD. The resulting data barely indicated an intermolecular interaction between NBD-TEG and CB7 in an aqueous solution.
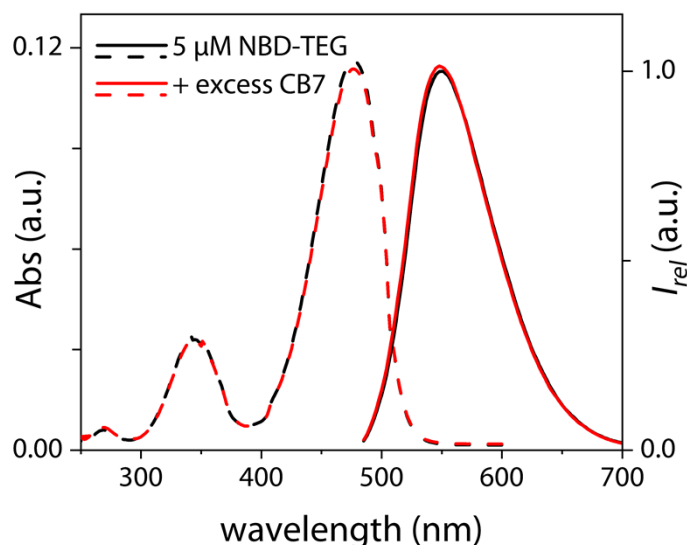
Figure 5.1 Absorption (dashed line) and emission (solid line) spectra of NBD-TEG (5 μM, black line) upon addition of excess CB7 (red line), λ_{ex} = 475 nm.

Likewise, *via* an azide-alkyne Husigen cycloaddition reaction, NBD-TEG was covalently tethered to the propargyl-functionalized monosubstituted CB7 to obtain the CB7-NBD conjugate, as shown in Figure 5.2. The detailed synthesis and characterization information is given in the experimental section.
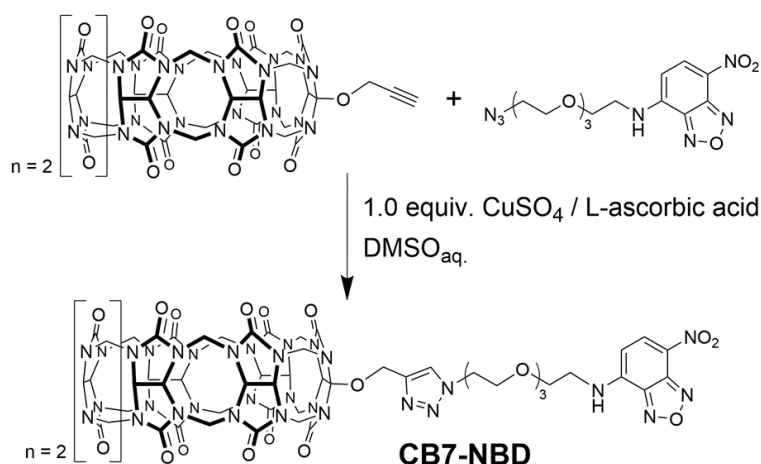
Figure 5.2 Preparation of CB7-NBD conjugate *via* an azide-alkyne Huisgen cycloaddition.

The chemical structure and conformation of obtained CB7-NBD in aqueous media were investigated by ^{1}H NMR experiments. Due to the limited solubility of this conjugate in water, the sample dissolution

was assisted with NaCl addition. This phenomenon proved the interaction between CB7-NBD and salt intuitively and will further analyze this phenomenon from the perspective of spectroscopy. From the proton NMR spectra of NBD-TEG and CB7-NBD, it was observed that the significant upfield shift of peaks belonging to NBD moiety after tethering to CB7 (Figure 5.3 (a) and (b)). This phenomenon provided solid evidence that NBD was encapsulated into the cavity of CB7 in a folded, unimolecular conformation.
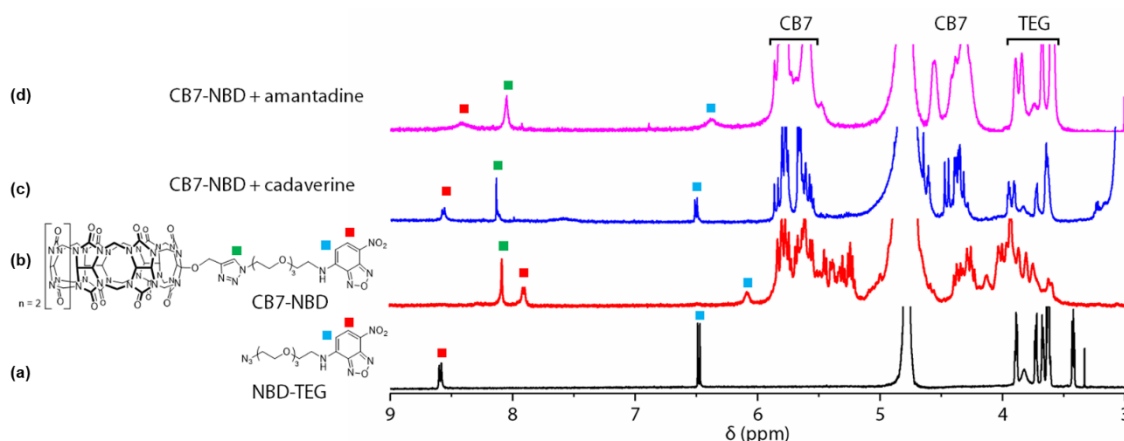
Figure 5.3 Overlay of ^{1}H NMR (500 MHz, D$_2$O) spectra of (a) NBD-TEG (black), (b) CB7-NBD (red), (c) CB7-NBD with an excess of cadaverine (blue), and (d) CB7-NBD with an excess of amantadine (pink). The appearance of the singlet peak at 8.04 ppm (marked with a green square) confirmed the triazole formation *via* click reaction.

5.2.2. Photophysical features of CB7-NBD in aqueous solution

In contrast with the result of NBD-TEG shown in Figure 5.1, the absorption and emission spectra of CB7-NBD in the aqueous phase were characterized that the maximum absorbance peak and emission wavelength were at 475 nm and 540 nm around, respectively, and displayed highly emissive intensity than NBD-TEG at the same concentration (Figure 5.4).
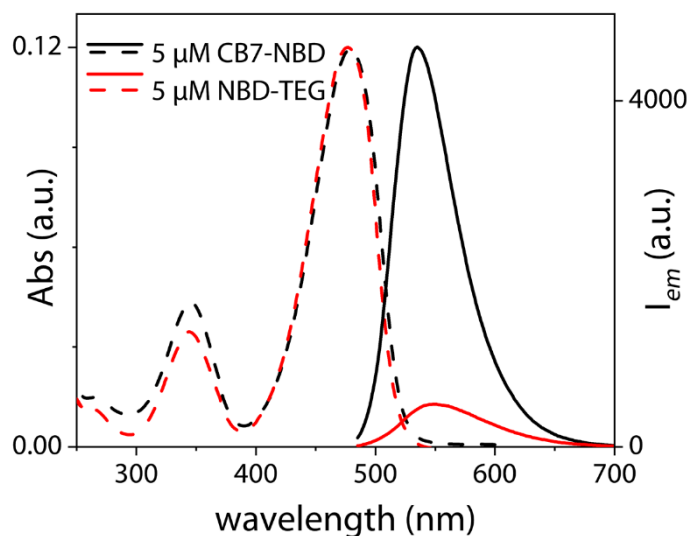
Figure 5.4 Absorption (dashed line) and emission (solid line) spectra of CB7-NBD (5 μM, black line) and NBD-TEG (5 μM, red line), λ_{ex} = 475 nm.

It is noteworthy that the significant emission enhancement of CB7-NBD solution occurred upon the addition of salts from the emission spectra (Figure 5.5 (a) and (b)). In the aspect of the absorption spectra, the maxima shifts were also observed and attributed to a strengthening of the unimolecular self-inclusion complex through cation co-binding.
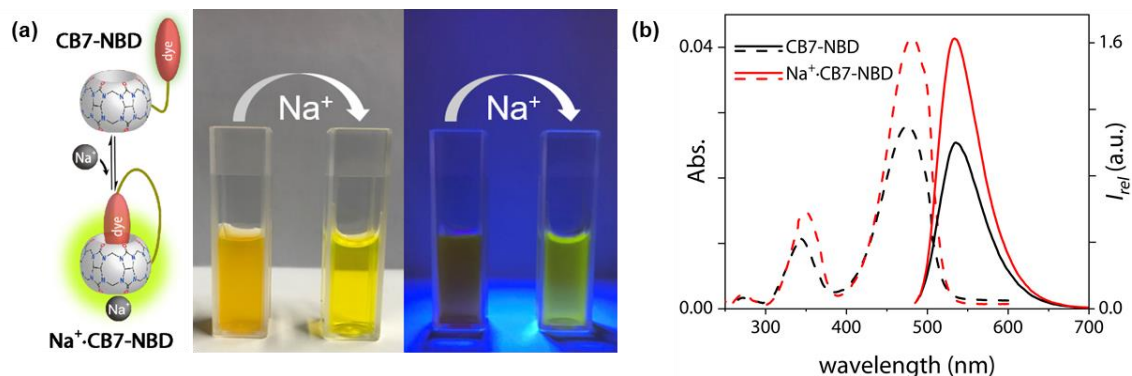
Figure 5.5 (a) Schematic illustration of emission enhancement of CB7-NBD induced upon addition of NaCl and photographic images of 200 µM CB7-NBD in MiliQ water in the absence (left cuvette) and presence (right cuvette) of 20 mM NaCl. Images were recorded at 'day light' (left image) and under UV irradiation (right image). (b) Absorption (dashed line) and emission (solid line) spectra of CB7-NBD in the absence (black line) and presence (red line) of excess NaCl, λ_{ex} = 475 nm.

In order to demonstrate the stability of CB7-NBD in high salinity solution, two examples of traditional non-covalent binary CBn⊃dye chemosensors (CB7⊃BC and CB7⊃MDAP) and another unimolecular conjugated chemosensor (CB7-BC) were involved into the NaCl titration experiments as well. The decreasing emission intensity of chemosensor solution with the increasing NaCl concentration revealed the gradual expulsion of dye from the cavity of CB7 upon salt addition (Figure 5.6).
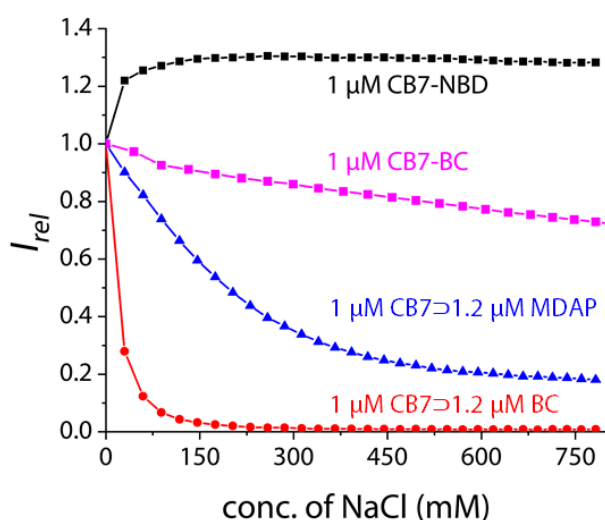
Figure 5.6 Plot of emission intensity of CB7-NBD conjugate (black) (λ_{ex} = 475 nm, λ_{em} = 550 nm), CB7-BC conjugate (purple) (λ_{ex} = 350 nm, λ_{em} = 540 nm), CB7⊃BC complex (red) (λ_{ex} = 350 nm, λ_{em} = 540 nm) and CB7⊃MDAP complex (blue) (λ_{ex} = 339 nm, λ_{em} = 454 nm) in MiliQ water as a function of increasing concentration of NaCl.

5.2.3.Interaction of CB7-NBD with biorelevant analytes

Two typical CB7 binding guests, cadaverine and amantadine, were utilized to investigate the binding performances between CB7-NBD and competitive guests. As shown in Figures 5.3 (c) and (d), the displacement of NBD from the CB7 cavity can be concluded from the characteristic ^{1}H NMR shifts. Addition of excess analytes into a solution of CB7-NBD results in the NBD protons (marked with red and blue squares) undergoing significant downfield shifts ($\Delta\delta$ = 0.5 and 0.3 ppm, respectively). Furthermore, the interpretation of NBD displacement was supported by the significant intensity decrease (Figure 5.7 (a)) and slight bathochromic shift (Figure 5.7 (b)) in the prospective of the emission signal of CB7-NBD, which gave the evidence of the dye displaced from the cavity and exposure into the polar solvent environment upon the addition of guests.
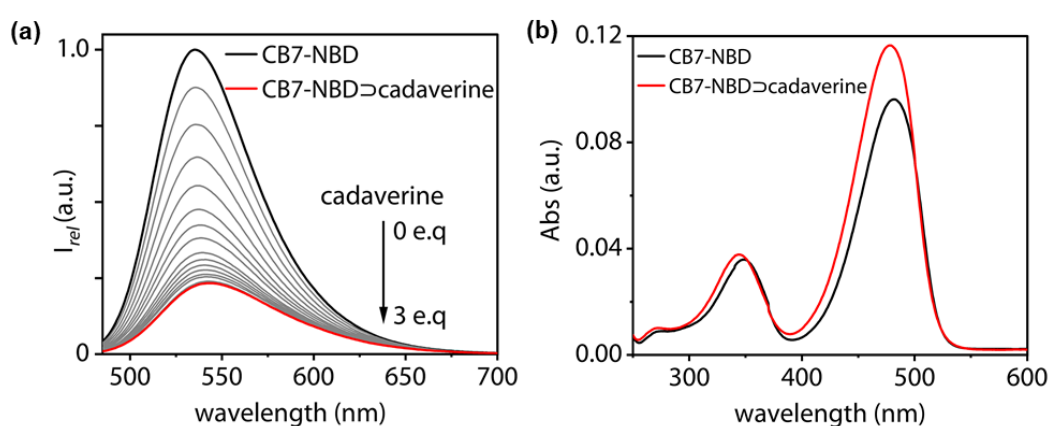
Figure 5.7 (a) Emission spectra (λ_{ex} = 475 nm) of CB7-NBD (1.0 µM) upon addition of cadaverine. (b) Absorbance spectra in the water of 5 µM CB7-NBD upon addition of 66.8 µM cadaverine.

Afterwards, the binding affinity of CB7-NBD with typical CB7-binding organic guests was investigated by the emission-based titration experiment in water and saline buffered media. As shown in Table 5.1, it was observed that only modestly reduced binding affinity to CB7-NBD with guests compared to the parent CB7 alone, such as $\log K_a$ = 7.0 *versus* 7.5 for PheGly[161] or 6.7 *versus* 7.4 for methyl viologen (M_2V)[283] complexation in deionized water. It demonstrated that the low energetic cost was consumed on the expulsion of NBD from the CB7 cavity rather than the strong affinity reducing of CB7-BC with corresponding guest displacement. On top of that, the data in the table also provided an intuitive comparison of binding affinity between deionized water and 1X PBS as medium. While an attenuated affinity of CB7-NBD with guests was observed in the presence of salt, the residual binding strength is still appreciable high in contrast to other reported synthetic receptors that become disfunctional in the presence of salts. In conclusion, this novel chemosensor may possess the capability for analyte detection in buffered biologically media.

Table 5.1 Binding affinities of CB7-NBD with (bio)organic analytes from fluorescence titration experiments in aqueous media*.

analytes	log K_a (M^{-1})	
	H$_2$O	1X PBS
putrescine (Put)	5.2	$\leq 3.0^a$
cadaverine (Cad)	7.0	4.0
spermidine (Spd)	6.3	3.3
spermine (Spm)	7.8	3.9
agmatine (Agm)	5.5	$\leq 3.0^a$
tyramine (Tyr)	5.8	3.8
amantadine (AdNH$_2$)	$\geq 8.0^b$	$\geq 8.0^b$
L-phenylalanyl glycine (PheGly)	7.0	4.5
nandrolone (Nan)	-^{c}	4.2
methyl viologen (M$_2$V)	6.7	4.1
1-adamantanol (AdOH)	$\geq 8.0^b$	-^{c}
pinacol	5.2	4.1
4-fluorophenethylamine (4F-PEA)	6.4	4.1
1,8-octanediyl-bis(methylimidazolium) (C$_8$mim)	$\geq 8.0^b$	5.9

$^{a,\ b}$ Binding curves too flat or too steep, respectively, thus K_a determination was not attempted.
^{c} K_a determination not attempted due to slow equilibration. *10 μM NaCl was added to CB7-NBD (1 μM) for solubility reasons. The estimated error in log K_a is 0.2. 1X PBS consists of 137 mM NaCl, 2.7 mM KCl, 10 mM Na$_2$HPO$_4$, and 1.8 mM KH$_2$PO$_4$.

5.2.4. Response of CB7-NBD⊃guest complexes to salts

Although the universal trend of attenuated affinity in the presence of high salt in the medium can be found among the different analytes, it was also observed that the degree of affinity weakening is not quite the same between different analytes. For instance, logK_a of spermine dropped from 7.8 in water to 3.9 in 1X PBS, but logK_a of pinacol was only reduced from 5.2 in water to 4.1 in 1X PBS. I concluded that the sensitivity of each CB7-NBD⊃guest to salt concentration varies significantly between the different analytes, which provides an unprecedented opportunity to create a salt-tunable supramolecular differential sensing system for analytes distinction.

Afterwards, a fluorescent emission-based titration of NaCl into CB7-NBD⊃guest complex was carried out, as shown in Figure 5.8. A unique intensity restoring behavior of CB7-NBD⊃cadaverine complexes was observed upon the addition of NaCl into their aqueous solution, which demonstrated the repulsion of protonated cadaverine from CB7 cavity and the re-binding of NBD moiety occurred in the presence of sodium cations.
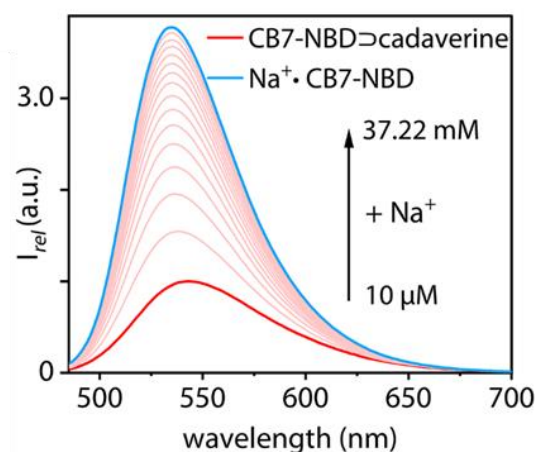
Figure 5.8 Representative emission-based titration of the CB7-NBD⊃cadaverine complex with $NaCl_{aq}$ ($\lambda_{ex} = 475$ nm).

The corresponding absorbance spectra of CB7-NBD with other typical analytes upon the salt addition were investigated, as shown in Figure 5.9. Conversely, for the ultra-high binding and part of non-charged guests, the spectral reversal caused by the addition of NaCl is not very pronounced, which indicates that the high-affinity guests remain buried in the cavity while the NBD fluorophore is located mostly outside. Especially, CB7-NBD inclusion complexes with ultra-high affinity guests (*e.g.,* amantadine and 1-adamantanol) were almost irresponsive to the addition of NaCl.
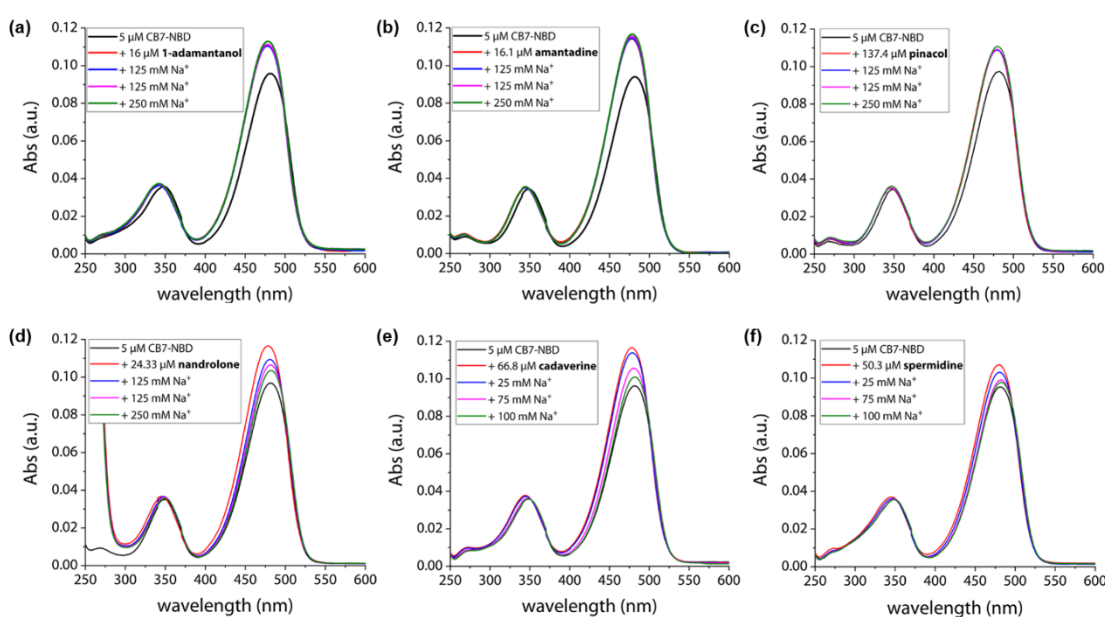
Figure 5.9 Absorbance spectra in water of 5 µM CB7-NBD upon addition of (a) 1-adamantanol, (b) amantadine, (c) pinacol, (d) nandrolone, (e) cadaverine, (f) spermidine, and subsequent addition of NaCl.

After all, adding salt into the CB7-NBD complex with different guests can lead to the competitive displacement of guests and induce the adaptation of different supramolecular conformations, as shown in Figure 5.10, which is dependent on the type of guests and salts, and salt concentration. The variation in fluorescent signal is determined by a combination of factors. Therefore, the change in the fluorescence signal is characteristic for different analytes.
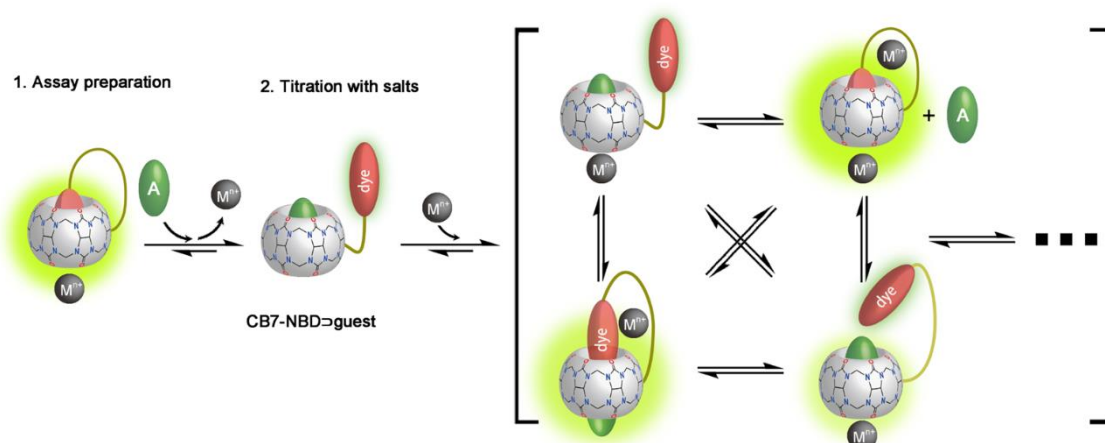
Figure 5.10 Schematic representation of salt-induced analyte distinction by CB7-NBD. Upon titrating with salts, some analyte types are expelled from the chemosensor while the dye-moiety is rebound. Other CB7-NBD analyte complexes may adopt a different binding geometry but remain intact in the presence of salts. One or more equivalents of metal cations can be co-complexed as a function of salt concentration and type. These processes provide analyte-indicative information and enable their distinction.

An assay that enables differential sensing of analytes has been proposed and preliminarily validated. The distinction of analytes can be achieved *via* the differential emission responses of CB7-NBD complexes with analytes to the addition of different types and concentrations of salts.

5.2.5. Analytes distinction by microplate assay

The array-based analytes distinction assay *via* the salt addition was carried out in a fluorescence plate reader, satisfying the emission responses of different CB7-NBD analytes complex *versus* various increasing salts concentration in parallel experiments.

Firstly, a series of typical CB7-binding biorelevant guests with various affinities and features (*e.g.,* charge, size, *etc.*) was chosen in Figure 5.11. In the assay preparation stage, a sub-stoichiometric concentration of CB7-NBD was added to the aqueous solution of the analytes to ensure that a high degree of complexation with the chemosensors is relatively independent of the binding affinity. Then, the aqueous stock solution of salt was titrated stepwise into the mixture solution, and the emission was recorded after a certain interval between each titration. The intensity was plotted against the salt concentration in the final mixture in the microplate wells.
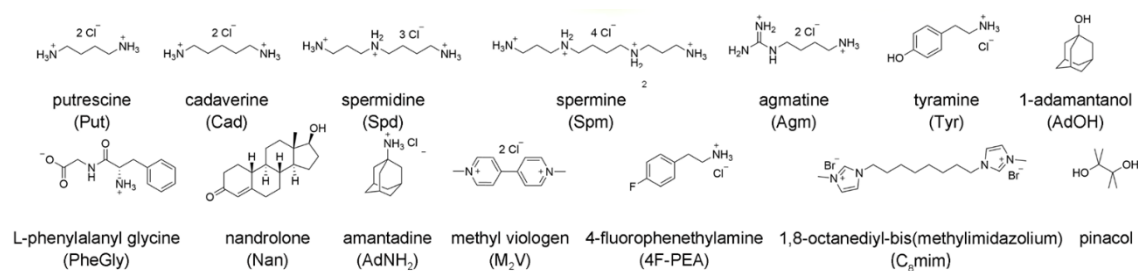
Figure 5.11 Chemical structures of the tested analytes. All compounds are shown in their native charge state in water, pH 7.

Taking $NaCl_{aq}$ as a titration example, the normalized plot curves of emission intensity *versus* concentration of NaCl was demonstrated in Figure 5.12 (a). Compared to the spectral information, these curves were more intuitive in contrasting the differences between each analyte with CB7-NBD in response to salt. To demonstrate this unique feature belonging to CB7-NBD, two traditional non-covalent IDA chemosensors (CB7⊃BC and CB7⊃MDAP) and one unimolecular conjugated chemosensor (CB7-BC) were carried out in the same experiments as the control (Figure 5.12 (b)). Much more steeply increasing curves for CB7-NBD can be observed for polyamines and dicationic guests. In contrast, the non-charged guests, nandrolone (Nan), phenylalanine glycol (PheGly), and pinacol, caused only modest emission responses as their complexes with CB7-NBD (Figure 5.12 (a)). Meanwhile, flat signal response curves were found for amantadine ($AdNH_2$) and 1-adamantanol (AdOH), whose host-guest complexes with CB7-NBD are mostly inert to salt addition. This subgroup of ultra-high analytes can be directly identified among the numerous analytes by this strategy. It is noteworthy that the emission intensity of one analyte with CB7-NBD at different salt concentrations could also offer specific information compared to other analytes. For instance, before 500 mM NaCl in the mixture, the plot traces of C_8mim and pinacol were mostly identical, but the obviously accelerated differentiation appeared after 600 mM of NaCl addition. The intensity of C_8mim continued to rise while pinacol leveled off. In contrast, the traditional non-covalent chemosensors (Figure 5.12 (b) and (c)) or cationic unimolecular chemosensors (Figure 5.12 (d)) were not able to distinguish the analytes in this way.
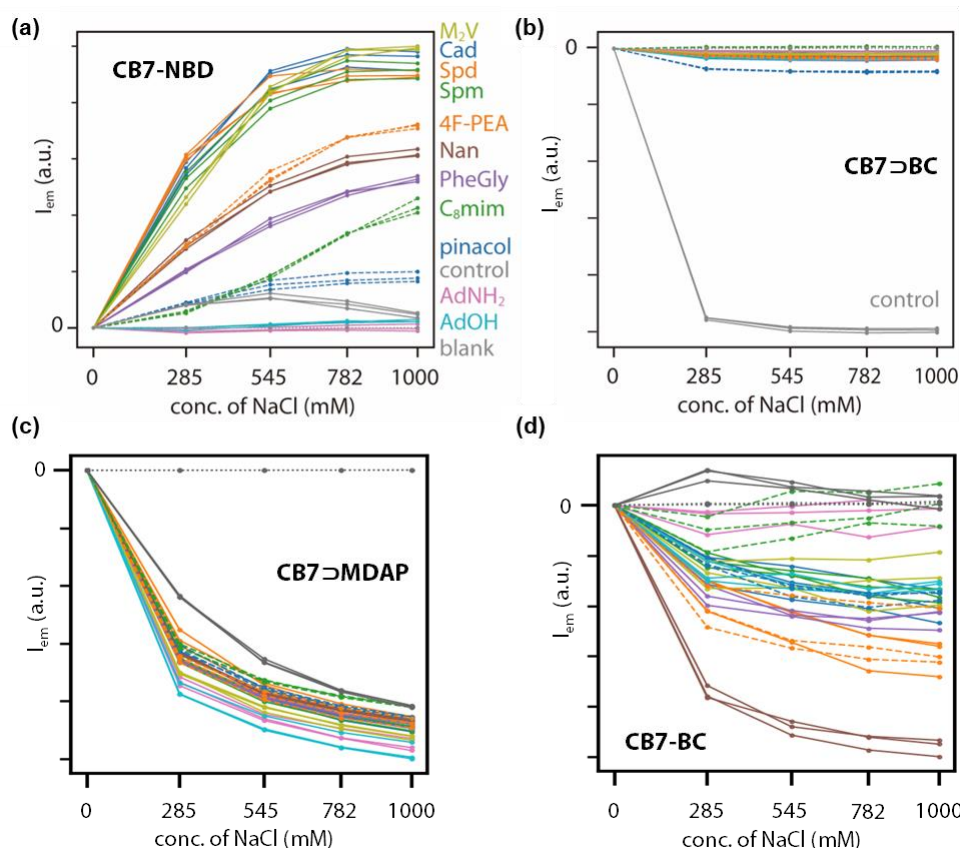
Figure 5.12 Normalized plot of the emission intensity as a function of NaCl concentration. The assay was initiated by preparing a mixture of chemosensor ((a) 1.0 μM CB7-NBD, (b) 1.0 μM CB7 + 1.2 μM BC, (c) 1 μM CB7 and 1.2 μM MDAP, and (d) 1 μM CB7-BC) and 200 μM of the analyte in 10 mM phosphate buffer, pH 7.45, followed by the subsequent titration with stock solutions of inorganic salts. Three replicas of the emission responses for each analyte-salt combination are shown.

In addition, titrating with other inorganic salts can harvest additional and complementary information to distinguish analytes. For instance, when titrating LiCl$_{aq}$ into the mixture of CB7-NBD analytes complex in solution, an obviously different emission intensity plot for spermidine can be observed among the numerous curves when NaCl$_{aq}$ or KCl$_{aq}$ titrating.
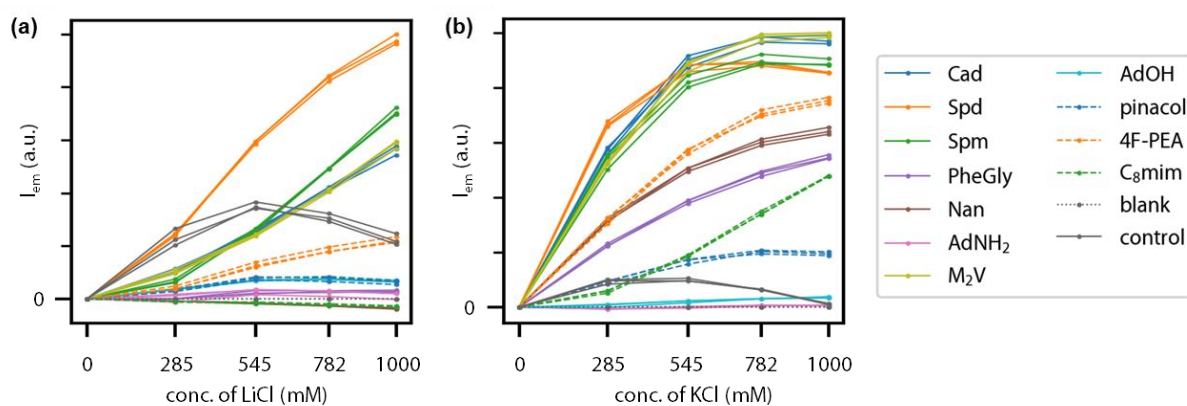
Figure 5.13 Plot of the emission intensity at 550 nm of 1 μM CB7-NBD in the presence of 200 μM analytes as a function of the concentration of (a) LiCl and (b) KCl in 10 mM PB (λ_{ex} = 475 nm).

5.2.6. Data analysis of analyte salt-response differences

The PCA and pairwise pattern analysis was carried out in cooperation with Thomas Jochmann.

In order to integrate the multi-dimensional information from various concentrations of salt and analytes into a more visible and intuitional presentation way, the principal component analysis (PCA) was introduced into differential sensing studies for analyzing the above results. For instance, PCA was performed solely on the single-salt NaCl-addition data with all analytes processed together and visualized the first two principal components of the emission curves, as shown in Figure 5.14. For most analytes, distinct data clusters were observed and substantiated by non-overlapping 95% confidence ellipses computed from each analyte's replica measurements. Except for ultra-high binding affinity analytes, other analytes can be fully separated from each other without serious overlapping areas. Conversely, the PCA data resulting from differential sensing assay by the traditional non-covalent chemosensor CB7⊃BC cannot supply a clear differential performance as CB7-NBD, where the large overlap among the confidence ellipses of each analyte was observed basically.
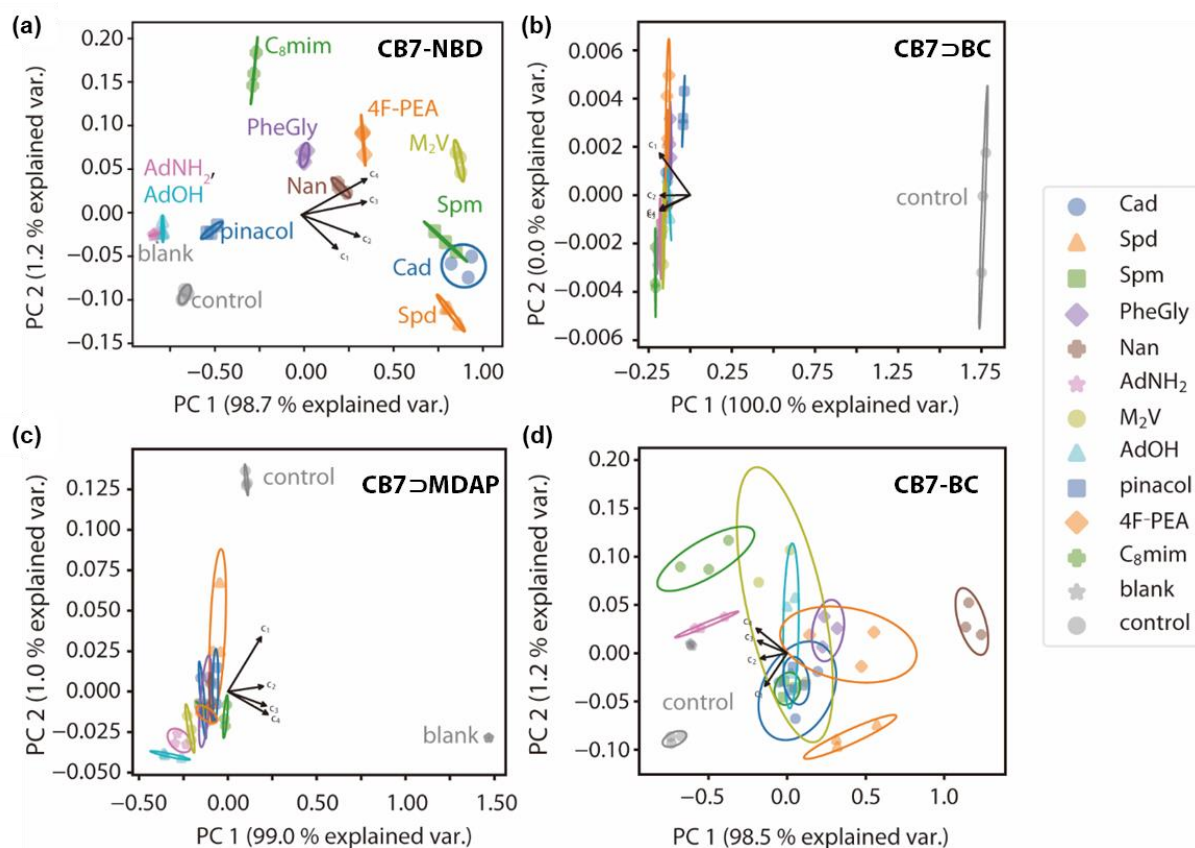
Figure 5.14 PCA plot with 95% confidence ellipses resulting from the emission intensity at 550 nm (λ_{ex} = 475 nm) as a function of the concentration of NaCl with (a) 1 μM CB7-NBD, (b) 1 μM CB7 + 1.2 μM BC, (c) 1 μM CB7 + 1.2 μM MDAP and (d) 1 μM CB7-BC in 10 mM PB spiked with 200 μM analytes. The black *loading* vectors reflect the influence of each concentration on the first two principal components. Orthogonal vectors indicate uncorrelated information between the corresponding measurements, whereas parallel vectors indicate redundant information.

Besides NaCl, other alkaline salts were also capable of demonstrating great performance for analytes distinction in the perspective of PCA results. The slight but clear distinction between AdOH and AdNH$_2$ was achieved by the addition of RbCl, CsCl, or CsF. Although the results obtained by titration of alkaline earth metal salts were not as ideal as alkaline salt (probably due to the multivalent cations or precipitates forming with phosphate ions), they also enriched dimensionally the differential sensing information. See the data from experimental sections.

Meanwhile, the analytes distinction capability can be enhanced by jointly processing the data from all salt-addition data into one, namely, combining the dependence of salt types with salt concentration. The two-dimensional PCA was utilized again for this analysis and is shown in Figure 5.15.
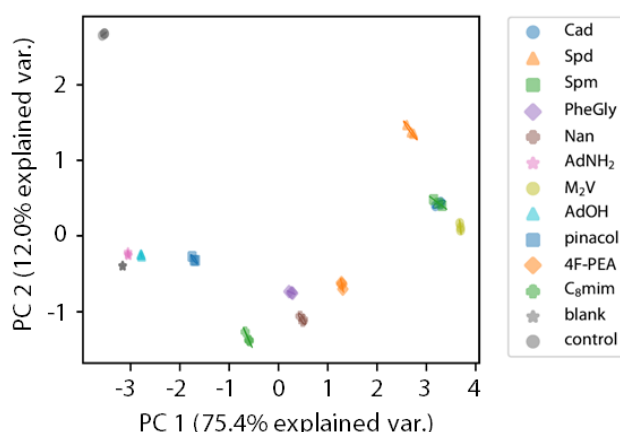
Figure 5.15 PCA plot with 95% confidence ellipses resulting from processing all above data input.

The main superiority of the system is to harvest additional data by salt addition with one chemosensor instead of the traditional receptor-library-based approaches that faces additional synthetic efforts. Furthermore, it is not required to employ redundant types of salt at various concentrations, but one or two types of salts added at four different concentrations were already enough to reach the goal of analyte distinction.

In order to present the differences between the salt-responses of any pairs of specimens in a single and intuitive quantity, the root mean squared difference of the salt-induced emission response I_{em} was calculated at each salt concentration (offset-corrected ($I_{em}(c) = I_{em}(c) - I_{em}(c = 0)$)) and normalized ($I_{em}(c) = I_{em}(c)/\max(|I_{em}(\text{all concentrations and analytes})|)$):

$$\Delta(I_a, I_b) = \sqrt{\frac{\sum_c (I_a(c) - I_b(c))^2}{N_{conc}}}, \tag{5.1}$$

Where c stands for the salt concentration and, again, N_{conc} for the number of different salt concentrations used in the assay.

The corresponding plots that depict the pairwise distance $\Delta (I_a, I_b)$ between any two specimens (replicas/samples) are shown in Figure 5.12. When NaCl was the titrant, except CB7-NBD complexes with ultra-high affinity guests (AdNH$_2$ and AdOH) were unresponsive, it is generally feasible to pairwise distinguish any of the two analytes from each other in this colorimetric pattern. Likewise, the standard

non-covalent chemosensors (CB7⊃BC and CB7⊃MDAP) did not allow for a clear distinction of the analytes from their corresponding emission response patterns due to the full dissociation in the presence high concentration of salt. In addition, strong unimolecular chemosensor (CB7-BC) can only distinct a few high-affinity guests, *e.g.,* Nan, AdNH$_2$ or C$_8$mim, rather than other low-affinity analytes.
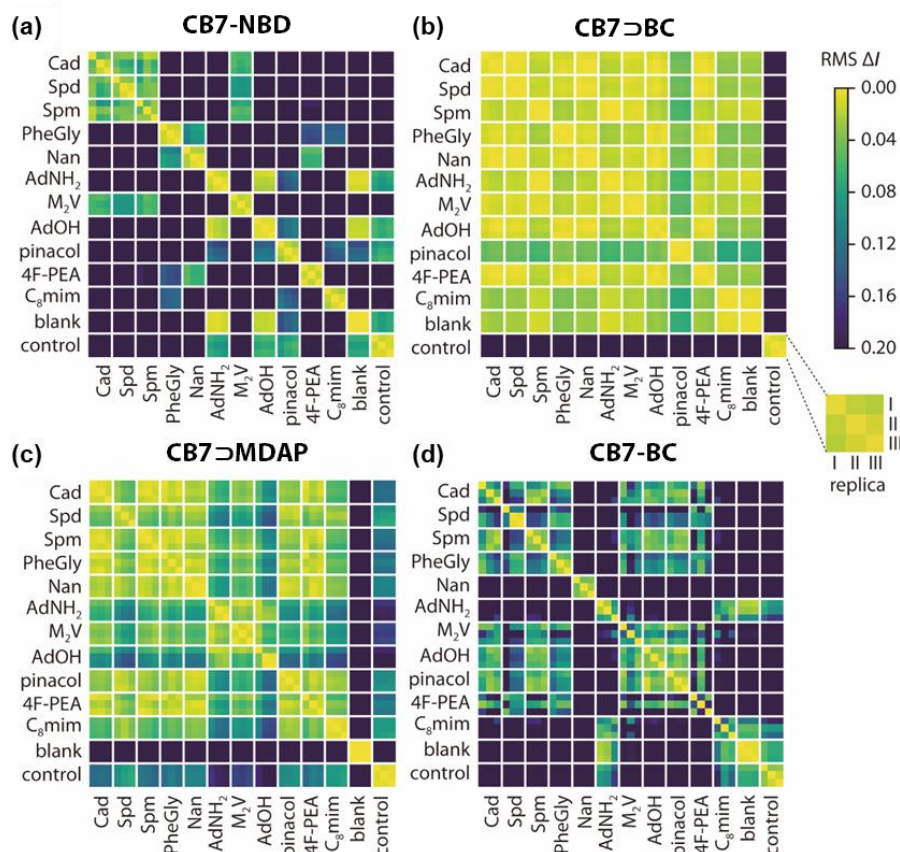
Figure 5.16 Pairwise pattern of difference between emission responses of the three individual replicas for each analyte with (a) 1 μM CB7-NBD, (b) 1 μM CB7 + 1.2 μM BC, (c) 1 μM CB7 + 1.2 μM MDAP and (d) 1 μM CB7-BC in 10 mM PB spiked with 200 μM analytes. The three replicas per analyte are depicted inside the blocks as smaller squares. The blocks correspond to different analytes and are separated by thick white lines. Yellow color marks small distances (curves are very similar); violet marks larger distances (curves are more different).

To further demonstrate the different salt-responses, differential sensing of the analytes mixture was carried out following the same salt-addition procedure. For example, the mixture of spermine and nandrolone was investigated and found to be distinguishable through titration with NaCl, as shown in Figure 5.16.
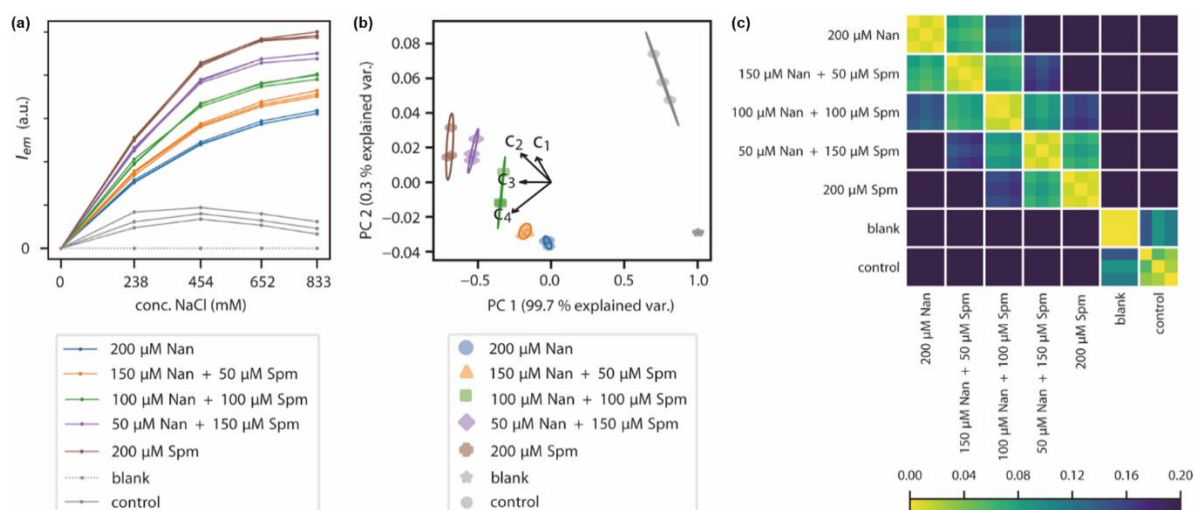
Figure 5.17 (a) Plot of the emission intensity, (b) PCA plot with 95% confidence ellipses resulting from the emission intensity at 550 nm of 1 μM CB7-NBD in the presence of 200 μM nandrolone (Nan) and spermine (Spm) mixture as a function of the concentration of NaCl in 10 mM PB (λ_{ex} = 475 nm). (c) Pairwise pattern of differences between emission responses of the three individual replicas for each analyte.

5.2.7. Differentiation of biorelevant amines by salt-addition assays

I also investigated the salt-addition responses of CB7-NBD for a series of biorelevant amines. Six universal and important biogenic amines were chosen here, *i.e.,* putrescine, cadaverine, agmatine, tyramine, spermidine, and spermine. Some are important biomarkers for disease diagnosis or important metabolites for health quantification. Besides, their similar chemical structure and binding affinity to CB7 is a challenge to test the system and assay for analytes distinction. The array-based emission data for salt-addition (alkali chlorides) to the solution containing the mixture of amines (500 μM, for fully complexing the CB7 at most) and CB7-NBD (1 μM) in 10 mM phosphate buffer at pH 7.45, was carried out. Fortunately, the obvious distinction between each pair of analytes by salt-addition assay can be observed in both the PCA and pairwise pattern plots, as the example of LiCl addition shows in Figure 5.18. In addition, similar experiments were carried out with the concentration of amines at 200 μM, and a great distinction was also obtained that revealed the assay is not disturbed by concentration differences if the analyte is more excess than the chemosensor.
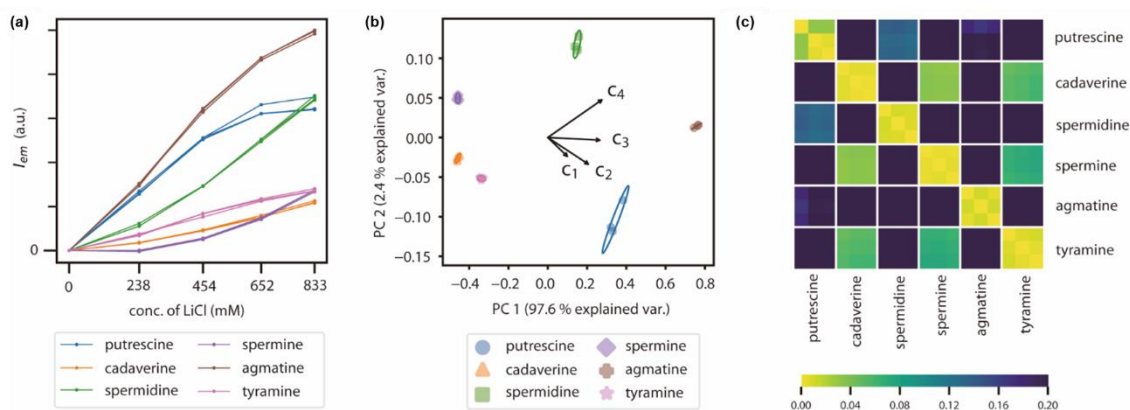
Figure 5.18 (a) Plot of the emission intensity, (b) PCA plot with 95% confidence ellipses resulting from the emission intensity at 550 nm of 1 μM CB7-NBD in the presence of 500 μM amines as a function of the concentration of LiCl in 10 mM PB (λ_{ex} = 475 nm) and (c) pairwise pattern of difference between emission responses of the three individual replicas for each amine.

5.2.8. Differential sensing of analytes by salt-addition assay in biofluids

Encouraged by the successful application for analytes distinction in 1X PBS by salt-addition assay, I moved forward to transform the assays in biofluid, where it is always a challenge for standard non-covalent CBn-based chemosensors for sensing applications due to their disintegration or unselective binding properties. Firstly, the salt-addition assay with CB7-NBD in analyte-spiked human urine and deproteinized human serum were tested. As shown in Figure 5.19, all spiked specimens can be distinguished from each other with the CB7-NBD by salt-addition assay, analogous to the aforementioned results in water and 1X PBS. Furthermore, the salt-addition assay was also successfully applied in artificial saliva and artificial synthetic urine (surine) for analytes distinction.
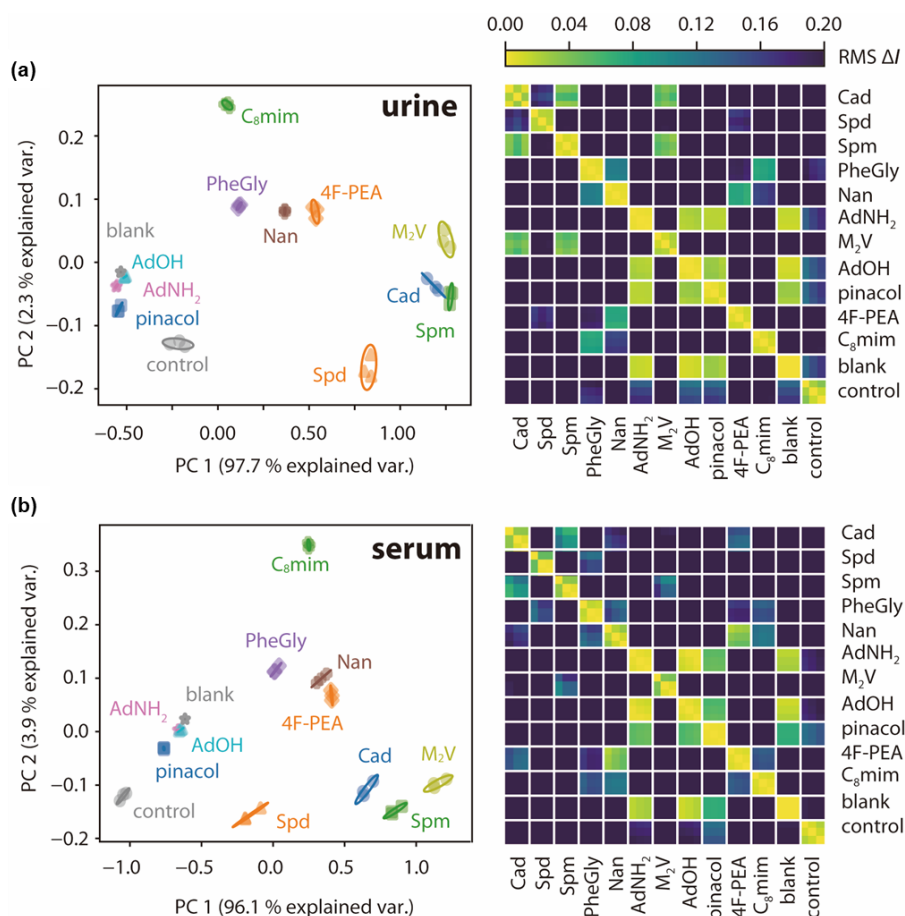
Figure 5.19 PCA plots with 95% confidence ellipses resulting from the emission intensity at 550 nm (λ_{ex} = 475 nm) as a function of the concentration of NaCl with 1 μM CB7-NBD in (a) human urine spiked with 200 μM analytes and (b) diluted human deproteinized serum spiked with 200 μM analytes. The corresponding colorimetric plots for differences in emission response between pairwise replicas/samples were presented on the right side.

5.2.9. Binding geometries by ion mobility experiments and DFT calculations

The part of mass spectrometry, ion mobilogram experiments and DFT calculation in this section were collaborated with Papri Chabraborty, Dr. Marco Neumaier and Prof. Dr. Manfred M. Kappes.

After exploring and applying CB7-NBD for analytes differential sensing by salt-addition assay, I was interested to study the geometry of its binding modes by ion mobility experiments in combination with DFT calculations to unravel the conformation of analyte-bound or unbound chemosensor. I also expected to identify differences in the complex geometries of literature-known CB*n*-guest complexes.[291, 356] Firstly, Na$^+$·CB7-NBD complex was geometry-optimized by dispersion-corrected DFT calculations and displayed as a representative energetically lowest structure out of ten investigated conformers in Figure 5.20 (a). It showed an expected inclusion structure in agreement with the aforementioned schematic illustration and NMR results. Meanwhile, the bonding interaction of Na$^+$ with -CO- groups of CB7 and the -NO$_2$ moiety of NBD with Na-O distances of 2.34 Å and 2.23 Å, respectively, was found from the DFT calculation. Herein, the structure and Mulliken charge distributions were then used to calculate Collision Cross Sections (CCSs) based on the trajectory-method (TM).[357] Based on this predicted result,

the direct experimental support for identifying the structure was obtained from ion mobility experiments, and only one conformer of the $Na^+ \cdot CB7$-NBD complex was observed in the gas phase, as shown in Figure 5.20 (b). Moreover, a great match was found between the experimentally determined CCSs (336 Å) and calculated CCSs (359 Å) with only a 6.9% deviation. In comparison with the inclusion conformation of $Na^+ \cdot CB7$-NBD, the other conformation with the unbound NBD moiety exhibited the higher DFT energies (+1.64 eV for folded and +3.84 eV for unfolded) and much larger CCSs values (388 Å for folded and 489 Å for unfolded) than the experimental values.
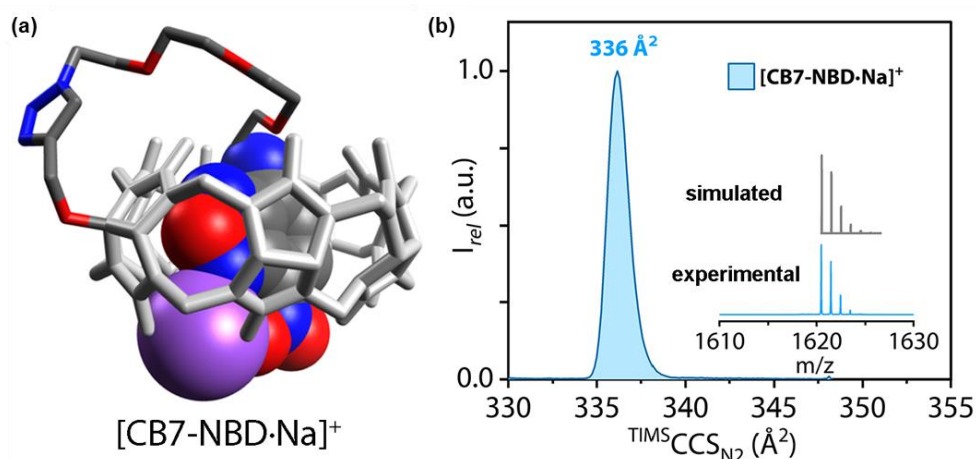
Figure 5.20 (a) Structures of [CB7-NBD·Na]$^+$ obtained at the DFT level (BP86/disp3-bj/def2-SV(P)). The NBD moiety inside the cavity is depicted with van der Waals spheres. Hydrogen atoms are not shown for clarity. The CB7 unit is shown in light grey. Atoms in blue, red and grey refer to nitrogen, oxygen and carbon atoms, respectively. The sodium cation is shown in purple. (b) Mass spectra and ion mobilograms of [CB7-NBD·Na]$^+$.

Likewise, the DFT calculation and ion mobility experiments were carried out to characterize three representative CB7-NBD complexes, AdNH$_2$, AdOH, and Cad, respectively. The results from calculation and experiments for [CB7-NBD·Na⊃adamantanol]$^+$ and the [CB7-NBD·Na⊃amantadine·H]$^{2+}$ complex demonstrated that an exclusion type complex exhibited the lowest DFT energy with the NBD moiety inside of the CB7 cavity. However, the inclusion type complex showed larger DFT energy and calculated CCSs than the experimental value. This was a converse situation compared to an aqueous solution, where the AdOH and AdNH$_2$ were bound inside the CB7 cavity while NBD was displaced and exposed to the solution environment corresponding to the results from NMR data. It can be interpreted that molecules are in an isolated state in the gas phase, and there is less existing the conventional driving force between host and guest. This might cause the different topologies in the gas phase in contrast to the solution phase. There are two protonated cadaverine states for the chemosensor complex with cadaverine in solution to investigate separately. Similar to the previous two analytes, the monoprotonated [CB7-NBD⊃cadaverine·H]$^+$ complex was also in an exclusion-type conformation as the energetically lowest candidate than others, which was calculated by DFT and in agreement with the ion mobility experiment. All of the corresponding computational and experimental CCSs values were summarized in Table 5.2.

Table 5.2 Experimental and theoretical data relevant to CB7-NBD/guest system with experimental collision cross-sections ($^{TIMS}CCS_{N2}$), calculated collision cross-sections ($^{calc}CCS_{N2}$), and relative DFT energies ΔE_{DFT} (0 eV refers to the structure with the highest stability). Bold structures best agree with the experimental CCSs and exhibit the highest stability.

Compound	m/z	$^{TIMS}CCS_{N2}$ (Å²)	$^{calc}CCS_{N2}$ (Å²)	ΔE_{DFT} (eV)	Topology	CCSs deviation exp. vs calc. (%)
[CB6·Na]⁺	1019	270	**285.3**	-	-	**5.6**
[CB7·H]⁺	1163	305	**322.7**	-	-	**5.8**
[CB7-NBD·H]⁺	1598	337	**366.9**	**0.00**	**inclusion**	**8.7**
			384.0	0.86	folded	13.8
			492.6	3.22	unfolded	46.0
[CB7-NBD·Na]⁺	1620	336	**359.3**	**0.00**	**inclusion**	**6.9**
			387.8	1.64	folded	15.3
			489.4	3.84	unfolded	45.6
[CB7-NBD⊃cadaverine·2H]²⁺	851	375	**387.7**	**0.00**	**dual inclusion**	**3.4**
			389.5	**0.16**	**exclusion**	**3.9**
			426.9	0.67	inclusion	13.9
[CB7-NBD⊃cadaverine·H]⁺	1700	349	**381.0**	**0.00**	**exclusion**	**9.2**
			369.7	0.50	dual inclusion	6.0
			413.1	1.22	inclusion	18.4
[CB7-NBD·Na⊃AdOH]⁺	1772	352	**386.7**	**0.00**	**exclusion**	**9.9**
			395.4	0.71	inclusion	12.4
[CB7-NBD·Na⊃AdNH₂·H]²⁺	886	386	**403.0**	**0.00**	**exclusion**	**4.4**
			399.5	0.47		3.5
			419.4	0.63	inclusion	8.6

Next, for the double protonated [CB7-NBD⊃cadaverine•2H]²⁺ complex, DFT calculated suggested a very unusual dual CB7-inclusion complex that the lowest energetically conformation is simultaneous inclusion of NBD moiety and cadaverine•2H⁺ inside the cavity as shown in Figure 5.21. Indeed, the CCSs

value was in agreement with the measured one as well. The other inclusion structure that NBD dangling over the CB7 portal is out of consideration due to its high DFT value and large deviation from the experimental value.
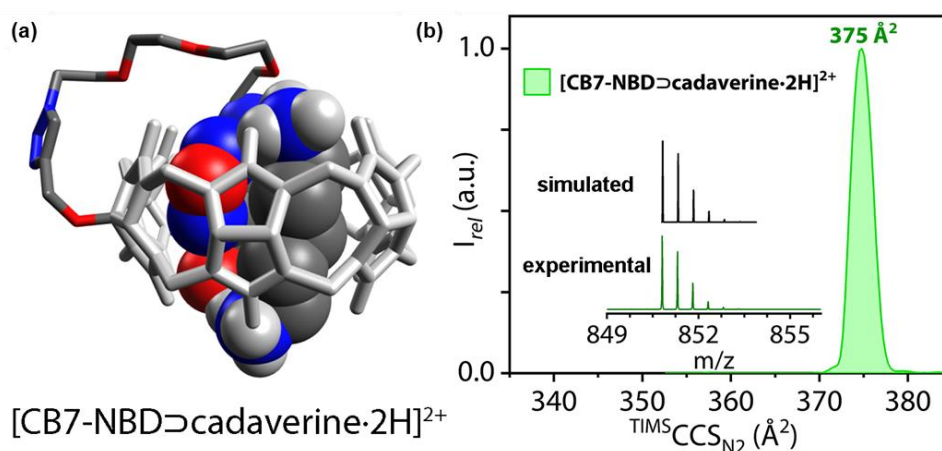
Figure 5.21 (a) Structures of [CB7-NBD⊃cadaverine·2H]$^{2+}$ obtained at the DFT level (BP86/disp3-bj/def2-SV(P)). The guest molecules and the NBD unit inside the cavity are depicted with van der Waals spheres. Hydrogen atoms are not shown for clarity, *except for the two protonated amino groups of cadaverine*. The CB7 unit is shown in light grey. Atoms in blue, red and grey refer to nitrogen, oxygen and carbon atoms, respectively. The sodium cation is shown in purple. (b) Mass spectra and ion mobilograms of [CB7-NBD⊃cadaverine·2H]$^{2+}$.

5.3. Conclusion

In this chapter, a unimolecular cucurbit[7]uril-dye conjugate system (CB7-NBD) was established and introduced for differential sensing of analyte by its unique salt-adaptive behaviors in buffered media and biofluids. Compared to the dissociation of traditional IDA-based non-covalent supramolecular systems in high salinity media, CB7-NBD exhibited the required dilution stability and salt resistance and maintained the binding affinity to a broad scope of analytes accompanied by fluorescent responses. Importantly, the binding behavior with analytes can be modulated through the addition of salts. The characterization of analytes binding with CB7-NBD was investigated by NMR, photophysics, ion mobility experiments, and DFT calculations. A salt-addition assay for analytes differential sensing strategy was developed to take advantage of the salt-adaptive responses. Instead of needing to synthesize a series of "differentially selective" receptors, merely the concentration and type of salts sufficed as parameters for creating high dimensional information for analytes differential sensing. After processing by data analysis, the results were visualized by PCA plots. Moreover, another intuitive colorimetric depiction was utilized to quantify the differences between each analyte (including replica). The presented CB7-NBD chemosensor combined with the salt-addition assay enables the sensing of biorelevant analytes in biofluids, such as urine, saliva, and serum.

5.4. Experimental part

5.4.1. Material and methods

All solvents and purchased chemicals were used as received from suppliers without any further purification. The stock buffer solutions of phosphate-buffered saline (1X PBS) (137 mM NaCl, 2.7 mM KCl, 10 mM Na_2HPO_4, and 1.8 mM KH_2PO_4) at pH 7.45 were prepared from GibcoTM PBS tablets by dissolving a tablet in 500 mL of distilled water. The stock solution of 10 mM phosphate buffer (PB) was prepared with sodium dihydrogen phosphate (0.6 g) in 500 mL of distilled water, and the pH was adjusted by 0.1 M NaOH to 7.45. Artificial saliva was purchased from Pickering Laboratories and used as received. Artificial synthetic urine (surine) was purchased from Cerilliant and was used as received. Healthy coworkers voluntarily donated their own urine. See also the section "ethical approval and informed consent" below. Human serum was purchased from Sigma and used in a deproteinized form. The deproteinization was performed according to the literature procedure.[358] Specifically, 500 μL of 4 M perchloric acid was added to 5 mL of cold human serum, mixed by shaking and centrifuged for 5 min at 10000 rpm at 4°C. The supernatant was removed from the precipitated protein, and the pH was adjusted to 7.0 by dropwise addition of KOH (4 M). $KClO_4$ that precipitated was removed by centrifugation, and the deproteinized serum was diluted with 70% 1X PBS buffer for further measurements. The stock solution concentrations of cucurbit[7]uril-tetraethylene glycol-nitrobenzoxadiazole (CB7-NBD) were determined by fluorescence titration upon the addition of known concentration of amantadine hydrochloride by exciting the sample at 475 nm and collecting the emission intensity at 550 nm in Milli-Q water. The amantadine hydrochloride and 1-adamantanol stock solution concentration were determined by fluorescence titration against a known CB7⊃berberine receptor complex by exciting the sample at 350 nm and collecting the emission intensity at 540 nm in Milli-Q water. The concentrations of stock solutions of berberine chloride (BC), L-phenylalanyl glycine (PheGly), methyl viologen (M_2V), and nortestosterone (nandrolone) were determined by using their molar absorption coefficients (berberine chloride: $22300\ M^{-1}\,cm^{-1}$ at 344 nm, L-phenylalanyl glycine: $195\ M^{-1}\,cm^{-1}$ at 257.6 nm, methyl viologen: $20700\ M^{-1}\,cm^{-1}$ at 257 nm, and 19-nortestosterone: $15320\ M^{-1}\,cm^{-1}$ at 248 nm) by UV-Vis absorption titration measurements in Milli-Q water. The stock solutions of other analytes were prepared as the aqueous solution with a certain concentration directly by weighing. In general, chemosensor solutions should be stirred for 30 minutes in the desired medium to ensure full equilibration along with a stable baseline for spectroscopical measurements.

5.4.1.1. Nuclear Magnetic Resonance (NMR) Spectroscopy.

^{1}H and ^{13}C NMR spectra were recorded either in deuterium oxide or chloroform-d_3 on a Bruker Avance 500 spectrometer at 25°C. The ^{1}H and ^{13}C NMR chemical shifts (δ) are given in ppm and refer to residual protons on the corresponding deuterated solvent.

5.4.1.2. High-Performance Liquid Chromatography (HPLC).

Preparative HPLC was performed on an LC-2000Plus HPLC system equipped with a UV-2075 UV-Vis detector, a Kromasil 100 C18 5 μM LC precolumn (50 × 20 mm, Agela), and a Kromasil 100 C18 5

μM LC preparative column (250 × 50 mm, Agela) for purification of CB7-NBD at a flow rate of 12 mL/min. All crude samples were dissolved in a mixture of water and ACN (v/v = 65/35) to get a final concentration of 1.5 mg/mL with one drop of TFA to improve the solubility.

5.4.1.3. Absorbance Spectra.

Absorbance spectra were measured at 25°C in Milli-Q water or PBS buffer on a JASCO V-730 double-beam UV-Vis spectrophotometer. PMMA cuvettes with a light path of 10 mm and dimensions of 10 × 10 mm from Brand with a spectroscopic cut-off at 220 nm were utilized for UV-Vis absorption experiments. The samples were equilibrated using a water thermostatic cell holder STR-812, while the cuvettes were equipped with a stirrer allowing rapid mixing.

5.4.1.4. Fluorescence Spectra.

Steady-state emission spectra and time-resolved emission profiles were recorded on a JASCO FP-8300 fluorescence spectrometer equipped with a 450 W Xenon arc lamp, double-grating excitation, and emission monochromators. Emission spectra were corrected for source intensity (lamp and grating) and the emission spectral response (detector and grating) by standard correction curves. All of the titration and kinetic experiments were carried out at 25°C by using a water thermostatic cell holder STR-812, while the cuvettes were equipped with a stirrer allowing rapid mixing. PMMA cuvettes with a light path of 10 mm and dimensions of 10 × 10 mm from Brand with a spectroscopic cut-off at 220 nm were utilized for fluorescence-based titration experiments.

5.4.1.5. 96-well Plate Reader.

Salt-adaptive analytes distinction assay was performed in a CLARIOstar Plus fluorescence plate reader (BMG Labtech). The total volume of solution before titration was 200 μL in each microplate well. All of the titration and kinetic experiments were carried out at 25°C with a temperature control system. For detection settings, the excitation was in the wavelength range from 450 nm to 490 nm, and emission was collected from 530 nm to 570 nm with a dichroic mirror at 511.2 nm. The pump speed of the injector was selected as 430 μL/s for the titration steps. Shaking of the microplate was carried out at 300 rpm frequency for 60 seconds before each cycle.

5.4.1.6. Ethical Approval and Informed Consent.

All procedures performed in studies involving human participants were in accordance with the formal statement of ethical principles published by the World Medical Association in the declaration of Helsinki in 1964 and its later amendments or comparable ethical standards.[359] Informed consent was obtained from all individual participants included in the study.[360, 361]

5.4.1.7. Trapped Ion Mobility Spectrometry (TIMS).

This part was carried out by Papri Chabraborty.

Ion mobility spectrometry (IMS) is a technique that can be coupled to mass spectrometry (MS). IMS provides collision cross sections (CCSs) of ions and thus insights into their gas-phase structures. All IMS measurements were performed with a Bruker TIMS TOF instrument. TIMS is a type of the various IMS methods which can determine the ion mobilities at a very high resolution (~200). In TIMS, ions are

accumulated, and an electric field gradient (EFG) traps the ions against a constant flow of buffer gas (N_2). The difference in pressure (Δp) between the entry and exit of the TIMS tunnel is the source of this flow. Lowering the EFG results in ion elution according to their mobilities. In my experiments, Δp of 1.7 mbar, inverse mobility gap of 0.1 Vs/cm^2, ramp time of 500 ms, and accumulation time of 10 ms were used. Source conditions for electrospraying the ions in TIMS TOF were capillary voltage 5 kV, nebulizer 0.3 bar, dry gas 3.5 L/min, and dry temperature 200°C.

For the determination of the collision cross-section of the ions from TIMS, a calibration is necessary. Commercially available Agilent Tune Mix and the drift tube CCSs values (in N_2) published by Stow et al.[362] were as used for calibration. TIMS records inverse mobilities (1/k) of ions which were then converted to $^{TIMS}CCS_{N2}$.

5.4.1.8. DFT Method and Calculation of Collision Cross Sections.

This part was carried out by Papri Chabraborty and Dr. Marco Neumaier.

The quantum chemical calculations were performed with the TURBOMOLE package[363] with the BP86-functional[364, 365] and def2-SV(P)[366] basis set. For dispersion correction, the DISP3[367] method with Becke and Johnson damping (BJ-damping) was used.[368] Prior density-functional theory (DFT) calculations structures were generated manually in Avogadro[369] (version 1.2.0) and preoptimized with the Merck molecular force field MMFF94.[370-375]

We used the Mulliken population analysis as implemented in TURBOMOLE to assign partial charges on each atom. The atomic coordinates of the optimized DFT structures and the partial charges were used as input data for the IMoS 1.09[376] package in order to calculate Collision Cross Sections (CCSs) based on the trajectory method (TM). In IMoS, the interaction of the cucurbituril ions with the collision gas nitrogen is modeled with a Lennard-Jones (LJ)-type interaction plus an ion-induced dipole potential. Since nitrogen is anisotropic, the ion–quadrupole[377] interaction can also be taken into account. Based on the cucurbituril-nitrogen interaction potential, the scattering angle (χ) was calculated by a series of trajectory calculations, and the momentum transfer cross section ($^{calc}CCS_{N2}$) was obtained by numerical integration of χ.[378]

5.4.1.9. Data Analysis Details

For each of the considered analytes, the emission intensities from CB7-NBD as a function of the concentration of the salt was plotted. The overall distinguishability of different analytes was assessed and visualized: First, the curve distance between any two replicas based on the root mean squared difference of the emission intensities at the measured concentrations was quantified. Second, these distances into colored maps of pair-wise distance were translated separately for each salt.

5.4.2. Synthesis and characterization

5.4.2.1.   Chemical structures of non-covalent reporter dyes for CB7

2,7-dimethyldiazapyrenium iodide
(MDAP)

berberine chloride
(BC)
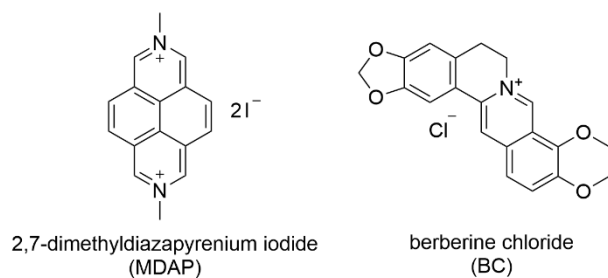
Figure 5.22 Chemical structures of reporter dyes for CB7.

5.4.2.2.   Synthesis of NBD-tetraethylene glycol-azide (NBD-TEG)
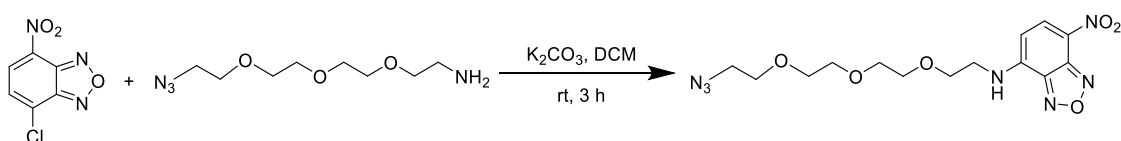
11-azido-3,6,9-trioxaundecan-1-amine (20.0 mg, 91.6 μmol, 18.2 μL) was added to a suspension of K_2CO_3 (28.5 mg, 206.2 μmol) in 2 mL dry DCM under nitrogen and stirred for 10 min. Subsequently, the solution of NBD-chloride (27.4 mg, 137.5 μmol) in 1 mL dry DCM was added and keep the reaction stirring at room temperature for 3 h under nitrogen. The solvent was removed by rotary evaporation and the crude product was purified by a column chromatography (gradient 0-50 % ethyl acetate in hexane) to give a brown viscous liquid of NBD-TEG (25.0 mg, 65.6 μmol, 71.6 %). ^{1}H NMR (500 MHz, CDCl$_3$) δ 8.52 (d, J = 8.6 Hz, 1H), 7.03 (br, 1H), 6.21 (d, J = 8.6 Hz, 1H), 3.93 – 3.88 (t, J = 4.8 Hz, 2H), 3.74 (s, 12H), 3.44 – 3.39 (t, J = 4.8 Hz, 2H). ^{13}C NMR (126 MHz, CDCl$_3$) δ 144.5, 144.3, 144.1, 136.6, 124.2, 98.8, 70.9, 70.9, 70.8, 70.7, 70.2, 68.3, 50.8, 43.9 ppm. ESI-MS: Calcd. For [M+Na]$^+$: 404.1289; found: 404.1337.
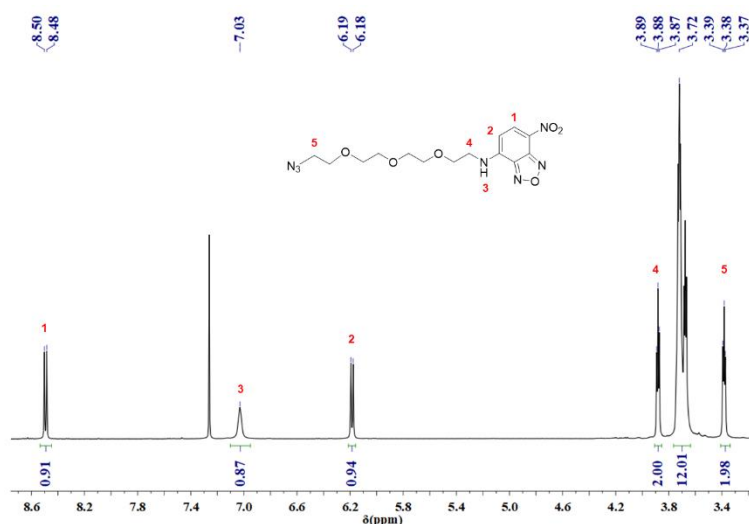
Figure 5.23 ^{1}H NMR spectrum (500 MHz) of NBD-TEG in CDCl$_3$.
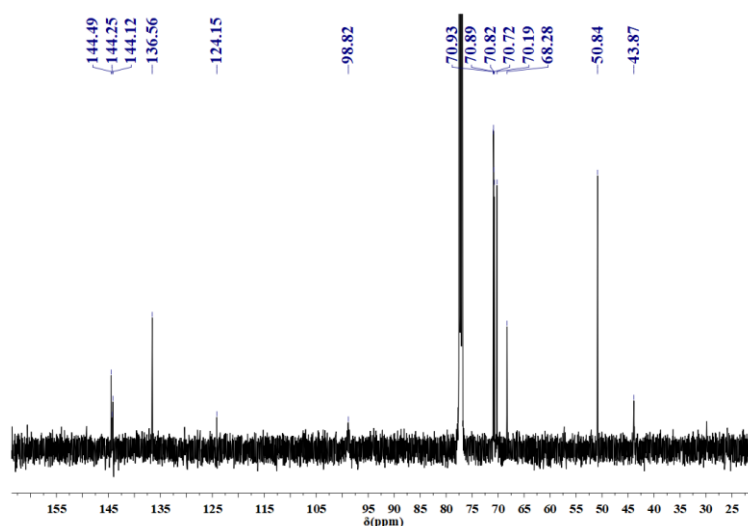
Figure 5.24 ^{13}C NMR spectrum (126 MHz) of NBD-TEG in CDCl$_3$.
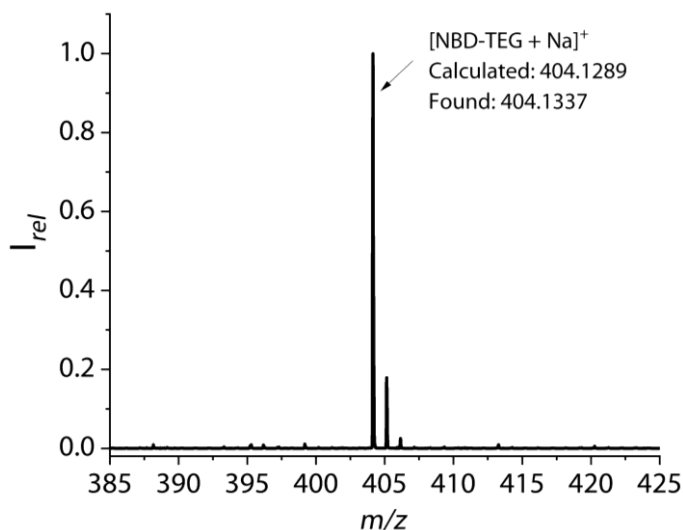
Additional information on details is available *via* the Chemotion repository:

https://dx.doi.org/10.14272/reaction/SA-FUHFF-UHFFFADPSC-ZTJNWVOHDV-UHFFFADPSC-NUHFF-NUHFF-NUHFF-ZZZ

5.4.2.3. Synthesis of cucurbit[7]uril-TEG-NBD conjugate (CB7-NBD)
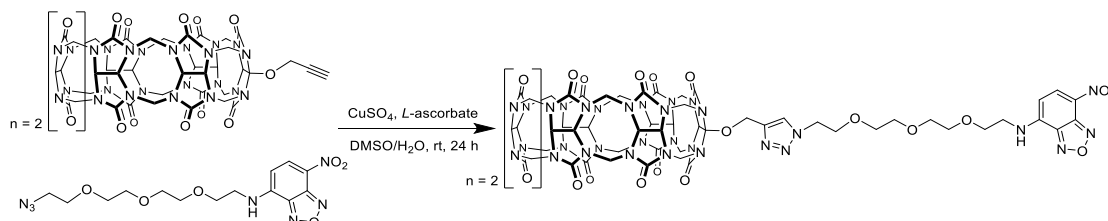
CB7-(Opr)$_1$ (20.0 mg, 16.4 μmol) and NBD-TEG (9.4 mg, 24.7 μmol) were dispersed in 3 mL DMSO. Then, sodium *L*-ascorbate (3.3 mg, 16.4 μmol) was added into 55% DMSO aqueous solution (2 mL) containing CuSO$_4$ (2.6 mg, 16.4 μmol). Both solutions were mixed, and the reaction was kept stirring at room temperature for 24 h. Afterwards, 10 mL MeOH was added to the mixture, and the resulting precipitate was washed with MeOH (3 x 35 mL). Drying under 80℃ in the oven and afforded a dark

solid. The product was purified by HPLC (C18, v (acetonitrile) / v (0.1% TFA aqueous) = 35%/65%) and obtained the product as yellow flappy solid after freeze-drying (3.6 mg, 1.9 µmol, 27 %). ESI-MS: [M + Na]+ Calcd. for: 1620.486; found: 1620.483. Due to the complex structure, a precise peak assignment by ^{1}H and ^{13}C NMR was not possible.
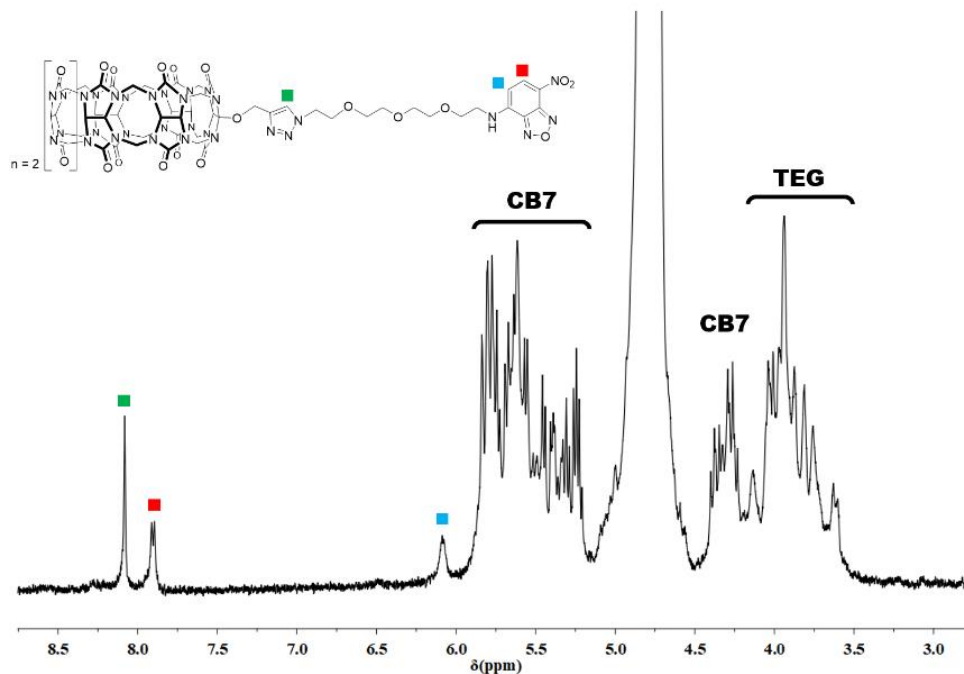
Figure 5.25 ^{1}H NMR spectrum (500 MHz) of CB7-NBD in D$_2$O.
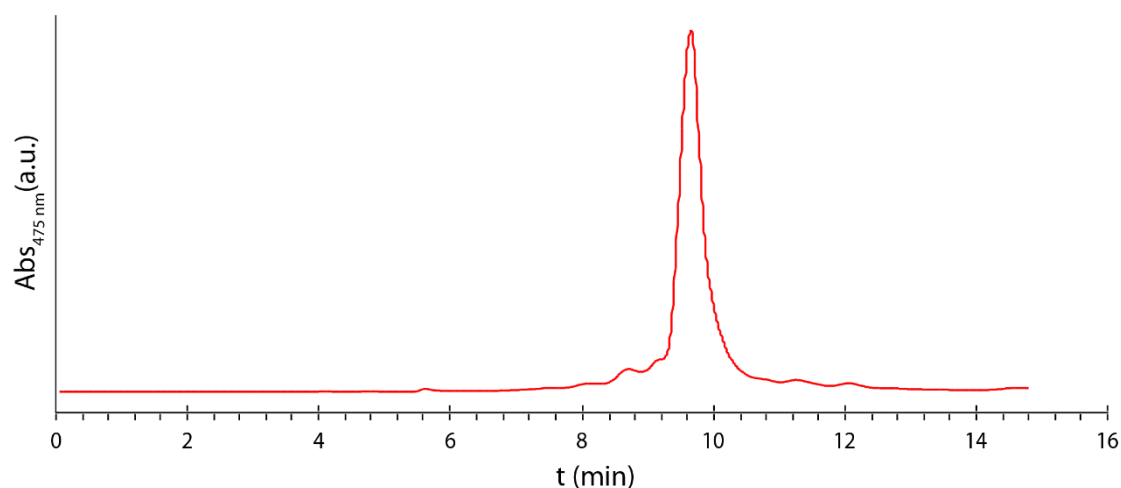
Figure 5.26 Analytical HPLC trace of CB7-NBD recorded at 475 nm using a mixture of 35 % acetonitrile/65 % 0.1 % TFA aqueous as eluent.

Additional information on details is available *via* the Chemotion repository:

https://dx.doi.org/10.14272/reaction/SA-FUHFF-UHFFFADPSC-ICDIQORYLK-UHFFFADPSC-NUHFF-NUHFF-NUHFF-ZZZ

5.5. Supplementary data

5.5.1.Binding affinities for analytes with CB7-NBD in water and 1X PBS
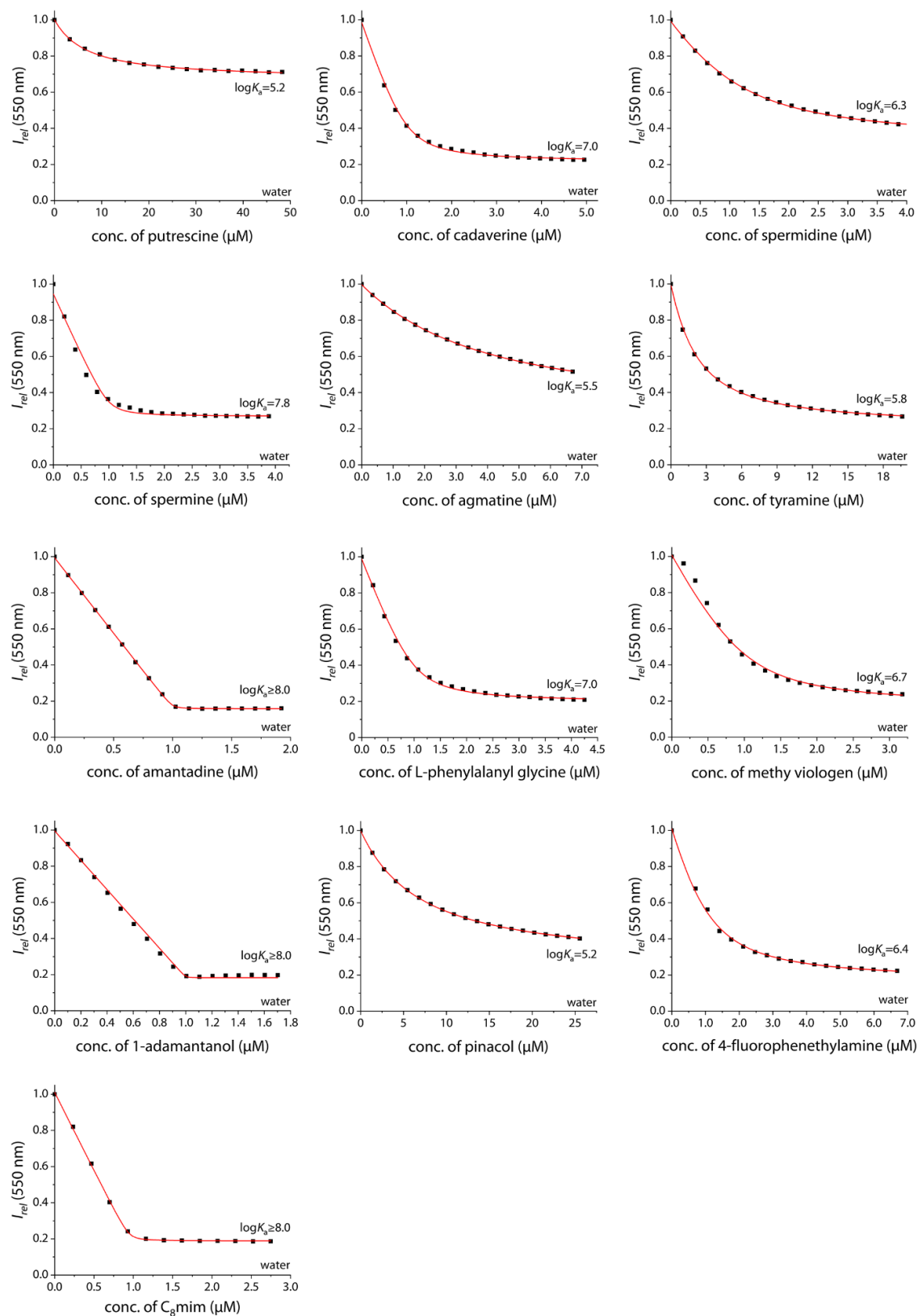
Figure 5.27 Fitting plot of normalized emission intensity at 550 nm $(\lambda_{ex} = 475$ nm) of 1 μM CB7-NBD in water at 25°C, upon addition of analytes (except nandrolone).
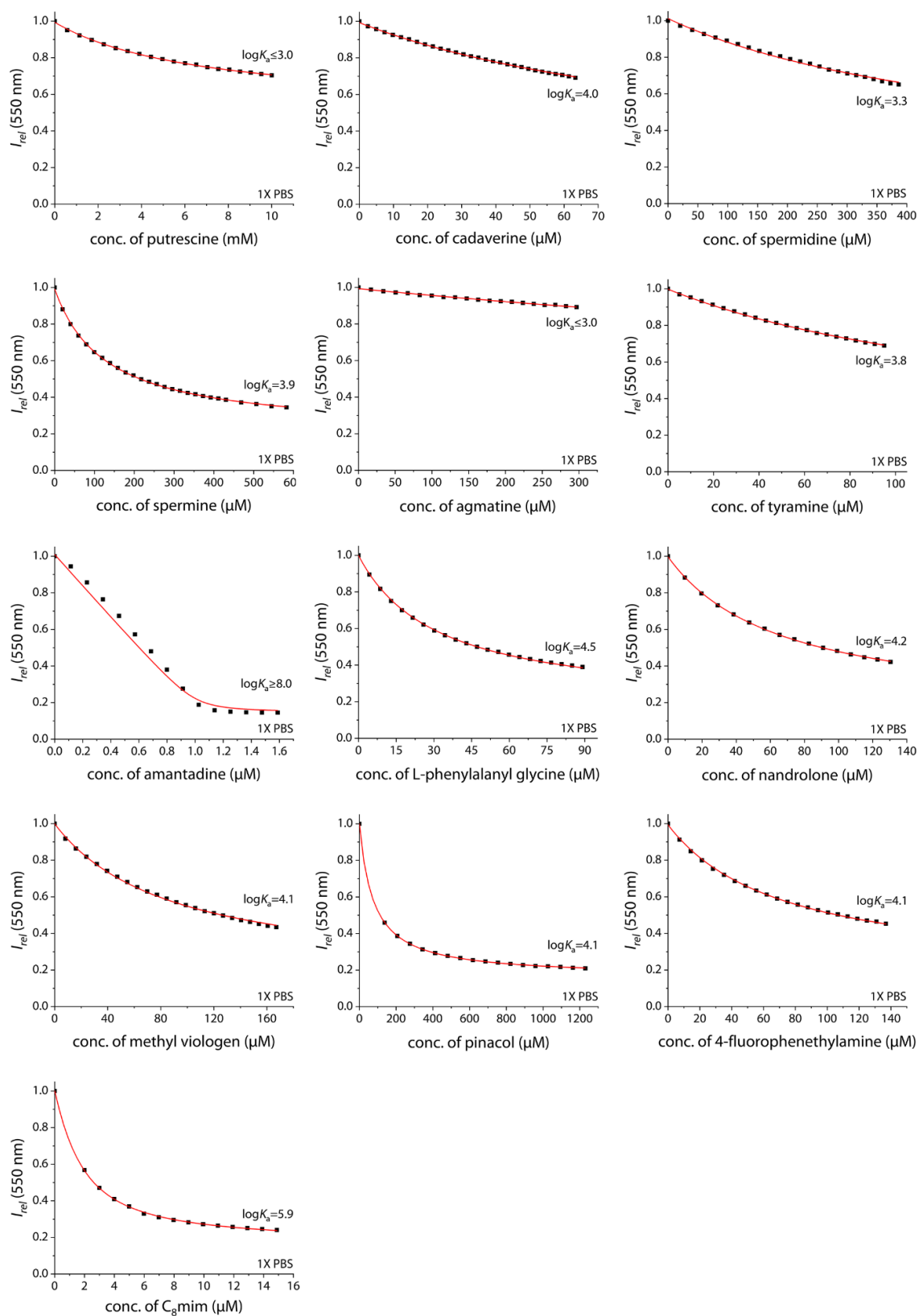
Figure 5.28 Fitting plot of normalized emission intensity at 550 nm $(\lambda_{ex} = 475$ nm) of 1 μM CB7-NBD in 1X PBS at 25°C, upon addition of aliquots of the analyte.

5.5.2.Emission-based titration of salts to CB7-NBD with analytes
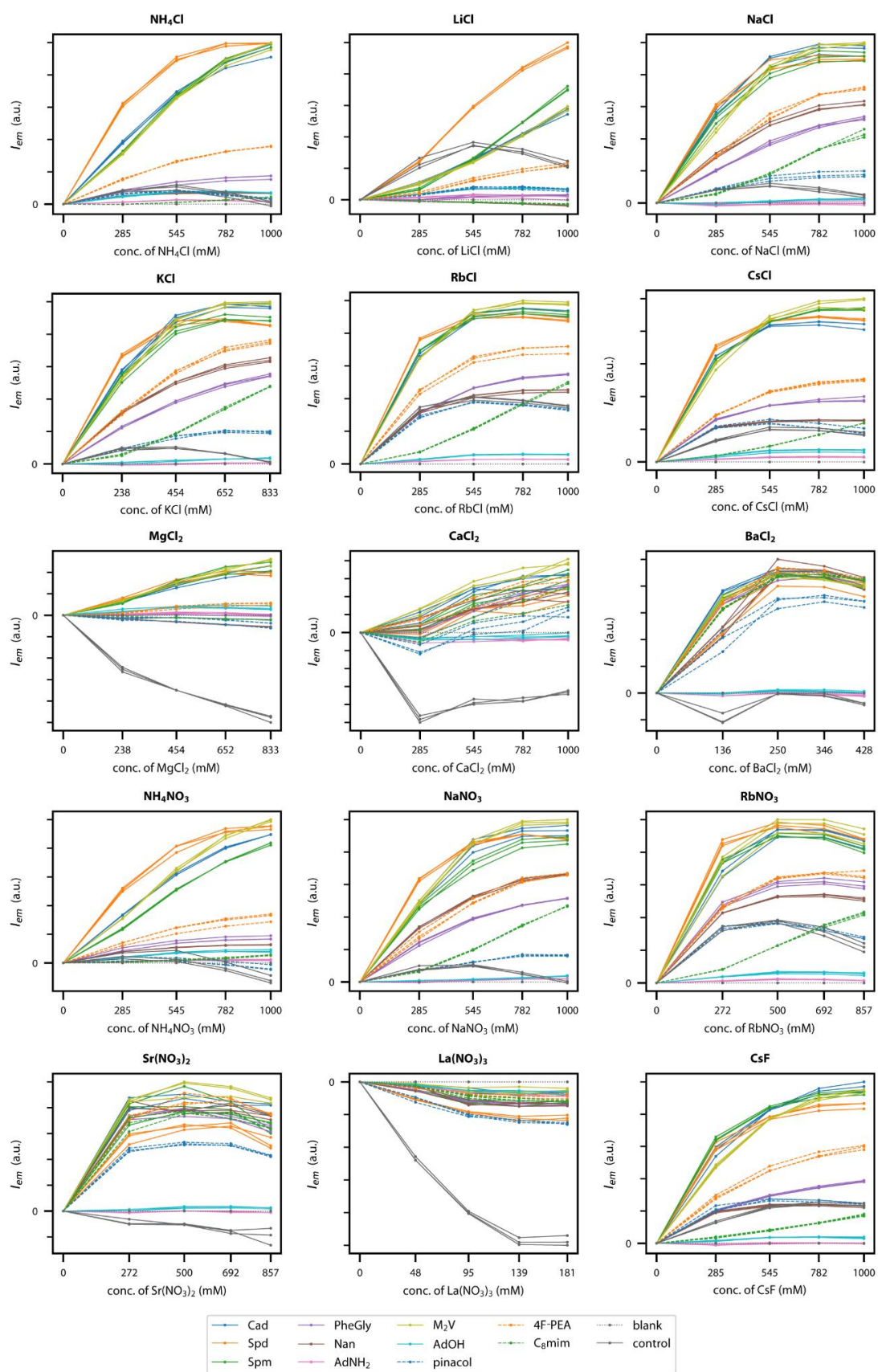
Figure 5.29 Plot of the emission intensity at 550 nm of 1 μM CB7-NBD in the presence of 200 μM analytes as a function of the concentration of different salts in 10 mM PB (λ_{ex} = 475 nm).

5.5.3. PCA plots for analytes resulting from salt-addition assays
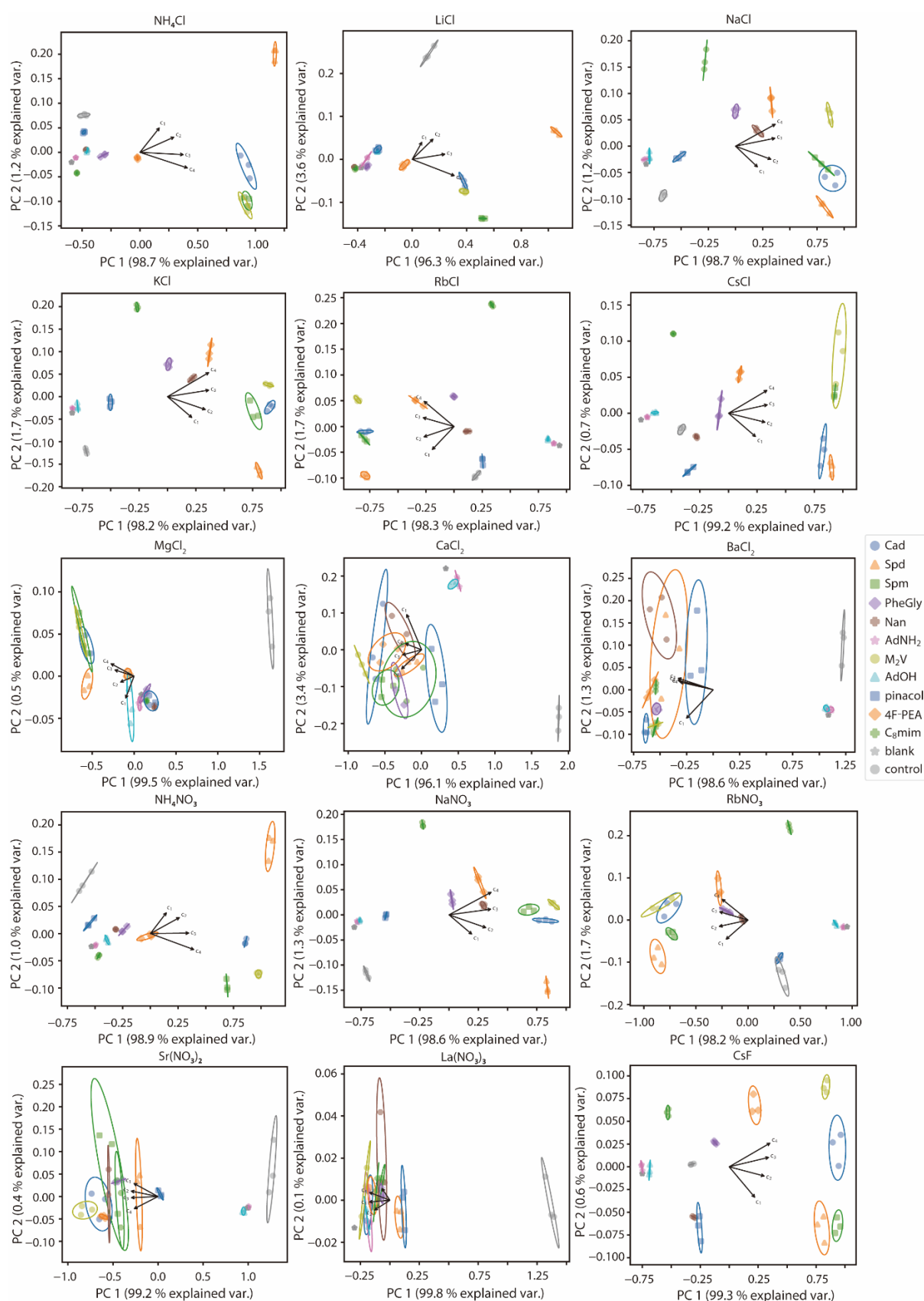
Figure 5.30 PCA plot with 95% confidence ellipses resulting from the emission intensity at 550 nm (λ_{ex} = 475 nm) as a function of the concentration of salt with 1 µM CB7-NBD in 10 mM PB spiked with 200 µM analytes.

5.5.4.Pairwise plot of the difference between analytes by using salt-addition assay
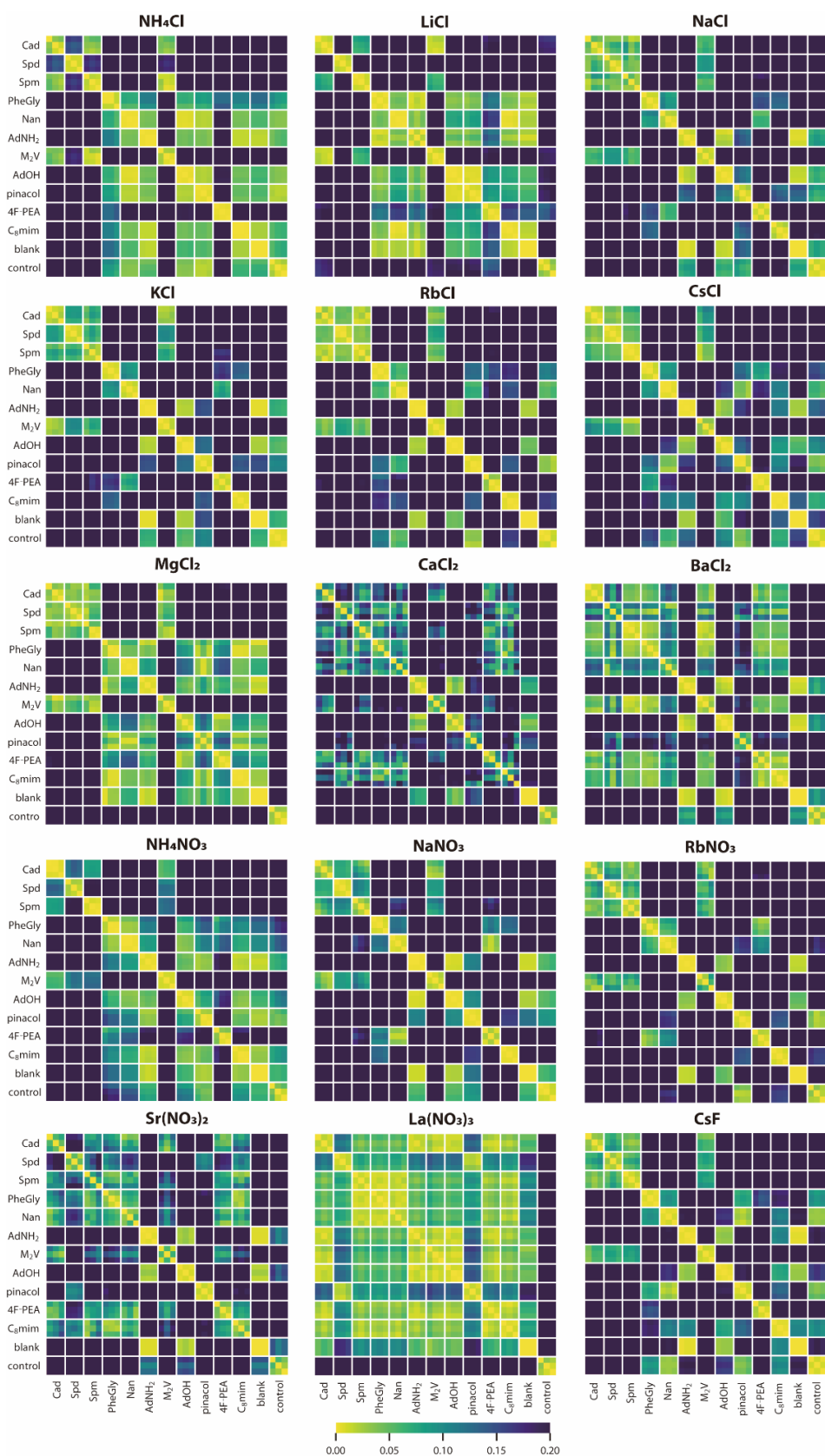
Figure 5.31 Pairwise pattern of difference between emission responses at 550 nm of the three individual replicas for each analyte (200 μM) in the presence of 1 μM CB7-NBD with the titration of salt in 10 mM PB (λ_{ex} = 475 nm).

5.5.5.Emission-based titration of salts to CB7-NBD with biorelevant amines
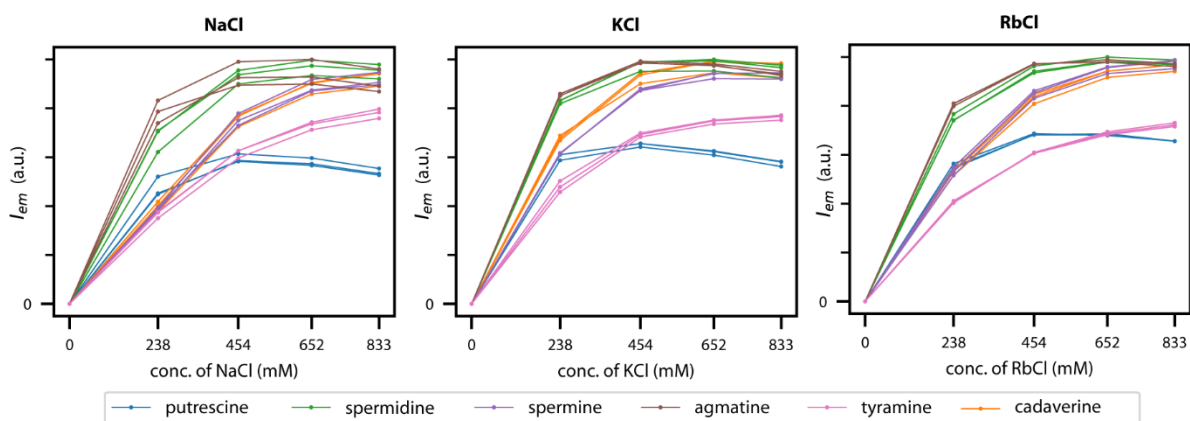
Figure 5.32 Plot of the emission intensity at 550 nm of 1 μM CB7-NBD in the presence of 500 μM amines as a function of the concentration of different salts in 10 mM PB (λ_{ex} = 475 nm).

5.5.6.PCA plots for biorelevant amines resulting from salt-addition assays
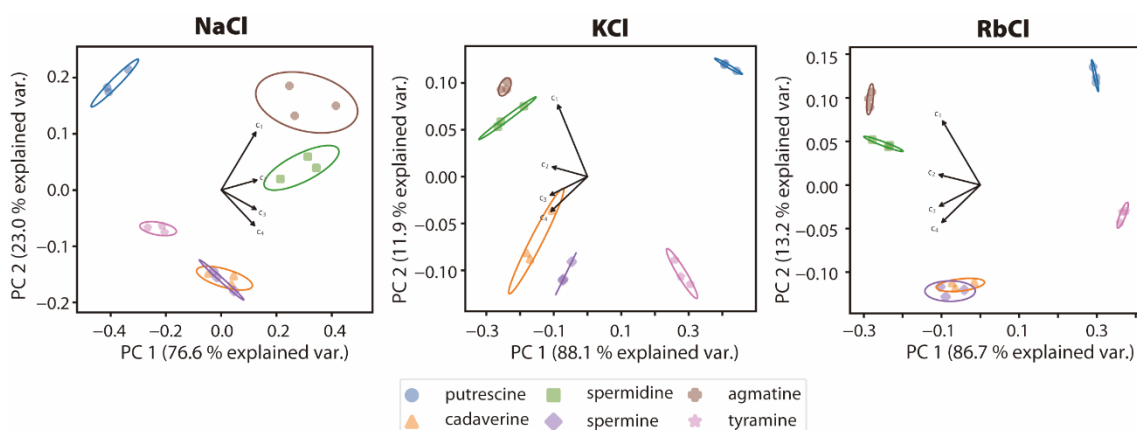
Figure 5.33 PCA plot with 95% confidence ellipses resulting from the emission intensity at 550 nm (λ_{ex} = 475 nm) as a function of the salt concentration with 1 μM CB7-NBD in 10 mM PB spiked with 500 μM amines.

5.5.7. Pairwise plot of the difference between amines by using salt-addition assay
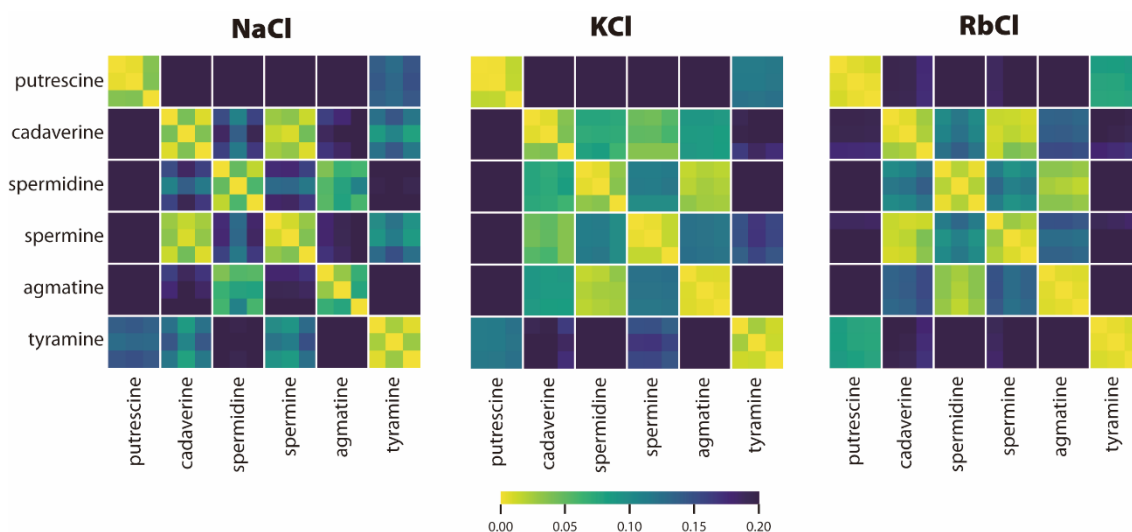
Figure 5.34 Pairwise pattern of difference between emission responses at 550 nm of the three individual replicas for each amine (500 μM) in the presence of 1 μM CB7-NBD with the titration of salt in 10 mM PB (λ_{ex} = 475 nm).

5.5.8. Emission-based titration of NaCl to CB7-NBD with analytes in biofluids
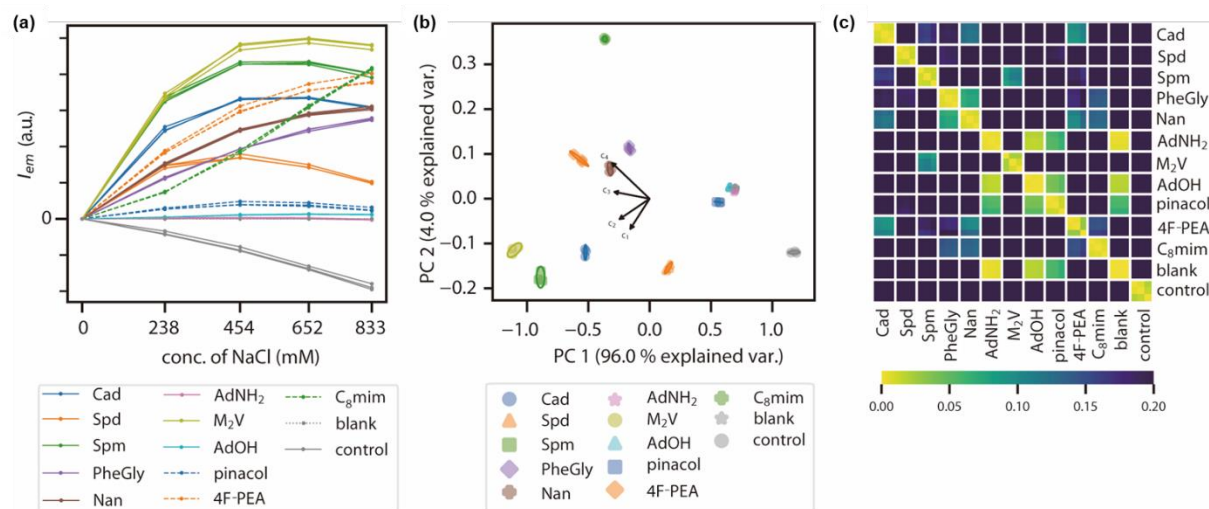
Figure 5.35 (a) Plot of the emission intensity, (b) PCA plot with 95% confidence ellipses resulting from the emission intensity at 550 nm of 1 μM CB7-NBD in the presence of 200 μM analytes as a function of the concentration of NaCl in surine (λ_{ex} = 475 nm) and (c) pairwise pattern of difference between emission responses of the three individual replicas for each analyte.
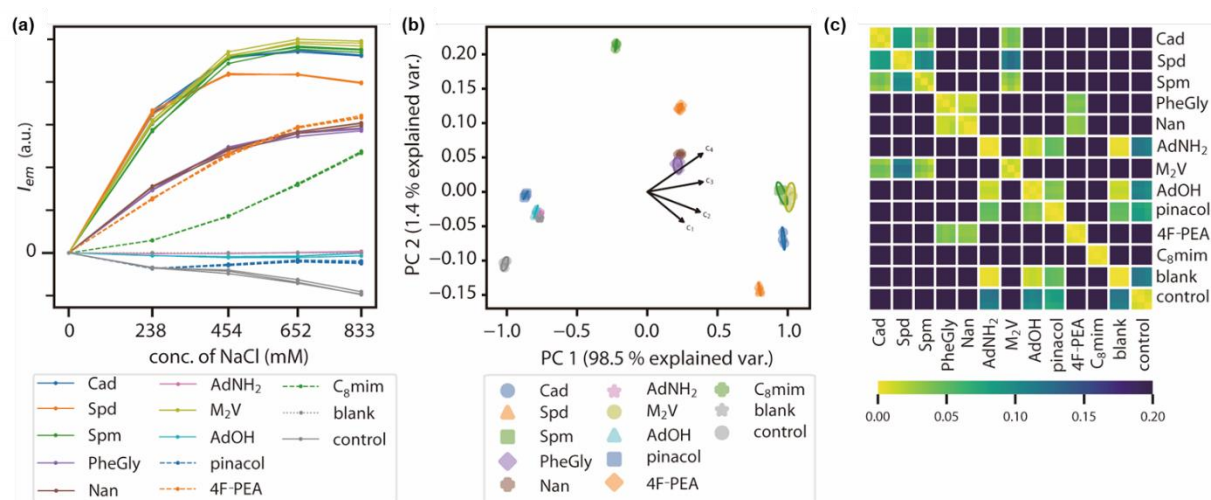
Figure 5.36 (a) Plot of the emission intensity, (b) PCA plot with 95% confidence ellipses resulting from the emission intensity at 550 nm of 1 μM CB7-NBD in the presence of 200 μM analytes as a function of the concentration of NaCl in artificial saliva (λ_{ex} = 475 nm) and (c) pairwise pattern of difference between emission responses of the three individual replicas for each analyte.

5.5.9. Geometry-optimized molecular structures and corresponding DFT calculations

The part was collaborated with Dr. Marco Neumaier.

The DFT calculations were performed without and with dispersion correction and generally found more compact structures in the latter case when considering the same topology. This difference is least pronounced for the pure cucurbit[n]uril ions [CB6·Na]$^+$ and [CB7·H]$^+$ with differences in the collision cross sections (CCSs) of below 0.5%. For the studied CB7-NBD structures and for the intermolecular complexes CB7-NBD⊃cadaverine and CB7-NBD⊃1-adamantanol, the CCSs of the dispersion corrected structures (considering the same topology) can be smaller by up to ~6%. Similar to other studies[291], it was also found a different DFT stability order in some cases when accounting for dispersion (*e.g.,* for doubly and singly protonated CB7-NBD⊃cadaverine) and inclusion complexes are typically more favored compared to exclusion complexes. Studying the influence of dispersion is not the scope of this work and will possibly be addressed in a future publication. Therefore, I focus on the dispersion corrected structures, which also show better agreement with experimentally determined CCSs from the ion mobility measurements. Note that due to the flexibility and size of the molecule, it is not readily possible to sample the whole potential energy surface. Therefore, I focus more on the differences in topologies (*e.g.,* folded *versus* open/unfolded structures) with respect to CCSs.

IMoS TM calculations in which the ion–quadrupole interaction was explicitly taken into account led to CCSs being consistently smaller (by ~6-8 %) than the pure LJ (plus ion-induced dipole) potential based CCSs, also showing overall a better agreement with the experimental CCSs of the gas-phase structures. Therefore, the results based on the additional inclusion of the ion–quadrupole interaction will be shown only.

5.5.9.1.   [CB6·Na]$^+$ and [CB7·H]$^+$

For [CB6·Na]$^+$ (Figure 5.37 (a)) and [CB7·H]$^+$ (Figure 5.37 (b)), which were chosen as test systems, a good agreement of ~5-6% between the experimentally determined N$_2$ collision cross sections ($^{TIMS}CCS_{N2}$) (Figure 5.38) and the calculated CCSs ($^{calc}CCS_{N2}$) was found with $^{calc}CCS_{N2}$ being somewhat larger (Table S2).
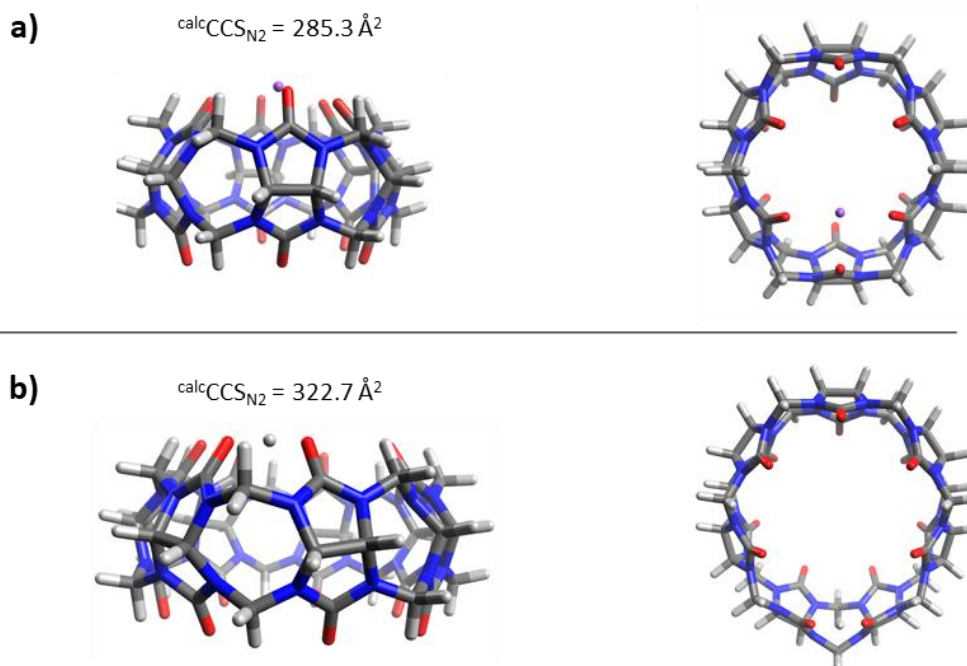
Figure 5.37 Side views (left) and top views (right) of (a) [CB6·Na]$^+$ and (b) [CB7·H]$^+$
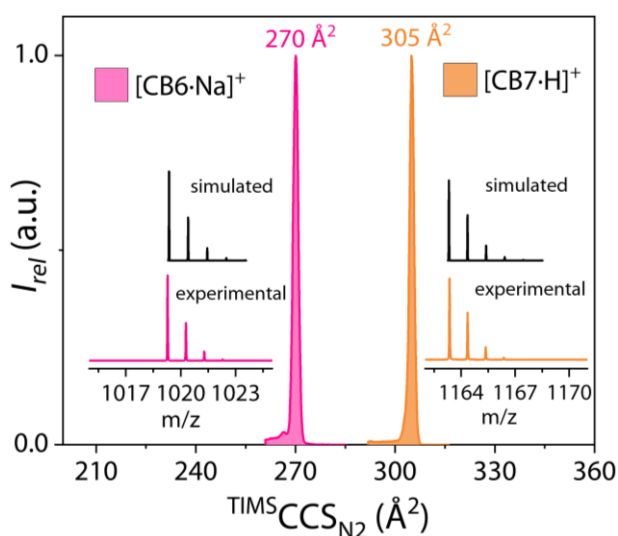
Figure 5.38 Mass spectra and ion mobilogram of [CB6·Na]$^+$ and [CB7·H]$^+$.

5.5.9.2.   [CB7-NBD·Na]$^+$ and [CB7-NBD·H]$^+$

The gas-phase structures of [CB7-NBD·Na]$^+$ and [CB7-NBD·H]$^+$ unfolded (Figure 5.39) and folded (Figure 5.40) structures can be ruled out based on the high DFT energies and based on the large $^{calc}CCS_{N2}$ of ~490Å^2 and ~385Å^2 which is ~45% and ~15% larger than the corresponding experimental values (Table S2). The best agreement with $^{TIMS}CCS_{N2}$ was found for an inclusion type complex (Figure 5.41) which also exhibits the lowest DFT energy. Note that all structures were fully geometry optimized, and structures of [CB7-NBD·Na]$^+$ and [CB7-NBD·H]$^+$ of the same topology cannot readily be compared, *i.e.,* they can differ in relative DFT energy and to some extent in topology and consequently CCSs as well.
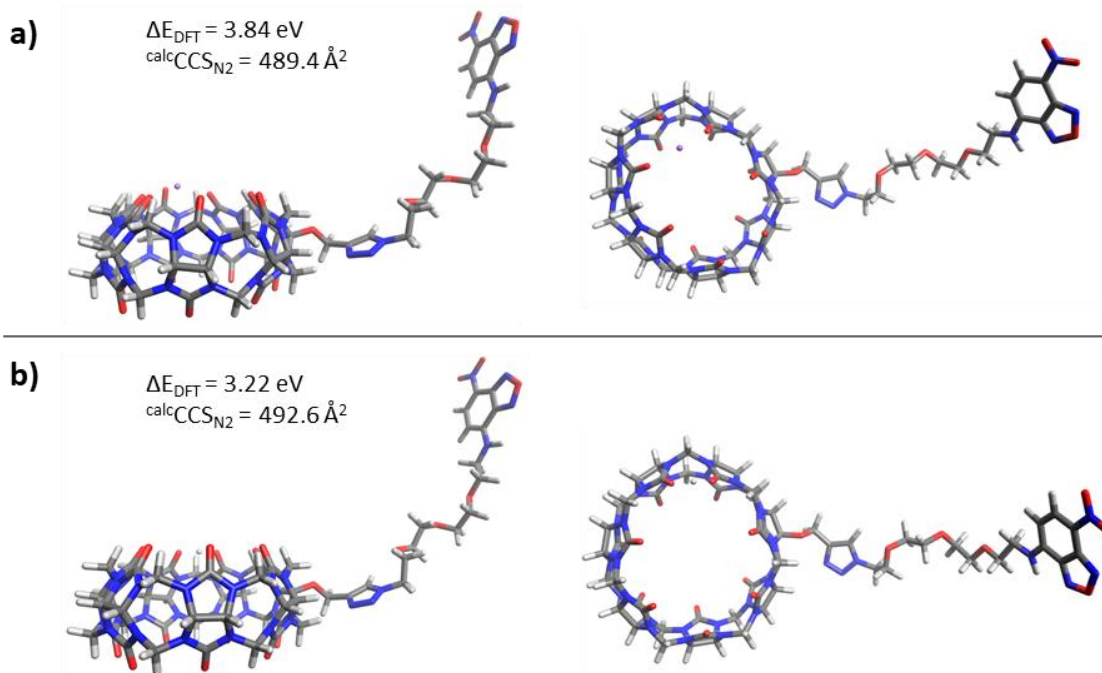
Figure 5.39 Side views (left) and top views (right) of the unfolded complexes a) [CB7-NBD·Na]$^+$ (3.84 eV) and b) [CB7-NBD·H]$^+$ (3.22 eV).
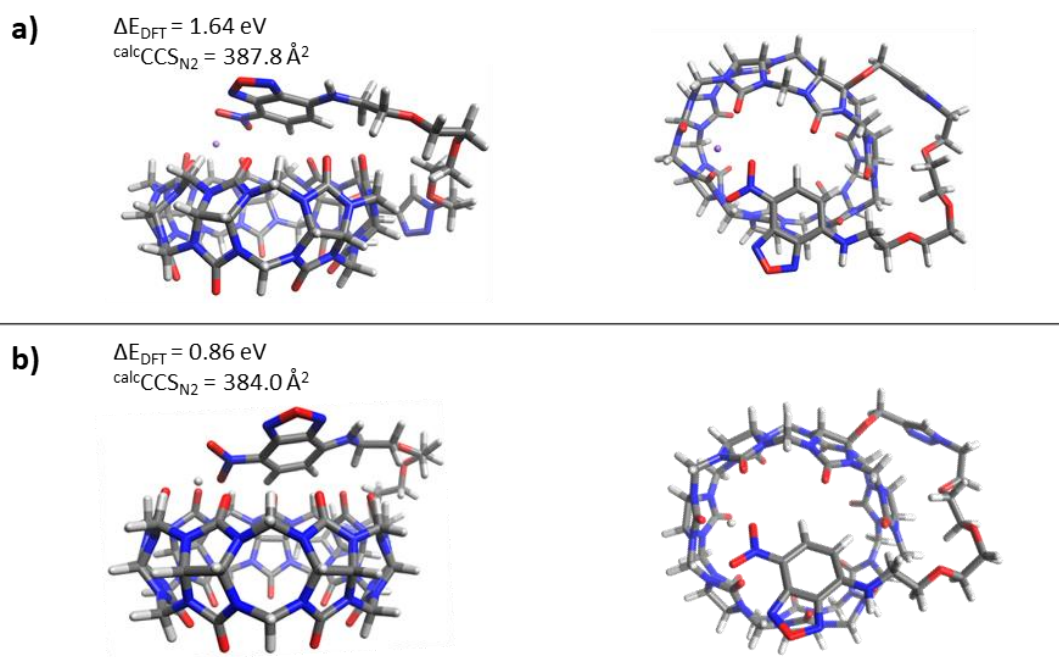
Figure 5.40 Side views (left) and top views (right) of the folded complexes (a) [CB7-NBD·Na]$^+$ (1.64 eV) and (b) [CB7-NBD·H]$^+$ (0.86 eV).
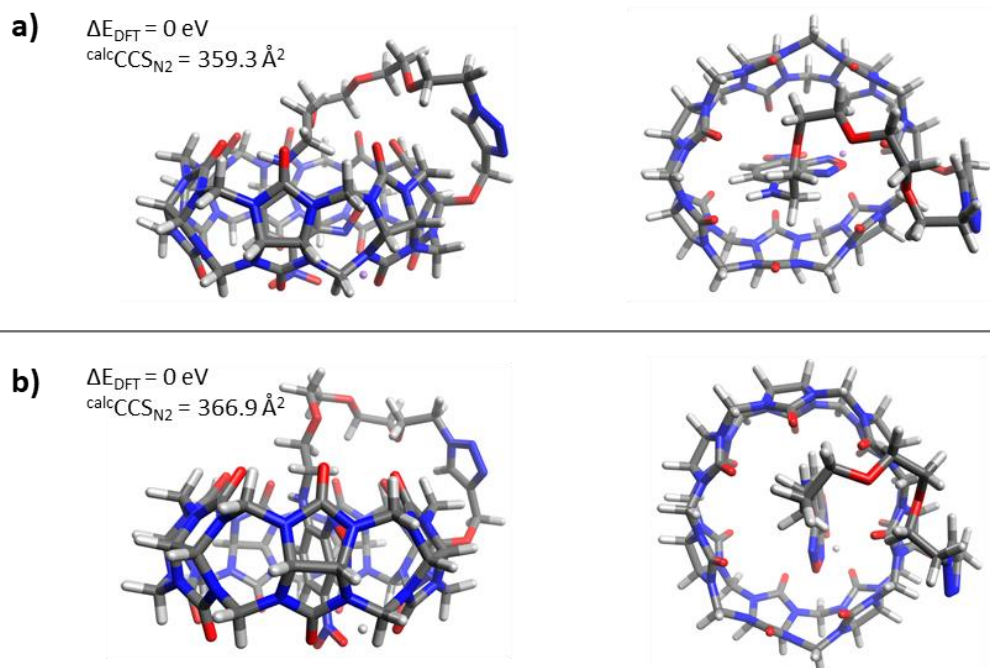
Figure 5.41 Side views (left) and top views (right) of the inclusion complexes (a) [CB7-NBD·Na]$^+$ (0 eV) and (b) [CB7-NBD·H]$^+$ (0 eV).
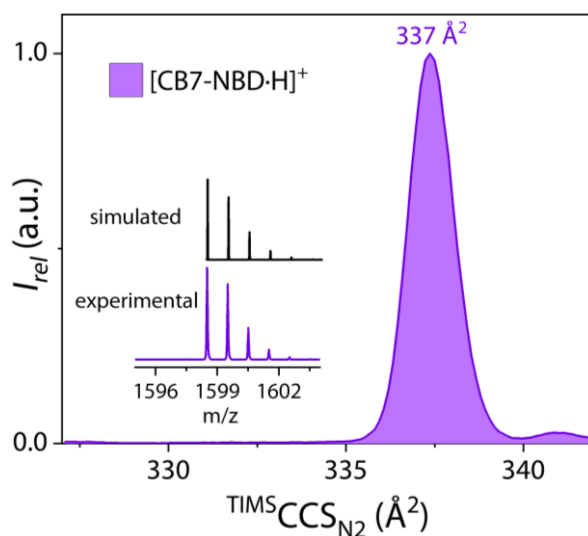
Figure 5.42 Mass spectra and ion mobilogram of [CB7-NBD·H]$^+$.

5.5.9.3. [CB7-NBD⊃cadaverine·2H]$^{2+}$

For [CB7-NBD⊃cadaverine·2H]$^{2+}$, two structures were found that have almost the same $^{calc}CCS_{N2}$ showing very good agreement with the experiment (~3%) and that are close in energy (Figure 5.43 (a) and (b)). As the CCSs resolution of the timsTOF mass spectrometer is not sufficient to distinguish between these two structures, a mixture of both or only one of the structures might be present in the gas phase. An inclusion complex, as shown in Figure 5.43 (c), can be ruled out based on $^{calc}CCS_{N2}$ and ΔE_{DFT}.

a) $\Delta E_{DFT} = 0$ eV
$^{calc}CCS_{N2} = 387.7$ Å^2

b) $\Delta E_{DFT} = 0.16$ eV
$^{calc}CCS_{N2} = 389.5$ Å^2

c) $\Delta E_{DFT} = 0.67$ eV
$^{calc}CCS_{N2} = 426.9$ Å^2
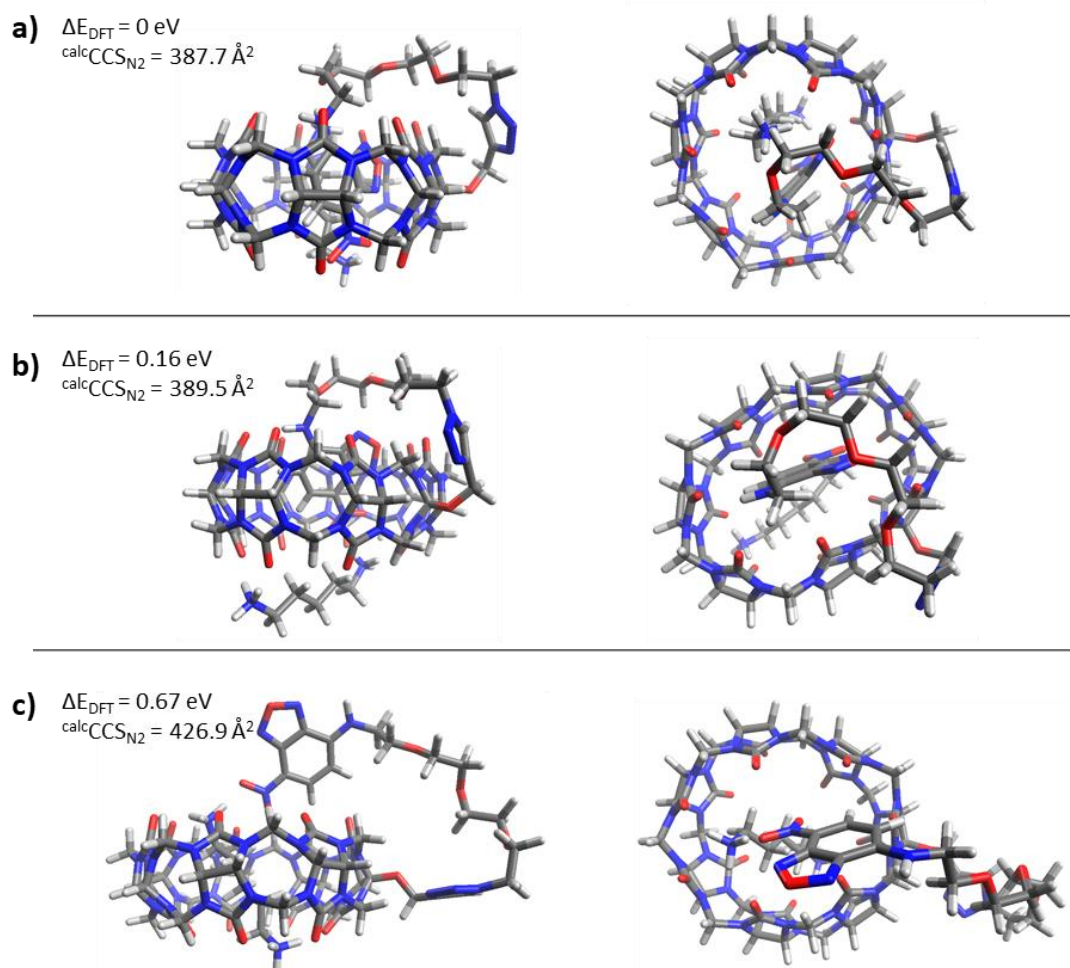
Figure 5.43 Side views (left) and top views (right) of the a) dual inclusion (0 eV), b) exclusion (0.16 eV) and c) inclusion complex (0.67 eV) of [CB7-NBD⊃cadaverine·2H]$^{2+}$.

5.5.9.4.   [CB7-NBD⊃cadaverine·H]$^+$

For [CB7-NBD⊃cadaverine·H]$^+$ an exclusion type complex, as shown in Figure 5.44 (b), was found to be most stable, and its calculated CCSs of 381.0 Å^2 show a reasonably good agreement with the experimental value (348.9 Å^2). A dual inclusion complex (Figure 5.44 (a)) exhibits higher DFT energy (0.50 eV) but shows a similarly good agreement with the experimental CCSs. See Figure 5.45 for ion mobility spectra and experimental CCS. An inclusion complex where the NBD moiety is replaced by [cadaverine·H]$^+$ (Figure 5.44 (c)) can clearly be ruled out as a gas-phase structure as it shows a much larger $^{calc}CCS_{N2}$ (413.1 Å^2) and a considerably higher relative DFT energy of 1.22 eV.
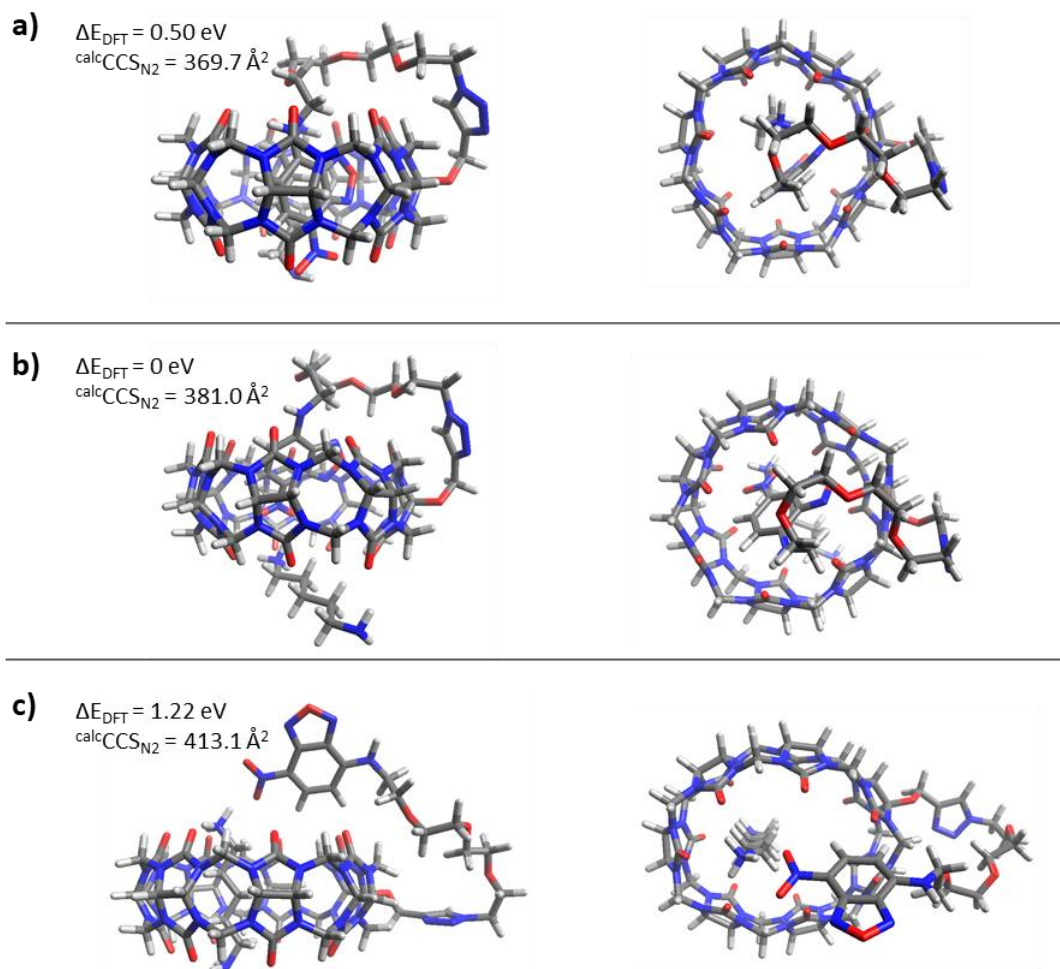
Figure 5.44 Side views (left) and top views (right) of the a) dual inclusion (0.50 eV), b) exclusion (0 eV) and c) inclusion complex (1.22 eV) of [CB7-NBD⊃cadaverine·H]⁺.
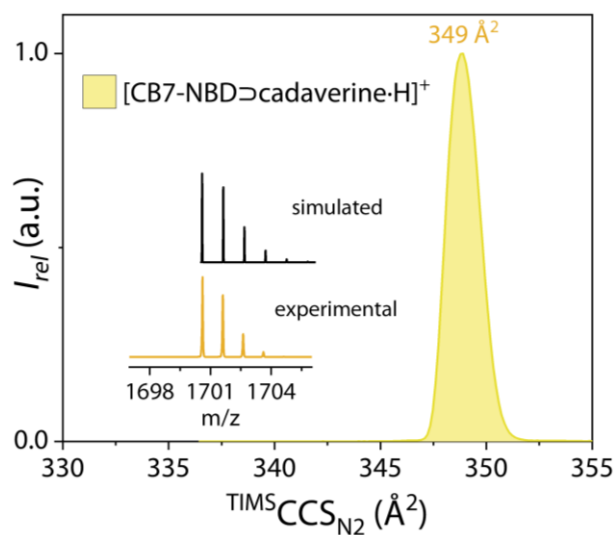
Figure 5.45 Mass spectra and ion mobilogram of [CB7-NBD⊃cadaverine·H]⁺.

5.5.9.5. [CB7-NBD·Na⊃AdOH]+

For [CB7-NBD·Na⊃AdOH]+, the best possible agreement in terms of CCSs was found for an exclusion complex, as shown in Figure 5.46 (a). This structure also exhibits higher stability compared to the inclusion complex (Figure 5.46 (b)).

a)
$\Delta E_{DFT} = 0$ eV
$^{calc}CCS_{N2} = 386.7$ Å^2

b)
$\Delta E_{DFT} = 0.71$ eV
$^{calc}CCS_{N2} = 395.4$ Å^2
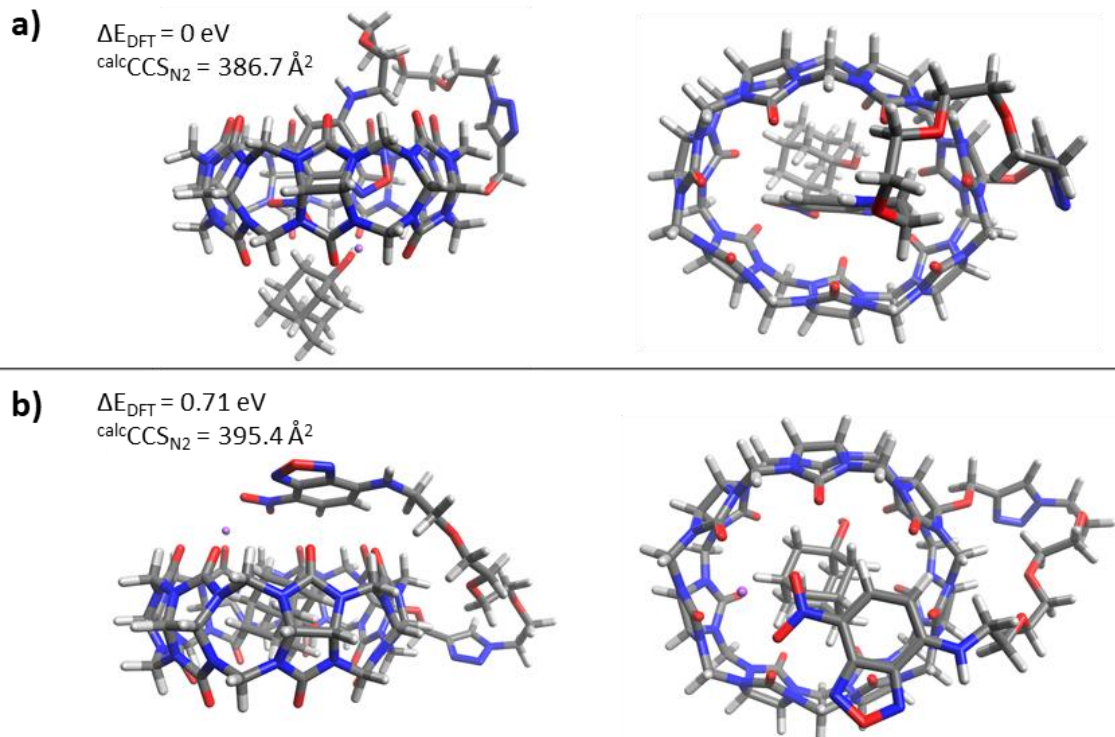
Figure 5.46 Side views (left) and top views (right) of the a) exclusion (0 eV) and b) inclusion complex (0.71 eV) of [CB7-NBD·Na⊃AdOH]+.
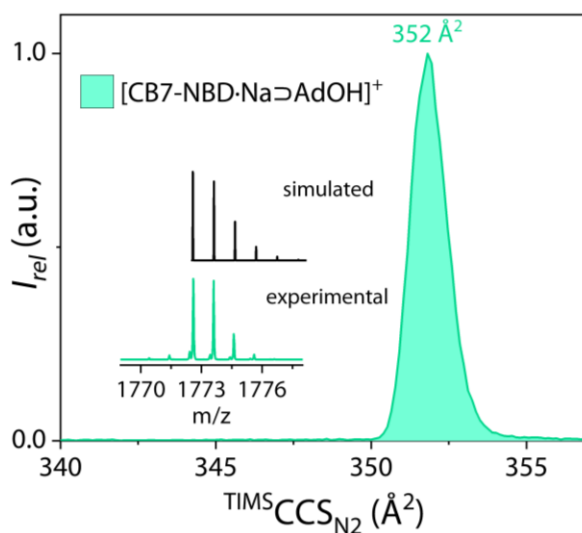
Figure 5.47 Mass spectra and ion mobilogram of [CB7-NBD·Na⊃AdOH]+.

127

5.5.9.6. [CB7-NBD·Na⊃AdNH₂·H]²⁺

For [CB7-NBD·Na⊃amandatine·H]²⁺, best agreement with the experimental collision cross-section ($^{TIMS}CCS_{N2}$ = 386.1 Å²) is found within ~4% for exclusion complexes, whereas the structure shown in Figure 5.48 (a) also exhibits the lowest DFT energy. The inclusion type complex (Figure 5.48 (c)) has a larger $^{calc}CCS_{N2}$ of 419.4 Å² which is ~9% larger compared to the experimental value and also exhibits higher DFT energy (0.63 eV).
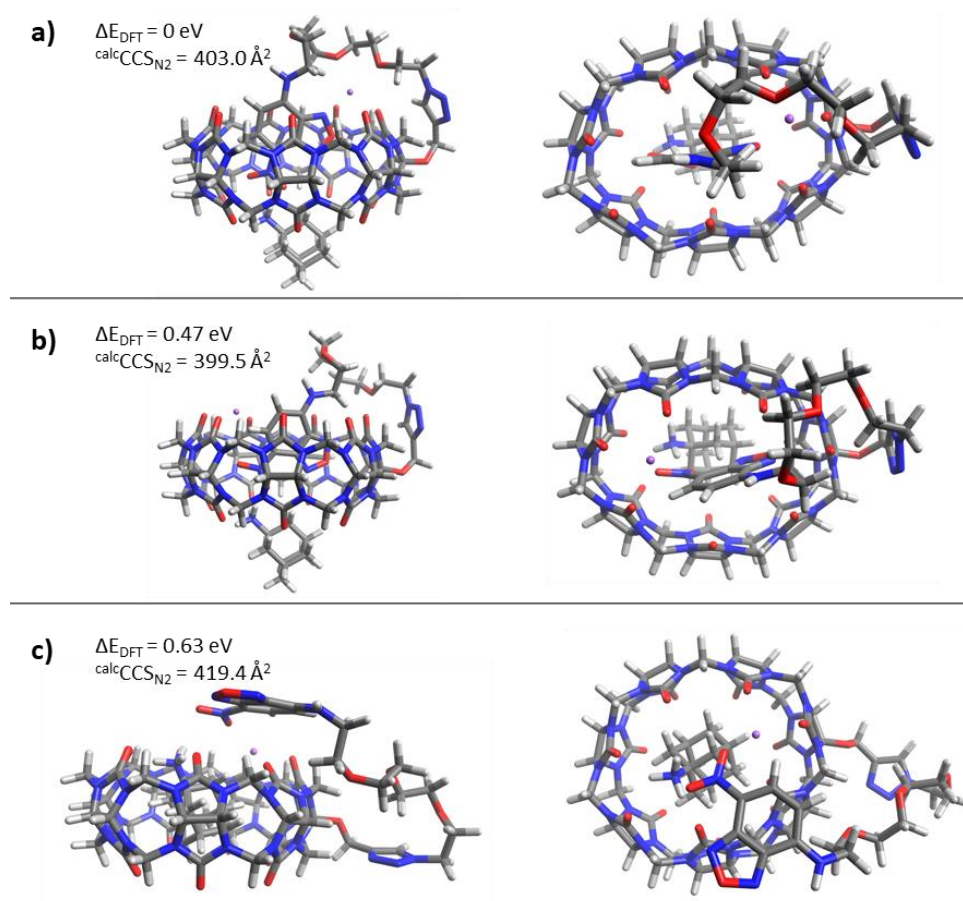
Figure 5.48 Side views (left) and top views (right) of the two exclusion complexes a) (0 eV) and b) (0.47 eV) and c) inclusion complex (0.63 eV) of [CB7-NBD·Na⊃AdNH₂·H]²⁺.
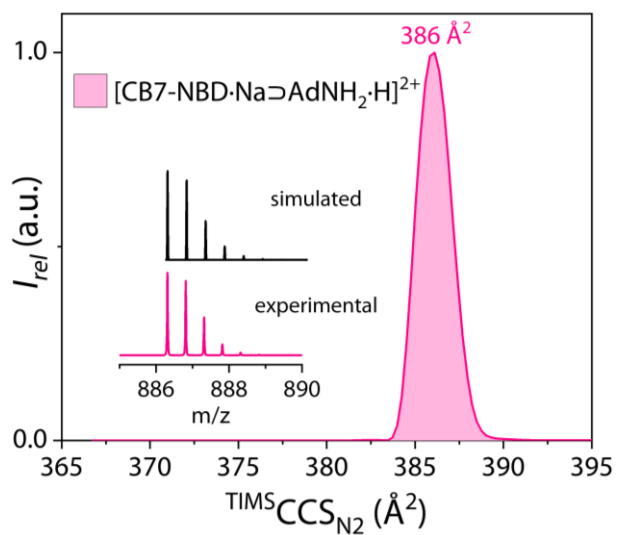
Figure 5.49 Mass spectra and ion mobilogram of $[CB7\text{-}NBD \cdot Na \supset AdNH_2 \cdot H]^{2+}$.

6. Conclusion and outlook

Cucurbit[*n*]urils represent one of the most attractive macrocyclic receptors that can be used for molecular sensing and imaging applications due to its specific binding affinity to a broad range of guests and excellent physical and chemical properties. The well-established IDA-based chemosensor consisting of CB*n* and reporter dyes is a powerful tool for fluorescence-based sensing of biologically relevant small molecules. However, a major drawback of CB*n*-based chemosensors is the inevitable dissociation of their host-guest complexes in the presence of cations, *e.g.,* in buffers or biofluids. My thesis aims to address this problem by designing and characterizing novel CB*n*-based chemosensors that have improved salt-resistance and are thus able to overcome current limiting obstacles that exist for the use of this class of macrocycles as future chemosensors.

In chapter 4, unimolecular covalent CB7-dye conjugates with both lengths of the tethered linker (TEG and HEG) were synthesized and characterized. Furthermore, their potential and advantages for sensing application in saline media and biofluids are presented. Berberine was chosen as the reporter dye because of the strong emission enhancement observed upon CB7-binding and the possibility for its chemical modification, which is required for covalent etherification to yield CB7-dye conjugates. The macrocyclic CB7-berberine conjugate was successfully prepared *via* copper-catalyzed cycloaddition between the CB7-alkyne and the azide-terminated berberine-linker, which allowed covalently tethering of the dye at the periphery of CB7. The conformation of the resulting CB7-BC conjugates was characterized as a unimolecular self-capsulated structure by ion mobility experiments in the gas phase and by photophysical measurements in the solution phase. Regarding their stability in high-salt media, both conjugates showed good resistance to cation- and dilution-induced disassembly, which is typically observed in previously reported CB7⊃BC or CB7⊃MDAP pairs. Importantly, the CB7-dye conjugate can be used to detect high-affinity analytes, *e.g.,* nortestosterone (nandrolone) and adamantyl derivatives, as confirmed by NMR and photophysical technology.

Furthermore, the binding kinetics of CB7-BC to the two structurally similar analytes (amantadine and adamantanol) was investigated based on their emission changes as a function of time and compared with the dysfunction of the non-covalent CB7 dye. In biologically relevant buffered saline and biofluid (human real urine and saliva), the detection and quantification of the Parkinson's drug amantadine were achieved at the medically relevant concentration range and a unique chemosensor addition method was utilized herein to circumvent the matrix influences between different samples. In the end, an estimated S_N2-type guest exchange mechanism was suggested to interpret the prominent properties of unimolecular conjugated CB7-dye in contrast with the traditional non-covalent pairs.

Inspired by the findings on how unimolecular CB*n*-based chemosensors perform in a high salinity medium, it was realized that salt plays a delicate role in this type of supramolecular system and that salt effects could be explored to tune the chemosensor performance to the point where even differential sensing is possible. In chapter 5, in order to extend the sensing capability for weak binding affinity analytes and make salt involved as a tunable factor for mediating the supramolecular binding between

host and guest, a novel unimolecular CB7 conjugate was equipped with a neutral and highly emissive dye (nitrobenzoxadiazole, NBD) with a modest affinity to CB7 than berberine. Indeed, CB7-NBD can be used in 1X PBS to detect analytes with weak affinity, which was not possible with CB7-BC and non-covalent reporter pairs in such an environment. Meanwhile, the conformation of obtained CB7-NBD complexes with different analytes was investigated by NMR, ion mobility experiments, and DFT calculations. In particular, emission-based titration experiments were performed to evaluate the binding affinity of CB7-NBD with dozens of biorelevant analytes, and the emission recovery observed upon subsequent addition of salts was characterized. According to the different responses upon salt addition into different CB7-NBD analyte complexes, a 'salt-addition assay' strategy for differential analyte sensing was developed. The PCA plot and the other data-driven approach to convert the data differences into an intuitive pairwise colorimetric pattern were utilized to evaluate the distinction of analytes by this assay. Meanwhile, the type of salt was also a new parameter to provide more dimensional information for analytes differential sensing. This salt-adaptive chemosensor system was also exploited for analytes sensing capability in real biofluids in analogy with the previous chapter.

Overall, the unimolecular CBn-based conjugate for sensing application in this work opens a range of multiple possibilities for the design and preparation of more attractive chemosensors with specific and smart features combined with their current existing strengths in the future. Concerning the choice of receptors, other CBn homologues (mainly for CB6 and CB8) and other artificial could be utilized to satisfy the requirements for different classes of analytes sensing. Especially for CB8, the larger cavity can provide more potential binding conformation between analytes and conjugate, *e.g.,* in the ABA model, to create more novel sensing mechanisms and target a wider scope of specific analytes with high but flexible affinity. As an outlook, one strategy for expanding the potential applications of chemosensors, which is equipping the conjugate with a 'controllable button,' can be envisioned. For example, a light-responsive linker connecting the host and the indicator could be installed in the chemosensor design in the future to release the tethered indicator when exposed to light, resulting in chemosensors with spatiotemporally controlled on/off function. This concept also applies to other stimulus-dependent groups typically used in dynamic covalent chemistry, such as -S-S bonds (redox responsive) or Schiff bonds (pH-responsive). For indicators, the readout signal is not only limited to the fluorescent emission but also other detection forms, such as absorbance, chemical shifts in NMR (^{1}H, ^{13}C, ^{15}N, or ^{19}F), circular dichroism (CD), and so on. For instance, using the fluoroalkane or fluoro aromatic compound as the indicator and monitoring the process of guest displacement by ^{19}F NMR or MRI technique for imaging application is one of the idea frameworks. For the prospect of applications, the objects for sensing or analyzing may not be limited to the small molecules, and it is likely used as the chemosensor for macromolecular detection, *e.g.,* peptides, antibodies, and proteins. The abundant structural features on these macromolecules can provide more multi-dimensional interactions and responses to conjugated chemosensors and potentially harvest the identical fingerprint information for each analyte. Meanwhile, the conjugated chemosensors could also be applied in cellular imaging or real-time monitoring for drug

metabolism taking advantage of its resistance to salt and the lack of background from the free dye in contrast to the non-covalent reporter pairs.

7. List of abbreviations

Å	Angstrom
ABA	Associative binding assays
ACN	Acetonitrile
aq.	Aqueous
BC	Berberine (chloride)
°C	Degree Celsius
CB14	Cucurbit[14]urils
CB5	Cucurbit[5]urils
CB6	Cucurbit[6]urils
CB7	Cucurbit[7]urils
CB8	Cucurbit[8]urils
CBn	Cucurbit[n]urils
CCSs	Collision Cross Sections
CD	Circular dichroism
$CuSO_4$	Copper(II) sulfate
D_2O	Deuterium oxide
DASAP	*trans*-4-[4-(Dimethylamino)styryl]-1-adamantylpyridinium
DCM	Dichloromethane
de novo	New
DFT	Density functional calculation
DMF	Dimethylformamide
DMSO	Dimethyl sulfoxide
e.g.,	*exemplari gratia*, for example
eq.	Equation
Et_2O	Diethyl ether
etc.	*et cetera,* and so forth
eV	Electron volts
FRET	Fluorescence resonance energy transfer
GDA	Guests displacement assays
h	Hour
H_2O_2	Hydrogen peroxide
HEG	Hexaethylene glycol
HPLC	High-Performance Liquid Chromatography
i.e.,	*id est,* that is to say
IDA	Indicator displacement assay
ITC	Isothermal titration calorimetry

$K_2S_2O_8$	Potassium persulfate
K_a	Association constant
k_{in}	Complexation rates
k_{out}	Decomplexation rates
L	Liter
LOD	Limit of detection
M	Mole
MDAP	2,7-Dimethyldiazapyrenium dication
MeOH	Methanol
mg	Milligram
mL	Millilitre
mM	Millimolar
MRI	Magnetic resonance imaging
MS	Mass spectrum
ms	Milliseconds
MTS	3-(4,5-dimethylthiazol-2-yl)-5-(3-carboxymethoxyphenyl) -2-(4-sulfophenyl)-2H-tetrazolium)
NBD	Nitrobenzoxadiazole
NBS	*N*-Bromosuccinimide
nm	Nanometer
nM	Nanomolar
NMR	Nuclear magnetic resonance
PB	Phosphate buffer
PBS	Phosphate buffered saline
PC	Packing coefficient
PCA	Principal component analysts
PDT	Photodynamic therapy
PLA	Polylactic Acid
PLGA	Poly(lactic-co-glycolic acid)
PMMA	Poly(methyl methacrylate)
SDA-PAGE	Sodium dodecyl sulfate polyacrylamide gel electrophoresis
S_N2	Substitution nucleophilic (bi-molecular)
SSM	Solid-state metathesis
TEG	Tetraethylene glycol
TFA	Trifluoroacetic acid
TIMS	Trapped Ion Mobility Spectrometry
UV	Ultraviolet

UV-Vis	Ultraviolet-visible
β-CD	β-cyclodextrin
λ_{ex}	Excitation wavelength
μM	Micromolar
σ	Standard deviation
Abs	Absorption of a photon
conc.	Concentration
DNA	Deoxyribonucleic acid
ESI	Electrospray ionization
g	Gram
I_{abs}	Intensity of transmitted light
I_{rel}	Normalized intensity
μmol	Micromole

8. Appendices

8.1. Curriculum Vitae

Name	Changming Hu
Nationality	Chinese
Email	changming.hu@partner.kit.edu
Date of birth	11.10.1992
Address	76344 Eggenstein-Leopoldshafen, Germany
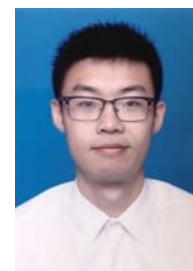
Education

Since 10/2018	PhD candidate, Chemistry, Institute of Nanotechnology (INT) of the Karlsruhe Institute of Technology (KIT)
	Supervised by Dr. Frank Biedermann and Prof. Dr. Pavel Levkin
	Research Direction: supramolecular host-guest conjugate for biorelevant recognition and detection
09/2015-06/2018	Master of Science, Polymer Chemistry, College of Chemistry, Chemical Engineering and Materials Science of Soochow University
	Supervised by Prof. Dr. Hong Chen and Prof. Dr. Qian Yu
	Research Direction: Fabrication of biofunctionalized surface based on host-guest interaction
09/2011-06/2015	Bachelor, Material science and Engineering, College of Chemistry, Chemical Engineering and Materials Science of Soochow University

Scholarships and Honors

09/2018-09/2022	Funded by Chinese Scholarship Council (CSC) for PhD student (48 months)
2018	1st class scholarship
2017	3rd class scholarship
2016	1st class scholarship
2014	2nd class scholarship

Skills

- Professional skills: Organic synthesis and characterization, Polymer synthesis and characterization, Spectroscopic instrumental analysis, biomolecules relevant detection, cell/bacterial culture and operation, interface analysis and characterization, etc.

- Software: Microsoft office, Origin Lab, ChemOffice, Endnote, Citavi, Illustrator, Photoshop, MestReNova, etc.

- Instrument Operation: NMR, ESI-MS, LC-MS, HPLC, UV-vis spectrometer, Fluorescent spectrometer, Circular dichroism, Dynamic light scattering, SEC (GPC), FT-IR, microscope, TEM, SEM, etc.

8.2. Publications

Hu, C.; Jochmann, T; Chabraborty, P; Neumaier, M; Levkin, P. A.; Kappes, M. M.; Biedermann, F., Further Dimensions for Sensing in Biofluids: Distinguishing Bioorganic Analytes by the Salt-Induced Adaptation of a Cucurbit[7]uril-Based Chemosensor. *J. Am. Chem. Soc.* **2022,** *144,* 13084-13095.

Kumar, N. M.; Picchetti, P.; **Hu, C.;** Grimm, L. M.; Biedermann, F., Chemiluminescent Cucurbit[n]uril-Based Chemosensor for the Detection of Drugs in Biofluids. *ACS Sens.* **2022**.

Zhong, C.; **Hu, C.**; Kumar, R.; Trouillet, V.; Biedermann, F.; Hirtz, M., Cucurbit[n]uril-Immobilized Sensor Arrays for Indicator-Displacement Assays of Small Bioactive Metabolites. *ACS Appl. Nano Mater.* **2021,** *4*, 4676-4687.
This publication was featured as front cover in Chemical Science.

Hu, C.; Grimm, L.; Prabodh, A.; Baksi, A.; Siennicka, A.; Levkin, P. A.; Kappes, M. M.; Biedermann, F., Covalent cucurbit[7]uril–dye conjugates for sensing in aqueous saline media and biofluids. *Chem. Sci.* **2020,** *11*, 11142-11153.;
This publication was featured with the front cover in Chemical Science.

Hu, C.; Wu, J.; Wei, T.; Zhan, W.; Qu, Y.; Pan, Y.; Yu, Q.; Chen, H., A supramolecular approach for versatile biofunctionalization of magnetic nanoparticles. *J. Mater. Chem. B* **2018,** *6*, 2198-2203.;
This publication was featured with the inside front cover in the Journal of Materials Chemistry B.

Wu, J.; **Hu, C.**; Tang, Z.; Yu, Q.; Liu, X.; Chen, H., Tissue-engineered Vascular Grafts: Balance of the Four Major Requirements. *Colloid Interface Sci. Commun*. **2018,** 23, 34-44.

Hu, C.; Qu, Y.; Zhan, W.; Wei, T.; Cao, L.; Yu, Q.; Chen, H., A supramolecular bioactive surface for specific binding of protein. Colloids Surf., B 2017, 152, 192-198.

Wang, L.; Wu, J.; Hu, Y.; **Hu, C**.; Pan, Y.; Yu, Q.; Chen, H., Using porous magnetic iron oxide nanomaterials as a facile photoporation nanoplatform for macromolecular delivery. *J. Mater. Chem. B* **2018**, 6, 4427-4436.

Zhan, W.; Qu, Y.; Wei, T.; **Hu, C.;** Pan, Y.; Yu, Q.; Chen, H., Sweet Switch: Sugar-Responsive Bioactive Surfaces Based on Dynamic Covalent Bonding. *ACS Appl. Mater. Interfaces* **2018**, 10, 10647-10655.

Zhan, W.; Wei, T.; Cao, L.; **Hu, C.**; Qu, Y.; Yu, Q.; Chen, H., Supramolecular Platform with Switchable Multivalent Affinity: Photo-Reversible Capture and Release of Bacteria. *ACS Appl. Mater. Interfaces* **2017**, 9, 3505-3513.

Qu, Y.; Wei, T.; Zhan, W.; **Hu, C.**; Cao, L.; Yu, Q.; Chen, H., A reusable supramolecular platform for the specific capture and release of proteins and bacteria. *J. Mater. Chem. B* **2017**, 5, 444-453.

Wei, T.; Zhan, W.; Cao, L.; **Hu, C.**; Qu, Y.; Yu, Q.; Chen, H., Multifunctional and Regenerable Antibacterial Surfaces Fabricated by a Universal Strategy. *ACS Appl. Mater. Interfaces* **2016**, 8, 30048-30057.

Cao, L.; Qu, Y.; **Hu, C.**; Wei, T.; Zhan, W.; Yu, Q.; Chen, H., A Universal and Versatile Approach for Surface Biofunctionalization: Layer-by-Layer Assembly Meets Host-Guest Chemistry. *Adv. Mater. Interfaces* **2016**, 3, 1600600.

8.3. Acknowledgments

In this section, I would like to express my sincere appreciation to all of the people who accompanied and help with me during this long but brief period of my PhD life.

First of all, I would like to thank my supervisor, Dr. Frank Biedermann, who gave me this precious opportunity to be a PhD candidate and learn about the knowledge of supramolecular chemistry. During this academic period under his patient guidance, I benefit tremendously from his rigorous thinking and active mind, especially his meticulous attitude toward paper writing. Meanwhile, I greatly admire his capability to mostly take care of all the projects belonging to several students at the same time. By the time I was plagued by scientific distress and despair, I thank Frank could motivate and encourage me with optimistic and positive willing with practical and constructive suggestions. I would also like to express my gratitude to Prof. Dr. Pavel Levkin for accepting my application for a doctorate in this research group and thank the guidance and organization on some cooperative projects.

I would like to appreciate my former and present colleagues during this four-year life in the Biedermann group. I am thankful to Dr. Stephan Sinn for teaching me about photophysical related knowledge and training the fundamental operations for all instruments when I first came, and I am thankful to Dr. Pierre Picchetti for sharing me with lots of experiences and suggestions on organic synthesis work and chatting with me about many interesting scientific ideas and career perspective in my final year. I thank Dr. Laura Grimm for plenty of detailed instrument training (HPLC, titrator, freeze dryer, etc.) and help with data analysis (constant binding fitting). I thank Philipp Avon and Alicja Siennicka for introducing all of the regulations in labs and institute and offering me assistance with the synthesis of cucurbit[*n*]uril and other compounds when I had problems. I thank Amrutha Prabodh, Rui Kang and Joana Krämer for their help and skills in photophysical related works in analysis labs, *i.e.,* absorption, fluorescent, circular dichroism spectrometry and platereader use. I thank Dr. Pronay Biswas, Dr. Yanan Luo, Yichuan Wang, Chunting Zhong, Manoj Nilima, Wenjing Wang, and Patrick Gruhs for sharing a pleasant time in the lab.

I would also like to gratitude the cooperated colleagues in charge of supporting the additional techniques, which is out of my major but greatly improved the scientific level of my projects. I thank Prof. Dr. Manfred Kappes, Dr. Macro Neumaier, Dr. Ananya Baksi, and Papri Chakraborty for your important contribution to mass spectrometry, ion mobility experiments, and DFT calculations. Your professional works provided strong support for your research and publication. I thank Thomas Jochmann for data analysis by the machine learning approach in my analysis differential sensing section.

I would like to thank the China Scholarship Council (CSC) for funding my whole PhD period and offering this great opportunity to study in Germany.

Particularly, I would love to thank my family and friends for your far-away support and concern over the long four years. It is hard not to be touched by the passage of time when suddenly realizing those important life nodes passing on to the surrounding person and myself. Thanks to my parents for your never stoppable emotional support and belief without any hesitation from start to end. Thanks to my

grandfather for your encouragement and support when I was obstructed by troubles in deep distress. Thanks to my friends for your sharing their experiences and life to enrich my view and keep in contact with the world outside of academics. Finally and importantly, I would like to thank my dearest girlfriend for your everlasting love and endless support in the past nearly nine years. From the inseparable life during our college and master periods to our separated life by time and space in these four years, you never hesitate to company with me and contribute the efforts for our future. Like the mirror and soul of life, I appreciate the patient listening and the most useful advice from you.

9. Reference

(1) Lehn, J.-M., Supramolecular Chemistry. *Science* **1993,** *260*, 1762-1763.

(2) Schneider, H.-J., Binding Mechanisms in Supramolecular Complexes. *Angew. Chem. Int. Ed.* **2009,** *48*, 3924-3977.

(3) Lehn, J.-M., Supramolecular chemistry: Where from? Where to? *Chem. Soc. Rev.* **2017,** *46*, 2378-2379.

(4) Mattia, E.; Otto, S., Supramolecular systems chemistry. *Nat. Nanotechnol.* **2015,** *10*, 111-119.

(5) Cram, D. J., The Design of Molecular Hosts, Guests, and Their Complexes (Nobel Lecture). *Angew. Chem., Int. Ed. Engl.* **1988,** *27*, 1009-1020.

(6) Pedersen, C. J., The Discovery of Crown Ethers (Noble Lecture). *Angew. Chem., Int. Ed. Engl.* **1988,** *27*, 1021-1027.

(7) Lehn, J.-M., Supramolecular Chemistry—Scope and Perspectives Molecules, Supermolecules, and Molecular Devices (Nobel Lecture). *Angew. Chem., Int. Ed. Engl.* **1988,** *27*, 89-112.

(8) Fischer, E., Einfluss der Configuration auf die Wirkung der Enzyme. *Ber. Dtsch. Chem. Ges.* **1894,** *27*, 2985-2993.

(9) Yu, G.; Chen, X., Host-Guest Chemistry in Supramolecular Theranostics. *Theranostics* **2019,** *9*, 3041-3074.

(10) Feringa, B. L., The Art of Building Small: From Molecular Switches to Motors (Nobel Lecture). *Angew. Chem. Int. Ed.* **2017,** *56*, 11060-11078.

(11) Sauvage, J.-P., From Chemical Topology to Molecular Machines (Nobel Lecture). *Angew. Chem. Int. Ed.* **2017,** *56*, 11080-11093.

(12) Stoddart, J. F., Mechanically Interlocked Molecules (MIMs)—Molecular Shuttles, Switches, and Machines (Nobel Lecture). *Angew. Chem. Int. Ed.* **2017,** *56*, 11094-11125.

(13) Amabilino, D. B.; Smith, D. K.; Steed, J. W., Supramolecular materials. *Chem. Soc. Rev.* **2017,** *46*, 2404-2420.

(14) Geng, W.-C.; Sessler, J. L.; Guo, D.-S., Supramolecular prodrugs based on host–guest interactions. *Chem. Soc. Rev.* **2020,** *49*, 2303-2315.

(15) Uhlenheuer, D. A.; Petkau, K.; Brunsveld, L., Combining supramolecular chemistry with biology. *Chem. Soc. Rev.* **2010,** *39*, 2817-2826.

(16) Webber, M. J.; Langer, R., Drug delivery by supramolecular design. *Chem. Soc. Rev.* **2017,** *46*, 6600-6620.

(17) Webber, M. J.; Appel, E. A.; Meijer, E. W.; Langer, R., Supramolecular biomaterials. *Nat. Mater.* **2016,** *15*, 13-26.

(18) Lehn, J.-M., From supramolecular chemistry towards constitutional dynamic chemistry and adaptive chemistry. *Chem. Soc. Rev.* **2007,** *36*, 151-160.

(19) Zhang, M.; Yan, X.; Huang, F.; Niu, Z.; Gibson, H. W., Stimuli-Responsive Host–Guest Systems Based on the Recognition of Cryptands by Organic Guests. *Acc. Chem. Res.* **2014,** *47*, 1995-2005.

(20) Yan, X.; Wang, F.; Zheng, B.; Huang, F., Stimuli-responsive supramolecular polymeric materials. *Chem. Soc. Rev.* **2012,** *41*, 6042-6065.

(21) Jones, C. D.; Steed, J. W., Gels with sense: supramolecular materials that respond to heat, light and sound. *Chem. Soc. Rev.* **2016,** *45*, 6546-6596.

(22) Lu, W.; Le, X.; Zhang, J.; Huang, Y.; Chen, T., Supramolecular shape memory hydrogels: a new bridge between stimuli-responsive polymers and supramolecular chemistry. *Chem. Soc. Rev.* **2017,** *46*, 1284-1294.

(23) Panja, S.; Adams, D. J., Stimuli responsive dynamic transformations in supramolecular gels. *Chem. Soc. Rev.* **2021,** *50*, 5165-5200.

(24) Biedermann, F.; Schneider, H.-J., Experimental Binding Energies in Supramolecular Complexes. *Chem. Rev.* **2016,** *116*, 5216-5300.

(25) Schneider, H.-J.; Yatsimirsky, A. K., Selectivity in supramolecular host–guest complexes. *Chem. Soc. Rev.* **2008,** *37*, 263-277.

(26) Kuah, E.; Toh, S.; Yee, J.; Ma, Q.; Gao, Z., Enzyme Mimics: Advances and Applications. *Chem. Eur. J.* **2016,** *22*, 8404-8430.

(27) Wankar, J.; Kotla, N. G.; Gera, S.; Rasala, S.; Pandit, A.; Rochev, Y. A., Recent Advances in Host–Guest Self-Assembled Cyclodextrin Carriers: Implications for Responsive Drug Delivery and Biomedical Engineering. *Adv. Funct. Mater.* **2020,** *30*, 1909049.

(28) Braegelman, A. S.; Webber, M. J., Integrating Stimuli-Responsive Properties in Host-Guest Supramolecular Drug Delivery Systems. *Theranostics* **2019,** *9*, 3017-3040.

(29) Hu, Q.-D.; Tang, G.-P.; Chu, P. K., Cyclodextrin-Based Host–Guest Supramolecular Nanoparticles for Delivery: From Design to Applications. *Acc. Chem. Res.* **2014,** *47*, 2017-2025.

(30) Dickert, F. L.; Haunschild, A., Sensor materials for solvent vapor detection—donor–acceptor and host–guest interactions. *Adv. Mater.* **1993,** *5*, 887-895.

(31) Karmakar, A.; Samanta, P.; Desai, A. V.; Ghosh, S. K., Guest-Responsive Metal–Organic Frameworks as Scaffolds for Separation and Sensing Applications. *Acc. Chem. Res.* **2017,** *50*, 2457-2469.

(32) Yeung, M. C.-L.; Yam, V. W.-W., Luminescent cation sensors: from host–guest chemistry, supramolecular chemistry to reaction-based mechanisms. *Chem. Soc. Rev.* **2015,** *44*, 4192-4202.

(33) Teresa Albelda, M.; Frías, J. C.; García-España, E.; Schneider, H.-J., Supramolecular complexation for environmental control. *Chem. Soc. Rev.* **2012,** *41*, 3859-3877.

(34) Sahoo, S. K.; Sharma, D.; Bera, R. K.; Crisponi, G.; Callan, J. F., Iron(iii) selective molecular and supramolecular fluorescent probes. *Chem. Soc. Rev.* **2012,** *41*, 7195-7227.

(35) Yao, Y. Q.; Chen, K.; Hua, Z. Y.; Zhu, Q. J.; Xue, S. F.; Tao, Z., Cucurbit[n]uril-based host–guest-metal ion chemistry: an emerging branch in cucurbit[n]uril chemistry. *J. Inclusion Phenom. Macrocyclic Chem.* **2017,** *89*, 1-14.

(36) Takashima, Y.; Harada, A., Stimuli-responsive polymeric materials functioning via host–guest interactions. *J. Inclusion Phenom. Macrocyclic Chem.* **2017,** *88*, 85-104.

(37) Karim, A. A.; Dou, Q.; Li, Z.; Loh, X. J., Emerging Supramolecular Therapeutic Carriers Based on Host–Guest Interactions. *Chem. Asian J.* **2016,** *11*, 1300-1321.

(38) Yang, X.; Yuan, D.; Hou, J.; Sedgwick, A. C.; Xu, S.; James, T. D.; Wang, L., Organic/inorganic supramolecular nano-systems based on host/guest interactions. *Coord. Chem. Rev.* **2021,** *428*, 213609.

(39) Meyer, E. Über die Condensation des Harnstoffs mit Glyoxal und des Glykolurils mit Formaldehyd. 1904.

(40) Behrend, R.; Meyer, E.; Rusche, F., I. Ueber Condensationsproducte aus Glycoluril und Formaldehyd. *Justus Liebigs Ann. Chem.* **1905,** *339*, 1-37.

(41) Freeman, W. A.; Mock, W. L.; Shih, N. Y., Cucurbituril. *J. Am. Chem. Soc.* **1981,** *103*, 7367-7368.

(42) Kim, J.; Jung, I.-S.; Kim, S.-Y.; Lee, E.; Kang, J.-K.; Sakamoto, S.; Yamaguchi, K.; Kim, K., New Cucurbituril Homologues: Syntheses, Isolation, Characterization, and X-ray Crystal Structures of Cucurbit[n]uril (n = 5, 7, and 8). *J. Am. Chem. Soc.* **2000,** *122*, 540-541.

(43) Day, A.; Arnold, A. P.; Blanch, R. J.; Snushall, B., Controlling Factors in the Synthesis of Cucurbituril and Its Homologues. *J. Org. Chem.* **2001,** *66*, 8094-8100.

(44) Isaacs, L.; Park, S.-K.; Liu, S.; Ko, Y. H.; Selvapalam, N.; Kim, Y.; Kim, H.; Zavalij, P. Y.; Kim, G.-H.; Lee, H.-S.; Kim, K., The Inverted Cucurbit[n]uril Family. *J. Am. Chem. Soc.* **2005,** *127*, 18000-18001.

(45) Huang, W.-H.; Zavalij, P. Y.; Isaacs, L., Chiral Recognition inside a Chiral Cucurbituril. *Angew. Chem. Int. Ed.* **2007,** *46*, 7425-7427.

(46) Cheng, X.-J.; Liang, L.-L.; Chen, K.; Ji, N.-N.; Xiao, X.; Zhang, J.-X.; Zhang, Y.-Q.; Xue, S.-F.; Zhu, Q.-J.; Ni, X.-L.; Tao, Z., Twisted Cucurbit[14]uril. *Angew. Chem. Int. Ed.* **2013,** *52*, 7252-7255.

(47) Germain, P.; Létoffé, J. M.; Merlin, M. P.; Buschmann, H. J., Thermal behaviour of hydrated and anhydrous Cucurbituril: A DSC, T.G. and calorimetric study in temperature range from 100 to 800K. *Thermochim. Acta* **1998,** *315*, 87-92.

(48) Uzunova, V. D.; Cullinane, C.; Brix, K.; Nau, W. M.; Day, A. I., Toxicity of cucurbit[7]uril and cucurbit[8]uril: an exploratory in vitro and in vivo study. *Org. Biomol. Chem.* **2010,** *8*, 2037-2042.

(49) Hettiarachchi, G.; Nguyen, D.; Wu, J.; Lucas, D.; Ma, D.; Isaacs, L.; Briken, V., Toxicology and Drug Delivery by Cucurbit[n]uril Type Molecular Containers. *PLOS ONE* **2010,** *5*, e10514.

(50) Saleh, N. i.; Ghosh, I.; Nau, W. M., Cucurbiturils in drug delivery and for biomedical applications. *Supramolecular systems in biomedical fields* **2013**, 164.

(51) Aktanova, A.; Abramova, T.; Pashkina, E.; Boeva, O.; Grishina, L.; Kovalenko, E.; Kozlov, V., Assessment of the Biocompatibility of Cucurbiturils in Blood Cells. *Nanomaterials* **2021,** *11*, 1356.

(52) Zhang, X.; Xu, X.; Li, S.; Wang, L.-H.; Zhang, J.; Wang, R., A systematic evaluation of the biocompatibility of cucurbit[7]uril in mice. *Sci. Rep.* **2018,** *8*, 8819.

(53) Lee, J. W.; Samal, S.; Selvapalam, N.; Kim, H.-J.; Kim, K., Cucurbituril Homologues and Derivatives: New Opportunities in Supramolecular Chemistry. *Acc. Chem. Res.* **2003,** *36*, 621-630.

(54) Márquez, C.; Hudgins, R. R.; Nau, W. M., Mechanism of Host−Guest Complexation by Cucurbituril. *J. Am. Chem. Soc.* **2004,** *126*, 5806-5816.

(55) Lagona, J.; Mukhopadhyay, P.; Chakrabarti, S.; Isaacs, L., The Cucurbit[n]uril Family. *Angew. Chem. Int. Ed.* **2005,** *44*, 4844-4870.

(56) Sinn, S.; Biedermann, F., Chemical Sensors Based on Cucurbit[n]uril Macrocycles. *Isr. J. Chem.* **2018,** *58*, 357-412.

(57) Mock, W. L.; Shih, N. Y., Structure and selectivity in host-guest complexes of cucurbituril. *J. Org. Chem.* **1986,** *51*, 4440-4446.

(58) Mock, W.; Shih, N., Host-guest binding capacity of cucurbituril. *J. Org. Chem.* **1983,** *48*, 3618-3619.

(59) Biedermann, F.; Scherman, O. A., Cucurbit[8]uril Mediated Donor–Acceptor Ternary Complexes: A Model System for Studying Charge-Transfer Interactions. *J. Phys. Chem. B* **2012,** *116*, 2842-2849.

(60) Nau, W. M.; Florea, M.; Assaf, K. I., Deep Inside Cucurbiturils: Physical Properties and Volumes of their Inner Cavity Determine the Hydrophobic Driving Force for Host–Guest Complexation. *Isr. J. Chem.* **2011,** *51*, 559-577.

(61) Mecozzi, S.; Rebek, J., Julius, The 55 % Solution: A Formula for Molecular Recognition in the Liquid State. *Chem. Eur. J.* **1998,** *4*, 1016-1022.

(62) Biedermann, F.; Nau, W. M.; Schneider, H.-J., The Hydrophobic Effect Revisited—Studies with Supramolecular Complexes Imply High-Energy Water as a Noncovalent Driving Force. *Angew. Chem. Int. Ed.* **2014,** *53*, 11158-11171.

(63) Biedermann, F.; Uzunova, V. D.; Scherman, O. A.; Nau, W. M.; De Simone, A., Release of High-Energy Water as an Essential Driving Force for the High-Affinity Binding of Cucurbit[n]urils. *J. Am. Chem. Soc.* **2012,** *134*, 15318-15323.

(64) Biedermann, F.; Vendruscolo, M.; Scherman, O. A.; De Simone, A.; Nau, W. M., Cucurbit[8]uril and Blue-Box: High-Energy Water Release Overwhelms Electrostatic Interactions. *J. Am. Chem. Soc.* **2013,** *135*, 14879-14888.

(65) Zhang, S.; Grimm, L.; Miskolczy, Z.; Biczók, L.; Biedermann, F.; Nau, W. M., Binding affinities of cucurbit[n]urils with cations. *Chem. Commun.* **2019,** *55*, 14131-14134.

(66) Buschmann, H. J.; Cleve, E.; Jansen, K.; Wego, A.; Schollmeyer, E., Complex Formation between Cucurbit[n]urils and Alkali, Alkaline Earth and Ammonium Ions in Aqueous Solution. *J. Inclusion Phenom. Macrocyclic Chem.* **2001,** *40*, 117-120.

(67) Buschmann, H. J.; Cleve, E.; Jansen, K.; Schollmeyer, E., Determination of complex stabilities with nearly insoluble host molecules: cucurbit[5]uril, decamethylcucurbit[5]uril and cucurbit[6]uril as ligands for the complexation of some multicharged cations in aqueous solution. *Anal. Chim. Acta* **2001,** *437*, 157-163.

(68) Kellersberger, K. A.; Anderson, J. D.; Ward, S. M.; Krakowiak, K. E.; Dearden, D. V., Encapsulation of N2, O2, Methanol, or Acetonitrile by Decamethylcucurbit[5]uril(NH4+)2 Complexes in the Gas Phase: Influence of the Guest on "Lid" Tightness. *J. Am. Chem. Soc.* **2001,** *123*, 11316-11317.

(69) He, S.; Biedermann, F.; Vankova, N.; Zhechkov, L.; Heine, T.; Hoffman, R. E.; De Simone, A.; Duignan, T. T.; Nau, W. M., Cavitation energies can outperform dispersion interactions. *Nat. Chem.* **2018,** *10*, 1252-1257.

(70) Miyahara, Y.; Abe, K.; Inazu, T., "Molecular" Molecular Sieves: Lid-Free Decamethylcucurbit[5]uril Absorbs and Desorbs Gases Selectively. *Angew. Chem. Int. Ed.* **2002,** *41*, 3020-3023.

(71) Huber, G.; Legrand, F.-X.; Lewin, V.; Baumann, D.; Heck, M.-P.; Berthault, P., Interaction of Xenon with Cucurbit[5]uril in Water. *ChemPhysChem* **2011,** *12*, 1053-1055.

(72) Liu, J.-X.; Long, L.-S.; Huang, R.-B.; Zheng, L.-S., Interesting Anion-Inclusion Behavior of Cucurbit[5]uril and Its Lanthanide-Capped Molecular Capsule. *Inorg. Chem.* **2007,** *46*, 10168-10173.

(73) Liu, J.-X.; Long, L.-S.; Huang, R.-B.; Zheng, L.-S., Molecular Capsules Based on Cucurbit[5]uril Encapsulating "Naked" Anion Chlorine. *Cryst. Growth Des.* **2006,** *6*, 2611-2614.

(74) Zhang, Y.-Q.; Zhu, Q.-J.; Xue, S.-F.; Tao, Z., Chlorine Anion Encapsulation by Molecular Capsules Based on Cucurbit[5]uril and Decamethylcucurbit[5]uril. *Molecules* **2007,** *12*, 1325-1333.

(75) Barrow, S. J.; Kasera, S.; Rowland, M. J.; del Barrio, J.; Scherman, O. A., Cucurbituril-Based Molecular Recognition. *Chem. Rev.* **2015,** *115*, 12320-12406.

(76) Mock, W. L.; Shih, N. Y., Organic ligand-receptor interactions between cucurbituril and alkylammonium ions. *J. Am. Chem. Soc.* **1988,** *110*, 4706-4710.

(77) Rekharsky, M. V.; Ko, Y. H.; Selvapalam, N.; Kim, K.; Inoue, Y., Complexation Thermodynamics of Cucurbit[6]uril with Aliphatic Alcohols, Amines, and Diamines. *Supramol. Chem.* **2007,** *19*, 39-46.

(78) Liu, L.; Zhao, N.; Scherman, O. A., Ionic liquids as novel guests for cucurbit[6]uril in neutral water. *Chem. Commun.* **2008**, 1070-1072.

(79) Zhao, N.; Liu, L.; Biedermann, F.; Scherman, O. A., Binding Studies on CB[6] with a Series of 1-Alkyl-3-methylimidazolium Ionic Liquids in an Aqueous System. *Chem. Asian J.* **2010,** *5*, 530-537.

(80) Kolman, V.; Marek, R.; Strelcova, Z.; Kulhanek, P.; Necas, M.; Svec, J.; Sindelar, V., Electron Density Shift in Imidazolium Derivatives upon Complexation with Cucurbit[6]uril. *Chem. Eur. J.* **2009,** *15*, 6926-6931.

(81) Jiao, D.; Scherman, O. A., Isolation of cucurbit[n]uril homologues with imidazolium salts in a recyclable manner. *Green Chem.* **2012,** *14*, 2445-2449.

(82) Zhao, N.; Lloyd, G. O.; Scherman, O. A., Monofunctionalised cucurbit[6]uril synthesis using imidazolium host–guest complexation. *Chem. Commun.* **2012,** *48*, 3070-3072.

(83) da Silva, F. F.; de Oliveira, C. A. F.; Falcão, E. H. L.; Chojnacki, J.; Neves, J. L.; Alves, S., New lanthanide–CB[6] coordination compounds: relationships between the crystal structure and luminescent properties. *Dalton Trans.* **2014,** *43*, 5435-5442.

(84) Gerasko, O. A.; Mainicheva, E. A.; Naumova, M. I.; Yurjeva, O. P.; Alberola, A.; Vicent, C.; Llusar, R.; Fedin, V. P., Tetranuclear Lanthanide Aqua Hydroxo Complexes with Macrocyclic Ligand Cucurbit[6]uril. *Eur. J. Inorg. Chem.* **2008,** *2008*, 416-424.

(85) Schnurr, M.; Sloniec-Myszk, J.; Döpfert, J.; Schröder, L.; Hennig, A., Supramolecular Assays for Mapping Enzyme Activity by Displacement-Triggered Change in Hyperpolarized 129Xe Magnetization Transfer NMR Spectroscopy. *Angew. Chem. Int. Ed.* **2015,** *54*, 13444-13447.

(86) Zhang, B.; Guo, Q.; Luo, Q.; Zhang, X.; Zeng, Q.; Zhao, L.; Yuan, Y.; Jiang, W.; Yang, Y.; Liu, M.; Ye, C.; Zhou, X., An intracellular diamine oxidase triggered hyperpolarized 129Xe magnetic resonance biosensor. *Chem. Commun.* **2018,** *54*, 13654-13657.

(87) Finbloom, J. A.; Slack, C. C.; Bruns, C. J.; Jeong, K.; Wemmer, D. E.; Pines, A.; Francis, M. B., Rotaxane-mediated suppression and activation of cucurbit[6]uril for molecular detection by 129Xe hyperCEST NMR. *Chem. Commun.* **2016,** *52*, 3119-3122.

(88) Osaka, I.; Kondou, M.; Selvapalam, N.; Samal, S.; Kim, K.; Rekharsky, M. V.; Inoue, Y.; Arakawa, R., Characterization of host–guest complexes of cucurbit[n]uril (n = 6, 7) by electrospray ionization mass spectrometry. *J. Mass Spectrom.* **2006,** *41*, 202-207.

(89) Danylyuk, O.; Fedin, V. P.; Sashuk, V., Host–guest complexes of cucurbit[6]uril with isoprenaline: the effect of the metal ion on the crystallization pathway and supramolecular architecture. *CrystEngComm* **2013,** *15*, 7414-7418.

(90) Alnajjar, M. A.; Nau, W. M.; Hennig, A., A reference scale of cucurbit[7]uril binding affinities. *Org. Biomol. Chem.* **2021,** *19*, 8521-8529.

(91) Shetty, D.; Khedkar, J. K.; Park, K. M.; Kim, K., Can we beat the biotin–avidin pair?: cucurbit[7]uril-based ultrahigh affinity host–guest complexes and their applications. *Chem. Soc. Rev.* **2015,** *44*, 8747-8761.

(92) Cao, L.; Šekutor, M.; Zavalij, P. Y.; Mlinarić-Majerski, K.; Glaser, R.; Isaacs, L., Cucurbit[7]uril·Guest Pair with an Attomolar Dissociation Constant. *Angew. Chem. Int. Ed.* **2014,** *53*, 988-993.

(93) Ko, Y. H.; Hwang, I.; Lee, D.-W.; Kim, K., Ultrastable Host–Guest Complexes and Their Applications. *Isr. J. Chem.* **2011,** *51*, 506-514.

(94) Kim, H.-J.; Heo, J.; Jeon, W. S.; Lee, E.; Kim, J.; Sakamoto, S.; Yamaguchi, K.; Kim, K., Selective Inclusion of a Hetero-Guest Pair in a Molecular Host: Formation of Stable Charge-Transfer Complexes in Cucurbit[8]uril. *Angew. Chem. Int. Ed.* **2001,** *40*, 1526-1529.

(95) Jon, S. Y.; Ko, Y. H.; Park, S. H.; Kim, H.-J.; Kim, K., A facile, stereoselective [2 + 2] photoreaction mediated by cucurbit[8]uril. *Chem. Commun.* **2001**, 1938-1939.

(96) Pazos, E.; Novo, P.; Peinador, C.; Kaifer, A. E.; García, M. D., Cucurbit[8]uril (CB[8])-Based Supramolecular Switches. *Angew. Chem. Int. Ed.* **2019,** *58*, 403-416.

(97) Smith, L. C.; Leach, D. G.; Blaylock, B. E.; Ali, O. A.; Urbach, A. R., Sequence-Specific, Nanomolar Peptide Binding via Cucurbit[8]uril-Induced Folding and Inclusion of Neighboring Side Chains. *J. Am. Chem. Soc.* **2015,** *137*, 3663-3669.

(98) Rajgariah, P.; Urbach, A. R., Scope of amino acid recognition by cucurbit[8]uril. *J. Inclusion Phenom. Macrocyclic Chem.* **2008,** *62*, 251-254.

(99) Appel, E. A.; Biedermann, F.; Rauwald, U.; Jones, S. T.; Zayed, J. M.; Scherman, O. A., Supramolecular Cross-Linked Networks via Host−Guest Complexation with Cucurbit[8]uril. *J. Am. Chem. Soc.* **2010,** *132*, 14251-14260.

(100) Rauwald, U.; Scherman, O. A., Supramolecular Block Copolymers with Cucurbit[8]uril in Water. *Angew. Chem. Int. Ed.* **2008,** *47*, 3950-3953.

(101) Liu, Y.; Yang, H.; Wang, Z.; Zhang, X., Cucurbit[8]uril-Based Supramolecular Polymers. *Chem. Asian J.* **2013,** *8*, 1626-1632.

(102) Zou, H.; Liu, J.; Li, Y.; Li, X.; Wang, X., Cucurbit[8]uril-Based Polymers and Polymer Materials. *Small* **2018,** *14*, 1802234.

(103) Flinn, A.; Hough, G. C.; Stoddart, J. F.; Williams, D. J., Decamethylcucurbit[5]uril. *Angew. Chem. Int. Ed.* **1992,** *31*, 1475-1477.

(104) Zhao, J.; Kim, H.-J.; Oh, J.; Kim, S.-Y.; Lee, J. W.; Sakamoto, S.; Yamaguchi, K.; Kim, K., Cucurbit[n]uril Derivatives Soluble in Water and Organic Solvents. *Angew. Chem. Int. Ed.* **2001,** *40*, 4233-4235.

(105) Lin, R.-L.; Liu, J.-X.; Chen, K.; Redshaw, C., Supramolecular chemistry of substituted cucurbit[n]urils. *Inorg. Chem. Front.* **2020,** *7*, 3217-3246.

(106) Isobe, H.; Sato, S.; Nakamura, E., Synthesis of Disubstituted Cucurbit[6]uril and Its Rotaxane Derivative. *Org. Lett.* **2002,** *4*, 1287-1289.

(107) Wu, L.-H.; Ni, X.-L.; Wu, F.; Zhang, Y.-Q.; Zhu, Q.-J.; Xue, S.-F.; Tao, Z., Crystal structures of three partially cyclopentano-substituted cucurbit[6]urils. *J. Mol. Struct.* **2009,** *920*, 183-188.

(108) Wu, F.; Wu, L.-H.; Xiao, X.; Zhang, Y.-Q.; Xue, S.-F.; Tao, Z.; Day, A. I., Locating the Cyclopentano Cousins of the Cucurbit[n]uril Family. *J. Org. Chem.* **2012,** *77*, 606-611.

(109) Vinciguerra, B.; Zavalij, P. Y.; Isaacs, L., Synthesis and Recognition Properties of Cucurbit[8]uril Derivatives. *Org. Lett.* **2015,** *17*, 5068-5071.

(110) Yang, X.; Zhao, W.; Wang, Z.; Huang, Y.; Lee, S. M. Y.; Tao, Z.; Wang, R., Toxicity of hemimethyl-substituted cucurbit[7]uril. *Food Chem. Toxicol.* **2017,** *108*, 510-518.

(111) Zhao, Y.; Mandadapu, V.; Iranmanesh, H.; Beves, J. E.; Day, A. I., The Inheritance Angle: A Determinant for the Number of Members in the Substituted Cucurbit[n]uril Family. *Org. Lett.* **2017,** *19*, 4034-4037.

(112) Cao, L.; Zhang, Y.-Q.; Lin, R.-L.; Liu, J.-X.; Tao, Z., Controllable Synthesis of Dodecamethylcucurbit[6]uril and Its Application in Separating Phenylenediamine Isomers. *Cryst. Growth Des.* **2021,** *21*, 2993-2999.

(113) Kim, K.; Selvapalam, N.; Ko, Y. H.; Park, K. M.; Kim, D.; Kim, J., Functionalized cucurbiturils and their applications. *Chem. Soc. Rev.* **2007,** *36*, 267-279.

(114) Jon, S. Y.; Selvapalam, N.; Oh, D. H.; Kang, J.-K.; Kim, S.-Y.; Jeon, Y. J.; Lee, J. W.; Kim, K., Facile Synthesis of Cucurbit[n]uril Derivatives via Direct Functionalization: Expanding Utilization of Cucurbit[n]uril. *J. Am. Chem. Soc.* **2003,** *125*, 10186-10187.

(115) Ayhan, M. M.; Karoui, H.; Hardy, M.; Rockenbauer, A.; Charles, L.; Rosas, R.; Udachin, K.; Tordo, P.; Bardelang, D.; Ouari, O., Comprehensive Synthesis of Monohydroxy–Cucurbit[n]urils (n = 5, 6, 7, 8): High Purity and High Conversions. *J. Am. Chem. Soc.* **2015,** *137*, 10238-10245.

(116) Lucas, D.; Minami, T.; Iannuzzi, G.; Cao, L.; Wittenberg, J. B.; Anzenbacher, P.; Isaacs, L., Templated Synthesis of Glycoluril Hexamer and Monofunctionalized Cucurbit[6]uril Derivatives. *J. Am. Chem. Soc.* **2011,** *133*, 17966-17976.

(117) Minami, T.; Esipenko, N. A.; Zhang, B.; Kozelkova, M. E.; Isaacs, L.; Nishiyabu, R.; Kubo, Y.; Anzenbacher, P., Supramolecular Sensor for Cancer-Associated Nitrosamines. *J. Am. Chem. Soc.* **2012,** *134*, 20021-20024.

(118) Minami, T.; Esipenko, N. A.; Zhang, B.; Isaacs, L.; Anzenbacher, P., "Turn-on" fluorescent sensor array for basic amino acids in water. *Chem. Commun.* **2014,** *50*, 61-63.

(119) Cao, L.; Isaacs, L., Daisy Chain Assembly Formed from a Cucurbit[6]uril Derivative. *Org. Lett.* **2012,** *14*, 3072-3075.

(120) Vinciguerra, B.; Cao, L.; Cannon, J. R.; Zavalij, P. Y.; Fenselau, C.; Isaacs, L., Synthesis and Self-Assembly Processes of Monofunctionalized Cucurbit[7]uril. *J. Am. Chem. Soc.* **2012,** *134*, 13133-13140.

(121) Bockus, A. T.; Smith, L. C.; Grice, A. G.; Ali, O. A.; Young, C. C.; Mobley, W.; Leek, A.; Roberts, J. L.; Vinciguerra, B.; Isaacs, L.; Urbach, A. R., Cucurbit[7]uril–Tetramethylrhodamine Conjugate for Direct Sensing and Cellular Imaging. *J. Am. Chem. Soc.* **2016,** *138*, 16549-16552.

(122) Li, M.; Lee, A.; Kim, S.; Shrinidhi, A.; Park, K. M.; Kim, K., Cucurbit[7]uril-conjugated dyes as live cell imaging probes: investigation on their cellular uptake and excretion pathways. *Org. Biomol. Chem.* **2019,** *17*, 6215–6220.

(123) Li, M.; Lee, A.; Kim, K. L.; Murray, J.; Shrinidhi, A.; Sung, G.; Park, K. M.; Kim, K., Autophagy Caught in the Act: A Supramolecular FRET Pair Based on an Ultrastable Synthetic Host–Guest Complex Visualizes Autophagosome–Lysosome Fusion. *Angew. Chem. Int. Ed.* **2018,** *57*, 2120-2125.

(124) Gong, B.; Choi, B.-K.; Kim, J.-Y.; Shetty, D.; Ko, Y. H.; Selvapalam, N.; Lee, N. K.; Kim, K., High Affinity Host–Guest FRET Pair for Single-Vesicle Content-Mixing Assay: Observation of Flickering Fusion Events. *J. Am. Chem. Soc.* **2015,** *137*, 8908-8911.

(125) Lee, A.; Li, M.; Ko, Y. H.; Park, S.; Seo, J.; Park, K. M.; Kim, K., Visualization of lipophagy using a supramolecular FRET pair. *Chem. Commun.* **2021,** *57*, 12179-12182.

(126) Li, M.; Kim, S.; Lee, A.; Shrinidhi, A.; Ko, Y. H.; Lim, H. G.; Kim, H. H.; Bae, K. B.; Park, K. M.; Kim, K., Bio-orthogonal Supramolecular Latching inside Live Animals and Its Application for in Vivo Cancer Imaging. *ACS Appl. Mater. Interfaces* **2019,** *11*, 43920-43927.

(127) Kim, K. L.; Sung, G.; Sim, J.; Murray, J.; Li, M.; Lee, A.; Shrinidhi, A.; Park, K. M.; Kim, K., Supramolecular latching system based on ultrastable synthetic binding pairs as versatile tools for protein imaging. *Nat. Commun.* **2018,** *9*, 1712.

(128) Sasmal, R.; Das Saha, N.; Pahwa, M.; Rao, S.; Joshi, D.; Inamdar, M. S.; Sheeba, V.; Agasti, S. S., Synthetic Host–Guest Assembly in Cells and Tissues: Fast, Stable, and Selective Bioorthogonal Imaging via Molecular Recognition. *Anal. Chem.* **2018,** *90*, 11305-11314.

(129) Sasmal, R.; Das Saha, N.; Schueder, F.; Joshi, D.; Sheeba, V.; Jungmann, R.; Agasti, S. S., Dynamic host–guest interaction enables autonomous single molecule blinking and super-resolution imaging. *Chem. Commun.* **2019,** *55*, 14430-14433.

(130) Chen, J.; Li, S.; Wang, Z.; Pan, Y.; Wei, J.; Lu, S.; Zhang, Q.-W.; Wang, L.-H.; Wang, R., Synthesis of an AIEgen functionalized cucurbit[7]uril for subcellular bioimaging and synergistic photodynamic therapy and supramolecular chemotherapy. *Chem. Sci.* **2021,** *12*, 7727-7734.

(131) Lee, H.-K.; Park, K. M.; Jeon, Y. J.; Kim, D.; Oh, D. H.; Kim, H. S.; Park, C. K.; Kim, K., Vesicle Formed by Amphiphilc Cucurbit[6]uril: Versatile, Noncovalent Modification of the Vesicle Surface, and Multivalent Binding of Sugar-Decorated Vesicles to Lectin. *J. Am. Chem. Soc.* **2005,** *127*, 5006-5007.

(132) Kim, E.; Kim, D.; Jung, H.; Lee, J.; Paul, S.; Selvapalam, N.; Yang, Y.; Lim, N.; Park, C. G.; Kim, K., Facile, Template-Free Synthesis of Stimuli-Responsive Polymer Nanocapsules for Targeted Drug Delivery. *Angew. Chem. Int. Ed.* **2010,** *49*, 4405-4408.

(133) Park, K. M.; Lee, D.-W.; Sarkar, B.; Jung, H.; Kim, J.; Ko, Y. H.; Lee, K. E.; Jeon, H.; Kim, K., Reduction-Sensitive, Robust Vesicles with a Non-covalently Modifiable Surface as a Multifunctional Drug-Delivery Platform. *Small* **2010,** *6*, 1430-1441.

(134) Jung, H.; Park, K. M.; Yang, J.-A.; Oh, E. J.; Lee, D.-W.; Park, K.; Ryu, S. H.; Hahn, S. K.; Kim, K., Theranostic systems assembled in situ on demand by host-guest chemistry. *Biomaterials* **2011,** *32*, 7687-7694.

(135) Kim, S.; Yun, G.; Khan, S.; Kim, J.; Murray, J.; Lee, Y. M.; Kim, W. J.; Lee, G.; Kim, S.; Shetty, D.; Kang, J. H.; Kim, J. Y.; Park, K. M.; Kim, K., Cucurbit[6]uril-based polymer nanocapsules as a non-covalent and modular bioimaging platform for multimodal in vivo imaging. *Mater. Horiz.* **2017,** *4*, 450-455.

(136) Cheng, Q.; Li, S.; Sun, C.; Yue, L.; Wang, R., Stimuli-responsive perallyloxycucurbit[6]uril-based nanoparticles for selective drug delivery in melanoma cells. *Mater. Chem. Front.* **2019,** *3*, 199-202.

(137) Park, K. M.; Suh, K.; Jung, H.; Lee, D.-W.; Ahn, Y.; Kim, J.; Baek, K.; Kim, K., Cucurbituril-based nanoparticles: a new efficient vehicle for targeted intracellular delivery of hydrophobic drugs. *Chem. Commun.* **2009**, 71-73.

(138) Park, K. M.; Baek, K.; Ko, Y. H.; Shrinidhi, A.; Murray, J.; Jang, W. H.; Kim, K. H.; Lee, J.-S.; Yoo, J.; Kim, S.; Kim, K., Mono-allyloxylated Cucurbit[7]uril Acts as an Unconventional Amphiphile To Form Light-Responsive Vesicles. *Angew. Chem. Int. Ed.* **2018,** *57*, 3132-3136.

(139) Chen, H.; Zhang, J.; Yu, Q.; Chen, Y.; Tan, Y., Hexanoate-Cucurbit[7]uril: Highly Soluble with Controlled Release Ability. *Chem. Eur. J.* **2020,** *26*, 9445-9448.

(140) Yu, Y.; Li, J.; Zhang, M.; Cao, L.; Isaacs, L., Hydrophobic monofunctionalized cucurbit[7]uril undergoes self-inclusion complexation and forms vesicle-type assemblies. *Chem. Commun.* **2015,** *51*, 3762-3765.

(141) Cao, L.; Hettiarachchi, G.; Briken, V.; Isaacs, L., Cucurbit[7]uril Containers for Targeted Delivery of Oxaliplatin to Cancer Cells. *Angew. Chem. Int. Ed.* **2013,** *52*, 12033-12037.

(142) Samanta, S. K.; Quigley, J.; Vinciguerra, B.; Briken, V.; Isaacs, L., Cucurbit[7]uril Enables Multi-Stimuli-Responsive Release from the Self-Assembled Hydrophobic Phase of a Metal Organic Polyhedron. *J. Am. Chem. Soc.* **2017,** *139*, 9066-9074.

(143) Sun, C.; Zhang, H.; Li, S.; Zhang, X.; Cheng, Q.; Ding, Y.; Wang, L.-H.; Wang, R., Polymeric Nanomedicine with "Lego" Surface Allowing Modular Functionalization and Drug Encapsulation. *ACS Appl. Mater. Interfaces* **2018,** *10*, 25090-25098.

(144) Huang, X.; Chen, T.; Mu, N.; Lam, H. W.; Sun, C.; Yue, L.; Cheng, Q.; Gao, C.; Yuan, Z.; Wang, R., Supramolecular micelles as multifunctional theranostic agents for synergistic photodynamic therapy and hypoxia-activated chemotherapy. *Acta Biomater.* **2021,** *131*, 483-492.

(145) Yang, H.; Yuan, B.; Zhang, X.; Scherman, O. A., Supramolecular Chemistry at Interfaces: Host–Guest Interactions for Fabricating Multifunctional Biointerfaces. *Acc. Chem. Res.* **2014,** *47*, 2106-2115.

(146) Wiemann, M.; Jonkheijm, P., Stimuli-Responsive Cucurbit[n]uril-Mediated Host-Guest Complexes on Surfaces. *Isr. J. Chem.* **2018,** *58*, 314-325.

(147) Hwang, I.; Baek, K.; Jung, M.; Kim, Y.; Park, K. M.; Lee, D.-W.; Selvapalam, N.; Kim, K., Noncovalent Immobilization of Proteins on a Solid Surface by Cucurbit[7]uril-Ferrocenemethylammonium Pair, a Potential Replacement of Biotin−Avidin Pair. *J. Am. Chem. Soc.* **2007,** *129*, 4170-4171.

(148) Ahn, Y.; Jang, Y.; Selvapalam, N.; Yun, G.; Kim, K., Supramolecular Velcro for Reversible Underwater Adhesion. *Angew. Chem. Int. Ed.* **2013,** *52*, 3140-3144.

(149) Zhong, C.; Hu, C.; Kumar, R.; Trouillet, V.; Biedermann, F.; Hirtz, M., Cucurbit[n]uril-Immobilized Sensor Arrays for Indicator-Displacement Assays of Small Bioactive Metabolites. *ACS Appl. Nano Mater.* **2021,** *4*, 4676-4687.

(150) An, Q.; Li, G.; Tao, C.; Li, Y.; Wu, Y.; Zhang, W., A general and efficient method to form self-assembled cucurbit[n]uril monolayers on gold surfaces. *Chem. Commun.* **2008**, 1989-1991.

(151) Young , J. F.; Nguyen , H. D.; Yang, L.; Huskens, J.; Jonkheijm, P.; Brunsveld , L., Strong and Reversible Monovalent Supramolecular Protein Immobilization. *ChemBioChem* **2010,** *11*, 180-183.

(152) Gomez-Casado, A.; Jonkheijm, P.; Huskens, J., Recognition Properties of Cucurbit[7]uril Self-Assembled Monolayers Studied with Force Spectroscopy. *Langmuir* **2011,** *27*, 11508-11513.

(153) Neirynck, P.; Brinkmann, J.; An, Q.; van der Schaft, D. W. J.; Milroy, L.-G.; Jonkheijm, P.; Brunsveld, L., Supramolecular control of cell adhesion via ferrocene–cucurbit[7]uril host–guest binding on gold surfaces. *Chem. Commun.* **2013,** *49*, 3679-3681.

(154) Lee, D.-W.; Park, K. M.; Gong, B.; Shetty, D.; Khedkar, J. K.; Baek, K.; Kim, J.; Ryu, S. H.; Kim, K., A simple modular aptasensor platform utilizing cucurbit[7]uril and a ferrocene derivative as an ultrastable supramolecular linker. *Chem. Commun.* **2015,** *51*, 3098-3101.

(155) An, Q.; Brinkmann, J.; Huskens, J.; Krabbenborg, S.; de Boer, J.; Jonkheijm, P., A Supramolecular System for the Electrochemically Controlled Release of Cells. *Angew. Chem. Int. Ed.* **2012,** *51*, 12233-12237.

(156) González-Campo, A.; Brasch, M.; Uhlenheuer, D. A.; Gómez-Casado, A.; Yang, L.; Brunsveld, L.; Huskens, J.; Jonkheijm, P., Supramolecularly Oriented Immobilization of Proteins Using Cucurbit[8]uril. *Langmuir* **2012,** *28*, 16364-16371.

(157) Lee, D.-W.; Park, K. M.; Banerjee, M.; Ha, S. H.; Lee, T.; Suh, K.; Paul, S.; Jung, H.; Kim, J.; Selvapalam, N.; Ryu, S. H.; Kim, K., Supramolecular fishing for plasma membrane proteins using an ultrastable synthetic host–guest binding pair. *Nat. Chem.* **2011,** *3*, 154-159.

(158) Murray, J.; Sim, J.; Oh, K.; Sung, G.; Lee, A.; Shrinidhi, A.; Thirunarayanan, A.; Shetty, D.; Kim, K., Enrichment of Specifically Labeled Proteins by an Immobilized Host Molecule. *Angew. Chem. Int. Ed.* **2017,** *56*, 2395-2398.

(159) Bush, M. E.; Bouley, N. D.; Urbach, A. R., Charge-Mediated Recognition of N-Terminal Tryptophan in Aqueous Solution by a Synthetic Host. *J. Am. Chem. Soc.* **2005,** *127*, 14511-14517.

(160) Heitmann, L. M.; Taylor, A. B.; Hart, P. J.; Urbach, A. R., Sequence-Specific Recognition and Cooperative Dimerization of N-Terminal Aromatic Peptides in Aqueous Solution by a Synthetic Host. *J. Am. Chem. Soc.* **2006,** *128*, 12574-12581.

(161) Rekharsky, M. V.; Yamamura, H.; Ko, Y. H.; Selvapalam, N.; Kim, K.; Inoue, Y., Sequence recognition and self-sorting of a dipeptide by cucurbit[6]uril and cucurbit[7]uril. *Chem. Commun.* **2008**, 2236-2238.

(162) Urbach, A. R.; Ramalingam, V., Molecular Recognition of Amino Acids, Peptides, and Proteins by Cucurbit[n]uril Receptors. *Isr. J. Chem.* **2011,** *51*, 664-678.

(163) Chinai, J. M.; Taylor, A. B.; Ryno, L. M.; Hargreaves, N. D.; Morris, C. A.; Hart, P. J.; Urbach, A. R., Molecular Recognition of Insulin by a Synthetic Receptor. *J. Am. Chem. Soc.* **2011,** *133*, 8810-8813.

(164) Li, W.; Bockus, A. T.; Vinciguerra, B.; Isaacs, L.; Urbach, A. R., Predictive recognition of native proteins by cucurbit[7]uril in a complex mixture. *Chem. Commun.* **2016,** *52*, 8537-8540.

(165) Webber, M. J.; Appel, E. A.; Vinciguerra, B.; Cortinas, A. B.; Thapa, L. S.; Jhunjhunwala, S.; Isaacs, L.; Langer, R.; Anderson, D. G., Supramolecular PEGylation of biopharmaceuticals. *Proc. Natl. Acad. Sci. U.S.A.* **2016,** *113*, 14189-14194.

(166) Zhang, S.; Assaf, K. I.; Huang, C.; Hennig, A.; Nau, W. M., Ratiometric DNA sensing with a host–guest FRET pair. *Chem. Commun.* **2019,** *55*, 671-674.

(167) Sun, C.; Wang, Z.; Yue, L.; Huang, Q.; Cheng, Q.; Wang, R., Supramolecular Induction of Mitochondrial Aggregation and Fusion. *J. Am. Chem. Soc.* **2020,** *142*, 16523-16527.

(168) Yeom, J.; Kim, S. J.; Jung, H.; Namkoong, H.; Yang, J.; Hwang, B. W.; Oh, K.; Kim, K.; Sung, Y. C.; Hahn, S. K., Supramolecular Hydrogels for Long-Term Bioengineered Stem Cell Therapy. *Adv. Funct. Mater.* **2015,** *4*, 237-244.

(169) Mutihac, R.-C.; Bunaciu, A. A.; Buschmann, H.-J.; Mutihac, L., A brief overview on supramolecular analytical chemistry of cucurbit[n]urils and hemicucurbit[n]urils. *J. Inclusion Phenom. Macrocyclic Chem.* **2020,** *98*, 137-148.

(170) Pinalli, R.; Pedrini, A.; Dalcanale, E., Biochemical sensing with macrocyclic receptors. *Chem. Soc. Rev.* **2018,** *47*, 7006-7026.

(171) Beatty, M. A.; Hof, F., Host–guest binding in water, salty water, and biofluids: general lessons for synthetic, bio-targeted molecular recognition. *Chem. Soc. Rev.* **2021,** *50*, 4812-4832.

(172) Wiskur, S. L.; Ait-Haddou, H.; Lavigne, J. J.; Anslyn, E. V., Teaching Old Indicators New Tricks. *Acc. Chem. Res.* **2001,** *34*, 963-972.

(173) Nguyen, B. T.; Anslyn, E. V., Indicator–displacement assays. *Coord. Chem. Rev.* **2006,** *250*, 3118-3127.

(174) Sedgwick, A. C.; Brewster, J. T.; Wu, T.; Feng, X.; Bull, S. D.; Qian, X.; Sessler, J. L.; James, T. D.; Anslyn, E. V.; Sun, X., Indicator displacement assays (IDAs): the past, present and future. *Chem. Soc. Rev.* **2021,** *50*, 9-38.

(175) Rather, I. A.; Ali, R., Indicator displacement assays: from concept to recent developments. *Org. Biomol. Chem.* **2021,** *19*, 5926-5981.

(176) Jo, H. H.; Lin, C.-Y.; Anslyn, E. V., Rapid Optical Methods for Enantiomeric Excess Analysis: From Enantioselective Indicator Displacement Assays to Exciton-Coupled Circular Dichroism. *Acc. Chem. Res.* **2014,** *47*, 2212-2221.

(177) Dsouza, R. N.; Hennig, A.; Nau, W. M., Supramolecular Tandem Enzyme Assays. *Chem. Eur. J.* **2012,** *18*, 3444-3459.

(178) Ling, Y.; Wang, W.; Kaifer, A. E., A new cucurbit[8]uril-based fluorescent receptor for indole derivatives. *Chem. Commun.* **2007**, 610-612.

(179) Biedermann, F.; Hathazi, D.; Nau, W. M., Associative chemosensing by fluorescent macrocycle–dye complexes – a versatile enzyme assay platform beyond indicator displacement. *Chem. Commun.* **2015,** *51*, 4977-4980.

(180) Sinn, S.; Krämer, J.; Biedermann, F., Teaching old indicators even more tricks: binding affinity measurements with the guest-displacement assay (GDA). *Chem. Commun.* **2020,** *56*, 6620-6623.

(181) Prabodh, A.; Sinn, S.; Grimm, L.; Miskolczy, Z.; Megyesi, M.; Biczók, L.; Bräse, S.; Biedermann, F., Teaching indicators to unravel the kinetic features of host–guest inclusion complexes. *Chem. Commun.* **2020,** *56*, 12327-12330.

(182) Nie, H.; Wei, Z.; Ni, X.-L.; Liu, Y., Assembly and Applications of Macrocyclic-Confinement-Derived Supramolecular Organic Luminescent Emissions from Cucurbiturils. *Chem. Rev.* **2022**.

(183) Cong, H.; Zhu, Q.; Xue, S.; Tao, Z.; Wei, G., Direct coordination of metal ions to cucurbit[n]urils. *Chin. Sci. Bull.* **2010,** *55*, 3633-3640.

(184) Zhang, S.; Tian, Y.; Liu, M.; Hong-Meng, T.; Li, C.-R.; Zeng, X.; Xiao, X.; Redshaw, C., A cucurbit[6]uril-carbon dot system: a potentially new bioimaging agent. *Mater. Chem. Front.* **2022**.

(185) Xu, Y.; Panzner, M. J.; Li, X.; Youngs, W. J.; Pang, Y., Host–guest assembly of squaraine dye in cucurbit[8]uril: its implication in fluorescent probe for mercury ions. *Chem. Commun.* **2010,** *46*, 4073-4075.

(186) Chernikova, E.; Berdnikova, D.; Fedorov, Y.; Fedorova, O.; Peregudov, A.; Isaacs, L., Self-assembly of a ternary architecture driven by cooperative Hg2+ ion binding between cucurbit[7]uril and crown ether macrocyclic hosts. *Chem. Commun.* **2012,** *48*, 7256-7258.

(187) Aliaga, M. E.; García-Río, L.; Pessêgo, M.; Montecinos, R.; Fuentealba, D.; Uribe, I.; Martín-Pastor, M.; García-Beltrán, O., Host–guest interaction of coumarin-derivative dyes and cucurbit[7]uril: leading to the formation of supramolecular ternary complexes with mercuric ions. *New J. Chem.* **2015,** *39*, 3084-3092.

(188) Zhang, X.-D.; Zhao, Y.; Chen, K.; Wang, P.; Kang, Y.-S.; Wu, H.; Sun, W.-Y., Cucurbit[6]uril-based multifunctional supramolecular assemblies: synthesis, removal of Ba(ii) and fluorescence sensing of Fe(iii). *Dalton Trans.* **2018,** *47*, 3958-3964.

(189) Zhang, W.; Luo, Y.; Zhou, Y.; Liu, M.; Xu, W.; Bian, B.; Tao, Z.; Xiao, X., A highly selective fluorescent chemosensor probe for detection of Fe3+ and Ag+ based on supramolecular assembly of cucurbit[10]uril with a pyrene derivative. *Dyes Pigm.* **2020,** *176*, 108235.

(190) Sun, J.; Guo, P.; Liu, M.; Li, H., A novel cucurbit[6]uril-based supramolecular coordination assembly as a multi-responsive luminescent sensor for Fe3+, Cr2O72− and isoquinoline antibiotics in aqueous medium. *J. Mater. Chem. C* **2019,** *7*, 8992-8999.

(191) Zhang, W.; Luo, Y.; Yang, M.-X.; Lin, W.-H.; Redshaw, C.; Ni, X.-L.; Huang, Y.; Tao, Z.; Xiao, X., Twisted cucurbit[14]uril: A new type of CTE macrocycle for Fe3+ sensing. *Microchem. J.* **2022,** *178*, 107364.

(192) Luo, Y.; Xiang, W.; Zhang, X.; Hu, L.; Dong, Y., Electrogenerated chemiluminescence sensor for silver ions based on their coordination interaction with cucurbit[6]uril. *New J. Chem.* **2022,** *46*, 5026-5033.

(193) Shi, X.; Gu, W.; Zhang, C.; Zhao, L.; Li, L.; Peng, W.; Xian, Y., Construction of a Graphene/Au-Nanoparticles/Cucurbit[7]uril-Based Sensor for Pb2+ Sensing. *Chem. Eur. J.* **2016,** *22*, 5643-5648.

(194) Alzard, R. H.; Meyer, H.; Benyettou, F.; Trabolsi, A.; Saleh, N. i., pH-controlled preferential binding of cucurbit[7]uril-coated iron-oxide nanoparticles to 6-mercaptonicotinic acid for fluorescent detection of cadmium ions in the solid state. *Microchim. Acta* **2020,** *187*, 386.

(195) Geng, Q.-X.; Cong, H.; Tao, Z.; Lindoy, L. F.; Wei, G., Cucurbit[7]uril-improved recognition by a fluorescent sensor for cadmium and zinc cations. *Supramol. Chem.* **2016,** *28*, 784-791.

(196) Wang, Q.; Wei, K.-N.; Huang, S.-Z.; Tang, Q.; Tao, Z.; Huang, Y., "Turn-Off" Supramolecular Fluorescence Array Sensor for Heavy Metal Ion Identification. *ACS Omega* **2021,** *6*, 31229-31235.

(197) Deng, X. Y.; Xu, W. T.; Liu, M.; Yang, M. X.; Zhu, Q. J.; Lü, B.; Tao, Z., Cucurbit[8]uril-improved recognition using a fluorescent sensor for different metal cations. *Supramol. Chem.* **2019,** *31*, 616-624.

(198) Shinde, M. N.; Dutta Choudhury, S.; Barooah, N.; Pal, H.; Bhasikuttan, A. C.; Mohanty, J., Metal-Ion-Mediated Assemblies of Thiazole Orange with Cucurbit[7]uril: A Photophysical Study. *J. Phys. Chem. B* **2015,** *119*, 3815-3823.

(199) Zeng, Z.; Zhang, X.; Luo, G.; Meng, Y.; Zhang, L.; Zhao, W.; Tao, Z.; Zhang, Q., Chromone@cucurbit[7]uril triggers the luminescence of lanthanides in water. *J. Mater. Chem. C* **2021,** *9*, 6160-6165.

(200) Luo, Y.; Zhang, W.; Yang, M. X.; Feng, X. H.; Redshaw, C.; Li, Q.; Tao, Z.; Xiao, X., A Twisted Cucurbit[14]Uril-Based Fluorescent Supramolecular Polymer Mediated by Metal Ion. *Macromolecules* **2022,** *55*, 1642-1646.

(201) Li, C. F.; Du, L. M.; Wu, H.; Chang, Y. X., Determination of l-phenylalanine by cucurbit[7]uril sensitized fluorescence quenching method. *Chin. Chem. Lett.* **2011,** *22*, 851-854.

(202) Shan, P.-H.; Zhao, J.; Deng, X.-Y.; Lin, R.-L.; Bian, B.; Tao, Z.; Xiao, X.; Liu, J.-X., Selective recognition and determination of phenylalanine by a fluorescent probe based on cucurbit[8]uril and palmatine. *Anal. Chim. Acta* **2020,** *1104*, 164-171.

(203) Bodoor, K.; El-Barghouthi, M. I.; Assaf, K. I.; Al Hourani, B. J.; Rawashdeh, A. M. M.; Abuhasan, O. M.; Alhamad, D. F.; Abdel-Halim, H. M., A molecular dynamics study of the complexation of tryptophan, phenylalanine and tyrosine amino acids with cucurbit[7]uril. *J. Inclusion Phenom. Macrocyclic Chem.* **2022,** *102*, 159-168.

(204) Li, X.-X.; Xu, W.-T.; Deng, X.-Y.; Tian, L.-F.; Huang, Y.; Tao, Z., Selective Identification of Phenylalanine Using Cucurbit[7,8]uril-Based Fluorescent Probes. *Aust. J. Chem.* **2021,** *74*, 221-229.

(205) Shan, P.-H.; Kan, J.-L.; Deng, X.-Y.; Redshaw, C.; Bian, B.; Fan, Y.; Tao, Z.; Xiao, X., A fluorescent probe based on cucurbit[7]uril for the selective recognition of phenylalanine. *Spectrochim. Acta, Part A* **2020,** *233*, 118177.

(206) Lee, J. W.; Lee, H. H. L.; Ko, Y. H.; Kim, K.; Kim, H. I., Deciphering the Specific High-Affinity Binding of Cucurbit[7]uril to Amino Acids in Water. *J. Phys. Chem. B* **2015,** *119*, 4628-4636.

(207) Liu, S.; Ruspic, C.; Mukhopadhyay, P.; Chakrabarti, S.; Zavalij, P. Y.; Isaacs, L., The Cucurbit[n]uril Family: Prime Components for Self-Sorting Systems. *J. Am. Chem. Soc.* **2005,** *127*, 15959-15967.

(208) Rekharsky, M. V.; Mori, T.; Yang, C.; Ko, Y. H.; Selvapalam, N.; Kim, H.; Sobransingh, D.; Kaifer, A. E.; Liu, S.; Isaacs, L.; Chen, W.; Moghaddam, S.; Gilson, M. K.; Kim, K.; Inoue, Y., A synthetic host-guest system achieves avidin-biotin affinity by overcoming enthalpy–entropy compensation. *Proc. Natl. Acad. Sci. U.S.A.* **2007,** *104*, 20737-20742.

(209) Biedermann, F.; Rauwald, U.; Cziferszky, M.; Williams, K. A.; Gann, L. D.; Guo, B. Y.; Urbach, A. R.; Bielawski, C. W.; Scherman, O. A., Benzobis(imidazolium)–Cucurbit[8]uril Complexes for Binding and Sensing Aromatic Compounds in Aqueous Solution. *Chem. Eur. J.* **2010,** *16*, 13716-13722.

(210) Lagona, J.; Wagner, B. D.; Isaacs, L., Molecular-Recognition Properties of a Water-Soluble Cucurbit[6]uril Analogue. *J. Org. Chem.* **2006,** *71*, 1181-1190.

(211) Ma, D.; Hettiarachchi, G.; Nguyen, D.; Zhang, B.; Wittenberg, J. B.; Zavalij, P. Y.; Briken, V.; Isaacs, L., Acyclic cucurbit[n]uril molecular containers enhance the solubility and bioactivity of poorly soluble pharmaceuticals. *Nat. Chem.* **2012,** *4*, 503-510.

(212) Ma, D.; Zavalij, P. Y.; Isaacs, L., Acyclic Cucurbit[n]uril Congeners Are High Affinity Hosts. *J. Org. Chem.* **2010,** *75*, 4786-4795.

(213) Ganapati, S.; Isaacs, L., Acyclic Cucurbit[n]uril-type Receptors: Preparation, Molecular Recognition Properties and Biological Applications. *Isr. J. Chem.* **2018,** *58*, 250-263.

(214) Hassan, D. S.; De los Santos, Z. A.; Brady, K. G.; Murkli, S.; Isaacs, L.; Wolf, C., Chiroptical sensing of amino acids, amines, amino alcohols, alcohols and terpenes with π-extended acyclic cucurbiturils. *Org. Biomol. Chem.* **2021,** *19*, 4248-4253.

(215) Prabodh, A.; Bauer, D.; Kubik, S.; Rebmann, P.; Klärner, F. G.; Schrader, T.; Delarue Bizzini, L.; Mayor, M.; Biedermann, F., Chirality sensing of terpenes, steroids, amino acids, peptides and drugs with acyclic cucurbit[n]urils and molecular tweezers. *Chem. Commun.* **2020,** *56*, 4652-4655.

(216) Zebaze Ndendjio, S. A.; Isaacs, L., Molecular recognition properties of acyclic cucurbiturils toward amino acids, peptides, and a protein. *Supramol. Chem.* **2019,** *31*, 432-441.

(217) Shen, C.; Ma, D.; Meany, B.; Isaacs, L.; Wang, Y., Acyclic Cucurbit[n]uril Molecular Containers Selectively Solubilize Single-Walled Carbon Nanotubes in Water. *J. Am. Chem. Soc.* **2012,** *134*, 7254-7257.

(218) Gao, Z.-Z.; Kan, J.-L.; Chen, L.-X.; Bai, D.; Wang, H.-Y.; Tao, Z.; Xiao, X., Binding and Selectivity of Essential Amino Acid Guests to the Inverted Cucurbit[7]uril Host. *ACS Omega* **2017,** *2*, 5633-5640.

(219) Buschmann, H.-J.; Mutihac, L.; Mutihac, R.-C.; Schollmeyer, E., Complexation behavior of cucurbit[6]uril with short polypeptides. *Thermochim. Acta* **2005,** *430*, 79-82.

(220) Buschmann, H. J.; Schollmeyer, E.; Mutihac, L., The formation of amino acid and dipeptide complexes with α-cyclodextrin and cucurbit[6]uril in aqueous solutions studied by titration calorimetry. *Thermochim. Acta* **2003,** *399*, 203-208.

(221) Zhang, H.; Grabenauer, M.; Bowers, M. T.; Dearden, D. V., Supramolecular Modification of Ion Chemistry: Modulation of Peptide Charge State and Dissociation Behavior through Complexation with Cucurbit[n]uril (n = 5, 6) or α-Cyclodextrin. *J. Phys. Chem. A* **2009,** *113*, 1508-1517.

(222) Bai, Q.; Zhang, S.; Chen, H.; Sun, T.; Redshaw, C.; Zhang, J.-X.; Ni, X.-L.; Wei, G.; Tao, Z., Alkyl Substituted Cucurbit[6]uril Assisted Competitive Fluorescence Recognition of Lysine and Methionine in Aqueous Solution. *ChemistrySelect* **2017,** *2*, 2569-2573.

(223) Ma, F.; Zheng, X.; Xie, L.; Li, Z., Sequence-dependent nanomolar binding of tripeptides containing N-terminal phenylalanine by Cucurbit[7]uril: A theoretical study. *J. Mol. Liq.* **2021,** *328*, 115479.

(224) Lee, J. W.; Shin, M. H.; Mobley, W.; Urbach, A. R.; Kim, H. I., Supramolecular Enhancement of Protein Analysis via the Recognition of Phenylalanine with Cucurbit[7]uril. *J. Am. Chem. Soc.* **2015,** *137*, 15322-15329.

(225) Smith, A. A. A.; Maikawa, C. L.; Roth, G. A.; Appel, E. A., Site-selective modification of proteins using cucurbit[7]uril as supramolecular protection for N-terminal aromatic amino acids. *Org. Biomol. Chem.* **2020,** *18*, 4371-4375.

(226) Logsdon, L. A.; Urbach, A. R., Sequence-Specific Inhibition of a Nonspecific Protease. *J. Am. Chem. Soc.* **2013,** *135*, 11414-11416.

(227) Li, G.; Yang, W.-Y.; Zhao, Y.-F.; Chen, Y.-X.; Hong, L.; Li, Y.-M., Differential Modulation of the Aggregation of N-Terminal Truncated Aβ using Cucurbiturils. *Chem. Eur. J.* **2018,** *24*, 13647-13653.

(228) de Oliveira, O. V.; Gonçalves, A. d. S.; Almeida, N. E. C. d., Insights into β-amyloid transition prevention by cucurbit[7]uril from molecular modeling. *J. Biomol. Struct. Dyn.* **2021**, 1-11.

(229) Shang, H.; Zhou, A.; Jiang, J.; Liu, Y.; Xie, J.; Li, S.; Chen, Y.; Zhu, X.; Tan, H.; Li, J., Inhibition of the fibrillation of highly amyloidogenic human calcitonin by cucurbit[7]uril with improved bioactivity. *Acta Biomater.* **2018,** *78*, 178-188.

(230) Cao, W.; Qin, X.; Wang, Y.; Dai, Z.; Dai, X.; Wang, H.; Xuan, W.; Zhang, Y.; Liu, Y.; Liu, T., A General Supramolecular Approach to Regulate Protein Functions by Cucurbit[7]uril and Unnatural Amino Acid Recognition. *Angew. Chem. Int. Ed.* **2021,** *60*, 11196-11200.

(231) Li, L.; Liu, M.; Yue, L.; Wang, R.; Zhang, N.; Liang, Y.; Zhang, L.; Cheng, L.; Xia, J.; Wang, R., Host–Guest Protein Assembly for Affinity Purification of Methyllysine Proteomes. *Anal. Chem.* **2020,** *92*, 9322-9329.

(232) Guagnini, F.; Antonik, P. M.; Rennie, M. L.; O'Byrne, P.; Khan, A. R.; Pinalli, R.; Dalcanale, E.; Crowley, P. B., Cucurbit[7]uril-Dimethyllysine Recognition in a Model Protein. *Angew. Chem. Int. Ed.* **2018,** *57*, 7126-7130.

(233) Gamal-Eldin, M. A.; Macartney, D. H., Selective molecular recognition of methylated lysines and arginines by cucurbit[6]uril and cucurbit[7]uril in aqueous solution. *Org. Biomol. Chem.* **2013,** *11*, 488-495.

(234) Prabodh, A.; Wang, Y.; Sinn, S.; Albertini, P.; Spies, C.; Spuling, E.; Yang, L.-P.; Jiang, W.; Bräse, S.; Biedermann, F., Fluorescence detected circular dichroism (FDCD) for supramolecular host–guest complexes. *Chem. Sci.* **2021,** *12*, 9420-9431.

(235) Nguyen, H. D.; Dang, D. T.; van Dongen, J. L. J.; Brunsveld, L., Protein Dimerization Induced by Supramolecular Interactions with Cucurbit[8]uril. *Angew. Chem. Int. Ed.* **2010,** *49*, 895-898.

(236) de Vink, P. J.; Briels, J. M.; Schrader, T.; Milroy, L.-G.; Brunsveld, L.; Ottmann, C., A Binary Bivalent Supramolecular Assembly Platform Based on Cucurbit[8]uril and Dimeric Adapter Protein 14-3-3. *Angew. Chem. Int. Ed.* **2017,** *56*, 8998-9002.

(237) Das, D.; Assaf, K. I.; Nau, W. M., Applications of Cucurbiturils in Medicinal Chemistry and Chemical Biology. *Front. Chem.* **2019,** *7*.

(238) Kim, H.; Oh, J.; Jeon, W. S.; Selvapalam, N.; Hwang, I.; Ko, Y. H.; Kim, K., A new cucurbit[6]uril-based ion-selective electrode for acetylcholine with high selectivity over choline and related quaternary ammonium ions. *Supramol. Chem.* **2012,** *24*, 487-491.

(239) Jang, M.; Kim, H.; Lee, S.; Kim, H. W.; Khedkar, J. K.; Rhee, Y. M.; Hwang, I.; Kim, K.; Oh, J. H., Highly Sensitive and Selective Biosensors Based on Organic Transistors Functionalized with Cucurbit[6]uril Derivatives. *Adv. Funct. Mater.* **2015,** *25*, 4882-4888.

(240) You-Moon, J.; Dongmok, W.; Jaheon, K.; Kimoon, K., A Simple Construction of a Rotaxane and Pseudorotaxane: Syntheses and X-Ray Crystal Structures of Cucurbituril Threaded on Substituted Spermine. *Chem. Lett.* **1996,** *25*, 503-504.

(241) Isobe, H.; Tomita, N.; Lee, J. W.; Kim, H.-J.; Kim, K.; Nakamura, E., Ternary Complexes Between DNA, Polyamine, and Cucurbituril: A Modular Approach to DNA-Binding Molecules. *Angew. Chem. Int. Ed.* **2000,** *39*, 4257-4260.

(242) Im Jun, S.; Wook Lee, J.; Sakamoto, S.; Yamaguchi, K.; Kim, K., Rotaxane-based molecular switch with fluorescence signaling. *Tetrahedron Lett.* **2000,** *41*, 471-475.

(243) Buschmann, H.-j.; Mutihac, L.; Schollmeyer, E., Complex Formation of Crown Ethers with the Cucurbit[6]uril–Spermidine and Cucurbit[6]uril–Spermine Complex in Aqueous Solution. *J. Inclusion Phenom. Macrocyclic Chem.* **2005,** *53*, 85-88.

(244) Kim, K., Mechanically interlocked molecules incorporating cucurbituril and their supramolecular assemblies. *Chem. Soc. Rev.* **2002,** *31*, 96-107.

(245) Park, K. M.; Kim, J.; Ko, Y. H.; Ahn, Y.; Murray, J.; Li, M.; Shrinidhi, A.; Kim, K., Dye-Cucurbit[n]uril Complexes as Sensor Elements for Reliable Pattern Recognition of Biogenic Polyamines. *Bull. Chem. Soc. Jpn.* **2018,** *91*, 95-99.

(246) Naik, V. G.; Kumar, V.; Bhasikuttan, A. C.; Kadu, K.; Ramanan, S. R.; Bhosle, A. A.; Banerjee, M.; Chatterjee, A., Solid-Supported Amplification of Aggregation Emission: A Tetraphenylethylene–Cucurbit[6]uril@Hydroxyapatite-Based Supramolecular Sensing Assembly for the Detection of Spermine and Spermidine in Human Urine and Blood. *ACS Appl. Bio Mater.* **2021,** *4*, 1813-1822.

(247) Jiang, G.; Zhu, W.; Chen, Q.; Li, X.; Zhang, G.; Li, Y.; Fan, X.; Wang, J., Selective fluorescent probes for spermine and 1-adamantanamine based on the supramolecular structure formed between AIE-active molecule and cucurbit[n]urils. *Sens. Actuators, B* **2018,** *261*, 602-607.

(248) Ding, J.; Liu, S.; Xiao, H.-M.; Ye, T.-t.; Zhou, P.; Feng, Y.-Q., Matrix-assisted laser desorption/ionization mass spectrometry for the analysis of polyamines in plant micro-tissues using cucurbituril as a host molecule. *Anal. Chim. Acta* **2017,** *987*, 56-63.

(249) Galego, L. R.; Rodrigues, M. A. A.; Mendes, D. C.; Jockusch, S.; Da Silva, J. P., Quantitative analysis of biogenic polyamines in distilled drinks by direct electrospray ionization tandem mass spectrometry using a nanocontainer. *Rapid Commun. Mass Spectrom.* **2016,** *30*, 1963-1968.

(250) Zhang, H.; Liu, M.; Zhu, X.; Li, H., Detection of Spermine Using Cucurbit[7]uril-phenazopyridine Host-Guest Inclusion Complex as a Platform. *Chem. Lett.* **2021,** *50*, 154-157.

(251) Liu, K.; Yao, Y.; Kang, Y.; Liu, Y.; Han, Y.; Wang, Y.; Li, Z.; Zhang, X., A supramolecular approach to fabricate highly emissive smart materials. *Sci. Rep.* **2013,** *3*, 2372.

(252) Bhosle, A. A.; Banerjee, M.; Barooah, N.; Bhasikuttan, A. C.; Kadu, K.; Ramanan, S. R.; Chatterjee, A., ESIPT-active hydroxybenzothiazole-picolinium@CB[7]-HAp NPs based supramolecular sensing assembly for spermine, spermidine and cadaverine: Application in monitoring cancer biomarkers and food spoilage. *J. Photochem. Photobiol., A* **2022,** *426*, 113770.

(253) Zhang, C.-X.; Kong, X.; Li, H.-W.; Li, B.; Wu, L.; Wu, Y., A sustainable luminescence-enhanced tri-assembly of polyoxometalate-peptide-polyamine developed for ultrasensitive spermine determination and discrimination. *Colloids Surf., B* **2022,** *212*, 112379.

(254) Ganapati, S.; Grabitz, S. D.; Murkli, S.; Scheffenbichler, F.; Rudolph, M. I.; Zavalij, P. Y.; Eikermann, M.; Isaacs, L., Molecular Containers Bind Drugs of Abuse in Vitro and Reverse the Hyperlocomotive Effect of Methamphetamine in Rats. *ChemBioChem* **2017,** *18*, 1583-1588.

(255) Du, X.; Hao, H.; Qin, A.; Tang, B. Z., Highly sensitive chemosensor for detection of methamphetamine by the combination of AIE luminogen and cucurbit[7]uril. *Dyes Pigm.* **2020,** *180*, 108413.

(256) Li, H.; Hu, X.; Zhao, J.; Koh, K.; Chen, H., A label-free impedimetric sensor for the detection of an amphetamine-type derivative based on cucurbit[7]uril-mediated three-dimensional AuNPs. *Electrochem. Commun.* **2019,** *100*, 126-133.

(257) Shcherbakova, E. G.; Zhang, B.; Gozem, S.; Minami, T.; Zavalij, P. Y.; Pushina, M.; Isaacs, L. D.; Anzenbacher, P., Supramolecular Sensors for Opiates and Their Metabolites. *J. Am. Chem. Soc.* **2017,** *139*, 14954-14960.

(258) Mehranfar, A.; Izadyar, M.; Shamkhali, A. N., A joint MD/QM study on the possibility of alkaloids detection by cucurbiturils and graphene oxide-cucurbituril composites. *J. Mol. Liq.* **2018,** *272*, 963-972.

(259) Shi, L.; Liu, M.; Li, H., A cucurbit[6]uril-based supramolecular assembly as a highly sensitive and quickly responsive luminescent sensor for the detection of fluoroquinolone antibiotics in simulated wastewater. *CrystEngComm* **2020,** *22*, 3753-3758.

(260) Zhang, Y.; Yan, B., A novel cucurbit[7]uril anchored bis-functionalized metal-organic framework hybrid and its potential use in fluorescent analysis of illegal stimulants in saliva. *Sens. Actuators, B* **2020,** *324*, 128656.

(261) Minami, T.; Esipenko, N. A.; Akdeniz, A.; Zhang, B.; Isaacs, L.; Anzenbacher, P., Multianalyte Sensing of Addictive Over-the-Counter (OTC) Drugs. *J. Am. Chem. Soc.* **2013,** *135*, 15238-15243.

(262) Hennig, A.; Bakirci, H.; Nau, W. M., Label-free continuous enzyme assays with macrocycle-fluorescent dye complexes. *Nat. Methods* **2007,** *4*, 629-632.

(263) Bailey, D. M.; Hennig, A.; Uzunova, V. D.; Nau, W. M., Supramolecular Tandem Enzyme Assays for Multiparameter Sensor Arrays and Enantiomeric Excess Determination of Amino Acids. *Chem. Eur. J.* **2008,** *14*, 6069-6077.

(264) Nau, W. M.; Ghale, G.; Hennig, A.; Bakirci, H.; Bailey, D. M., Substrate-Selective Supramolecular Tandem Assays: Monitoring Enzyme Inhibition of Arginase and Diamine Oxidase by Fluorescent Dye Displacement from Calixarene and Cucurbituril Macrocycles. *J. Am. Chem. Soc.* **2009,** *131*, 11558-11570.

(265) Ghale, G.; Ramalingam, V.; Urbach, A. R.; Nau, W. M., Determining Protease Substrate Selectivity and Inhibition by Label-Free Supramolecular Tandem Enzyme Assays. *J. Am. Chem. Soc.* **2011,** *133*, 7528-7535.

(266) Ghale, G.; Nau, W. M., Dynamically Analyte-Responsive Macrocyclic Host–Fluorophore Systems. *Acc. Chem. Res.* **2014,** *47*, 2150-2159.

(267) Ghale, G.; Lanctôt, A. G.; Kreissl, H. T.; Jacob, M. H.; Weingart, H.; Winterhalter, M.; Nau, W. M., Chemosensing Ensembles for Monitoring Biomembrane Transport in Real Time. *Angew. Chem. Int. Ed.* **2014,** *53*, 2762-2765.

(268) Barba-Bon, A.; Pan, Y.-C.; Biedermann, F.; Guo, D.-S.; Nau, W. M.; Hennig, A., Fluorescence Monitoring of Peptide Transport Pathways into Large and Giant Vesicles by Supramolecular Host–Dye Reporter Pairs. *J. Am. Chem. Soc.* **2019,** *141*, 20137-20145.

(269) He, S.; Zhiti, A.; Barba-Bon, A.; Hennig, A.; Nau, W. M., Real-Time Parallel Artificial Membrane Permeability Assay Based on Supramolecular Fluorescent Artificial Receptors. *Front. Chem.* **2020,** *8*.

(270) Biedermann, F.; Ghale, G.; Hennig, A.; Nau, W. M., Fluorescent artificial receptor-based membrane assay (FARMA) for spatiotemporally resolved monitoring of biomembrane permeability. *Commun. Biol.* **2020,** *3*, 383.

(271) Hu, C.; Grimm, L.; Prabodh, A.; Baksi, A.; Siennicka, A.; Levkin, P. A.; Kappes, M. M.; Biedermann, F., Covalent cucurbit[7]uril–dye conjugates for sensing in aqueous saline media and biofluids. *Chem. Sci.* **2020,** *11*, 11142-11153.

(272) You, L.; Zha, D.; Anslyn, E. V., Recent Advances in Supramolecular Analytical Chemistry Using Optical Sensing. *Chem. Rev.* **2015,** *115*, 7840-7892.

(273) Bai, L.-M.; Zhou, H.; Liu, W.-E.; Chai, H.; Yang, L.-P.; Yan, W.; Zhang, W.; Yang, H.-H.; Jiang, W., Fluorescent monitoring of the reaction kinetics of nonfluorescent molecules enabled by a fluorescent receptor. *Chem. Commun.* **2019,** *55*, 3128-3131.

(274) Assaf, K. I.; Nau, W. M., Cucurbiturils: from synthesis to high-affinity binding and catalysis. *Chem. Soc. Rev.* **2015,** *44*, 394-418.

(275) Miskolczy, Z.; Megyesi, M.; Biczók, L.; Prabodh, A.; Biedermann, F., Kinetics and Mechanism of Cation-Induced Guest Release from Cucurbit[7]uril. *Chem. Eur. J.* **2020,** *26*, 7433-7441.

(276) Zhu, L.; Zhao, Z.; Zhang, X.; Zhang, H.; Liang, F.; Liu, S., A Highly Selective and Strong Anti-Interference Host-Guest Complex as Fluorescent Probe for Detection of Amantadine by Indicator Displacement Assay. *Molecules* **2018,** *23*, 947.

(277) Yang, H.; Liu, Y.; Yang, L.; Liu, K.; Wang, Z.; Zhang, X., Cucurbit[7]uril as a "protective agent": controlling photochemistry and detecting 1-adamantanamine. *Chem. Commun.* **2013,** *49*, 3905-3907.

(278) Sinn, S.; Spuling, E.; Bräse, S.; Biedermann, F., Rational design and implementation of a cucurbit[8]uril-based indicator-displacement assay for application in blood serum. *Chem. Sci.* **2019,** *10*, 6584-6593.

(279) Lazar, A. I.; Biedermann, F.; Mustafina, K. R.; Assaf, K. I.; Hennig, A.; Nau, W. M., Nanomolar Binding of Steroids to Cucurbit[n]urils: Selectivity and Applications. *J. Am. Chem. Soc.* **2016,** *138*, 13022-13029.

(280) Moghaddam, S.; Yang, C.; Rekharsky, M.; Ko, Y. H.; Kim, K.; Inoue, Y.; Gilson, M. K., New Ultrahigh Affinity Host−Guest Complexes of Cucurbit[7]uril with Bicyclo[2.2.2]octane and Adamantane Guests: Thermodynamic Analysis and Evaluation of M2 Affinity Calculations. *J. Am. Chem. Soc.* **2011,** *133*, 3570-3581.

(281) Ayhan, M. M.; Karoui, H.; Hardy, M.; Rockenbauer, A.; Charles, L.; Rosas, R.; Udachin, K.; Tordo, P.; Bardelang, D.; Ouari, O., Correction to "Comprehensive Synthesis of Monohydroxy–Cucurbit[n]urils (n = 5, 6, 7, 8): High Purity and High Conversions". *J. Am. Chem. Soc.* **2016,** *138*, 2060-2060.

(282) An, J.; Kim, S.; Shrinidhi, A.; Kim, J.; Banna, H.; Sung, G.; Park, K. M.; Kim, K., Purification of protein therapeutics via high-affinity supramolecular host–guest interactions. *Nat. Biomed. Eng.* **2020**.

(283) Dong, N.; He, J.; Li, T.; Peralta, A.; Avei, M. R.; Ma, M.; Kaifer, A. E., Synthesis and Binding Properties of Monohydroxycucurbit[7]uril: A Key Derivative for the Functionalization of Cucurbituril Hosts. *J. Org. Chem* **2018,** *83*, 5467-5473.

(284) Dsouza, R. N.; Pischel, U.; Nau, W. M., Fluorescent Dyes and Their Supramolecular Host/Guest Complexes with Macrocycles in Aqueous Solution. *Chem. Rev.* **2011,** *111*, 7941-7980.

(285) Shaikh, M.; Mohanty, J.; Singh, P. K.; Nau, W. M.; Pal, H., Complexation of acridine orange by cucurbit[7]uril and β-cyclodextrin: photophysical effects and pKa shifts. *Photochem. Photobiol. Sci.* **2008,** *7*, 408-414.

(286) LaManna, J. C.; McCracken, K. A., The use of Neutral Red as an intracellular pH indicator in rat brain cortex in vivo. *Anal. Biochem.* **1984,** *142*, 117-125.

(287) Megyesi, M.; Biczók, L.; Jablonkai, I., Highly Sensitive Fluorescence Response to Inclusion Complex Formation of Berberine Alkaloid with Cucurbit[7]uril. *J. Phys. Chem. C* **2008,** *112*, 3410-3416.

(288) Miskolczy, Z.; Biczók, L., Kinetics and Thermodynamics of Berberine Inclusion in Cucurbit[7]uril. *J. Phys. Chem. B* **2014,** *118*, 2499-2505.

(289) Cao, H.; Liao, S.; Zhong, W.; Xiao, X.; Zhu, J.; Li, W.; Wu, X.; Feng, Y., Synthesis, Characterization, and Biological Evaluations of 1,3,5-Triazine Derivatives of Metformin Cyclization with Berberine and Magnolol in the Presence of Sodium Methylate. *Molecules* **2017,** *22*, 1752.

(290) Lu, G.; Lam, S.; Burgess, K., An iterative route to "decorated" ethylene glycol-based linkers. *Chem. Commun.* **2006,** *42*, 1652-1654.

(291) Lee, T.-C.; Kalenius, E.; Lazar, A. I.; Assaf, K. I.; Kuhnert, N.; Grün, C. H.; Jänis, J.; Scherman, O. A.; Nau, W. M., Chemistry inside molecular containers in the gas phase. *Nat. Chem.* **2013,** *5*, 376-382.

(292) Biedermann, F.; Elmalem, E.; Ghosh, I.; Nau, W. M.; Scherman, O. A., Strongly Fluorescent, Switchable Perylene Bis(diimide) Host–Guest Complexes with Cucurbit[8]uril In Water. *Angew. Chem. Int. Ed.* **2012,** *51*, 7739-7743.

(293) Ong, W.; Kaifer, A. E., Salt Effects on the Apparent Stability of the Cucurbit[7]uril−Methyl Viologen Inclusion Complex. *J. Org. Chem.* **2004,** *69*, 1383-1385.

(294) Jeon, Y.-M.; Kim, J.; Whang, D.; Kim, K., Molecular Container Assembly Capable of Controlling Binding and Release of Its Guest Molecules: Reversible Encapsulation of Organic Molecules in Sodium Ion Complexed Cucurbituril. *J. Am. Chem. Soc.* **1996,** *118*, 9790-9791.

(295) Maciel, A. T.; Vitorio, D.; Salles, L. D.; Park, M., Sodium Concentration in Urine Greater than in the Plasma: Possible Biomarker of Normal Renal Function and Better Outcome in Critically Ill Patients. *Anaesth. Intes. Care.* **2014,** *42*, 584-591.

(296) Lee, E.-C.; Kim, H.-J.; Park, S. Y., Reversible Shape-Morphing and Fluorescence-Switching in Supramolecular Nanomaterials Consisting of Amphiphilic Cyanostilbene and Cucurbit[7]uril. *Chem. Asian J.* **2019,** *14*, 1457-1461.

(297) Marquez, C.; Nau, W. M., Two Mechanisms of Slow Host–Guest Complexation between Cucurbit[6]uril and Cyclohexylmethylamine: pH-Responsive Supramolecular Kinetics. *Angew. Chem. Int. Ed.* **2001,** *40*, 3155-3160.

(298) Francisco, V.; Piñeiro, A.; Nau, W. M.; García-Río, L., The "True" Affinities of Metal Cations to p-Sulfonatocalix[4]arene: A Thermodynamic Study at Neutral pH Reveals a Pitfall Due to Salt Effects in Microcalorimetry. *Chem. Eur. J.* **2013,** *19*, 17809-17820.

(299) Sindelar, V.; Cejas, M. A.; Raymo, F. M.; Kaifer, A. E., Tight inclusion complexation of 2,7-dimethyldiazapyrenium in cucurbit[7]uril. *New J. Chem.* **2005,** *29*, 280-282.

(300) Drugs.com Amantadine Dosage. https://www.drugs.com/dosage/amantadine.html.

(301) Bai, D.; PharmD What You Need to Know About Amantadine for Parkinson Disease. https://www.neurologylive.com/clinical-focus/what-you-need-to-know-about-amantadine-for-parkinson-disease.

(302) Wang, G.-Q.; Qin, Y.-F.; Du, L.-M.; Li, J.-F.; Jing, X.; Chang, Y.-X.; Wu, H., Determination of amantadine and rimantadine using a sensitive fluorescent probe. *Spectrochim. Acta, Part A* **2012,** *98*, 275-281.

(303) Kornhuber, J.; Quack, G.; Danysz, W.; Jellinger, K.; Danielczyk, W.; Gsell, W.; Riederer, P., Therapeutic brain concentration of the NMDA receptor antagonist amantadine. *Neuropharmacology* **1995,** *34*, 713-721.

(304) Aoki, F. Y.; Sitar, D. S., Clinical Pharmacokinetics of Amantadine Hydrochloride. *Clin. Pharmacokinet.* **1988,** *14*, 35-51.

(305) Bennett, J. E.; Dolin, R.; Blaser, M. J.; Mandell, G. L., *Mandell, Douglas, and Bennett's Principles and Practice of Infectious Diseases*. Elsevier Health Sciences: 2009.

(306) Goldberg, S.; Kozlovsky, A.; Gordon, D.; Gelernter, I.; Sintov, A.; Rosenberg, M., Cadaverine as a Putative Component of Oral Malodor. *J. Dent. Res.* **1994,** *73*, 1168-1172.

(307) Alnajjar, M. A.; Bartelmeß, J.; Hein, R.; Ashokkumar, P.; Nilam, M.; Nau, W. M.; Rurack, K.; Hennig, A., Rational design of boron-dipyrromethene (BODIPY) reporter dyes for cucurbit[7]uril. *Beilstein J. Org. Chem.* **2018,** *14*, 1961-1971.

(308) Masson, E.; Raeisi, M.; Kotturi, K., Kinetics Inside, Outside and Through Cucurbiturils. *Isr. J. Chem.* **2018,** *58*, 413-434.

(309) Appel, E. A.; Biedermann, F.; Hoogland, D.; del Barrio, J.; Driscoll, M. D.; Hay, S.; Wales, D. J.; Scherman, O. A., Decoupled Associative and Dissociative Processes in Strong yet Highly Dynamic Host–Guest Complexes. *J. Am. Chem. Soc.* **2017,** *139*, 12985-12993.

(310) Mako, T. L.; Racicot, J. M.; Levine, M., Supramolecular Luminescent Sensors. *Chem. Rev.* **2019,** *119*, 322-477.

(311) Cejas, M. A.; Raymo, F. M., Fluorescent Diazapyrenium Films and Their Response to Dopamine. *Langmuir* **2005,** *21*, 5795-5802.

(312) Jiao, D.; Biedermann, F.; Scherman, O. A., Size Selective Supramolecular Cages from Aryl-Bisimidazolium Derivatives and Cucurbit[8]uril. *Org. Lett.* **2011,** *13*, 3044-3047.

(313) Wingard, L. A.; Johnson, E. C.; Sabatini, J. J., Efficient method for the cycloaminomethylation of glycoluril. *Tetrahedron Lett.* **2016,** *57*, 1681-1682.

(314) Marquez, C.; Fang, H.; Nau, W. M., Cucurbiturils: molecular nanocapsules for time-resolved fluorescence-based assays. *IEEE Transactions on NanoBioscience* **2004,** *3*, 39-45.

(315) Shadrikova, V. A.; Golovin, E. V.; Klimochkin, Y. N., Adamantylation of Pyridine Derivatives. *Chem. Heterocycl. Compd.* **2015,** *50*, 1586-1594.

(316) Escobar, L.; Ballester, P., Molecular Recognition in Water Using Macrocyclic Synthetic Receptors. *Chem. Rev.* **2021,** *121*, 2445-2514.

(317) Hargrove, A. E.; Nieto, S.; Zhang, T.; Sessler, J. L.; Anslyn, E. V., Artificial Receptors for the Recognition of Phosphorylated Molecules. *Chem. Rev.* **2011,** *111*, 6603-6782.

(318) Bell, T. W.; Hext, N. M., Supramolecular optical chemosensors for organic analytes. *Chem. Soc. Rev.* **2004,** *33*, 589-598.

(319) Grimm, L. M.; Sinn, S.; Krstić, M.; D'Este, E.; Sonntag, I.; Prasetyanto, E. A.; Kuner, T.; Wenzel, W.; De Cola, L.; Biedermann, F., Fluorescent Nanozeolite Receptors for the Highly Selective and Sensitive Detection of Neurotransmitters in Water and Biofluids. *Adv. Mater.* **2021,** *33*, 2104614.

(320) Cram, D. J., Preorganization—From Solvents to Spherands. *Angew. Chem. Int. Ed.* **1986,** *25*, 1039-1057.

(321) Dydio, P.; Reek, J. N. H., Supramolecular control of selectivity in transition-metal catalysis through substrate preorganization. *Chem. Sci.* **2014,** *5*, 2135-2145.

(322) Alfonso, I.; Bolte, M.; Bru, M.; Burguete, M. I.; Luis, S. V.; Rubio, J., Supramolecular Control for the Modular Synthesis of Pseudopeptidic Macrocycles through an Anion-Templated Reaction. *J. Am. Chem. Soc.* **2008,** *130*, 6137-6144.

(323) Deng, C.; Liu, Z.; Ma, C.; Zhang, H.; Chi, L., Dynamic Supramolecular Template: Multiple Stimuli-Controlled Size Adjustment of Porous Networks. *Langmuir* **2020,** *36*, 5510-5516.

(324) Giuseppone, N.; Schmitt, J.-L.; Lehn, J.-M., Driven Evolution of a Constitutional Dynamic Library of Molecular Helices Toward the Selective Generation of [2 × 2] Gridlike Arrays under the Pressure of Metal Ion Coordination. *J. Am. Chem. Soc.* **2006,** *128*, 16748-16763.

(325) Ruff, Y.; Garavini, V.; Giuseppone, N., Reversible Native Chemical Ligation: A Facile Access to Dynamic Covalent Peptides. *J. Am. Chem. Soc.* **2014,** *136*, 6333-6339.

(326) Vantomme, G.; Jiang, S.; Lehn, J.-M., Adaptation in Constitutional Dynamic Libraries and Networks, Switching between Orthogonal Metalloselection and Photoselection Processes. *J. Am. Chem. Soc.* **2014,** *136*, 9509-9518.

(327) Atcher, J.; Moure, A.; Bujons, J.; Alfonso, I., Salt-Induced Adaptation of a Dynamic Combinatorial Library of Pseudopeptidic Macrocycles: Unraveling the Electrostatic Effects in Mixed Aqueous Media. *Chem. Eur. J.* **2015,** *21*, 6869-6878.

(328) Black, S. P.; Stefankiewicz, A. R.; Smulders, M. M. J.; Sattler, D.; Schalley, C. A.; Nitschke, J. R.; Sanders, J. K. M., Generation of a Dynamic System of Three-Dimensional Tetrahedral Polycatenanes. *Angew. Chem. Int. Ed.* **2013,** *52*, 5749-5752.

(329) Harrison, E. E.; Carpenter, B. A.; St. Louis, L. E.; Mullins, A. G.; Waters, M. L., Development of "Imprint-and-Report" Dynamic Combinatorial Libraries for Differential Sensing Applications. *J. Am. Chem. Soc.* **2021,** *143*, 14845-14854.

(330) Lafuente, M.; Solà, J.; Alfonso, I., A Dynamic Chemical Network for Cystinuria Diagnosis. *Angew. Chem. Int. Ed.* **2018,** *57*, 8421-8424.

(331) Pedersen, C. J., The Discovery of Crown Ethers. *Science* **1988,** *241*, 536-540.

(332) Cram, D. J., The Design of Molecular Hosts, Guests, and Their Complexes. *Science* **1988,** *240*, 760-767.

(333) Crini, G., Review: A History of Cyclodextrins. *Chem. Rev.* **2014,** *114*, 10940-10975.

(334) Kappe, T., The early history of calixarene chemistry. *J. Inclusion Phenom. Mol. Recognit. Chem.* **1994,** *19*, 3-15.

(335) Ogoshi, T.; Kanai, S.; Fujinami, S.; Yamagishi, T.-a.; Nakamoto, Y., para-Bridged Symmetrical Pillar[5]arenes: Their Lewis Acid Catalyzed Synthesis and Host–Guest Property. *J. Am. Chem. Soc.* **2008,** *130*, 5022-5023.

(336) Badjić, J. D.; Nelson, A.; Cantrill, S. J.; Turnbull, W. B.; Stoddart, J. F., Multivalency and Cooperativity in Supramolecular Chemistry. *Acc. Chem. Res.* **2005,** *38*, 723-732.

(337) Xue, W.; Zavalij, P. Y.; Isaacs, L., Pillar[n]MaxQ: A New High Affinity Host Family for Sequestration in Water. *Angew. Chem. Int. Ed.* **2020,** *59*, 13313-13319.

(338) Gibb, C. L. D.; Gibb, B. C., Well-Defined, Organic Nanoenvironments in Water: The Hydrophobic Effect Drives a Capsular Assembly. *J. Am. Chem. Soc.* **2004,** *126*, 11408-11409.

(339) Jordan, J. H.; Gibb, B. C., Molecular containers assembled through the hydrophobic effect. *Chem. Soc. Rev.* **2015,** *44*, 547-585.

(340) Assaf, K. I.; Nau, W. M., The Chaotropic Effect as an Assembly Motif in Chemistry. *Angew. Chem. Int. Ed.* **2018,** *57*, 13968-13981.

(341) Lehn, J. M.; Sauvage, J. P., Cryptates. XVI. [2]-Cryptates. Stability and selectivity of alkali and alkaline-earth macrobicyclic complexes. *J. Am. Chem. Soc.* **1975,** *97*, 6700-6707.

(342) Zhang, Z.; Yue, Y.-X.; Xu, L.; Wang, Y.; Geng, W.-C.; Li, J.-J.; Kong, X.-l.; Zhao, X.; Zheng, Y.; Zhao, Y.; Shi, L.; Guo, D.-S.; Liu, Y., Macrocyclic-Amphiphile-Based Self-Assembled Nanoparticles for Ratiometric Delivery of Therapeutic Combinations to Tumors. *Adv. Mater.* **2021,** *33*, 2007719.

(343) Beatty, M. A.; Selinger, A. J.; Li, Y.; Hof, F., Parallel Synthesis and Screening of Supramolecular Chemosensors That Achieve Fluorescent Turn-on Detection of Drugs in Saliva. *J. Am. Chem. Soc.* **2019,** *141*, 16763-16771.

(344) Selinger, A. J.; Cavallin, N. A.; Yanai, A.; Birol, I.; Hof, F., Template-Directed Synthesis of Bivalent, Broad-Spectrum Hosts for Neuromuscular Blocking Agents**. *Angew. Chem. Int. Ed.* **2022,** *61*, e202113235.

(345) Murray, J.; Kim, K.; Ogoshi, T.; Yao, W.; Gibb, B. C., The aqueous supramolecular chemistry of cucurbit[n]urils, pillar[n]arenes and deep-cavity cavitands. *Chem. Soc. Rev.* **2017,** *46*, 2479-2496.

(346) Biros, S. M.; Rebek, J. J., Structure and binding properties of water-soluble cavitands and capsules. *Chem. Soc. Rev.* **2007,** *36*, 93-104.

(347) Yang, J.-M.; Chen, Y.-Q.; Yu, Y.; Ballester, P.; Rebek, J., Rigidified Cavitand Hosts in Water: Bent Guests, Shape Selectivity, and Encapsulation. *J. Am. Chem. Soc.* **2021,** *143*, 19517-19524.

(348) Yang, L.-P.; Wang, X.; Yao, H.; Jiang, W., Naphthotubes: Macrocyclic Hosts with a Biomimetic Cavity Feature. *Acc. Chem. Res.* **2020,** *53*, 198-208.

(349) Huang, X.; Wang, X.; Quan, M.; Yao, H.; Ke, H.; Jiang, W., Biomimetic Recognition and Optical Sensing of Carboxylic Acids in Water by Using a Buried Salt Bridge and the Hydrophobic Effect. *Angew. Chem. Int. Ed.* **2021,** *60*, 1929-1935.

(350) Jia, F.; Schröder, H. V.; Yang, L.-P.; von Essen, C.; Sobottka, S.; Sarkar, B.; Rissanen, K.; Jiang, W.; Schalley, C. A., Redox-Responsive Host–Guest Chemistry of a Flexible Cage with Naphthalene Walls. *J. Am. Chem. Soc.* **2020,** *142*, 3306-3310.

(351) Wang, B.; Han, J.; Bojanowski, N. M.; Bender, M.; Ma, C.; Seehafer, K.; Herrmann, A.; Bunz, U. H. F., An Optimized Sensor Array Identifies All Natural Amino Acids. *ACS Sensors* **2018,** *3*, 1562-1568.

(352) Krämer, J.; Kang, R.; Grimm, L. M.; De Cola, L.; Picchetti, P.; Biedermann, F., Molecular Probes, Chemosensors, and Nanosensors for Optical Detection of Biorelevant Molecules and Ions in Aqueous Media and Biofluids. *Chem. Rev.* **2022,** *122*, 3459-3636.

(353) Buryak, A.; Severin, K., A Chemosensor Array for the Colorimetric Identification of 20 Natural Amino Acids. *J. Am. Chem. Soc.* **2005,** *127*, 3700-3701.

(354) Wright, A. T.; Anslyn, E. V., Differential receptor arrays and assays for solution-based molecular recognition. *Chem. Soc. Rev.* **2006,** *35*, 14-28.

(355) Ghosh, P. B.; Whitehouse, M. W., 7-chloro-4-nitrobenzo-2-oxa-1,3-diazole: a new fluorigenic reagent for amino acids and other amines. *Biochem. J.* **1968,** *108*, 155-156.

(356) Carroy, G.; Lemaur, V.; Henoumont, C.; Laurent, S.; De Winter, J.; De Pauw, E.; Cornil, J.; Gerbaux, P., Flying Cages in Traveling Wave Ion Mobility: Influence of the Instrumental Parameters on the Topology of the Host–Guest Complexes. *J. Am. Soc. Mass Spectrom.* **2018,** *29*, 121-132.

(357) Larriba, C.; Hogan, C. J., Free molecular collision cross section calculation methods for nanoparticles and complex ions with energy accommodation. *J. Comput. Phys.* **2013,** *251*, 344-363.

(358) Daykin, C. A.; Foxall, P. J. D.; Connor, S. C.; Lindon, J. C.; Nicholson, J. K., The Comparison of Plasma Deproteinization Methods for the Detection of Low-Molecular-Weight Metabolites by 1H Nuclear Magnetic Resonance Spectroscopy. *Anal. Biochem.* **2002,** *304*, 220-230.

(359) Association, W. M., World Medical Association Declaration of Helsinki: Ethical Principles for Medical Research Involving Human Subjects. *JAMA* **2013,** *310*, 2191-2194.

(360) Manti, S.; Licari, A., How to obtain informed consent for research. *Breathe* **2018,** *14*, 145-152.

(361) Nijhawan, L. P.; Janodia, M. D.; Muddukrishna, B. S.; Bhat, K. M.; Bairy, K. L.; Udupa, N.; Musmade, P. B., Informed consent: Issues and challenges. *J. Adv. Pharm. Technol. Res.* **2013,** *4*, 134-140.

(362) Stow, S. M.; Causon, T. J.; Zheng, X.; Kurulugama, R. T.; Mairinger, T.; May, J. C.; Rennie, E. E.; Baker, E. S.; Smith, R. D.; McLean, J. A.; Hann, S.; Fjeldsted, J. C., An Interlaboratory Evaluation of Drift Tube Ion Mobility–Mass Spectrometry Collision Cross Section Measurements. *Anal. Chem.* **2017,** *89*, 9048-9055.

(363) Furche, F.; Ahlrichs, R.; Hättig, C.; Klopper, W.; Sierka, M.; Weigend, F., Turbomole. *Wiley Interdisciplinary Reviews: Computational Molecular Science* **2014,** *4*, 91-100.

(364) Becke, A. D., Density-functional exchange-energy approximation with correct asymptotic behavior. *Phys. Rev. A* **1988,** *38*, 3098-3100.

(365) Perdew, J. P., Density-functional approximation for the correlation energy of the inhomogeneous electron gas. *Phys. Rev. B* **1986,** *33*, 8822-8824.

(366) Weigend, F.; Ahlrichs, R., Balanced basis sets of split valence, triple zeta valence and quadruple zeta valence quality for H to Rn: Design and assessment of accuracy. *Phys. Chem. Chem. Phys.* **2005,** *7*, 3297-3305.

(367) Grimme, S.; Antony, J.; Ehrlich, S.; Krieg, H., A consistent and accurate ab initio parametrization of density functional dispersion correction (DFT-D) for the 94 elements H-Pu. *J. Chem. Phys.* **2010,** *132*, 154104.

(368) Grimme, S.; Ehrlich, S.; Goerigk, L., Effect of the damping function in dispersion corrected density functional theory. *J. Comput. Chem.* **2011,** *32*, 1456-1465.

(369) Hanwell, M. D.; Curtis, D. E.; Lonie, D. C.; Vandermeersch, T.; Zurek, E.; Hutchison, G. R., Avogadro: an advanced semantic chemical editor, visualization, and analysis platform. *J. Cheminf.* **2012,** *4*, 17.

(370) Halgren, T. A., Merck molecular force field. I. Basis, form, scope, parameterization, and performance of MMFF94. *J. Comput. Chem.* **1996,** *17*, 490-519.

(371) Halgren, T. A., Merck molecular force field. II. MMFF94 van der Waals and electrostatic parameters for intermolecular interactions. *J. Comput. Chem.* **1996,** *17*, 520-552.

(372) Halgren, T. A., Merck molecular force field. III. Molecular geometries and vibrational frequencies for MMFF94. *J. Comput. Chem.* **1996,** *17*, 553-586.

(373) Halgren, T. A.; Nachbar, R. B., Merck molecular force field. IV. Conformational energies and geometries for MMFF94. *J. Comput. Chem.* **1996,** *17*, 587-615.

(374) Halgren, T. A., Merck molecular force field. V. Extension of MMFF94 using experimental data, additional computational data, and empirical rules. *J. Comput. Chem.* **1996,** *17*, 616-641.

(375) Halgren, T. A., MMFF VI. MMFF94s option for energy minimization studies. *J. Comput. Chem.* **1999,** *20*, 720-729.

(376) Larriba, C.; Hogan Jr, C. J., Ion mobilities in diatomic gases: measurement versus prediction with non-specular scattering models. *J. Phys. Chem. A* **2013,** *117*, 3887-3901.

(377) Kim, H., Experimental and theoretical investigation into the correlation between mass and ion mobility for choline and other ammonium cations in N 2. In *Multiscale and Multiphysics Computational Frameworks for Nano-and Bio-Systems*, Springer: 2011; pp 65-83.

(378) Shrivastav, V.; Nahin, M.; Hogan, C. J.; Larriba-Andaluz, C., Benchmark comparison for a multi-processing ion mobility calculator in the free molecular regime. *J. Am. Soc. Mass Spectrom.* **2017,** *28*, 1540-1551.